# *INFRARED OBSERVATIONS AND THERMAL EMISSION MODELS OF ASTEROIDS*

A Thesis submitted for the degree of Doctor of Philosophy

by

Simon F. Green

Department of Astronomy

University of Leicester

1985





ProQuest LLC
789 East Eisenhower Parkway
P.O. Box 1346
Ann Arbor, MI 48106-1346

## Acknowledgements

During the course of my work at Leicester I have received help from a number of people. I would like to express my thanks to the members of the department, who are always willing to help with any problem, and for making my stay so enjoyable. Also to those in the postgrad lab who put up with my verbal abuse of the computer, answering my questions when I was too lazy to consult the manuals, and spurring me on to ever more mediocre performances on the BBC. Particular thanks to the Solar System group: Nick for reducing some of the observational data and providing his analysis of the Tempel-2 tail particle dynamics; Robert for helping with the numerical taxonomy and lightcurve data for 44 Nysa and drawing a number of diagrams; John for "holding the fort" at RAL; and Charon for showing up some of my areas of ignorance by requiring explanations in words of one syllable.

I am also indebted to Mr. Mike Sackin for assistance with the use of the numerical taxonomy program; Mr. Gordon Taylor for providing accurate ephemerides and Dr. Andrew Sinclair for a copy of the RGO ephemeris program; Dr. Dave Aitken for the use of his spectrophotometer and assistance with the observations, and Dr. Pat Roche for preliminary analysis of the data; everyone who made my observing trips so successful and enjoyable; Dr. Brian Stewart for constant assistance with the fast-moving object software and data analysis, and others at RAL, too numerous to name, who helped make the project such a success.

Special appreciation is due to Professor Jack Meadows for supervising the project, providing valuable opportunities and advice, and for not being around when I didn't need him.

Finally, a thankyou to my parents for their continual support, and to C for her help and encouragement, and much more.

CONTENTS


| | | |
|---|---|---|
| CHAPTER 1 | INTRODUCTION. | 1.1 |
| | | 1.4 |
| CHAPTER 2 | CLASSIFICATION. | 2.1 |
| 2.1 | Introduction. | 2.2 |
| 2.2 | Orbit distribution and asteroid families. | 2.2 |
| 2.3 | Physical properties. | 2.5 |
| 2.4 | Numerical taxonomy. | 2.9 |
| 2.4.1 | Introduction. | 2.9 |
| 2.4.2 | The method. | 2.10 |
| 2.4.3 | Asteroid dendrograms. | 2.14 |
| | | 2.21 |
| CHAPTER 3 | ASTEROID THERMAL MODELS. | 3.1 |
| 3.1 | Introduction. | 3.2 |
| 3.1.1 | Asteroid diameters and thermal emission. | 3.2 |
| 3.1.2 | Thermal emission from the Moon. | 3.7 |
| 3.1.3 | Thermal emission from asteroids. | 3.10 |
| 3.2 | The radiometric method of diameter determination. | 3.15 |
| 3.3 | The standard model. | 3.16 |
| 3.4 | Emissivity effects - 8-13μm spectra. | 3.26 |
| 3.4.1 | Introduction. | 3.26 |
| 3.4.2 | Observations. | 3.27 |
| 3.4.3 | Discussion. | 3.27 |
| 3.4.4 | Conclusions. | 3.38 |
| 3.5 | Phase effects - modified standard models. | 3.39 |
| 3.5.1 | Projected model. | 3.39 |
| 3.5.2 | Modified projected model. | 3.41 |
| 3.5.3 | Fast rotating model. | 3.43 |
| 3.5.4 | Comparison of models. | 3.43 |
| 3.6 | Removal of emitted flux from reflection spectra. | 3.47 |
| 3.6.1 | Introduction. | 3.47 |
| 3.6.2 | Observations. | 3.49 |
| 3.6.3 | Discussion. | 3.54 |
| 3.7 | Thermophysical model. | 3.60 |
| 3.7.1 | Introduction. | 3.60 |
| 3.7.2 | Calculation of the model. | 3.61 |
| 3.7.3 | Application of the model. | 3.64 |
| | | 3.66 |
| CHAPTER 4 | IRAS SEARCH FOR FAST-MOVING SOLAR SYSTEM OBJECTS. | 4.1 |
| 4.1 | Introduction. | 4.2 |
| 4.2 | Earth-approaching asteroids. | 4.5 |
| 4.3 | The focal plane array. | 4.11 |
| 4.4 | Survey scan strategy. | 4.14 |
| 4.5 | The FMO software. | 4.16 |
| 4.6 | Selection parameters. | 4.20 |
| | | 4.22 |

CHAPTER 5 RESULTS OF THE FAST-MOVING OBJECT SEARCH. 5.1
5.1 Implementation of the program. 5.2
5.2 Selection effects in the FMO search. 5.4
5.3 Numbered asteroids. 5.5
5.3.1 Brightness detection limits. 5.6
5.3.2 Motion limits. 5.22
5.4 Main belt asteroid discoveries. 5.29
5.4.1 FMO detections. 5.29
5.4.2 1983QF and 1983QG. 5.30
5.4.3 Final asteroid data analysis. 5.33
5.5 Earth-crossing asteroid discoveries. 5.35
5.5.1 Selection effects and comparison with ground-based population estimates. 5.35
5.5.2 Diameter determinations. 5.38
5.6 1983TB - An extinct cometary nucleus? 5.45
5.6.1 Introduction. 5.45
5.6.2 Ground-based observations. 5.47
5.6.3 Discussion. 5.52
5.6.4 Conclusions. 5.57
5.7 Comets. 5.58
5.7.1 Comet discoveries and population estimates. 5.58
5.7.2 Temperatures and dust production. 5.66
5.7.3 The infrared tail of P/Tempel-2. 5.71
5.8 Unidentified FMO's. 5.78
5.80

CHAPTER 6 IRAS ADDITIONAL OBSERVATIONS. 6.1
6.1 The AO program. 6.2
6.2 44 Nysa. 6.4
6.2.1 Introduction. 6.4
6.2.2 Observations. 6.5
6.2.3 Discussion. 6.7
6.2.4 Conclusions. 6.14
6.14

CHAPTER 7 CONCLUSION. 7.1
7.6

REFERENCES. R.1
R.21

APPENDICES. A.1
A Published occultation diameters. A.2
B IRAS FMO alerts. A.5
C IRAS spectral responses and correction factors. A.9
D Orbital elements of IRAS discoveries. A.12
E Coordinate systems for calculation of thermal models. A.13
F Publications. A.17
A.19

# CHAPTER 1

# INTRODUCTION

After the discovery of the first four asteroids (1801-1807), and the end of the search for a "missing planet" between Mars and Jupiter, the interest in minor planets waned. No more were discovered until 1845, when, with improvements to star catalogues and charts, ~4 asteroids per year were found. In the 1890's, with the introduction of photography, the discoveries multiplied, but astronomers interests were in the new fields of spectroscopy and astrophysics. However, work continued, with the discovery of 433 Eros (1898) and its light variation, explained by rotation of an irregular body; discovery of the first Trojan (1906) orbiting at the Lagrangian point, $L_4$ of the Jupiter-Sun system; work on asteroid families by Hirayama and others; discovery of the first Earth-crossing asteroid (1932); and the setting up of minor planet centres where observations were catalogued and orbits calculated for the hundreds of new objects observed each year.

It was not until the 1970's that physical studies of asteroids became an important discipline, largely because of the space program and advances in meteoritics, observational techniques and instrumentation. Following large scale surveys of UBV photometry, spectrophotometry, polarimetry and radiometry, classification schemes were developed in an attempt to relate the physical properties of asteroids to mineral types. A review of the orbital and physical classification of asteroids is given in chapter 2 and the technique of numerical taxonomy is applied to some of the data.

Size determinations of the asteroids are of fundamental importance for the understanding of their reflectivities and

surface composition. Chapter 3 contains a review of the methods of diameter determination and an explanation of the importance of the radiometric method for systematic surveys of the size distribution of asteroids. This method involves observations in the optical and infrared coupled with thermal emission models. The radiometric method and the "standard" thermal model normally used for large main belt asteroids are described in sections 3.2 and 3.3. Medium resolution spectra from 8-13μm, taken to examine the possibility of wavelength dependent emissivity variations, are presented (section 3.4) which show the general validity of this model. The limitations of the standard model in particular circumstances are discussed and some modified models are presented in sections 3.3 and 3.5. The use of thermal models to remove the emitted flux from reflection spectra is explained in section 3.6 and observations of asteroids in the 3-4μm region are analysed. This region contains an absorption feature produced by water of hydration in clays or salts and found in many carbonaceous chondrite meteorites. In section 3.7, thermophysical models, which allow for conduction into the surface of the asteroid, are discussed, and the calculation of the model fluxes is explained.

The Infrared Astronomical Satellite (IRAS), launched in 1983, was designed to produce an all-sky survey at four infrared wavelengths. The sensitivity and wavelengths of the bands were such that it could potentially detect the majority of numbered, and many thousand unknown asteroids, from their thermal emission. As a consequence of the processing methods, all moving objects were removed from the data. When the final analysis was performed in the US, the rejected data

was saved to search for asteroid detections, but any new objects found would almost certainly not be recoverable. The data were initially received at the ground tracking station at the Rutherford Appleton Laboratories in the UK, where preliminary analysis was performed. The fastest moving Solar System objects were rejected at this stage, so software was written to search for new Earth-approaching asteroids in near real-time to allow for ground-based recovery. The properties and importance of these asteroids are discussed in section 4.2. The software is described in chapter 4, and the implementation of the search, and its results, in chapter 5. As well as detecting several hundred numbered asteroids and 5 known comets, 2 new main belt asteroids, 2 Apollo asteroids, 6 comets and an infrared tail on comet Tempel-2 were discovered. Chapter 5 contains an analysis of these data using the thermal models described in chapter 3, with emphasis on the results that may be expected from the final moving object data analysis. Some ground-based observations of the unusual Apollo asteroid (3200) 1983TB, which was discovered by the program, are also presented.

In addition to the all-sky survey, IRAS performed additional observations of selected objects. The AO program, and some of the asteroid observations are discussed in chapter 6.

Chapter 7 contains a summary of the results and conclusions from the work contained in this thesis, and suggestions for further studies.

# CHAPTER 2

# CLASSIFICATION OF ASTEROIDS

## 2.1 INTRODUCTION

The first asteroid 1 Ceres was discovered by Piazzi in 1801 after some years of speculation over the presence of a "missing planet" at 2.8 A.U., as predicted by the Titius-Bode "law". However the new planet's magnitude was much fainter than Mars or Jupiter, and after three more minor planets were found in the next six years, the suggestion by Olbers that they were fragments of an exploded planet appeared to have some foundation. By the turn of the century, with the advent of astronomical photography, several hundred asteroids were known. Today there are over three thousand numbered asteroids with reliable orbits and many more with preliminary elements.

The purpose of any classification scheme is to sort individual members of a population with similar properties into sub-groups in order to assess the significance of those properties, and to identify unusual objects. In the case of asteroids, classification is based both on orbital elements and observed optical properties in order to learn more about their physical properties and evolution.

## 2.2 ORBIT DISTRIBUTION AND FAMILIES

The non-random distribution of asteroid orbital elements was first noticed and explained by Kirkwood (1867). He identified the gaps in the frequency distribution of semi-major axes as corresponding to low order commensurabilities with Jupiter. There are also groups beyond the main belt

(2.2-3.2 A.U.) which have mean semi-major axes at particular commensurabilities: the Hildas at 3:2, Thule at 4:3 and the Trojans at 1:1. The positions of higher order resonances appear to correlate well with the radial distribution of asteroid orbits, some corresponding to minima or gaps in the distribution and some to maxima. More recently, gaps have been noticed in distributions of proper eccentricity and inclination which have also been identified with resonant phenomena, for example, those bordering the Phocaea region.

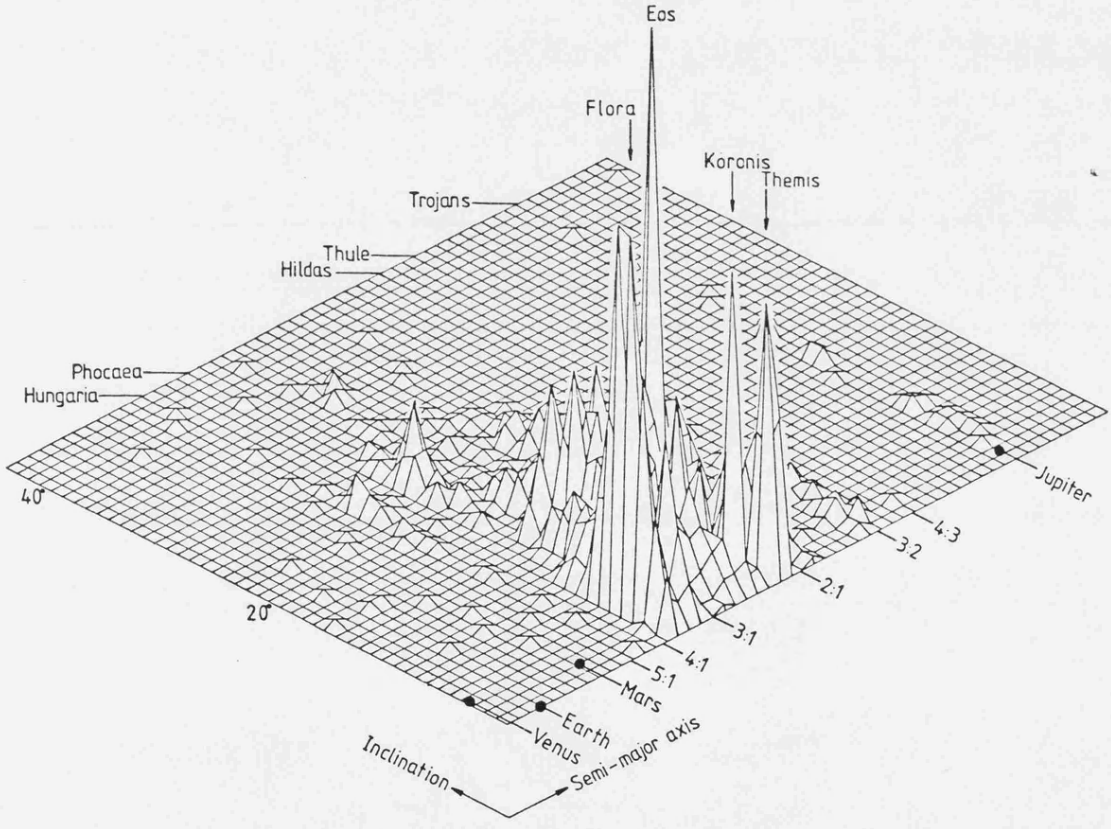


Fig 2.1 Distribution of asteroids in semi-major axis and inclination showing the main groups and four most populous families. Where possible, proper elements have been used. Data from TRIAD (Bender, 1979; Williams, 1979).

The first discussion of smaller scale asteroid groupings is found in a series of papers by Hirayama (1918;1919;1923; 1928;1933) in which he identified nine obvious clusters in proper orbital elements (i.e. corrected for perturbations of

the major planets) called "families". Brouwer (1951) confirmed these results using a larger sample of asteroids and improved orbital elements. Arnold (1969) extended these studies and made statistical tests for significant deviations from a random distribution of asteroid orbits. Since the Palomar-Leiden Survey (van Houten et al., 1970), a proliferation of families has been suggested, and the problem has been defining which are significant, and where family boundaries lie. Detailed searches for families have been made by Lindblad and Southworth (1971), and Williams (1971;1975) who reported over 100, with nearly half of the asteroids contained in them. However, Carusi and Messaro (1978), using a different approach, found that all but ten families did not have statistical relevance, although Gradie et al (1979) have suggested that this is due to an increase in the "noise level" of background asteroids in their method. Determination of family membership and the reality of a family is essential before any physical studies relating members of that family can be interpreted.

Although it was natural to assume (Olbers, 1805) that the asteroids were formed from an exploded planet, current evidence from physical properties of asteroids and meteorites suggests that this was not necessary, and that they were produced by accretion of kilometre-sized planetesimals condensing throughout the early solar nebula (see reviews by Safronov 1979, and Cameron 1979). At some point in the evolution, the velocities of the proto-asteroids were enhanced and they were drastically depleted, probably by scattering of objects passing close to Jupiter, and their subsequent encounters. At this point relative velocities

would be such that collisions would result in destruction rather than accretion. Attempts have been made to "reconstruct" asteroid families based on their physical properties, for example, the homogeneous Eos and Koronis families (Gradie and Zellner, 1977; Gradie, 1978), and the heterogeneous Nysa/Hertha families (Zellner et al., 1977c). Although these are necessarily speculative, it is clear that we may be observing material from the interiors of Solar System objects.

## 2.3 PHYSICAL PROPERTIES

The first astronomer to consider that asteroids might not be grey reflectors of sunlight was Bobrovnikoff (1929). From microphotometry of photographic spectra he deduced real differences between 12 asteroids and obtained a rotation period for 4 Vesta, close to the currently accepted one, from changes in its spectra. It was not until the 1950's when systematic UBV photometry was applied to asteroids that any classification was possible. Kitamura (1959) and Wood and Kuiper (1963) noted that asteroid colours appeared to cluster around certain regions in the U-B vs. B-V diagram. Hapke (1971) introduced four groups based on UBV colours, but they did not provide much insight into the physical properties of the asteroids' surfaces.

Chapman (1971) and Chapman et al. (1973) made spectrophotometric observations of over a hundred asteroids and related them to UBV photometry. This work was the basis of the subsequent development of taxonomic systems. They

grouped the spectra according to shape and steepness of slope, and looked for correlations with orbital elements and common meteorite types (Chapman 1973). This led to the recognition of the two main groups of asteroids when Zellner noted a correlation between U-V colour and the presence or absence of an absorption band in the spectra. The spectra of C and S type asteroids had similarities with carbonaceous and stony meteorites, respectively (Zellner, 1973; Chapman, 1974). This division became even more apparent when polarimetric and radiometric albedos became available (Zellner et al., 1974; Morrison, 1974) (See section 3.1). The C and S groups were further defined by Chapman et al. (1975), using a number of optical and near infrared parameters, and those that did not fit either type were designated U (for unclassifiable). They concluded that the C-types were more common, particularly in the outer belt, in a sample of 99 asteroids.

Earlier, McCord and Chapman (1975) had used a similar method to define 27 main groups, 13 of which contained only one object, so it was not surprising that new taxonomic types were subsequently introduced. Zellner et al. (1975) suggested that some of Chapman's U-types should be classified as new M-types (since it was tentatively suggested that their colours and spectra implied some metallic properties). Zellner and Gradie (1976) defined 44 Nysa and 63 Angelina as type E (colours and spectra similar to enstatite achondrite meteorites). Zellner and Bowell (1977) noted that 349 Dembowska seemed to have more properties in common with ordinary chondrites than the S-type asteroids. By 1977 the system proposed by Bowell et al. (1978) was becoming widely

used. This scheme, which was based solely on observed characteristics and was independent of mineralogical considerations, classified asteroids into the C,S,M,E and U types and added class R (reddish), which included 349 Dembowska.

At this time, Gaffey and McCord (1977) noted that this classification might be misleading since it was not necessarily equivalent to compositional groups. They proposed that asteroids should be classified according to their spectra with emphasis on the nature of the 1μm absorption feature and the curvature of the continuum at wavelengths shorter than 0.7μm. They separated 60 asteroids into about a dozen groups and sub-groups which were then interpreted in terms of asteroid mineralogy. Chapman et al. (1978), using a similar method, found 35 different spectral types which were grouped into 16 significantly different inferred mineralogies.

With the introduction of infrared photometry, Veeder et al. (1978) noted that the J-H vs. B-H colour diagram could distinguish between C and M type asteroids, which are coincident in UBV coordinates. Veeder and others have gone on to extend the existing classification schemes by the introduction of additional infrared data (Veeder et al., 1982;1983a). Hartmann et al. (1982) have employed VJHK colours to study the relationship between comets and asteroids, and used them to infer the ratios of volatile ices to dust in these objects. Feierberg et al. (1982) divided a number of S-types into nine groups according to their 0.3 to 2.5μm spectra, and compared them with spectra of meteoritic silicates.

TABLE 2.1

Summary of Asteroid Classes

| TYPE | VISUAL ALBEDO | SPECTRAL REFLECTIVITY |
|---|---|---|
| C | Low (<0.065) | Neutral; slightly less reflective shortward of 0.4μm. |
| S | Moderate (0.07-0.23) | Reddened; Typically an absorption band near 1.0μm. |
| M | Moderate (0.07-0.23) | Featureless; increasingly reflective into red. |
| F | Low (<0.065) | Flat. |
| P | Low (<0.065) | Similar to M, (pseudo-M). |
| D | Low (<0.065) | Very red longward of 0.7μm. |
| E | Very high (>0.23) | Featureless; flat or slopes up into red. |
| R ? | Very high (>0.23) | Very red, with deeper absorption bands than S. |
| A ? | High (0.17-0.25) | Similar to R; abruptly brighten from 1.6 to 2.2μm. |
| U | Varied | Unclassifiable in this system; includes Vesta, Pallas, and other unique objects that may be the sole members of undefined types. |

(From Gradie and Tedesco, 1982)

Recently, several new classes have been added to those of Bowell et al. (1978). Degewij and van Houten (1979) defined a new RD class with low albedos and red colours longward of 0.7μm. This has now been re-labelled D by Gradie and Tedesco (1982). They have also introduced the new classes P (from "pseudo M") which have M-like spectra, but low visual albedos and flat 0.3-1.1μm spectra. Veeder et al. (1983b) have re-examined the R-types and found that only 349 Dembowska could be assigned this type, with two others forming a new group A with very red infrared colours, and the remainder being S,SU,SRU or RAU. The designations are intended to minimise the number of mis-classifications. For

example, SRU means not C,M,E,P,F or A; "It does not deny the possibility that the groups [S or R] could be subdivided, nor that the object could ultimately be reclassified into a new, presently unrecognised type." (Zellner, 1979a). The implication is that new groups may be introduced, and some asteroids may be reclassified. This may be the case when a large sample have been observed using the new 8-colour photometric system, which has filters selected at wavelengths diagnostic of asteroid mineralogy (Tedesco et al., 1982). Gradie and Tedesco (1982) have used preliminary results for 400 asteroids in their investigations into the heliocentric distribution of the taxonomic types.

## 2.4 NUMERICAL TAXONOMY

### 2.4.1 Introduction

As new observational techniques have been developed, and instrumental sensitivity has improved, the number of parameters used for classification has increased, and groups have been revised and increased in number. Ultimately there may be a proliferation of small groups with a few members differing only slightly from each other. An alternative approach is to assume that each asteroid has unique properties, and to examine how close or distant its limits with other asteroids are. If the input parameters are quantitative this leads to some sort of numerical taxonomy.

Numerical taxonomy has been defined by Sokal and Sneath (1963) as the numerical evaluation of the affinity or similarity between taxonomic units, and the ordering of these

units into taxa on the basis of their affinities. By using numerical techniques and including many parameters without preselection, it should be possible, in principle, to produce stable taxonomies which are unlikely to be overthrown by later discoveries.

The technique of numerical taxonomy has been widely applied to biological systems, in which the same problems of grouping many unique but similar individual objects are found. The merit of the method is that it does not depend on preconceived ideas of physical links between the groups, and that it connects objects according to the similarity of a large number of observed characteristics.

## 2.4.2 The Method.

Using numerical taxonomy, the degree of similarity between individual members of a population is represented by similarity coefficients, with one coefficient for every pair of objects. This produces a series of points in classification space, with their separations or taxonomic distances being related to the degree of similarity. The results can conveniently be displayed as a tree diagram or dendrogram, with taxonomic distance as the vertical axis. the level at which branching occurs indicates the closeness of the relationship between individuals or groups.

For a population of m objects with n observed parameters $x_n$, the similarity coefficients $S_{ij}$ $(i<j<m)$ are calculated from

$$S_{ij} = \sum_{k=1}^{n} \left( [(\underline{x}_k)_i - (\underline{x}_k)_j]^2 / n^* \right)^{1/2}$$

where $n^*$ is the number of parameters which have been observed

Similarity matrix $S_{ij}$

| | | | | | |
|---|---|---|---|---|---|
| 2 | (.1) | | | | |
| 3 | .25 | .15 | | | |
| 4 | .4 | .6 | .7 | | |
| 5 | .5 | .3 | .8 | .9 | |
| 6 | .6 | .7 | .45 | .75 | .3 |
| j/i | 1 | 2 | 3 | 4 | 5 |

Circle round lowest similarity in matrix.

Object 1 joins object 2 at a taxonomic distance of 0.1

Recompute similarities - using unweighted average linkage

Each new similarity coefficient (underlined) is the average of previous values for objects 1 and 2.

| | | | | |
|---|---|---|---|---|
| 3 | (.2) | | | |
| 4 | .5 | .7 | | |
| 5 | .4 | .8 | .9 | |
| 6 | .65 | .45 | .75 | .3 |
| | 1,2 | 3 | 4 | 5 |

1,2 joins 3 at 0.2

| | | | |
|---|---|---|---|
| 4 | .567 | | |
| 5 | .533 | .9 | |
| 6 | .583 | .75 | (.3) |
| | (1,2),3 | 4 | 5 |

5 joins 6 at 0.3

| | | | |
|---|---|---|---|
| 4 | .567 | | |
| 5,6 | (.558) | .825 | |
| | (1,2),3 | 4 | |

(1,2),3 joins 5,6 at 0.558

| | |
|---|---|
| 4 | (.67) |
| ((1,2),3),(5,6) | |

((1,2),3),(5,6) joins 4 at 0.67

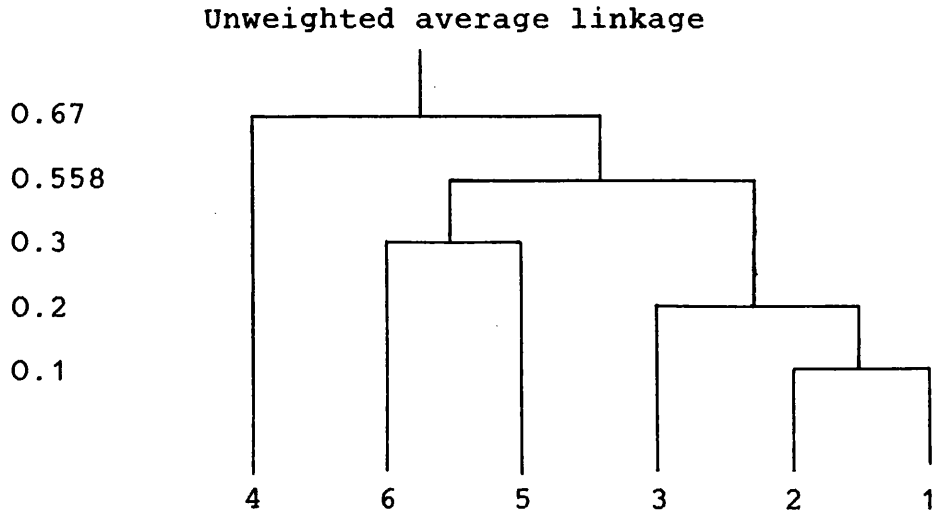


Fig. 2.2 Production of a dendrogram from similarity coefficients.

for both objects. This allows for missing data for some of the objects, but can bias the sample if too many data are missing. The $\underline{x}$ are data which have been scaled such that the separation between extreme values is unity (i.e. each observed parameter has equal weight). Weighting can be introduced here to emphasise the contribution of certain parameters to the classification. Fig. 2.2 illustrates the production of a dendrogram for an example where m=6, with no weighting factors.

The data used in the production of the asteroid dendrograms were obtained from TRIAD (Tucson Revised Index of Asteroid Data), Zellner (1979b). Two different data sets were employed:-

1) The parameters used by Bowell et al (1978)

$P_v$ The geometric visual albedo (obtained from a weighted mean of radiometric and polarimetric albedos).

$P_{min}$ The minimum percentage polarisation (see section 3.1.1).

U-B Colour.

B-V Colour.

R/B $R_{0.7}/R_{0.4}$ The ratio of reflectance at 0.7μm to that at 0.4μm - a measure of the redness of the visible spectrum.

BEND $(R_{0.56}-R_{0.4}) - (R_{0.73}-R_{0.56})$ a measure of curvature through the visible.

DEPTH The reflectance of the bottom of the $F^{++}$ absorption feature around 0.9μm divided by the highest reflectance on the short wavelength side of the band.

2) Spectrophotometry

The relative reflectance (reflectance at 0.56μm = 1.0) for a number of wavelengths in the 0.3-1.1μm range.

($p_v$ and $P_{min}$ from Morrison and Zellner (1979), U-B and B-V from Bowell et al (1979), other data from Chapman and Gaffey (1979).)

The spectrophotometry implicitly contains the information in U-B, B-V, R/B, BEND, and DEPTH. The two data sets can be used to compare a dendrogram based only on observed spectra with one based on a number of parameters selected as being potentially diagnostic of mineral type.

TRIAD contains complete data sets of type 1 for 60 asteroids (82 if $P_{min}$ is excluded), and 277 asteroids with type 2 data. The wavelength coverage of the spectrophotometry is variable, and although there are measurements at up to 26 wavelengths, only 12 of these are complete for all 277 asteroids. Although the calculation of similarity coefficients allows for missing data, any dendrogram based on a data set in which there are many objects with few characteristics in common will not be of much value. This effect will be discussed in the following section.

Although each parameter in the data set should be scaled to unity using the extreme values of those parameters before similarity coefficients are calculated, this has not been done for the asteroid data. This is because introduction of new asteroids may change the extreme values, and therefore the scaling for one or more parameters, and thus change the relative weight of those parameters. These new data could

then change the relative positions of other asteroids in the dendrograms. The solution is to select artificially the scaling factors, so that the weighting does not change. Fortunately, the range of variation of all the parameters in this study is a few tenths, so the relative weights of each are similar without the necessity for setting scaling factors.

### 2.4.3 Asteroid Dendrograms

Fig. 2.3 compares dendrograms produced from relative reflectance data: a) at all 26 wavelengths (0.33-1.1μm), b) with 12 selected wavelengths (0.4-0.8μm). The 12 selected wavelengths have complete spectrophotometry data sets, whereas in total about 25% of the reflectance data is missing with individual asteroids having from 13 to 24 non-zero reflectance values. Fig. 2.3a has branches at larger taxonomic distances due to the increased number of input parameters. Both dendrograms show the division into C and S-like regions together with a number of unusual objects. However, some individual objects or small groups have completely changed their positions. This is due in part to the creation of artificial differences between essentially similar spectra (because missing data points are not being compared during the computation of similarity coefficients). It is also partly because the complete wavelength sets cover a range of only 0.4-0.8μm and so do not extend to the absorption bands around 0.9μm which are highly diagnostic of mineral type. A complete spectrophotometry data set over the extended range of 0.3 to 1.1μm is required to evaluate the full potential of this type of dendrogram.

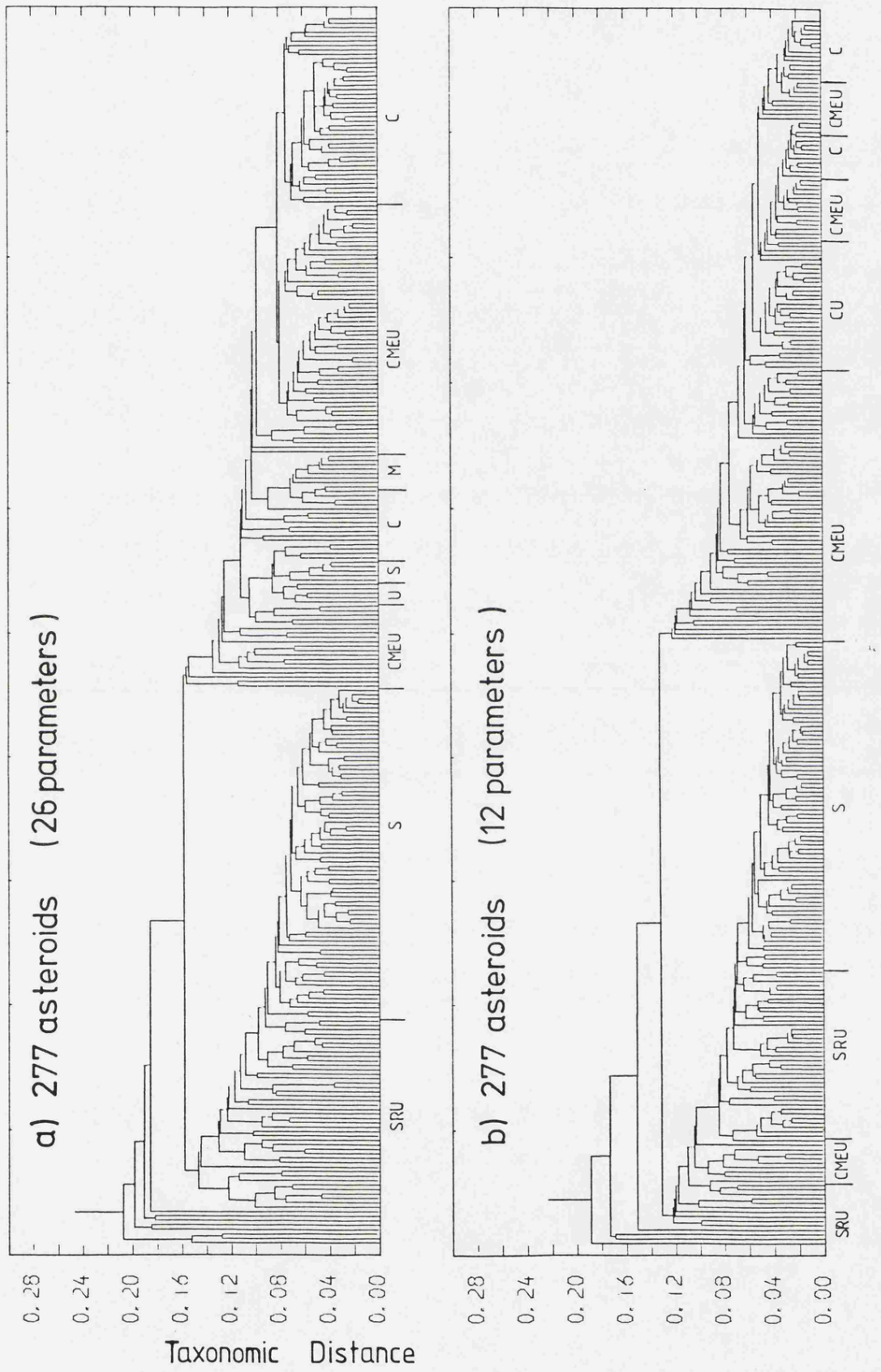


Fig. 2.3 Dendrograms produced for 277 asteroids with: a) 26 parameters - relative reflectance at wavelengths from 0.3 to 1.1μm with ~25% missing data. b) 12 parameters - relative reflectance at wavelengths from 0.4 to 0.8μm with no missing data. The main asteroid types in each region are indicated.

Fig. 2.4 is a dendrogram produced from the type 1 data for 60 asteroids. The division between C and S-like objects occurs at very high taxonomic distance, and further branches at high levels separate the regions labelled I to IV. Region I contains six asteroids, five of which are classified in TRIAD as C-types and 51 Nemausa designated U. This has a low albedo and high $P_{min}$ characteristic of C's, but colours which lie between the C and S ranges. Region II contains a number of C, M and U types, some of which have been re-classified as F,P or D. These all have low albedos and flattish spectra. Region III contains all but one of the S-types in this sample, and region IV a few high albedo objects.

82 asteroids have complete type 1 data sets when $P_{min}$ is excluded; the resultant dendrogram is presented as Fig. 2.5. The levels of branching are lower, reflecting the smaller number of input parameters. The C and S types are again well separated in regions I and III, respectively, but 51 Nemausa has moved into region IVb. The distinction between C-types in region I and CMFP-types in region II is less clear-cut, and, with the removal of $P_{min}$ (which is, in part, albedo dependent), the high albedo E-type asteroid 64 Angelina appears more closely related to M-types which have similar spectra. The reduction in the weight attached to the albedo has also allowed the other E-types to move across to region IVb. The main division in the dendrogram is now between sloping and flat spectra, rather than high and low albedo as in Fig. 2.4.

Fig. 2.6 is a dendrogram containing the same asteroids classified according to their 0.4-0.8μm spectra. The branching occurs at a still lower level due to the removal of

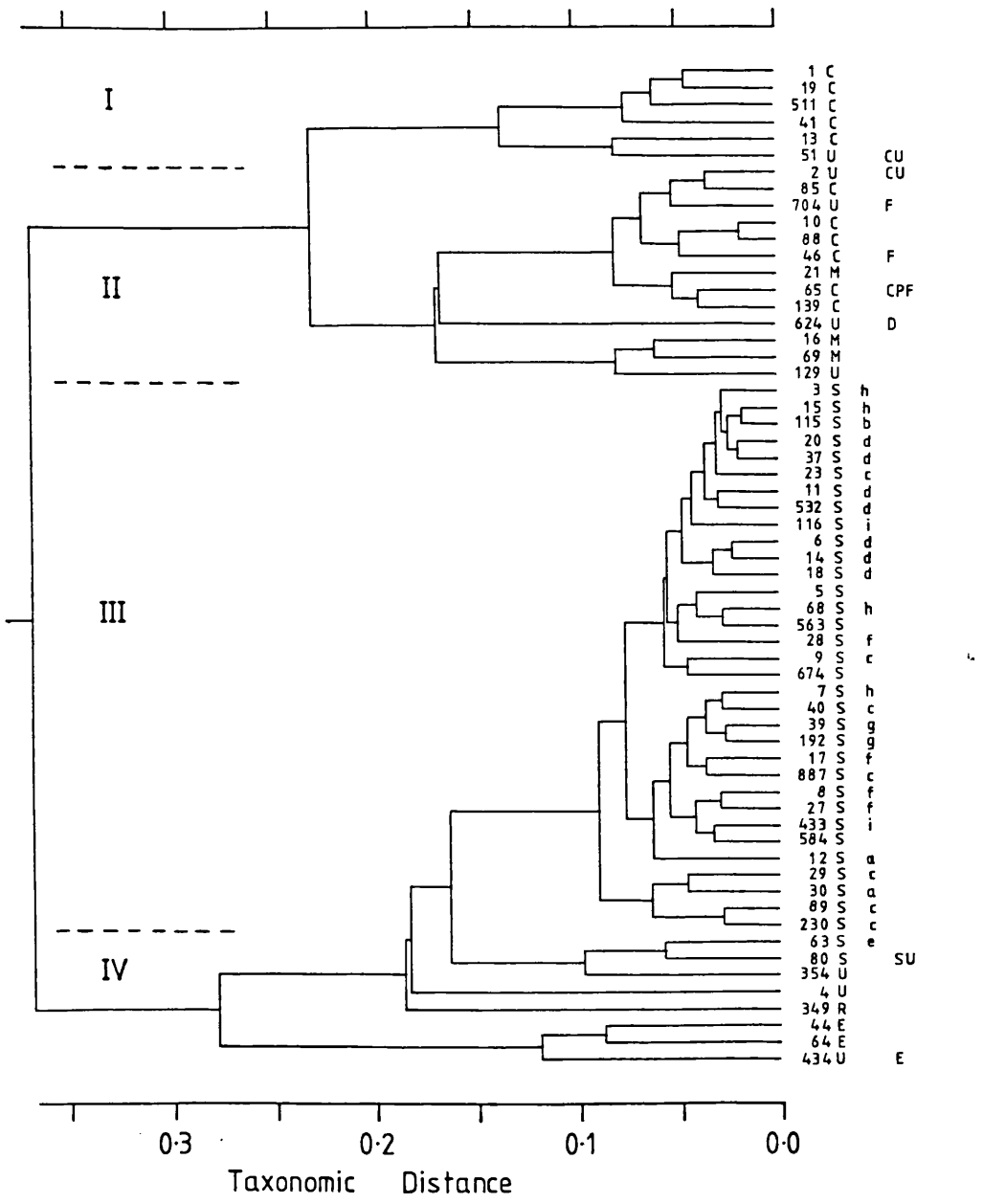


Fig. 2.4 Dendrogram for 60 asteroids using 7 parameters:- $p_v$, $P_{min}$, U-B, B-V, R/B, BEND, DEPTH. The asteroid numbers and TRIAD type designations are indicated, followed by groups defined by Feierberg et al. (1982), and more recent classification. See text for description of regions I-IV.

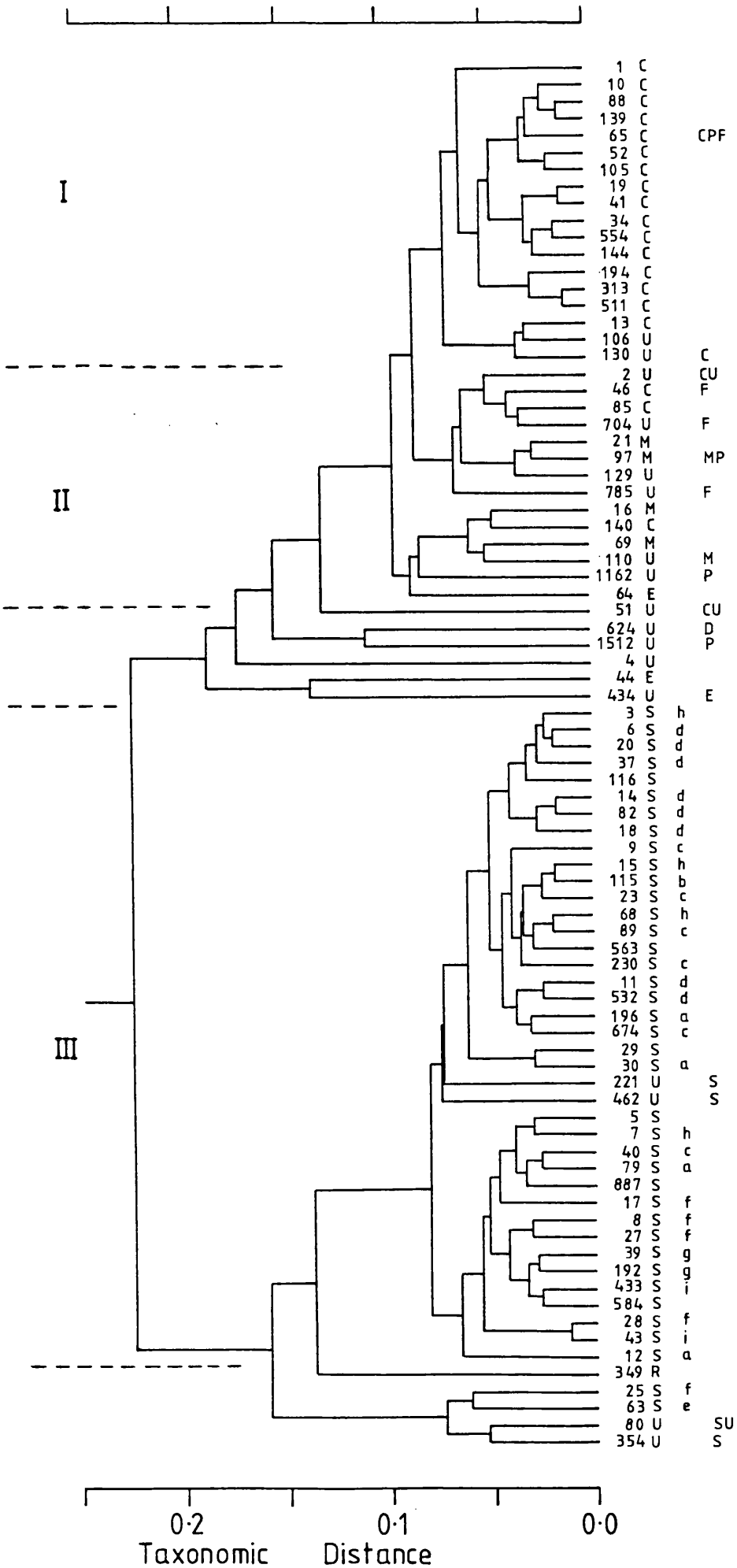


Fig. 2.5 As Fig 2.4, but for 82 asteroids with 6 parameters - $p_v$, U-B, B-V, R/B, BEND, DEPTH.


Fig. 2.6 As Fig 2.4, but for 82 asteroids with 12 parameters - relative reflectance (0.4-0.8μm).

any albedo factor. The distinctions between regions I, II and IVb are no longer apparent, but the bimodality is still present even though a few objects have changed sides. This is not surprising, since although albedo effects and the diverse features at the red end of the spectrum are not represented, the groups are discriminated by the slopes of their spectra. This demonstrates the capability of distinguishing between "S-like" and "C-like" on the basis of UBV colours alone.

Figs. 2.4-2.6 seem to agree well with existing classification schemes, although the distinction between M,P and F types is not marked. This indicates a diversity of properties within groups with rather arbitrarily defined boundaries (eg the original definition of C,S,M,E and R types in Bowell et al., 1978), but may also reflect observational errors in the parameters. Although the asteroids used in this study are "well-observed", errors of a few percent in each parameter would change the lowest levels of branching where taxonomic distances are small, while retaining the overall structure of the dendrogram.

Feierberg et al. (1982) examined the spectra of a number of S-type asteroids, dividing them into nine groups a to i. Fig. 2.6 shows very poor correlation and there are no clearly defined boundaries between groups, indicating that a range of spectral types exists rather than discrete groups. In this dendrogram all parameters are given equal weight, whereas human assessment may offset one feature against another in arriving at an overall result. The parameters used here are reflectance values at specific wavelengths, so regions containing features could be weighted to achieve the same

effect.

These dendrograms illustrate the value of numerical taxonomy in investigating the properties of asteroids both by indicating individual asteroids (or groups) with unusual properties and for comparing different classification schemes. Since types or groups are not pre-defined, new data can be readily introduced and the relative weights of parameters can be varied to emphasise the property of particular interest. With the publication of eight colour photometry, and albedos from IRAS data, a self-consistent data set ideal for this purpose should be available for a large proportion of the numbered asteroids.

# CHAPTER 3

# ASTEROID THERMAL MODELS

## 3.1 INTRODUCTION.

The application of new techniques, such as radiometry and polarimetry, for diameter and albedo determination and attempts to identify asteroid surface mineralogies using spectrophotometry have led to renewed interest in the study of minor planets. Knowledge of the composition and physical properties of asteroids was required in order to understand their role and importance in the formation and evolution of the Solar System. The size distribution of asteroids is fundamental to this understanding.

### 3.1.1 Asteroid Diameters and Thermal Emission.

Early attempts to estimate sizes were confined to direct micrometer measurements of the largest asteroids (e.g. Barnard, 1895) and interferometry (Hamy, 1899). As no asteroid attains an angular diameter larger than a few tenths of an arcsecond, exceptionally good seeing is required for the object to be resolved. The discrepancy between micrometer measurements and those from other methods, and the difficulties of micrometry of small discs close to the seeing limit (Dollfus, 1971) suggest possibly large errors in these measures.

Other direct methods of diameter determination are speckle interferometry and amplitude interferometry (see review by Worden, 1979), which have been applied to a few bright asteroids, and stellar occultations. The number of occultations that may be expected in a year can be calculated for any asteroid using estimates of its diameter, mean motion, horizontal parallax, and stellar density (O'Leary, 1972).

Although an apparently large number of occultations per year will occur, only a few have been successfully observed due to the following factors:-

- Time required for ephemeris/star catalogue comparison,
- Difficulty of predictions for non-catalogue stars,
- Requirement of astrometric refinement immediately before predicted occultations,
- Magnitude of occulted star,
- Occultation track must cross an area containing a number of observatories, permanent or mobile, with suitable telescopes and detectors,
- Weather.

This method does however provide the most reliable size and shape estimates for asteroids, particularly for regularly shaped bodies, when a circular or elliptical limb profile can be fitted to the observations, and light curve data have also been obtained. Millis and Elliot (1979) review the observation and reduction techniques. Appendix A lists successful occultation observations published to date. Occultations provide definitive sizes for a few asteroids but other indirect methods are required to provide a consistent data-base for a large number of catalogued asteroids.

The linear polarisation of light reflected from a solid surface depends on the scattering geometry, surface refractive index (indirectly the albedo and composition) and the surface texture. Due to the lack of detailed theoretical models, interpretation of the polarisation-phase curves of asteroids depends on laboratory simulations.

The percentage polarisation is defined as

$$P(\%)=(I_{\perp}-I_{\parallel})/(I_{\perp}+I_{\parallel}).$$

Figs. 3.1a and 3.1b show polarisation-phase curves for two asteroids. They have negative polarisation at small phases indicative of rough, porous or particulate surfaces. The curves are described by the parameters; $P_{min}$, the maximum depth of the negative branch; $\alpha$ the inversion angle, where the polarisation changes sign; H, the slope of the ascending branch measured at the inversion angle (Fig 3.1c).

Widorn (1967) and Kenknight et al. (1967) suggested a method by which geometric albedos could be derived from polarimetric observations. Bowell and Zellner (1974) showed that the polarimetric slope was to a first approximation independent of composition, texture or wavelength and correlated with geometric albedo [1] only. The relationship can be written

$$\log p = -C_1 \log H + C_2$$

where H is percentage polarisation per degree of phase. Zellner et al. (1977a) adopted $C_1=0.93$ and $C_2=-1.78$ from laboratory measurements of meteorites crushed to similar texture as that believed to exist on asteroids (Fig 3.1d). For the Moon and relatively dark particulate surfaces, limb effects are minor, so asteroid diameters can be computed from

$$2 \log d = 6.244 - 0.4\, V(1,0) - \log p_V$$

(Dollfus and Zellner, 1979). V(1,0) is the absolute visual magnitude, defined as the brightness in the V filter for the asteroid if placed at 1 A.U. and observed from the sun.

---

[1] The geometric albedo $p_\lambda$ at a given wavelength is defined as the ratio of backscattered light from an object compared with a flat Lambertian (diffuse reflecting) disk of unit albedo.

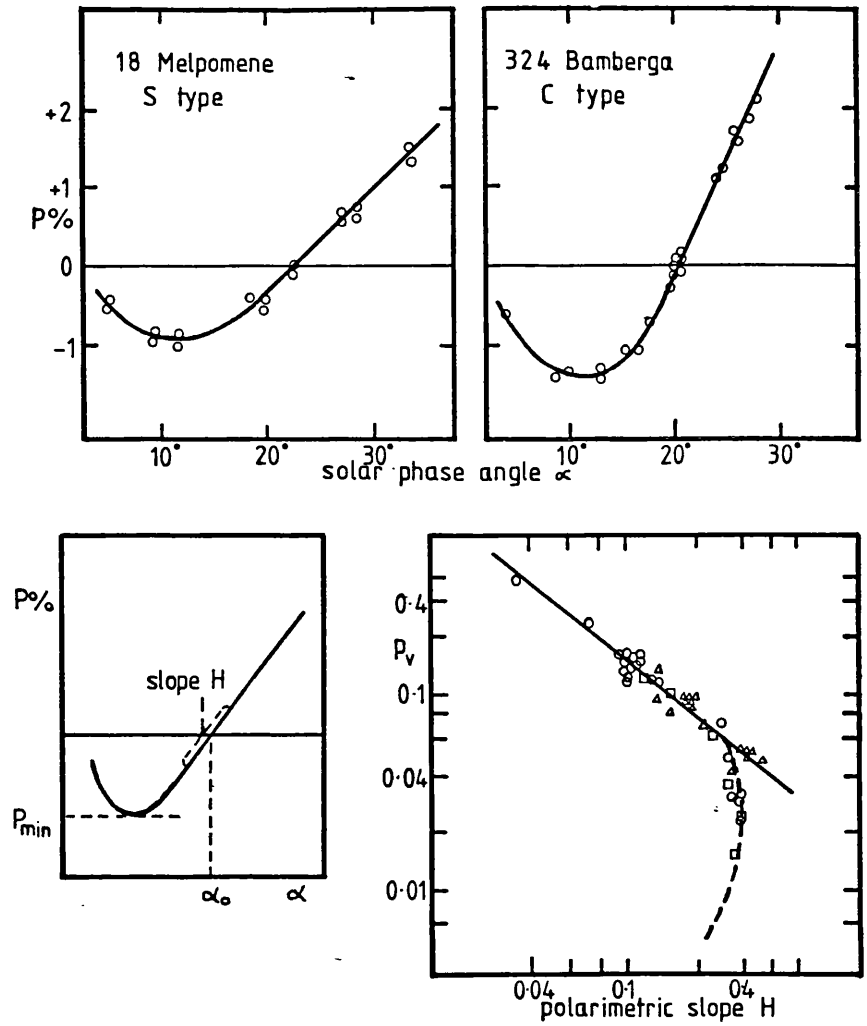


Fig. 3.1 Polarisation phase curves for a) an S-type and b) a C-type asteroid (from Zellner et al. 1977). c) These curves are described by the parameters: $P_{min}$, the maximum depth of the negative branch, $\alpha_0$ where the polarisation changes sign, and H, the slope of the ascending branch measured at the inversion angle. d) Geometric albedo vs. polarimetric slope for (□)artificial carbon-bearing silicates, (Δ) carbonaceous chondrites, and (o) asteroids. The solid line is the relationship log p =-0.93 log H -1.78 adopted from Zellner et al. (1977a) from laboratory polarimetry of meteorites. (From Zellner et al. 1977b.)

Although a large number of asteroids are bright enough for visual polarisation measures, the polarimetric slope-albedo "law" is only empirical and is not obeyed by minerals with albedos less than 0.06. It is therefore not applicable to large numbers of low albedo C and D type asteroids.

At distances of 2 to 4 A.U. the subsolar blackbody temperature is 280 to 200K, giving peak emission at wavelengths of 10 to 15μm. Measurements of asteroid thermal emission through the 10 and 20μm atmospheric windows, together with visual photometry, should in principle provide a method for determining albedos and diameters. The total thermal emission is proportional to the cross-sectional area and the absorbed insolation (i.e. $S_o(1-A)/r^2$ where $S_o$ is the solar constant, r the heliocentric distance in A.U., and A the bolometric Bond albedo [2]). If the surface is in equilibrium with the insolation, the emitted and reflected components must equal the total radiation intercepted. Since the visible and infrared components change in a complementary way with changes in albedo, simultaneous photometry will allow the albedo and effective diameter to be calculated using appropriate thermal models (section 3.2). The advantages of this method are the speed and relative simplicity of the observations, the accuracy (~10%) and the number of asteroids which can be observed with the increasingly sensitive instrumentation being

---

[2] The Bond albedo is defined as the ratio of total reflected to total incident radiation integrated over the surface of the object.

developed. Many hundred radiometric diameters have already been published.

Diameter determinations using the radiometric method require the use of a thermal model to describe the variation in surface temperature and emission. These models require assumptions about the photometric and thermal properties of the surface, since the balance between emitted and absorbed radiation is a global property and the measurements refer to a single orientation. The "standard" thermal model (section 3.3), which assumes spherical asteroids in instantaneous thermal equilibrium with insolation, and grey body emission from each surface element, appears to be valid for large main belt asteroids. More complex models may be required for small or irregularly shaped asteroids (sections 3.5 and 3.7).

### 3.1.2 Thermal Emission from the Moon.

The first measurements of thermal emission from a Solar System object, the Moon, were made in the last century (Rosse, 1869) but the first major studies were made in the 1920's by Pettit and Nicholson (Pettit and Nicholson, 1930; Pettit, 1935;1940). Although the Moon may not necessarily be representative of many of the smaller asteroids it is worth considering the results of these and subsequent studies.

The Moon is much closer to the Sun than most asteroids and therefore radiates at shorter wavelengths, as seen from the Earth it is also an extended source. This does mean, however, that surface temperature changes can be measured for individual surface elements throughout a lunation and during lunar eclipses, and the temperature distribution mapped.

Pettit and Nicholson found that the maximum observed

temperature on the lunar surface was 407K at the centre of the full Moon, rather higher than the blackbody subsolar temperature of 394K. However, they found that the apparent temperature of the subsolar point varied according to lunar phase, and was only 358K at quarter phase. The surface of the moon clearly did not radiate as a Lambert surface. The rapid temperature changes observed at lunar sunset and sunrise and during eclipses provided further evidence for a lunar regolith. A porous or particulate surface in near vacuum can conduct heat only through the small areas of contact and so will be close to equilibrium with the insolation. Numerous measurements of lunar temperature have been made over the lunar cycle and during eclipse, with different spatial resolution, and isothermal maps have been produced, as reviewed by Shorthill (1972). Although various small and large scale anomalies have been found due to albedo and surface terrain differences, the mean temperatures obtained for any given latitude are of most relevance to asteroid thermal models.

Early models (Wesselink, 1948; Jaeger and Harper, 1950; Jaeger, 1953a;1953b) described the Moon as a homogeneous, semi-infinite solid with constant thermal and physical properties. Under these conditions, the one-dimensional heat conduction equation reduces to the form

$$\frac{\delta T}{\delta t} = \frac{k}{\varrho c} \frac{\delta^2 T}{\delta x^2}$$

where $T$ = temperature, $k$ = thermal conductivity, $\varrho$ = density, $c$ = specific heat

with the boundary condition at the surface

$$F_e = F_i + F_c$$

where $F_e$ = emitted flux $\varepsilon\sigma T_o^4$ for a grey body

$F_c$ = conducted flux $k(dt/dx)_{x=0}$ upwards

$F_i$ = absorbed solar radiation

= 0 for lunar night

= $(1-A)\ (S_o/r^2)\ \cos\phi\ \cos(\omega t)$ for lunar day

A = Bond albedo; $\phi$ = lunar latitude of surface element;

$\omega$ = angular rotation rate.

Solution of this equation and boundary conditions for $T_o$ for points at a given lunar latitude, and comparison with observation, will, in principle, yield information on the thermal properties of the surface. In practice, the normalisation of the equations leads to a specific parameter, the thermal inertia $I = (k\varrho c)^{1/2}$. Due to the non-linearity of the boundary conditions, Fourier series methods cannot be used. Wesselink (1948) and Jaeger (1953b) employed different numerical techniques to solve the equations. The lunation data could be fitted using these simple models, giving a thermal inertia considerably smaller than for any terrestrial rocks. However, thermal inertia values obtained during eclipse, where much higher temperature gradients are observed, were not compatible. Jaeger and Harper suggested that this could be due to an increase of thermal conductivity with depth or temperature. The first analysis of microwave observations (Piddington and Minnett, 1949), which probe below the surface, emphasised the problem. They suggested a thin layer of dust on a better conducting sub-stratum. Later models (Muncey 1958;1963; Murray and Wildey, 1964; Linsky, 1966; Ingrao et al., 1966; Winter and Saari, 1969) attempted to take account of these effects.

In-situ measurements of the thermal gradient near the

surface were made in the 1960's, and with the return of samples from the Apollo missions, direct measurements of the properties of surface materials could be made, e.g. Cremers et al. (1971). Emphasis then shifted to the microscopic properties of the samples and studies of lunar "hot-spots" and temperature anomalies observed at high spatial resolution.

### 3.1.3 Thermal Emission from Asteroids.

Unlike the Moon, asteroids are unresolved objects, so direct temperature measurements cannot be made. Knowledge of the physical and thermal properties of their surfaces is far more restricted, and therefore any thermal model will have more free parameters. However, the larger asteroids appear to have similar global photometric properties, lack of atmosphere, low albedos, and particulate surfaces, to the Moon, and so the same general methods can be applied.

The first measurement of thermal flux from an asteroid for diameter determination was made by Allen (1970) of 4 Vesta. He derived a considerably larger diameter and smaller albedo than had been obtained from previous micrometer observations. He treated Vesta as a spherical blackbody in equilibrium with insolation - the basis of the standard thermal model. (This model will be described in detail in section 3.3.) He assumed that the phase dependence of the thermal flux would be linear over the range of [3] phase angles expected, and recognised the problem of an opposition surge in

---

[3] The phase angle is defined as the angle subtended at the asteroid by the Earth and Sun.

brightness due to a rough surface, as had been seen for the Moon. He noted that the effect of rotation on the measured flux (reduction in the solar direction and corresponding increase on the night side) would act in the opposite sense, and so his "infrared diameters" would bear a fairly close resemblance to the true dimensions for the large asteroids detectable at the time.

Matson (1971a;1971b) carried out a program to measure diameters for about 20 asteroids and found that at least one, 324 Bamberga, had an extremely low geometric albedo of less than 4 percent. Matson (1971a) and Hansen (1972) discussed calibration of the radiometric method by observations of the Galilean satellites and Allen (1971) reviewed the technique in the context of the study of asteroids.

Morrison (1973) described the radiometric method (section 3.2) and the effect of corrections to the simple model. He considered errors in the phase integral, q, (defined as the ratio of the Bond albedo to the geometric albedo - see section 3.3), departure of the emissivity from unity over either the passband of interest, or the whole spectrum, rotational or phase effects, and non-isotropic emissivity. He also discussed the problem of calibration of 10 and 20μm monochromatic fluxes from broad-band observations. Radiometric diameters of the Galilean satellites were found to agree with occultation and micrometer measurements to within 5%. Morrison concluded that the technique was not subject to major systematic errors, and diameters could be obtained to ~10% and albedos to 20-30%. Jones and Morrison (1974) calibrated the system by optimising a single parameter (the blackbody subsolar temperature at 1 A.U.) so that the

satellite diameters were fitted, thus implicitly allowing for the unknown peaking of infrared emissivity, the unknown limb darkening, and also the unknown mean infrared emissivity. One problem with this approach was that the Galilean satellites have much higher albedos, lower surface temperatures, and different surface mineralogies than typical main belt asteroids. Chapman et al. (1975) compared visual polarisation data for about twenty asteroids with radiometry to generate a calibration, but the polarisation albedo effect for very dark materials and the correlation used were later found to be invalid (Hansen, 1977; Zellner et al., 1977a; 1977b). By the time Morrison (1977a) produced a list of asteroid albedos and diameters combining radiometric and polarimetric measurements calibrated on this system, a total of almost 200 had been observed. These data were uniformly calibrated according to flux scales described by Morrison (1977b) and contained data from Cruikshank and Morrison (1973), Morrison (1974;1976;1977b), Morrison and Chapman (1976), Morrison et al. (1976), Hansen (1976a), and Cruikshank (1977). This gave a self-consistent uniform data set, but its absolute calibration remained uncertain and differed from that of Hansen (1976a). Although Hansen obtained simultaneous infrared and visible photometry, each asteroid was only measured once. Hansen's model was similar in principle, but assumed no peaking of infrared emission towards small phase angles. He solved simultaneously for 10 and 20μm data allowing the bolometric emissivity to appear as a free parameter in his solutions, assumed a non-zero flux from the unilluminated hemisphere, and implicitly assumed the radiometric phase coefficient to be identical to that of the

visible. Hansen's techniques caused his calculated diameters to be systematically larger and albedos smaller than those from Morrison's "standard model". However, in a later paper (Hansen, 1977), he included a modelled opposition effect due to beaming from craters, supported by data from the Moon and Mercury, and obtained results similar to those of Morrison. His opposition effect corrections were based on negative topography (craters), whereas other workers (Lebofsky et al., 1978; Matson et al., 1978) used a beaming parameter, $\beta$, which has the same effect as adjusting the effective temperature of the subsolar point (see section 3.3).

Recently, a direct calibration of radiometric diameters was made using occultation data for 2 Pallas and 3 Juno, Voyager imaging data of Callisto, and $\alpha$ Tau as a primary standard (Brown et al., 1982). Although a slight downward revision of the diameter scale was required, this work confirmed the general validity of the method. This calibration was used in the derivation of diameters and albedos of 36 more asteroids (Brown and Morrison, 1984) selected primarily to resolve taxonomic ambiguities resulting from the lack of albedo information.

In 1975 the close approach of Amor asteroid 433 Eros to the Earth provided an opportunity to make thermal observations of a small Solar System body. Morrison (1976) observed Eros at several large phase angles and calculated the effective diameter for maximum light by comparison with infrared and visible lightcurves. The asteroid was brighter at a phase angle of $-41^{\circ}$, before opposition, than at $+42^{\circ}$. This

confirmed that the sense of rotation was direct since the "afternoon" side of the asteroid would be hotter for an object with a finite thermal inertia. Morrison then assumed Eros to be a cylinder with hemispherical ends (Dunlap, 1976; Millis et al., 1976; Zellner, 1976) and solved the one dimensional conduction equation over the surface for different values of thermal inertia corresponding to a range of materials from "metallic" to "dusty". He concluded that Eros had a layer of dust at least 1cm in depth over its surface. Lebofsky and Rieke (1979) made observations near opposition with high time and spectral resolution and applied a more complex model taking into account the elongated shape and true polar axis direction (Scaltriti and Zappala, 1976; Millis et al., 1976; Dunlap, 1976), the entire thermal spectrum from 3 to 25μm and shadowing effects from macroscopic roughness through inclusion of an apparent limb darkening. They concluded that 10-50% of the surface of Eros is probably rocky material, or that it has a rocky subsurface covered with a thin layer of dust. Their models however were a best fit and did not exactly fit the observations over the whole lightcurve. This is not surprising since the true shape of Eros is probably considerably different from that modelled (cf O'Leary et al., 1976).

It is clear that a large amount of data is required for this type of analysis. Subsequent observations relied on limited data and comparisons with radar and polarimetric diameters to deduce "non-standard" surface properties. Examples are 1580 Betulia (Lebofsky et al., 1978), 1978RA=2100 Ra-shalom (Lebofsky et al., 1979) and possibly 1976AA=2062 Aten (Morrison et al., 1976). Thermal inertia models will be

described in section 3.7.

The thermal models outlined above all assume constant and isotropic emissivity for the asteroid surface. The first spectral measurements in the thermal region (Gillett and Merrill, 1975; Hansen, 1976b) showed no significant absorption or emission features. Feierberg et al. (1983) published 8 to 13μm spectra of six asteroids, two of which showed emission features of around 10% ascribed to silicate minerals. Although these features will not significantly affect the measured broadband 10μm fluxes, they cast doubt on the assumption of constant emissivity. In particular it may be difficult to assess the effects of variable emissivity on the predicted model fluxes in the 60 and 100μm IRAS windows. This subject will be discussed further in section 3.4.

## 3.2 THE RADIOMETRIC METHOD OF DIAMETER DETERMINATION.

The radiometric method is based on the fact that reflected and emitted fluxes are dependent on albedo in different ways. The reflected flux is directly proportional to the albedo, A, while the emitted flux is proportional to 1-A. This allows, in principle, the albedo and diameter of an asteroid to be estimated from broad-band observations at wavelengths which sample the reflected and emitted fluxes. For most asteroids these are the V filter, in which the Sun's spectrum peaks, and the N filter covering the 10μm atmospheric window and lying near the peak emission for main belt asteroids. The diameter and albedo can be obtained from the

simultaneous equations:-

$$V = V_o + 5\log\Delta - 5\log R - 2.5\log p_V + 5\log r + \alpha\gamma_V$$

$$N = N_o + 5\log\Delta - 5\log R - 2.5\log(I_{em}) + \alpha\gamma_N \qquad (1)$$

where V and N are observed magnitudes,

$V_o$ = V magnitude of the Sun,

$N_o$ = constant related to the zero points of the infrared magnitude system,

r = heliocentric distance,

$\Delta$ = geocentric distance,

$\alpha$ = phase angle,

R = radius of asteroid,

$p_V$ = geometric visual albedo,

$\gamma$ = phase coefficient[4]

$I_{em}$ = emitted flux from a body of unit radius over the wavelength range of the N filter.

$I_{em}$ is dependent on the albedo of the asteroid (as well as several other factors).

## 3.3 THE STANDARD MODEL.

The first attempt at determining albedos and diameters using the radiometric method (Allen, 1970) treated the asteroid as a sphere with each surface point in equilibrium with the insolation (equivalent to a non-rotating sphere).

---

[4]The phase coefficient is a measure of the rate of decrease in brightness (in magnitudes per degree) as an asteroid is observed at increasing phase angles. The decrease is approximately linear for $\alpha > \sim 7^\circ$.

Since this model was both simple and reasonably realistic for large airless regolith-covered bodies, it formed the basis for what has become known as the standard model.

For a spherical asteroid in instantaneous equilibrium with the insolation, energy absorbed = energy emitted for each surface element, da. Assuming grey body emission,

$$(1-A)\ da\ \cos\theta\ \cos\phi\ S_o/r^2 = \varepsilon\sigma T^4\ da$$

where $S_o$ = solar constant at 1 A.U.,

A = bolometric Bond albedo,

$\varepsilon$ = bolometric emissivity of asteroid surface,

$\sigma$ = Stefan-Boltzmann constant,

T = surface temperature.

So surface temperature $T = [(1-A)S_o/\varepsilon\sigma r^2]^{1/4}\ \cos^{1/4}\theta\ \cos^{1/4}\phi$

$$= T_{max}\ \cos^{1/4}\psi \quad \text{for } \psi<90^\circ$$

$$= 0 \quad \text{for } \psi>90^\circ$$

The bolometric Bond albedo, A, is unknown. The reflected flux depends upon the geometric albedo, $p_\lambda$, at any given wavelength. Since $p_\lambda$ varies with changes in the orientation of the asteroid, Russell (1916) introduced the phase integral, q, to relate the Bond albedo and geometric albedo.

The phase integral $q_\lambda = 2\int_0^\pi \varphi(\lambda,\alpha)\ \sin\alpha\ d\alpha$

where $\varphi(\lambda,\alpha)$ is the disk integrated brightness of the asteroid at phase angle $\alpha$ relative to its brightness at $\alpha=0^\circ$.

The Bond albedo $A_\lambda = q(\lambda) p_\lambda$,

and the bolometric Bond albedo $A=\overline{A_\lambda} \approx qp$.

Most asteroids can only be observed over a limited range of phase angles ($<30^\circ$) so q cannot be determined explicitly. For the Moon and Mercury $q\approx0.6$, although for the Galilean satellites with predominantly dirty ice surfaces $q\sim1.0$. For

asteroids the mean albedo $p \sim p_v$. In reality, the exact value of q is not important for low albedo objects since the infrared flux is proportional to 1-A. The effect of uncertainties in q increases with increasing albedo (Morrison 1973). Different authors favour different values of q: a value of q=0.6 has been adopted for all the models computed here.

Most asteroids are observed at non-zero phase angles. There is an approximately linear variation between phase angle and optical brightness described by the phase coefficient $\gamma$. Values of $\gamma$ vary between 0.015 and 0.04 mag/deg and are (on average) inversely proportional to albedo. At small phase angles a surge in brightness of $\sim 0^m.3$ is seen which is due to surface roughness effects. (The multiple scattering theory of Lumme and Bowell (1981a;1981b) describes the phase curves in a more rigorous manner in terms of surface roughness, density and scattering properties.) The standard model is defined at zero phase angle. Observations at non-zero phase angles must be corrected by an infrared phase coefficient. Most authors assume $\gamma_N = 0.01 \text{mag.deg}^{-1}$, although the limited observations of a few objects indicate a variety of true values (e.g. 0.05 for 4 Vesta (Matson, 1971b); 0.08 for 433 Eros (Morrison, 1976); 0.017 for 1580 Betulia (Lebofsky et al., 1978)). Only small corrections for phase are required for ground-based observations of main belt asteroids, since these are usually made when the asteroid is close to opposition. However, for Earth-crossing asteroids, and observations by IRAS which are constrained to pointing directions near quadrature (section 4.4), errors in the derived infrared flux can become

significant.

The standard model is also not suitable for analysing observations at large phase angles because the change in observed temperature distribution is not accounted for. As the phase angle increases more of the unilluminated hemisphere becomes visible. For a regolith-covered slowly rotating body only a few percent of the emitted flux is radiated from the unilluminated hemisphere, and most of the observed flux, particularly around 10μm, comes from the central region of the disk. However, at phase angles $>40^{\circ}$ these effects become dominant, and modifications to the model are necessary. These are discussed in section 3.5. It is, of course, possible to deduce the sense of rotation of an asteroid by comparing observations made at similar phase, but opposite sign, as for 433 Eros (Morrison 1976).

The standard model assumes a spherical shape, although most asteroids show variations in light indicating in some cases, extremely irregular shapes. These non-spherical shapes have different temperature distributions from those found on a sphere, which change as the asteroid rotates. Since, in general, the rotation poles and shape, and often the periods are not known, there is little which can be done about this. Quoted diameters can be regarded as "effective" diameters, particularly when a number of observations at different rotational phases have been used. Brown (1984) has incorporated ellipsoidal geometry into the standard model. For small departures from spherical shape there is good agreement, but substantial wavelength and temperature dependent effects become apparent for highly elliptical

objects, which may, in part, account for systematic differences in diameters derived radiometrically at 10 and 20μm. Thermal infrared lightcurves for ellipsoids have amplitudes which depend on wavelength as well as projected area, but phase curves for ellipsoids are indistinguishable from those calculated for spheres.

Most common rocks have bolometric emissivities, $\varepsilon$, between 0.8 and 1.0. A value of 0.9 is therefore usually assumed. Since infrared measurements for diameter determination are normally made in broad band passes at 10 or 20μm, near the peak of the asteroid thermal emission, errors in $\varepsilon$ do not significantly affect the derived diameters and albedos. The main effect is to change the temperature and therefore the shape of the spectrum.

The emissivity is regarded as constant over all the wavelengths of interest, and as equal to the bolometric emissivity. Wavelength dependence of emissivity will be discussed in section 3.4.

The standard model assumes not only constant emissivity, but uniform angular distribution of emission. For real surfaces this does not hold. Pettit and Nicholson (1930) recognised that features of positive relief (mountains, crater walls, etc) near the terminator of the Moon would intercept more insolation than expected for a spherical surface, resulting in a higher temperature. This would modify the angular distribution by radiating more in the direction of the sun. As a correction for this, a number of authors introduced a beaming parameter, $\beta$, which had the effect of increasing the effective temperature of the subsolar point $T_{max}$. A value of

$\beta \approx 0.9$ provided diameters and albedos in reasonable agreement with other methods. Buhl et al. (1968a)(1968b), Bastin and Gough (1969), Winter and Krupp (1971) and Sexl et al. (1971) developed models to fit the lunar data which included negative relief (craters) as well as positive relief. Hansen (1977), in an attempt to understand why asteroid diameters differed according to whether N (10μm) or Q (20μm) photometry was used, recognised that the spectrum would be a function of crater density. Negative relief will have the effect of increasing the temperatures near the subsolar point, since the floors of craters will receive sunlight directly and by reflection from the walls. The net effect would be to enhance the emission at shorter wavelengths at the expense of beaming a larger fraction of the total emission towards the sun. Observations of the Galilean satellites (Matson, 1983) show a decrease of brightness temperature with increasing wavelength, as do Voyager IRIS data between 30 and 45μm for Ganymede (Spencer, 1983), implying that the effects of negative topography are more significant.

Despite all the criticisms discussed above, the standard model appears to provide a useful method for diameter determination for large (i.e. regolith-covered) asteroids observed at small phase angles when broad-band measurements are used. There may be discrepancies between diameters obtained from observations made with the Q filter compared to the N filter. This could be partly due to systematic errors in the absolute calibration of the magnitude scale, but there do appear to be real differences between the predicted and observed fluxes due to emissivity variations or surface

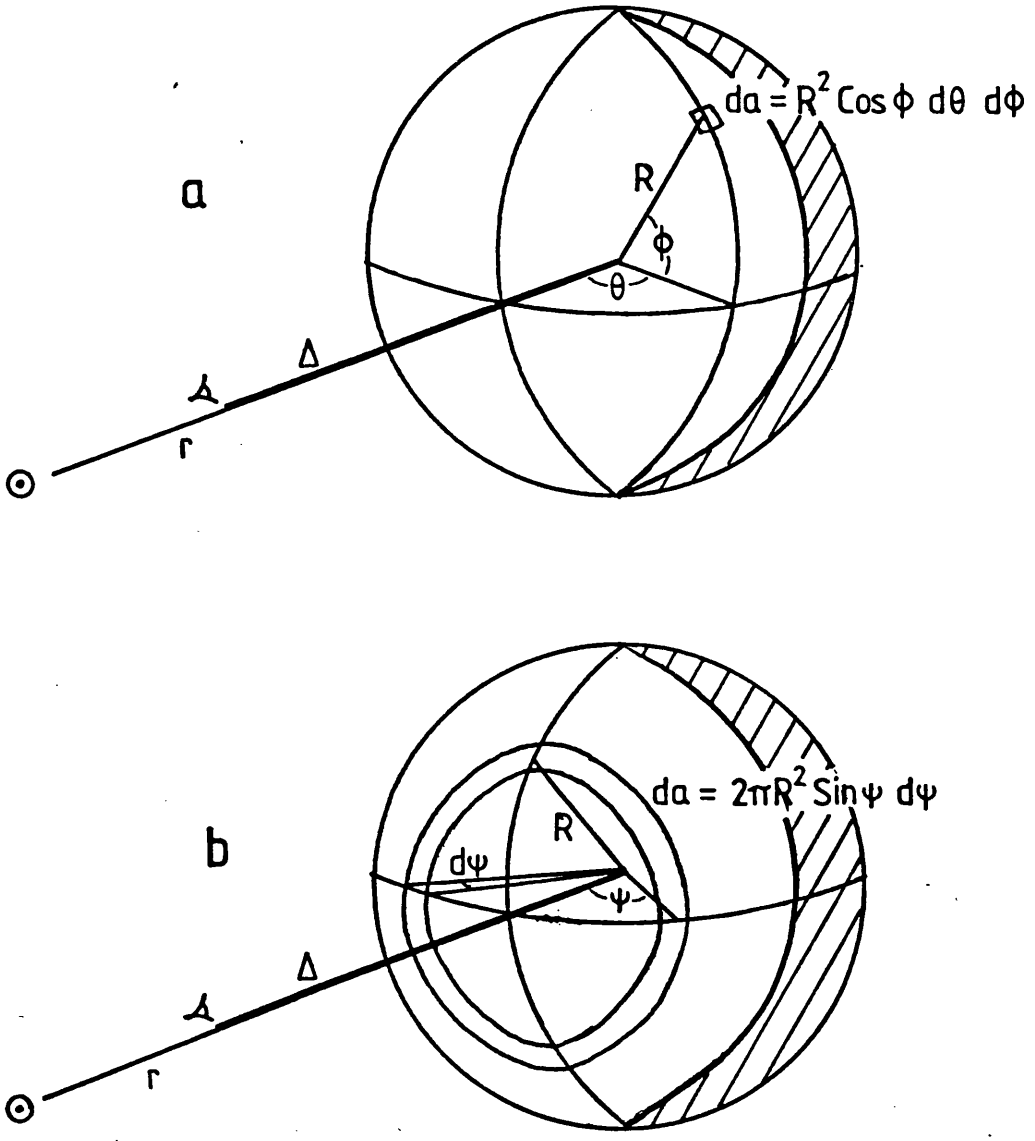


Fig. 3.2 The standard model. Definition of symbols and viewing geometry.

roughness effects (Matson et al., 1984).

The standard model is thus defined by the energy balance

$$\pi R^2 (1-A) S_o / r^2 = \varepsilon\sigma\beta R^2 \int_{-\pi/2}^{\pi/2} \int_{-\pi/2}^{\pi/2} T_{max}^4 \cos^2\theta \cos\phi \, d\phi \, d\theta$$

$$= \varepsilon\sigma\beta R^2 \int_0^{\pi/2} T_{max}^4 \cos\Psi \, d\Psi$$

Thus the emitted flux in equation (1) is given by

$$I_{em} = 2\pi\varepsilon \int_{\lambda 2}^{\lambda 1} \int_0^{\pi/2} B(\lambda, T_{max} \cos^{1/4}\Psi) \sin\Psi \cos\Psi \, d\Psi \, d\lambda$$

where $T_{max} = [(1-A) S_o / \varepsilon\sigma\beta r^2]$

bolometric Bond albedo $A = qp = qp_V$

Phase integral $q \sim 0.6$

Emissivity $\varepsilon \sim 0.9$

Modelling constant $\beta \sim 0.9$

$B(\lambda, T)$ is Planck function.

Flux received at observer

$$S(\lambda) = \left[ 2\pi\varepsilon \frac{R^2}{D^2} \int_0^{\pi/2} B(\lambda, T_{max}^4 \cos^{1/4}\Psi) \sin\Psi \cos\Psi \, d\Psi \right] . 10^{-0.4\alpha\gamma_N}$$

Fig 3.3 shows the predicted standard model fluxes combined with the reflected solar spectrum for a) Earth-crossing asteroids, b) main belt asteroids and c) a Trojan asteroid.

Fig 3.4 shows the effects of varying the standard model parameters discussed above. R is the ratio of a standard model with the quoted parameters to one with $q=0.6$, $\varepsilon=0.9$ and $\beta=0.9$. For all the models, $r=2.5$A.U. The range of values of the parameters $\beta$, $\varepsilon$ and $q$ show the extremes of the likely values. A value of $q \sim 1.0$ has been found for the Galilean satellites, but is unlikely for large asteroids. The points to note are that i) the spectrum for a low-albedo asteroid is virtually independent of q; ii) the shorter wavelength region is most sensitive to changes in the model parameters; iii)

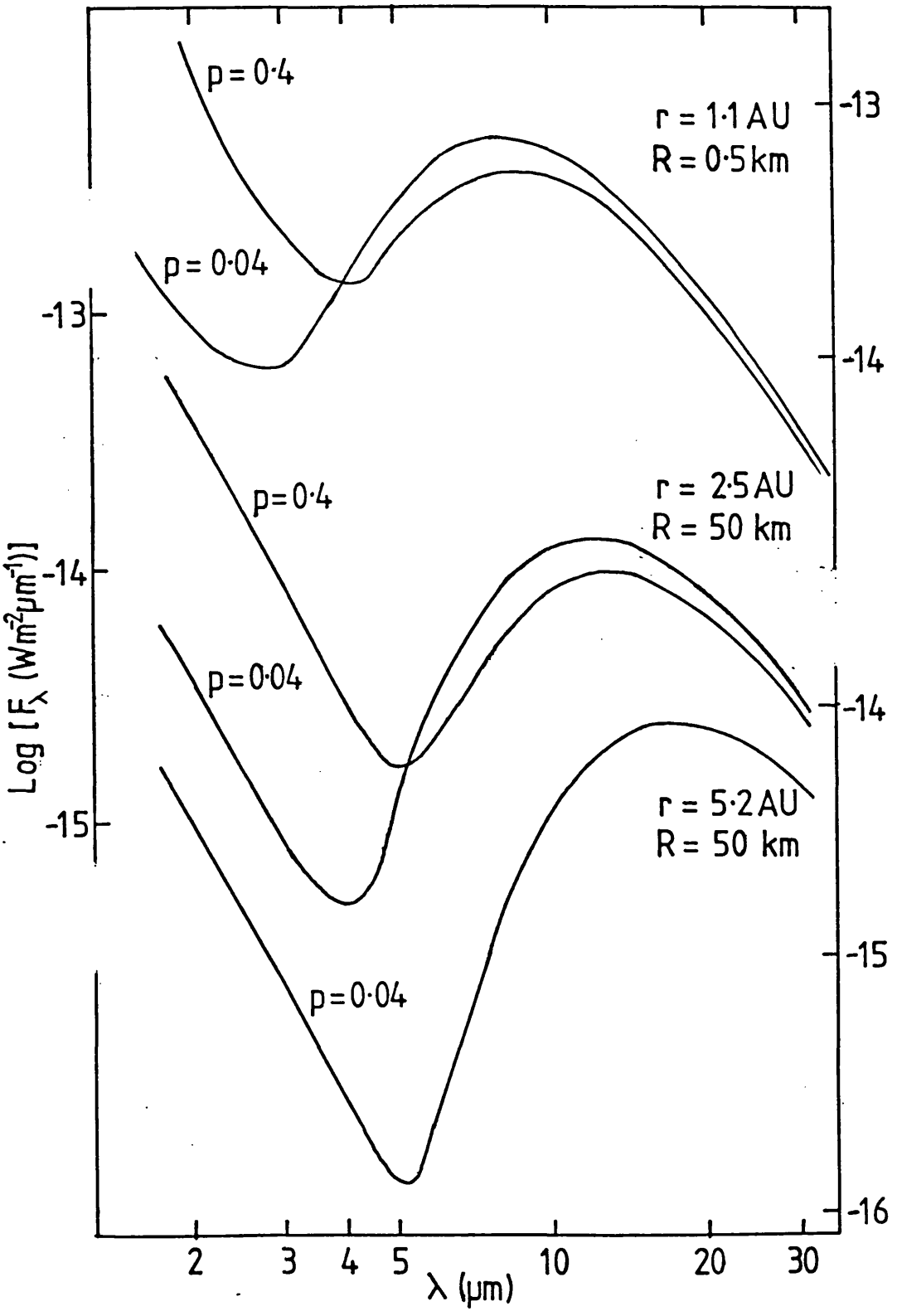


Fig. 3.3 Predicted standard model fluxes and reflected solar spectra for a) Earth-crossing asteroids, b) Main belt asteroids and c) a Trojan asteroid. Beyond ~6μm the emitted spectrum is only weakly dependent on albedo.

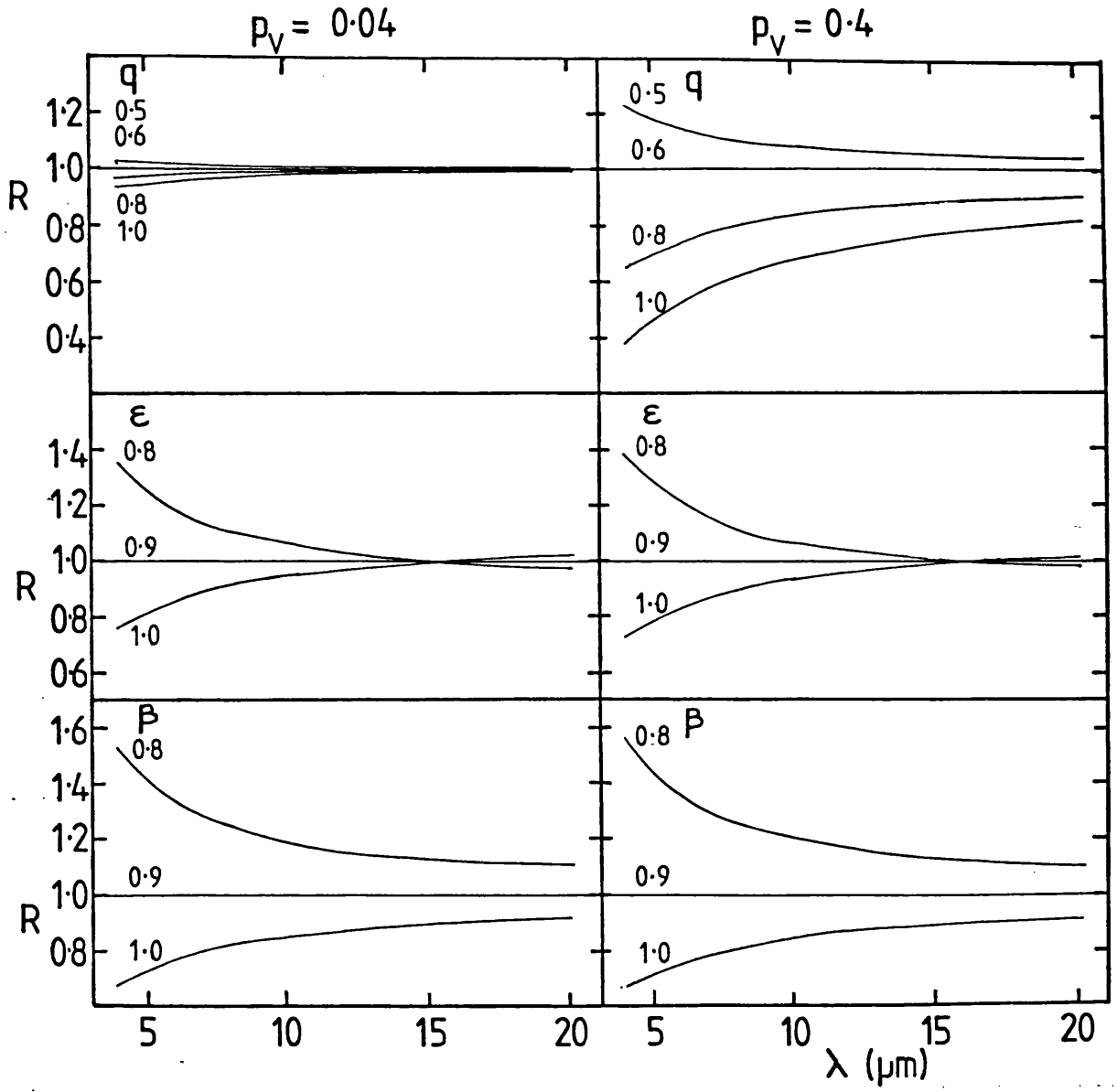


Fig. 3.4 Comparison of standard models with different values of the phase integral q, bolometric emissivity ε and modelling constant β. R is the ratio of a standard model with the quoted parameters to one with q=0.6, ε=0.9 and β=0.9. r=2.5A.U. for all the models.

diameters determined from wide-band photometry in the 10 or 20μm regions are unlikely to be in error by more than 15% (corresponding to ∿30% in the modelled flux) if the assumptions made in the standard model are reasonably valid.

## 3.4 EMISSIVITY EFFECTS - 8-13μm SPECTRA.

### 3.4.1 Introduction.

One of the assumptions of the standard model is that the emissivity is treated as a constant over the wavelengths of interest. Gillett and Merrill (1975) presented 7.5-13.5μm CVF spectra with a resolution of ∿0.2μm for the two brightest asteroids 1 Ceres and 4 Vesta, and found no deviations from grey body thermal emission greater than 10%. Hansen (1976b) observed 24 asteroids using wide and narrow bands in the 10 and 20μm windows and concluded that no significant absorption or emission features could be seen. Due to the limited resolution, and noise in his photometry, deviations of up to 25% from his model may not have been recognised.

Feierberg et al. (1983) observed six main belt asteroids in the 8-13μm region and found that two, 19 Fortuna and 21 Lutetia, appeared to show silicate emission features. By comparison with laboratory spectra of particulate surfaces (Hunt and Logan 1972), they concluded that these were restrahlen bands resulting from an optically thin layer of micron-sized particles. They suggested that the wavelength position of the emission maximum could be used to derive compositional information, particularly for C and M types which have relatively featureless reflection spectra.

3.4.2 Observations.

8-13μm spectrophotometry was carried out using the UCL liquid-helium-cooled array spectrometer on the 1.5m telescope of the Observatorio del Teide, Tenerife in April 1982. A low-resolution grating with $\Delta\lambda$ = 0.24μm was employed, so that 25 detectors spanned the 8-13μm atmospheric window. Two grating positions were employed, shifted by 1.5 resolution elements to ensure complete spectral sampling.

Flux calibration and atmospheric absorption correction was made with respect to standard stars observed at a similar airmass to the target objects, principally α Boo whose flux was taken to be 2.5 x $10^{-11}$ $W.m^{-2}\mu m^{-1}$ at 10μm, and assumed to be well represented by a blackbody at 4000K. (Gillett et al. (1968) observed α Boo between 2.8 and 13μm and found that, although a 4000K blackbody fitted between 2.8 and 4.0μm did not pass through the 7.5-13μm data, the shapes could not be distinguished over this wavelength range.) Wavelength calibration was by positioning the grating, with zeroth order as the reference position, and observations of known emission features in planetary nebulae, and was accurate to 0.08μm.

Each single integration was for approximately 10 seconds per point: the aspect data and integration times are listed in Table 3.1. The final data have been averaged and are plotted in Figs. 3.5-3.11. Relative errors between points in the averaged spectra are represented by the scatter in adjacent points.

3.4.3 Discussion.

All the observations have been fitted to a standard model

TABLE 3.1

8-13μm Spectra - Observation and aspect data.

| Asteroid | | Type | Date/Time UT | r (A.U.) | Δ (A.U.) | α (deg) | t (secs) |
|---|---|---|---|---|---|---|---|
| 1 | Ceres | C | 1982 Apr 9 0330 | 2.675 | 1.807 | 13.1 | 160 |
| 1 | Ceres | C | 18 0600 | 2.680 | 1.749 | 9.9 | 120 |
| 2 | Pallas | CU | 8 0115 | 2.464 | 1.514 | 9.4 | 160 |
| 2 | Pallas | CU | 10 0420 | 2.469 | 1.525 | 9.9 | 200 |
| 6 | Hebe | S | 9 2315 | 2.886 | 1.992 | 10.8 | 400 |
| 7 | Iris | S | 9 0145 | 2.752 | 1.800 | 8.0 | 240 |
| 10 | Hygeia | C | 9 2130 | 3.196 | 2.928 | 18.2 | 400 |
| 16 | Psyche | M | 18 0130 | 3.256 | 2.566 | 14.5 | 400 |
| 45 | Eugenia | C | 28 0045 | 2.573 | 1.899 | 19.5 | 400 |
| 51 | Nemausa | CU | 8 0445 | 2.237 | 1.304 | 12.2 | 280 |
| 56 | Melete | P | 16 0330 | 2.378 | 1.397 | 6.7 | 400 |
| 65 | Cybele | CPF | 18 0510 | 3.183 | 2.191 | 3.4 | 400 |
| 78 | Diana | C | 9 0245 | 2.415 | 1.428 | 5.3 | 200 |
| 451 | Patientia | C | 17 0200 | 3.211 | 2.247 | 6.0 | 400 |

r = Heliocentric distance
Δ = Geocentric distance
α = Solar phase angle
t = Integration time

in a manner essentially identical to that employed by Feierberg et al. (1983). The model (section 3.3) assumes an emissivity (ε) of 0.9 and modelling constant (β) of 0.9. An infrared phase coefficient of 0.01 $mag.deg^{-1}$ and a phase integral (q) of 0.6 have been used. Diameters and albedos are taken from TRIAD radiometry data (Morrison and Zellner, 1979): the values are listed in Table 3.2. Each model was matched to the observations by making a least squares fit to the total irradiance of the observed spectrum. The multiplying factors required are given in Table 3.2. These differ from unity because of the potentially large calibration errors, the possible errors in the diameters and albedos themselves, and

lightcurve effects.

Figs. 3.5-3.11 show the model spectra fitted to the observations. The ratio of observed-to-model flux has been smoothed with a three-point triangular filter. There is a deep atmospheric absorption due to ozone between 9.2 and 10.0μm., which can affect the spectra unless accurate calibration is achieved, and observations of standards could not generally be made very closely in time or direction. The 9-10μm. region should therefore be treated with caution. The symmetrical "wave" in the 2 Pallas data (Fig. 3.6a), due to a slight mismatch of wavelength calibration between asteroid and standard indicates a maximum error in wavelength positioning of less than 0.1μm.

The standard model using published properties appears to provide a good fit to the shape of the observed spectra, although small deviations can be seen in a number of cases. Several of the spectra show a systematic slope across the observed-to-model ratios which cannot be totally explained by possible errors in the wavelength calibration, since a shift >0.3μm is required. A "best fit" standard model was obtained by arbitrarily changing the maximum surface temperature $T_{max} = [(1-qp_v)S_o/r^2\varepsilon\sigma\beta]^{1/4}$ (section 3.3) of the model until a best fit to the shape of the spectrum (neglecting the 9-10μm region) was found. These are listed as $T^*_{max}$ in Table 3.2. The value of $T_{max}$ is fairly insensitive to the values of q and $p_v$ for low albedos, and the uncertainties in the albedos are probably no greater than $\pm$15%. Differences in the product $\varepsilon\beta$ of -10% for 2 Pallas and 7 Iris, -20% for 78 Diana and +20% for 6 Hebe, 16 Psyche and 45 Eugenia would account for the

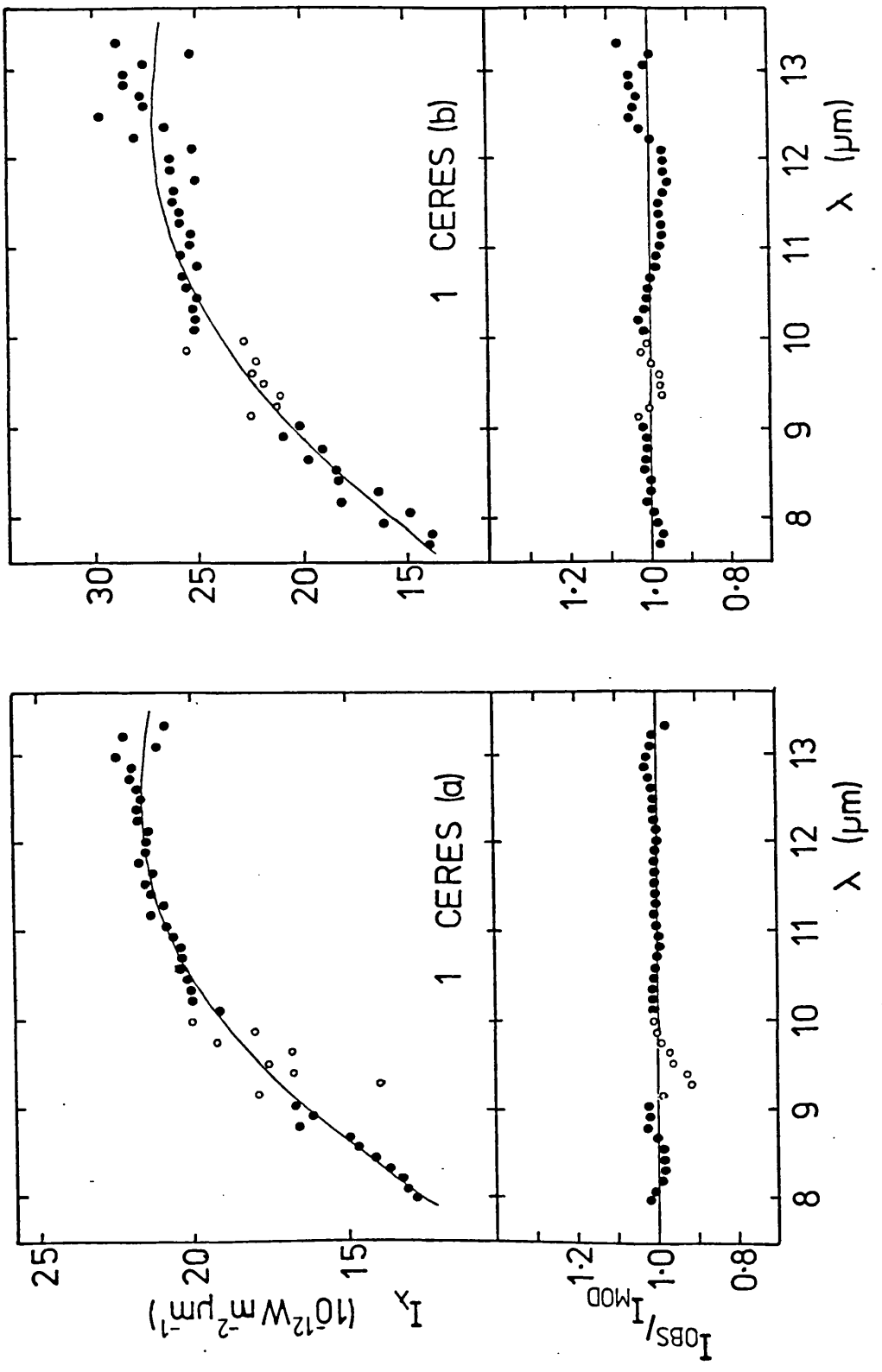


Fig. 3.5 8-13μm spectra of 1 Ceres with a standard thermal model fit. The lower diagrams show a triangular three point smooth across the ratio of observed-to-model fluxes. Errors are indicated by scatter in adjacent points. Open circles represent points which may be affected by poor removal of the atmospheric ozone absorption between 9.2 and 10.0μm.

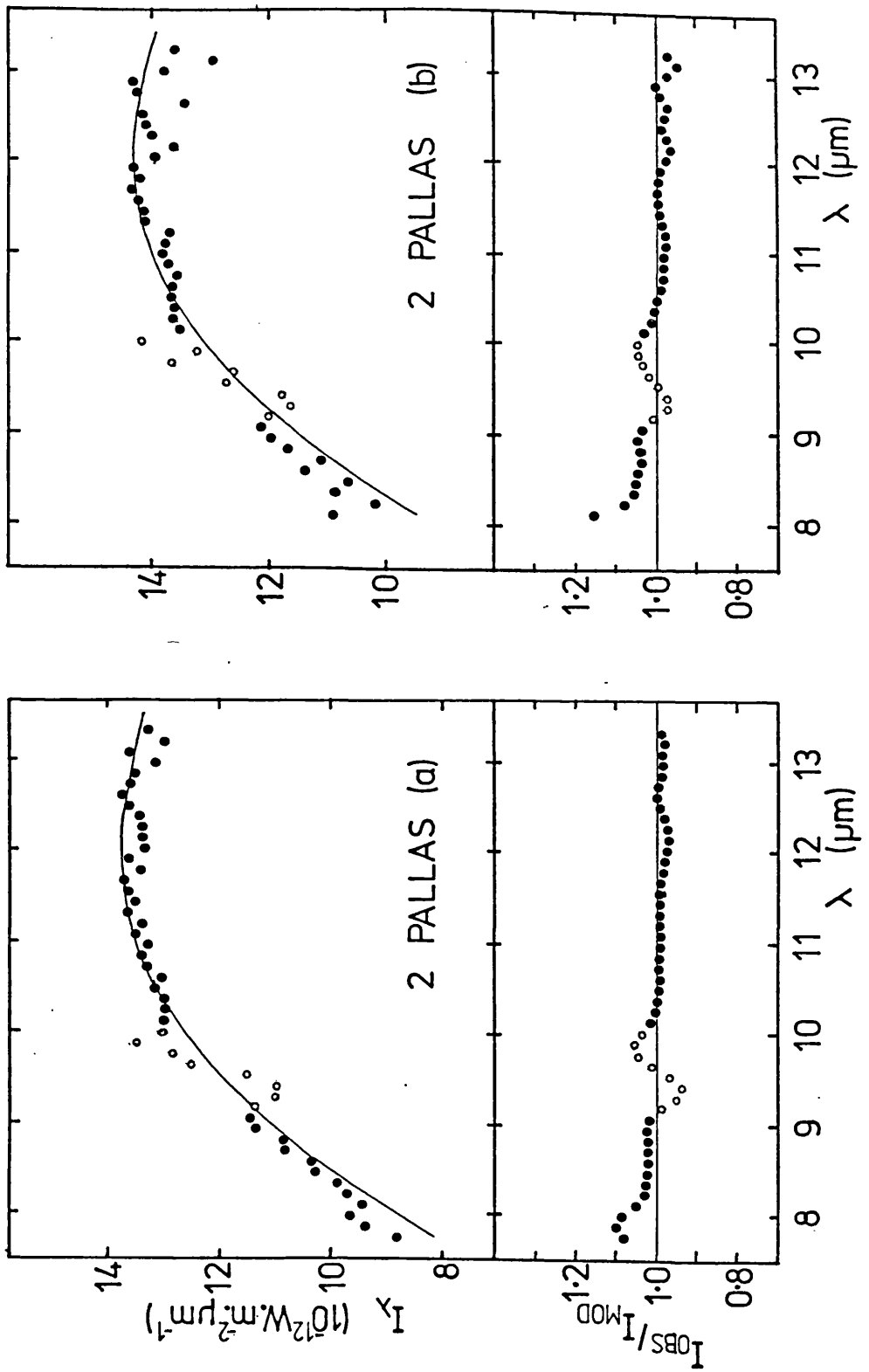


Fig. 3.6 As Fig. 3.5, for 2 Pallas.

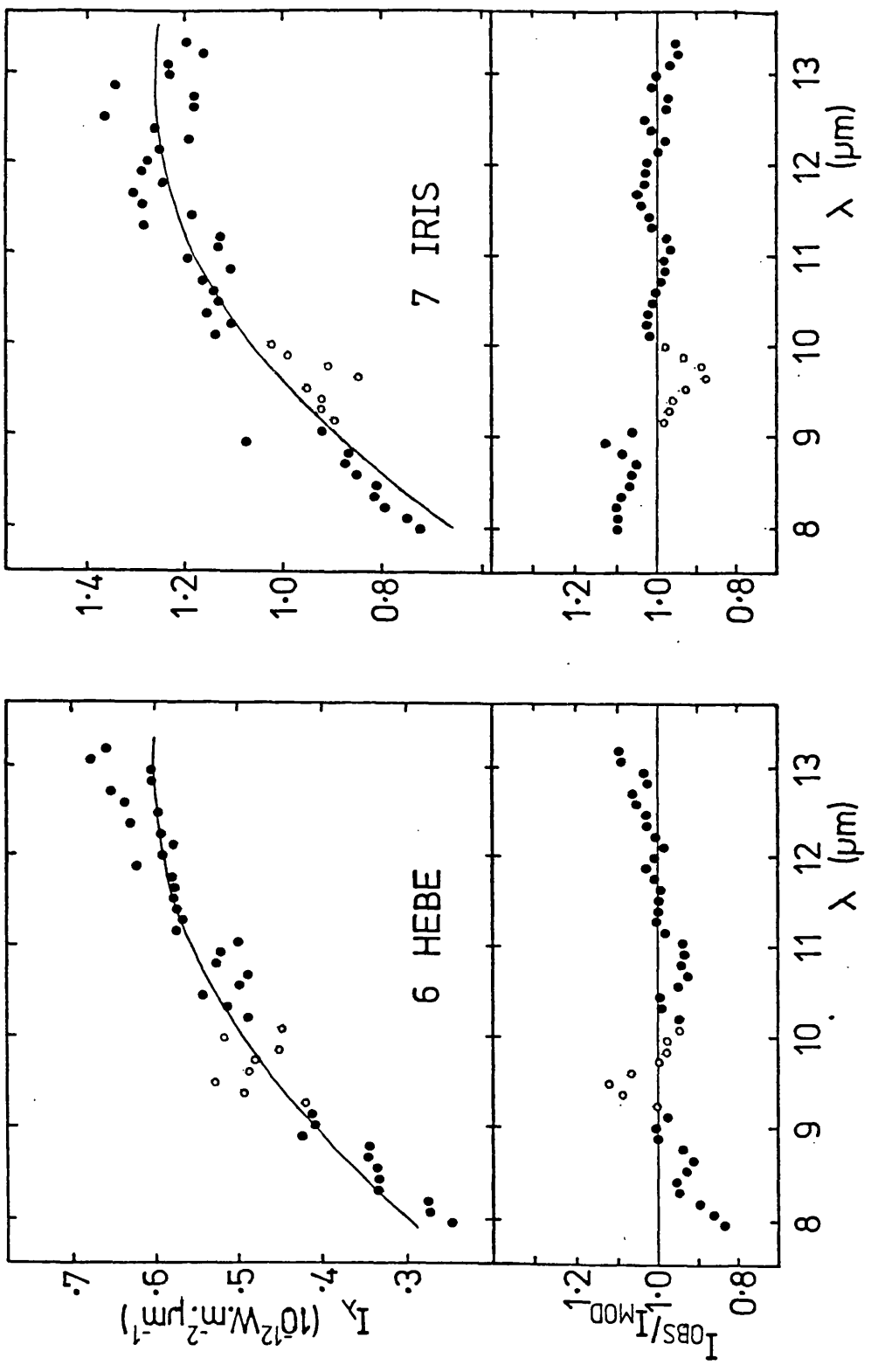


Fig. 3.7 As Fig. 3.5, for 6 Hebe and 7 Iris.

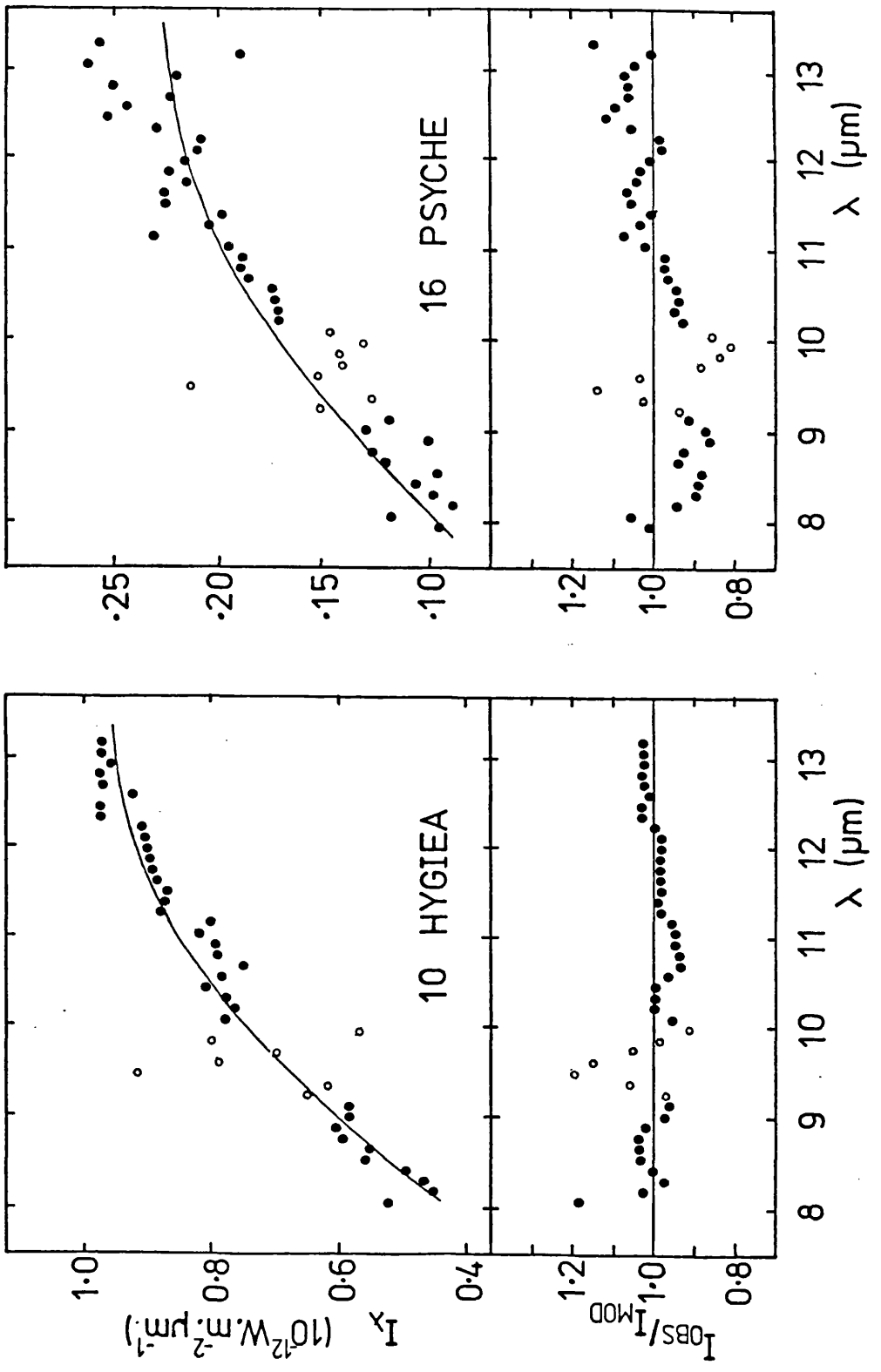


Fig. 3.8 As Fig. 3.5, for 10 Hygiea and 16 Psyche.

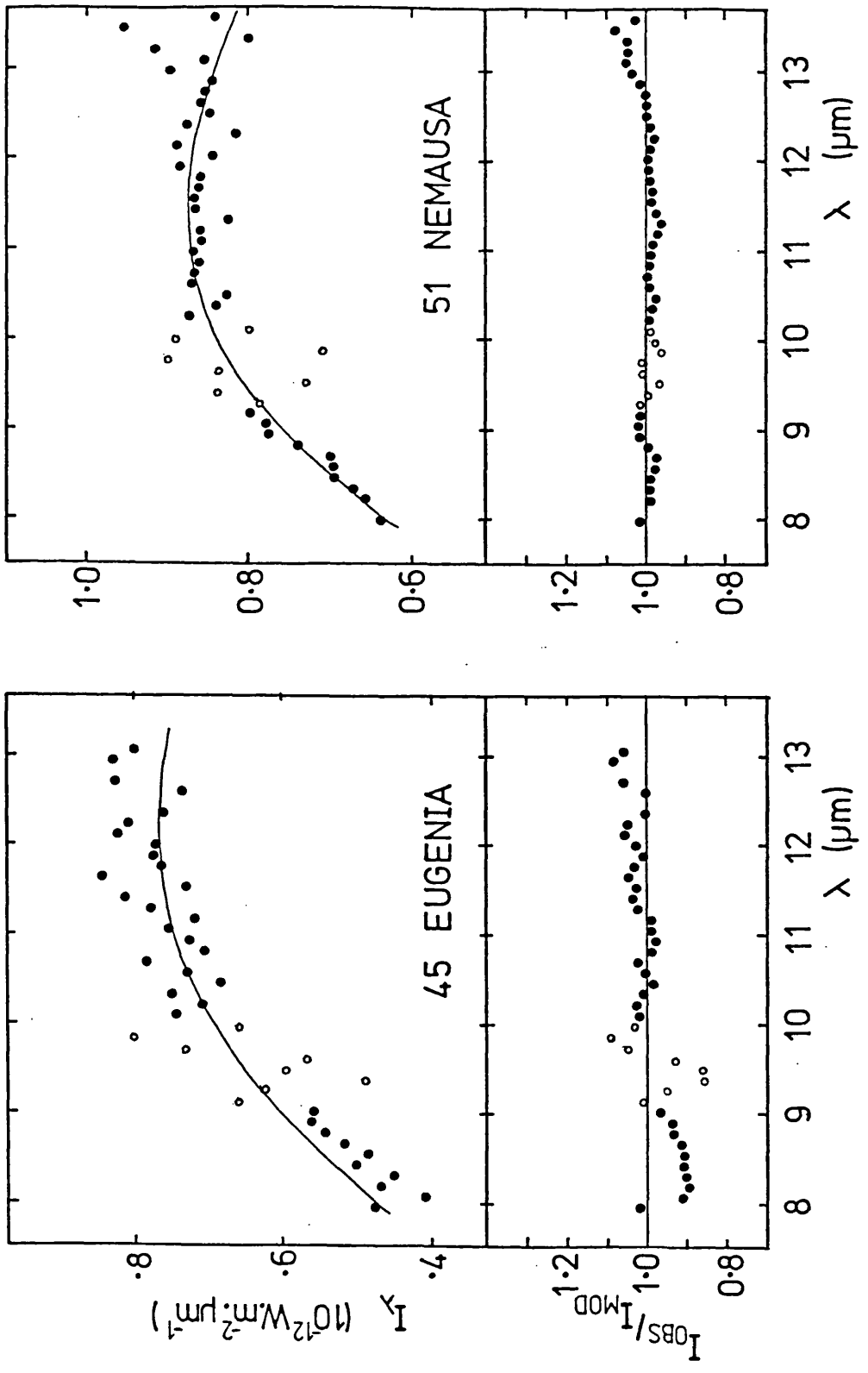


Fig. 3.9 As Fig. 3.5, for 45 Eugenia and 51 Nemausa.

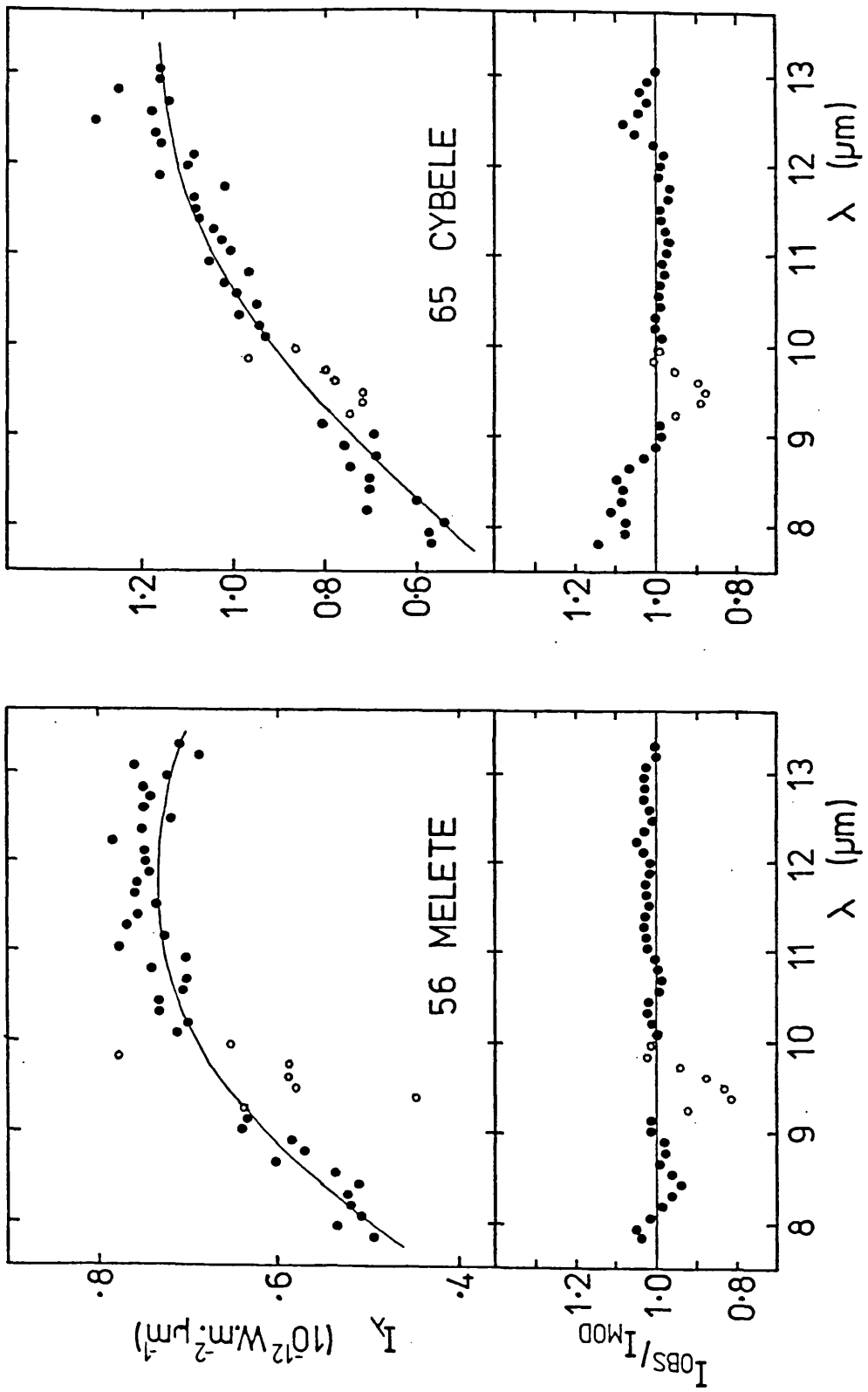


Fig. 3.10 As Fig. 3.5, for 56 Melete and 65 Cybele.

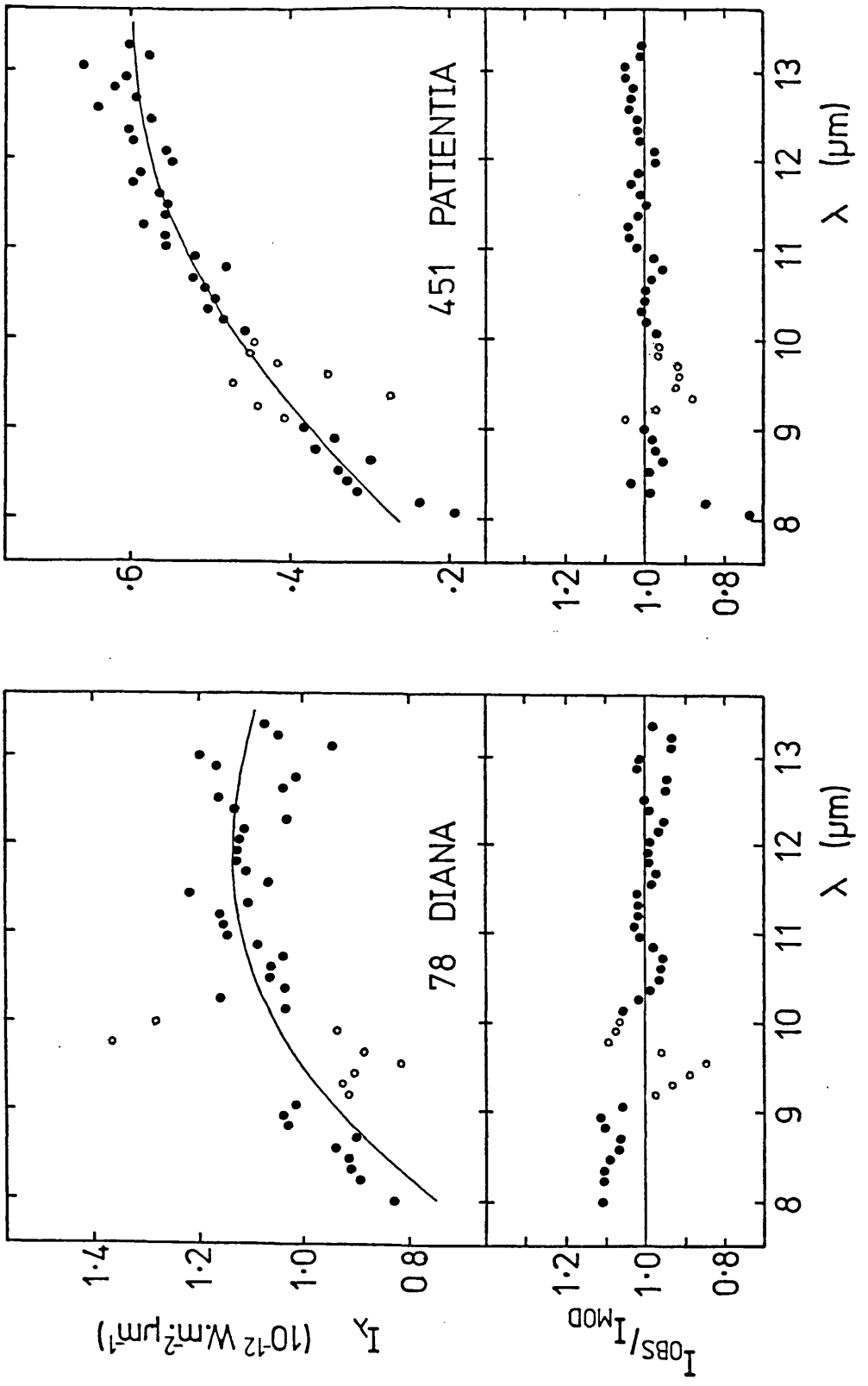


Fig. 3.11 As Fig. 3.5, for 78 Diana and 451 Patientia.

TABLE 3.2

Standard model fits.

| Asteroid | | Diam (km) | $p_v$ | $I_{obs}/I_{mod}$ | $T_{max}$ | $T^*_{max}$ |
|---|---|---|---|---|---|---|
| 1 | Ceres | 1014 | 0.059 | 0.99 | 251 | 251 |
| 1 | Ceres | | | 1.13 | 251 | 250 |
| 2 | Pallas | 589 | 0.093 | 1.05 | 261 | 267 |
| 2 | Pallas | | | 1.12 | 260 | 270 |
| 6 | Hebe | 204 | 0.162 | 1.06 | 238 | 224 |
| 7 | Iris | 208 | 0.196 | 1.57 | 242 | 250 |
| 10 | Hygiea | 430 | 0.050 | 1.01 | 231 | 230 |
| 16 | Psyche | 247 | 0.094 | 0.59 | 227 | 214 |
| 45 | Eugenia | 244 | 0.030 | 0.48 | 257 | 245 |
| 51 | Nemausa | 151 | 0.062 | 0.59 | 275 | 276 |
| 56 | Melete | 144 | 0.031 | 0.68 | 268 | 265 |
| 65 | Cybele | 309 | 0.027 | 1.16 | 232 | 235 |
| 78 | Diana | 144 | 0.04[+] | 1.13 | 265 | 277 |
| 451 | Patientia | 279 | 0.039 | 0.81 | 230 | 227 |

[*] [+]"Best fit" standard model.
Assumed.

observed discrepancies. Since a) the emissivities of most minerals range between ~0.8 and unity and asteroids exhibit a range of surface compositions inferred from reflectance data; and b) the application of the modelling constant $\beta$ to represent surface roughness has been called into question (Matson et al., 1983), discrepancies of this order are not unexpected. Apart from the noisy 9-10μm region, none of the asteroids show an emission feature at the 10% (5% for 1 Ceres and 2 Pallas) level. Smaller scale structure could be present.

Wide and narrow band observations of 19 Fortuna made at UKIRT on 25-28 march 1984 (Green et al., 1985) were not of sufficient quality to confirm the feature proposed by

Feierberg et al. (1983)

3.4.4 Conclusions.

The main conclusion from these results is that diagnostic emission features of the type observed by Feierberg et al. (1983) are not common in C and M type asteroids.

Although polarimetric studies (Dollfus and Zellner, 1979) do not rule out a surface texture which could produce emission maxima similar to those found by Hunt and Logan (1972), the emission features are quite sensitive to particle size, packing density, thickness of the particle layer, thermal gradient and composition. However, optical studies of 19 Fortuna do not reveal any unusual properties which distinguish it from other C-type asteroids observed here.

Feierberg (Private communication) reobserved 21 Lutetia in April 1984 and failed to confirm the presence of a 10μm emission feature at the 10-15% level, although a feature may be present at the 5% level. This led him to believe that the previous published spectrum of Lutetia was distorted by noise in the 9-10μm atmospheric absorption region.

Although no appreciable emission features were observed in these spectra, in some cases there was the possibility of the emissivity varying from the modelled value by ~10%. Data obtained from IRAS (Chapters 4-6) over the range 10-100μm could be affected by unknown emissivity variations with wavelength. LeVan and Price (1983) presented broad bandpass observations of four asteroids at 20, 27 and 85μm made during the Far Infrared Sky Survey Experiment (FIRSSE). They concluded that the observed flux at 85μm was a factor of 2 to

3 lower than expected for 2 Pallas, 15 Eunomia and 45 Eugenia. The effects of probing deeper into the surface (and therefore to lower temperatures on the sunlit side) at longer wavelengths is not sufficient to explain the observed decrease in flux, since observations of 2 Pallas at 6cm (Johnson et al., 1982) show only a 25% decrease in flux from the standard model. LeVan and Price therefore concluded that the average emissivity of the asteroids over the 60-100μm region must be about half the value at 20μm. Simpson et al. (1981) found a decrease in emissivity of the Moon from 40 to 100μm relative to Mars. They found similar decreases in emissivity for modeled particulate surfaces for certain minerals and particle size distributions. However, since IRAS observations (chapters 5 and 6)(Aumann and Walker, 1984) do not show deviations from the standard model of this magnitude between 25 and 60μm any emissivity variations must be relatively small.

## 3.5 PHASE EFFECTS - MODIFIED STANDARD MODELS.

### 3.5.1 Projected Model.

As discussed earlier (section 3.3) the standard model is calculated for an asteroid in instantaneous equilibrium and at zero phase. Non-zero phase angles are corrected for simply by applying an infrared phase coefficient, which changes the total predicted flux, but not the shape of the spectrum. Since there is no set of observations of an asteroid covering a range of phase angles and wavelengths, a value of $\gamma=0.01 mag.deg^{-1}$ has generally been used. The projected model

is calculated in a similar manner to the standard model, but allowing for phase effects. Thus, as the phase angle increases, the temperature contours gradually disappear around the limb. This provides a more realistic representation of the observed temperature distribution for asteroids at non-zero phase angles.

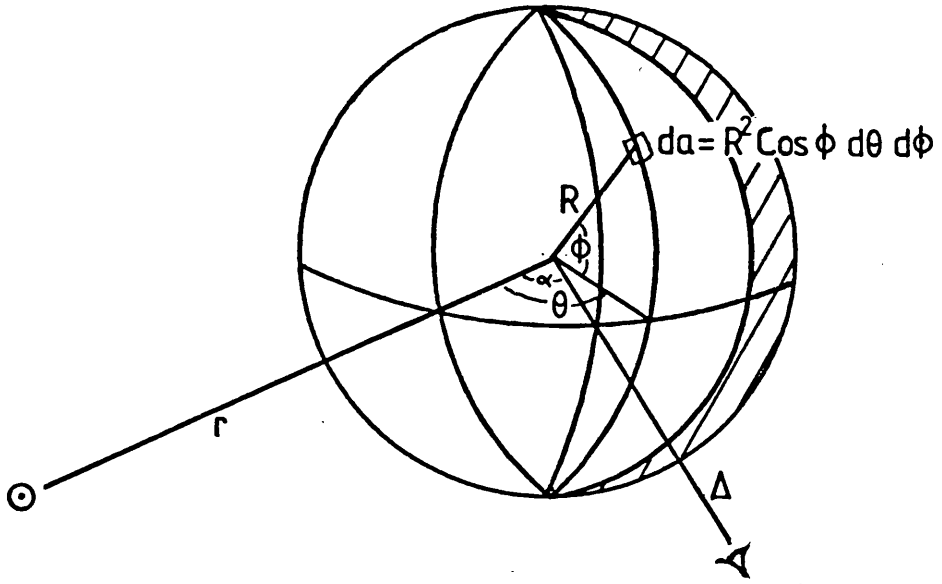


Fig. 3.12 The projected model. Definition of symbols and viewing geometry.

The projected model flux is given by

$$S(\lambda) = \frac{R^2}{\Delta^2}\varepsilon \int_{\alpha-\pi/2}^{\pi/2}\int_{-\pi/2}^{\pi/2} B(\lambda, T_{max}\cos^{1/4}\theta\cos^{1/4}\phi) \cdot\cos^2\phi\cos(\alpha-\theta)\,d\phi\,d\theta$$

$$T_{max} = [S_o(1-A)/\varepsilon\sigma r^2]^{1/4}$$

Since, in general, the asteroid is not viewed face on, the beaming parameter, $\beta$, is not included in the definition of $T_{max}$.

Although this model contains all the other assumptions and limitations of the standard model, it can provide some insight into phase effects.

### 3.5.2 Modified Projected Model.

The standard and projected models both assume instantaneous equilibrium with the insolation, implying a non-rotating body of low thermal inertia in which no flux is emitted from the dark side. For a low thermal inertia body with a slow rotation period (e.g. the Moon) the dark side, although well above zero Kelvin, will only contribute a small percentage of the total emitted flux ($\sim$1%) because of the fourth power relationship between temperature and flux. However, for fast rotation periods of a few hours (common among asteroids), and high thermal inertia surfaces, the dark side can emit an appreciable fraction of the total emitted flux. This would mean that the standard model would over-estimate the observed flux and therefore under-estimate the diameter. In reality, high thermal inertias would only be expected for objects with large areas of exposed bare rock. Observational evidence (polarimetry; comparison of radiometric diameter determination with other methods) and theoretical work (see Housen et al., 1979) indicate that asteroids down to a few kilometres diameter will be able to maintain a regolith of several centimetres. Thus, only km sized objects may be expected to show high dark side temperatures. Earth-crossing asteroids, which are in this size range, can also be observed at large phase angles where an appreciable part of the unilluminated hemisphere will be observable.

The modified projected model as defined here uses the parameter f to define the dark side temperature distribution. For latitude $\phi$ the dark side temperature is $f.\cos^{1/4}\phi.T_{max}$. The temperature distribution of the illuminated hemisphere is

then modified so that the total emitted flux is equal to the total absorbed. The energy balance equation

$$\pi R^2 (1-A) S_o / r^2 = R^2 \varepsilon \sigma \left[ \int_{-\pi/2}^{\pi/2} \int_{0}^{2\pi} G(T_{mod}^4 \cos\theta, f T_{max}^4) \cos^2\phi \, d\theta \, d\phi + \pi \int_{\pi}^{3\pi/2} f \, T_{max}^4 \cos^2\phi \, d\phi \right]$$

where $T_{max}=[S_o(1-A)/\varepsilon\sigma r^2]^{1/4}$, $T_{mod}<T_{max}$, and $G(x,y)=x$ if $x>y$ and $=y$ if $x<y$, can be solved iteratively to give $T_{mod}$.

The emitted flux is given by

$$S(\lambda)=\frac{R^2}{\Delta^2}\varepsilon \int_{-\pi/2}^{\pi/2} \left[ \int_{\alpha-\pi/2}^{\pi/2} B(\lambda, G(T_{mod}\cos^{1/4}\theta, f T_{max})\cos^{1/4}\phi)\cos(\alpha-\theta)\, d\theta + \int_{\pi/2}^{\alpha+\pi/2} B(\lambda, f.T_{max}\cos^{1/4}\phi)\cos(\alpha-\theta)\, d\theta \right] \cos^2\phi \, d\phi$$

In reality, the value of f depends on the thermal inertia, and the rotation period and pole position of the asteroid. For the Moon, with a low thermal inertia, long rotation period and a rotation pole perpendicular to the ecliptic, a single value of the dark side temperature for a given latitude is a reasonable approximation to the temperature distribution. For shorter periods, or higher thermal inertias, the temperature distribution across the dark side becomes more skew and the effects of viewing "morning" or "evening" terminators are consequently more important. A further complication is that rotation pole positions of asteroids appear to be randomly distributed in space (McCheyne, 1985). Since the calculation of pole positions requires extensive observations over a number of oppositions only a few pole positions are known, and most of these have low precision. The modified projected model therefore provides a useful first approximation to the temperature distribution derived using a thermophysical model (section 3.7), when little is known about the rotation pole or shape of

an asteroid. Results from the thermophysical model can be used to assess the physical significance of particular f values in certain circumstances (see section 5.6).

### 3.5.3 Fast-rotating Model.

A logical extension of the modified projected model to extreme values of rotation and thermal inertia is the fast-rotating model. In this model there is no diurnal temperature variation. It can be calculated by setting $T=T_{max}\,Cos^{1/4}\phi$ and $\beta=\pi$ in the standard model (Lebofsky et al., 1978), or by setting f to the maximum possible value in the modified projected model described above.

### 3.5.4 Comparison of models.

Fig 3.13 shows a comparison of spectra produced from the models described above. The standard model (1), projected model (2) and modified projected model with f=0.4 (3a) have almost identical spectra, because the phase effect is small and little or no energy is emitted from the dark side. For main belt asteroids larger than a few km in diameter observed at small phase angles, the derived diameter is not affected by the choice of model.

Fig 3.14 shows the same models for an Earth-crossing asteroid observed at a large phase angle. The projected model flux differs significantly from the standard model, because almost half the heated hemisphere is not in view. A single broad-band observation at 10μm would produce an overestimate of ~50% in flux and over 20% in derived diameter if the standard model is used. The nature of the surface of such an asteroid could be deduced from wide-band observations at 5, 10

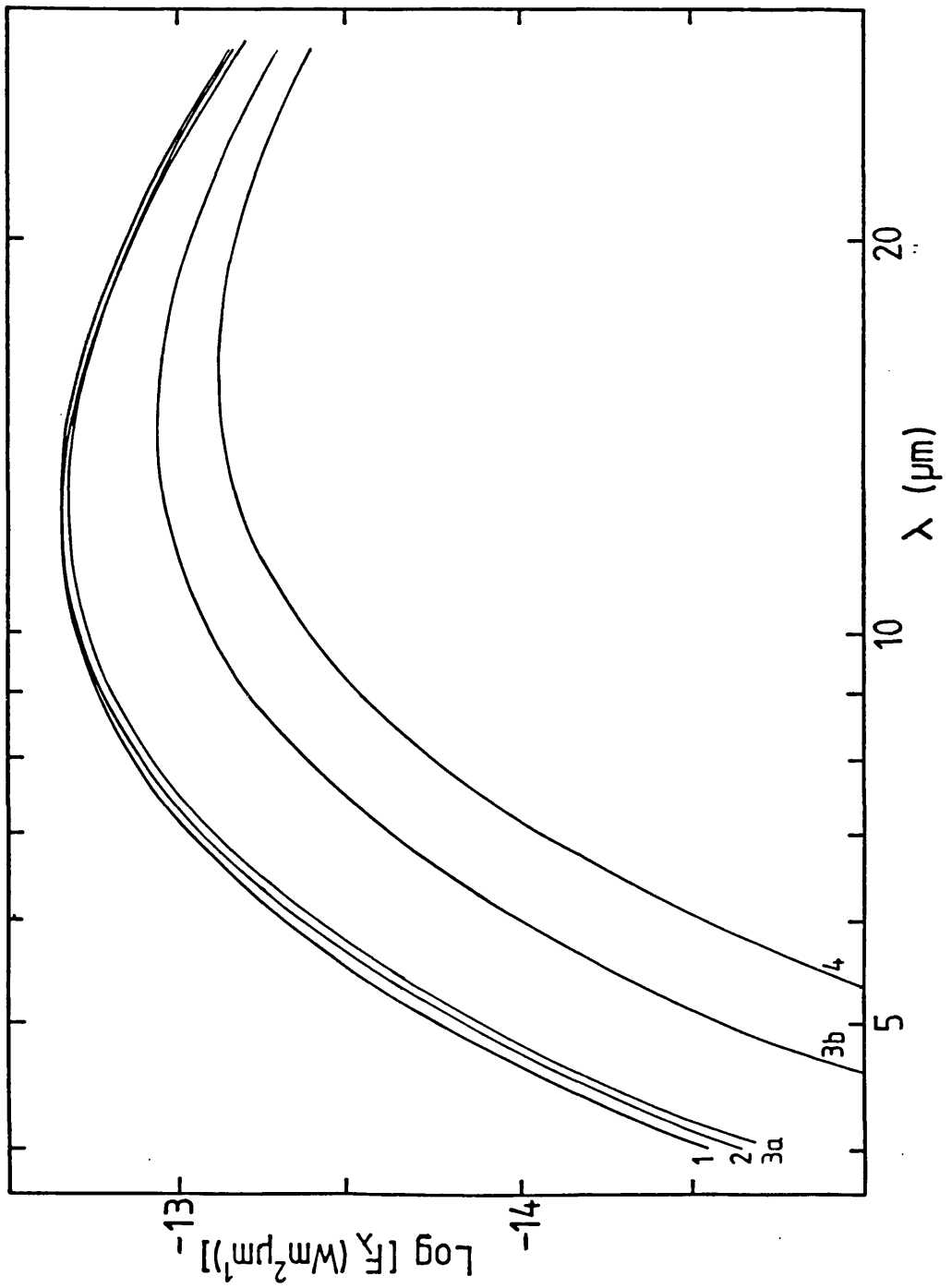


Fig. 3.13 Comparison of thermal model spectra for a main belt asteroid with r=2.5A.U., Δ=1.83A.U., α=20°, ε=0.9, q=0.6, $p_v$=0.1, R=50km. 1 - standard model (β=0.9). 2 - projected model. 3a - modified projected model (f=0.4). 3b - modified projected model (f=0.7). 4 - fast-rotating model.

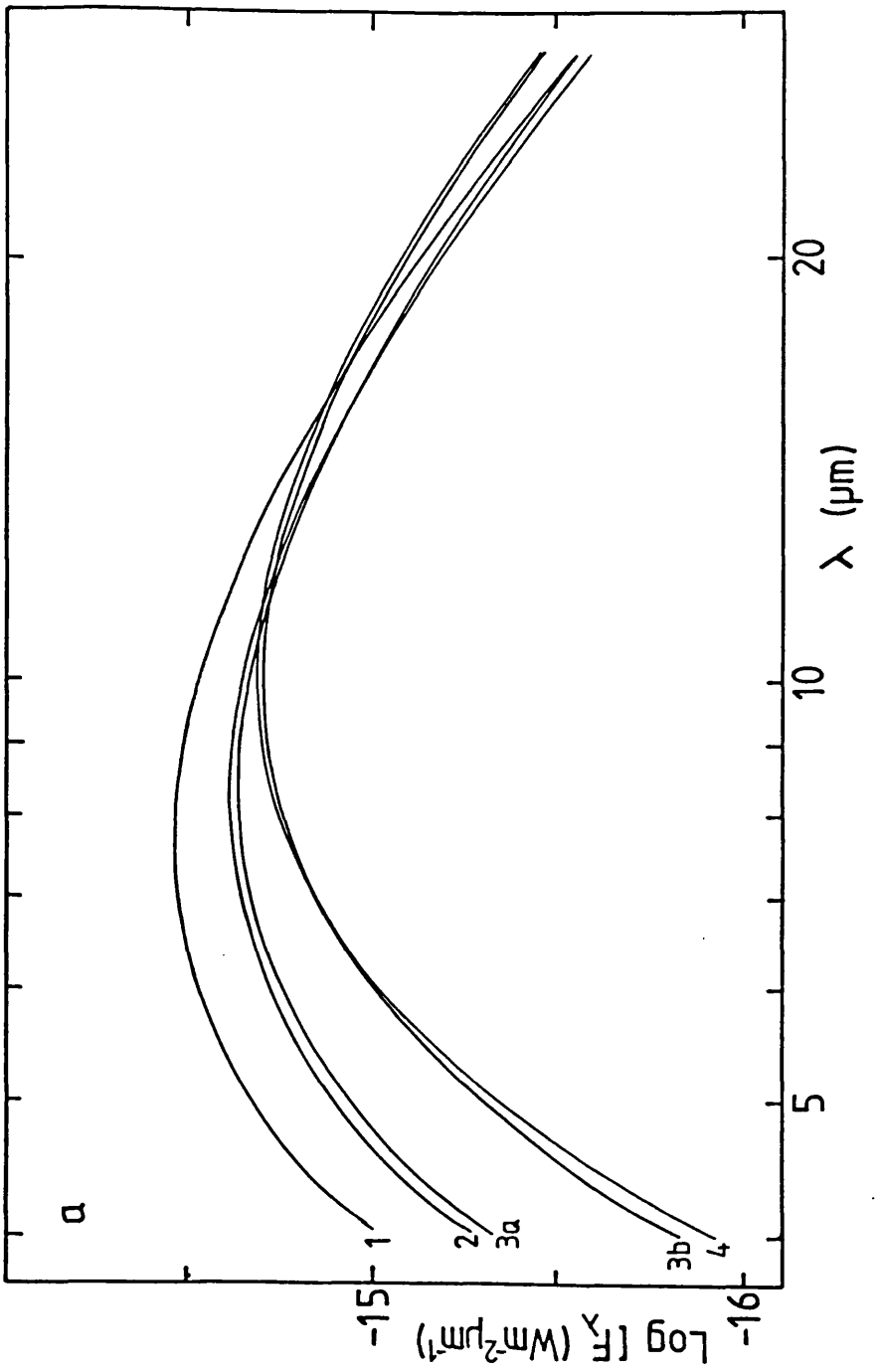


Fig. 3.14 As Fig. 3.13 for an Earth-crossing asteroid with r=1.0A.U., Δ=0.35A.U. α=80° and R=0.5km.

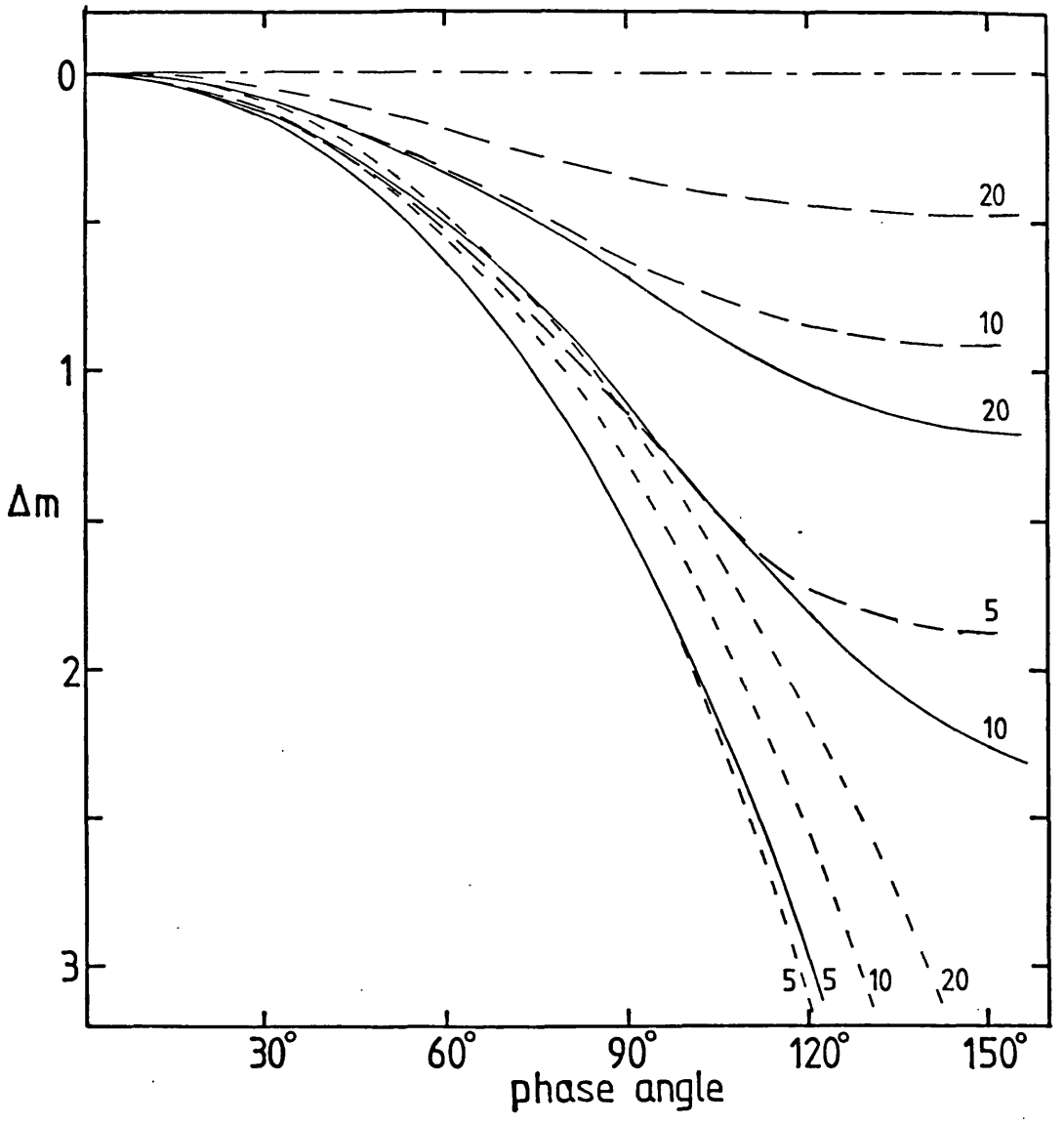


Fig. 3.15 Phase dependence of thermal model fluxes at 5, 10 and 20μm normalised to the flux at zero phase. Solid lines - projected model, short broken lines - modified projected model with f=0.4, long broken lines - modified projected model with f=0.7, dash dot line - fast rotating model. The standard model phase dependence is linear and defined as one of the model parameters.

and 20μm (see section 5.6).

One problem with determining diameters from single observations at large phase angles is the poorly known phase dependence of infrared brightness. Fig. 3.15 shows the predicted phase dependence of the thermal model fluxes at three wavelengths normalised to the flux at zero phase. Th fast-rotating model has no phase dependence since there is no change of temperature with rotation. The standard model is defined at zero phase with a linear phase coefficient entered as one of the parameters. For phase angles $<\sim 30^{\circ}$ the predicted phase coefficients are much less than the $0.01 mag.deg^{-1}$ normally assumed for the standard model. However, these models do not account for the peak in brightness observed close to opposition ($\alpha <\sim 7_{\circ}$). Observations at a range of wavelengths and phase angles would provide a useful method of determining the f value for different asteroids, since the effect of the dark-side emission becomes increasingly important at large phase angles. Further information on the thermal properties of the surface could be gained by detection of a different phase dependence on viewing the morning or evening hemispheres. Brown (1984) found that the phase dependence of ellipsoidal models was indistinguishable from that of spherical models so this could be applied to small Earth-crossing asteroids.

## 3.6 REMOVAL OF EMITTED FLUX FROM REFLECTANCE SPECTRA.

### 3.6.1 Introduction.

Asteroid reflection spectra (reflected spectrum divided

by the solar spectrum and normalised) exhibit features which are diagnostic of surface mineralogy (section 2.3). The amount of thermal emission from the asteroids themselves at a given wavelength depends on the heliocentric distance and albedo (Fig 3.3). Thus for Earth-crossing asteroids at ~1A.U. the emitted flux contributes more than the reflected flux at a wavelength of ~3μm. For a main belt asteroid at 2.5A.U. the corresponding wavelength is 4-5μm. Thus thermal models are required to remove the thermal contribution which would otherwise mask the features under investigation in these regions.

Surveys of asteroid spectra in the 1970's generally only extended to 1.1μm in the infrared (Chapman and Gaffey, 1979). Observations further into the infrared were first pursued by broad-band photometry, then by narrow-band photometry and multiplex spectroscopy (Larson and Veeder, 1979). Measurements at these longer wavelengths can be used to complement data below 1.1μm in attempts to classify asteroids and to derive information concerning their surface compositions. One important result of this work has been to show the presence of an absorption feature in the 3-4μm region of the spectrum for some C (or related U-type) asteroids. This has been related via laboratory measurements to an absorption band produced by water of hydration in clays or salts (Lebofsky 1980; Feierberg et al. 1981; Lebofsky et al. 1981; Larson et al. 1983) and found in many carbonaceous chondrite meteorites. These studies have produced more conclusive evidence for a compositional relationship between C-type asteroids and carbonaceous material. Medium resolution spectra in the 3-4μm region were obtained for a number of C, S

and M-type asteroids in 1982 at UKIRT.

3.6.2 Observations.

The observations were made between January 11 and 14, 1982 on the UK 3.8m infrared telescope in Hawaii. The UKT6 cryostat was used with a circular variable filter which measured the spectra from 2.9 to 4.0μm at 0.1μm intervals with a resolution of 0.08μm. A single spectrum consisted of two 5 second integrations per wavelength point. The signal-to-noise ratio for faint sources was increased by adding spectra. Aspect data and integration times are given in Table 3.3. Thin cirrus cloud was possibly present for the observations on January 11, 12 and 14. Since the UKIRT CVF integrates point by point, fast-moving cloud could contaminate the results. This effect has generally been removed from the data by repeat measurements.

The effects of atmospheric absorption on the raw data were removed by dividing the asteroid spectrum by that of a star, around A0 in spectral class and as close as possible to the asteroid in terms of airmass and time (see Fig. 3.16). This ratio was then multiplied by the blackbody spectrum appropriate to the star's temperature. In the 3-4μm region A0 stars have featureless spectra.

Before a reflectance spectrum can be obtained, the thermal component must be removed. This was done using the projected model (section 3.5.1). The composite asteroid spectrum (F) can be thought of as having three components: 1) the asteroid thermal emission ($F_t$); 2) the incident solar flux ($F_s$), which is modified by 3) the asteroid reflectance spectrum (R). $F = (R.F_s) + F_t$. The solar spectrum $F_s$ was

TABLE 3.3

Aspect data and integration times for asteroids observed at UKIRT January 1982.

| Asteroid | Type | $p_v$ | Date 1983 | Time (UT) | r (A.U.) | Δ (A.U.) | α (deg) | t (sec) | star | T (K) |
|---|---|---|---|---|---|---|---|---|---|---|
| 1 Ceres | C | 0.059 | Jan 13 | 1533 | 2.614 | 2.780 | 20.7 | 20 | SAO 139830 | 9850 |
| 2 Pallas | CU | 0.093 | 13 | 1439 | 2.282 | 1.983 | 25.4 | 20 | SAO 139830 | 9850 |
| 8 Flora | S | 0.144 | 13 | 0737 | 1.996 | 1.085 | 14.5 | 30 | SAO 94566 | 10600 |
| 10 Hygiea | C | 0.050 | 11 | 1300 | 3.296 | 2.331 | 3.9 | 20 | BS 4356 | 9850 |
| | | | 12 | 1148 | 3.296 | 2.327 | 3.5 | 40 | SAO 76126 | 12200 |
| | | | 13 | 1059 | 3.296 | 2.323 | 3.2 | 30 | SAO 97628 | 9120 |
| 15 Eunomia | S | 0.163 | 12 | 0722 | 2.326 | 1.462 | 14.6 | 20 | SAO 76126 | 12200 |
| 16 Psyche | M | 0.094 | 11 | 1433 | 3.182 | 2.533 | 15.0 | 30 | BS 4356 | 9850 |
| 22 Kalliope | M | 0.108 | 12 | 0509 | 2.624 | 1.886 | 16.8 | 40 | SAO 76228 | 11300 |
| 83 Beatrix | C | 0.05+ | 13 | 1217 | 2.366 | 1.396 | 5.0 | 60 | SAO 80113 | 10600 |
| 386 Siegena | C | 0.05+ | 13 | 0911 | 2.754 | 1.838 | 9.1 | 60 | SAO 134330 | 9850 |
| 433 Eros | S | 0.18 | 14 | 0544 | 1.150 | 0.313 | 51.1 | 20 | SAO 76126 | 12200 |
| 471 Papagena | S | 0.163 | 13 | 0554 | 2.393 | 1.530 | 14.1 | 40 | SAO 76126 | 12200 |

t = Integration time per point.

+ Assumed.

taken from Labs and Neckel (1970).

The absolute flux of the thermal model could not be exactly equated with the observed flux of the spectra, primarily because of lightcurve effects, and so a fitting procedure was employed. At this stage in the reduction, both the thermal flux, $F_t$, and the reflectance spectrum, R, are unknowns. As a first approximation, the reflectance spectrum was assumed to be a straight line of unknown slope over the last few wavelength points where the thermal flux is most significant. The flux of the thermal model (keeping the shape constant) and the slope of the assumed reflectance were then varied until the composite theoretical spectrum best fitted the observed data over the last few wavelength points. Having fixed the predicted thermal flux at one wavelength, the model fluxes could be determined at all wavelengths. The thermal component was subtracted from the observed data at each wavelength point. The remainder ($R.F_s$) was divided by the solar flux ($F_s$) to give the reflectance spectrum of the asteroid (R). This was normalised to a relative reflectance of 1.0 at 4.0μm. The modelled reflected and emitted components are shown for two of the asteroids in Fig. 3.17.

The relative reflectance spectrum for each asteroid is shown in Figs. 3.18-3.22. Three spectra were obtained of 10 Hygiea. The apparent absorption feature for Hygiea on January 12 (Fig. 3.22b) may be due to fast-moving cirrus. The error bars indicate the combined statistical variation of the average spectra for the asteroid and its corresponding calibration star.

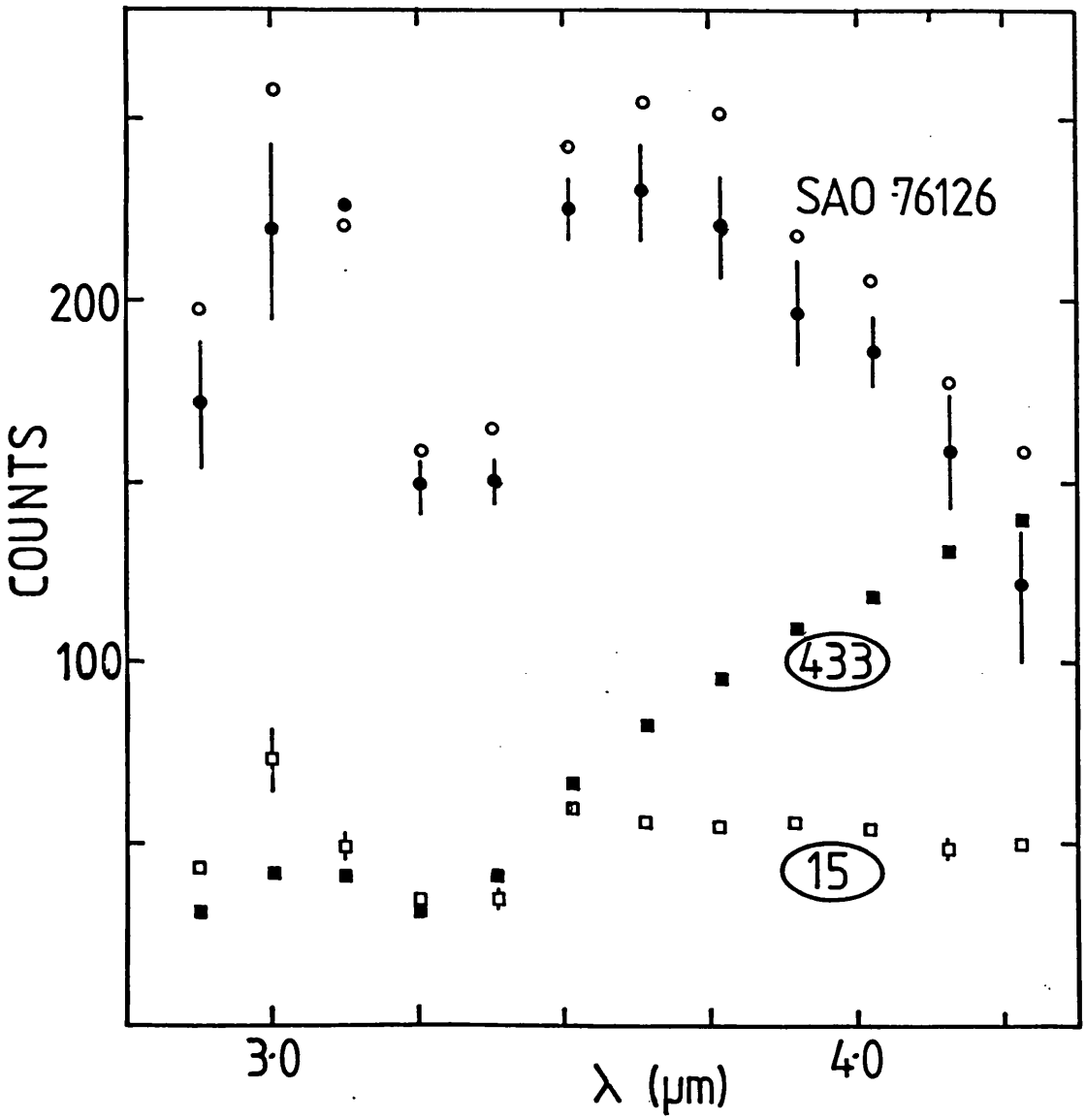


Fig. 3.16 Observed spectra of the asteroids (□) 15 Eunomia and (■) 433 Eros and the star SAO 76126 (○ and ●) used for atmospheric correction.

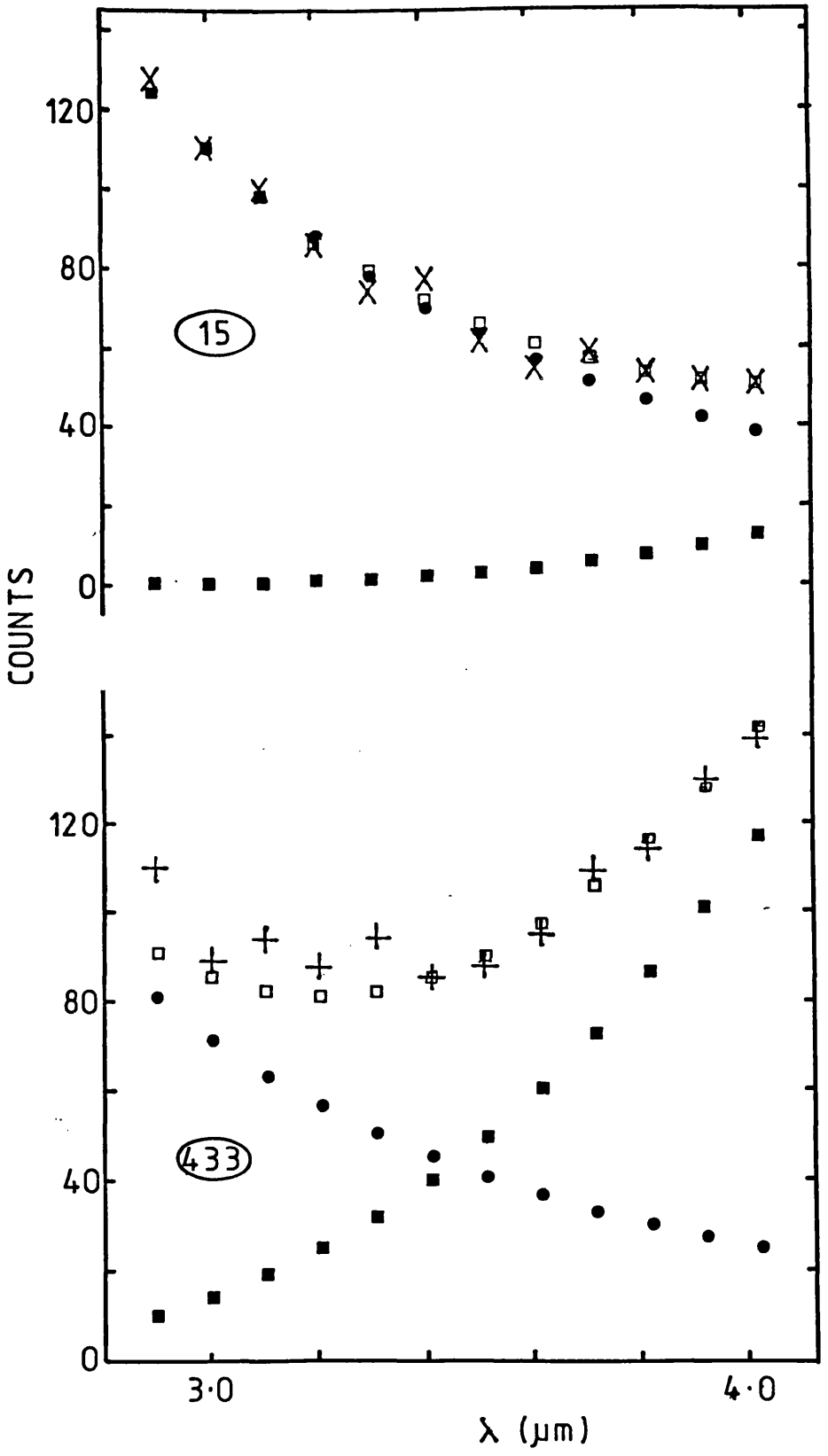


Fig. 3.17 Corrected spectra of the asteroids (X) 15 Eunomia and (+) 433 Eros. Also shown are (●) the calculated reflected solar and (■) thermal components of (□) the modelled spectra.

3.6.3 Discussion.

1 Ceres and 2 Pallas have both previously been shown to have an absorption feature in the 3-4μm region (Lebofsky, 1980), which is confirmed by these observations. The relative depths of the absorption for the two asteroids appear to differ somewhat from those obtained in earlier measurements. To test the fitting procedure, the data for Ceres from Lebofsky et al. (1981:their upper diagram, Fig. 1) was degraded to the same resolution. The technique described above was then applied. When normalised to the 4μm point given by Lebofsky et al., the relative reflectance spectra was in reasonable agreement with their results. The observations described above show a much deeper absorption band in Ceres than Lebofsky et al., (1981), and are more in line with the results obtained earlier by Lebofsky (1978;1980). The differences in the reflectance spectra, if not real, must occur in the removal of the thermal component. Errors in the model parameters affect the thermal spectrum most in this region (see fig.3.4).

With the exception of 8 Flora, the S and M-type asteroid spectra appear to be featureless within the errors of measurement. The spectrum obtained for Flora is unexpected, since it more nearly resembles the spectra of Ceres and Pallas than those of the remaining S-type asteroids. None of the calibration stars had intrinsic slopes to their spectra, over the observed wavelength range, differing by more than 7% from BS1140 (B7IV, J=5.52, K=5.51, L=5.52). In comparison, Flora's spectrum has a slope of 18% over this wavelength range (Fig. 3.20a). Feierberg et al. (1982) have shown, however, that between 2.0 and 2.5μm the reflectance spectrum of Flora

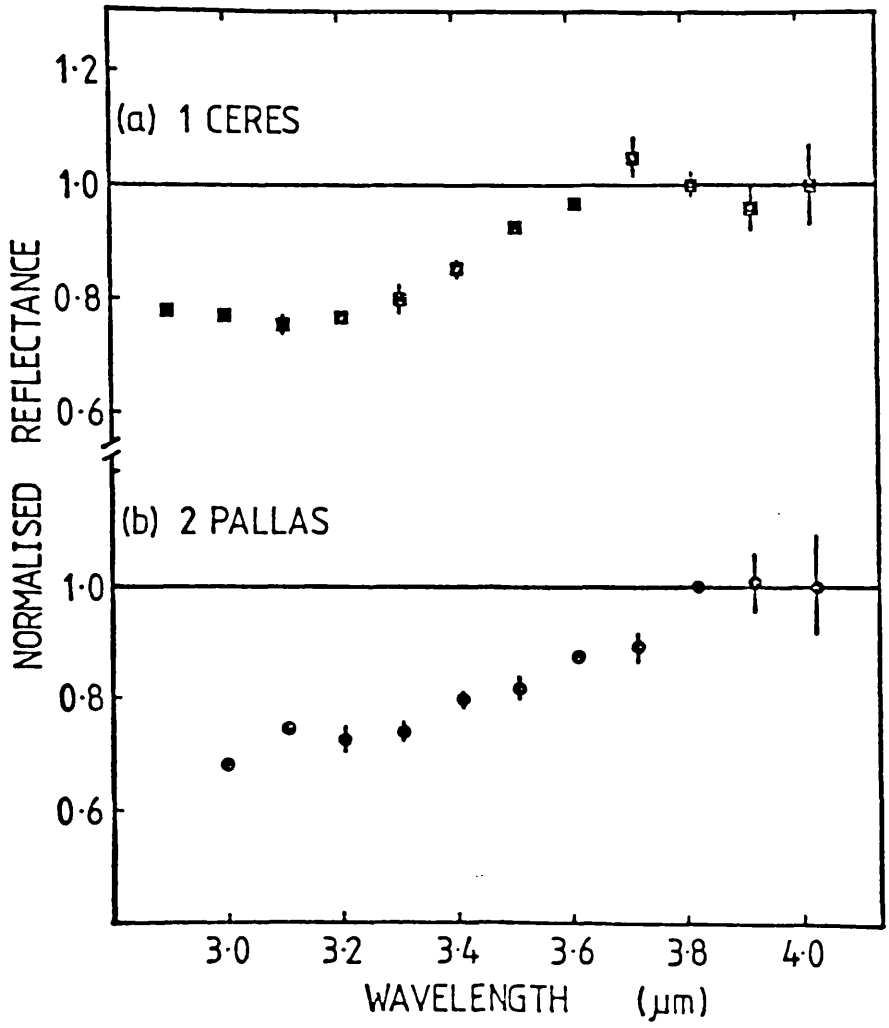


Fig. 3.18 The 2.9-4.0μm reflectance spectra of a) 1 ceres and b) 2 Pallas. Error bars are standard error of the mean.

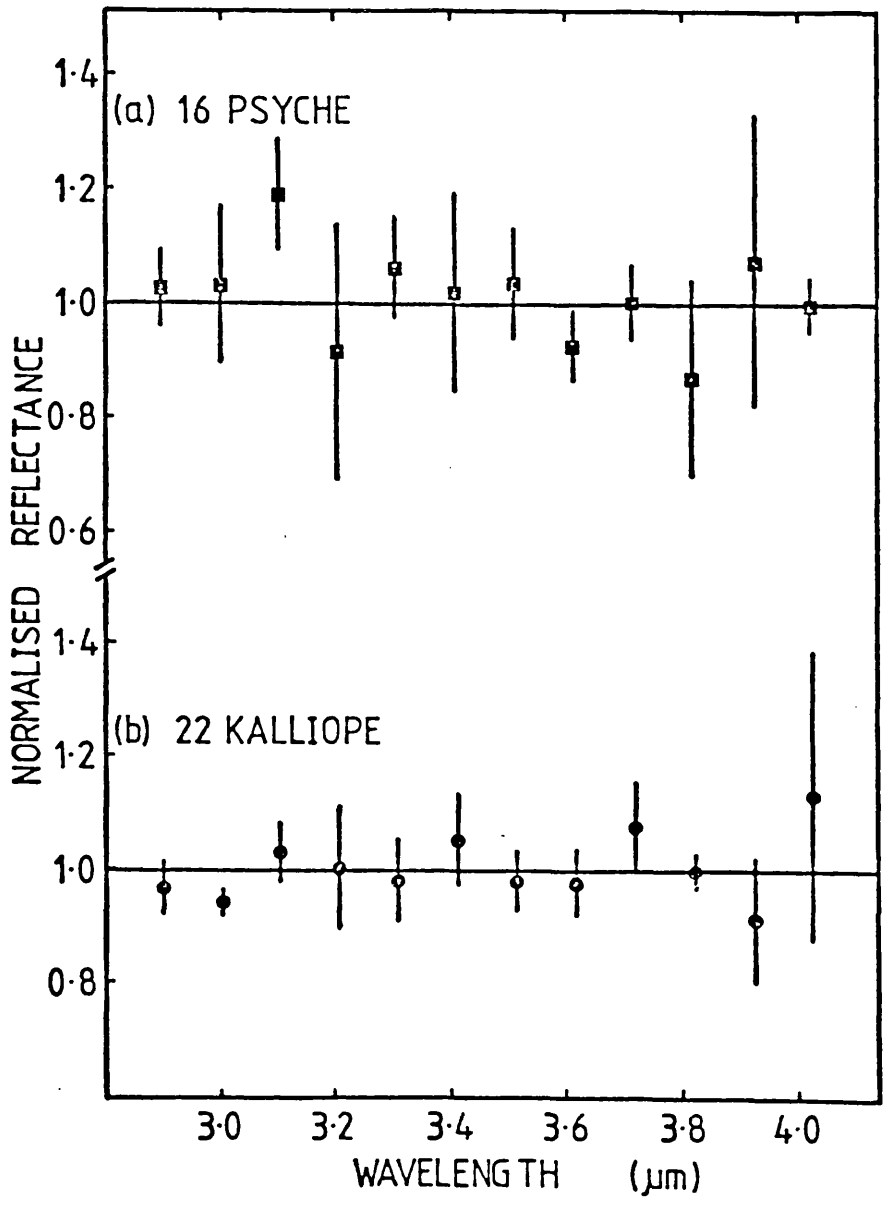


Fig. 3.19 As Fig. 3.18 for the M-type asteroids 16 Psyche and 22 Kalliope.

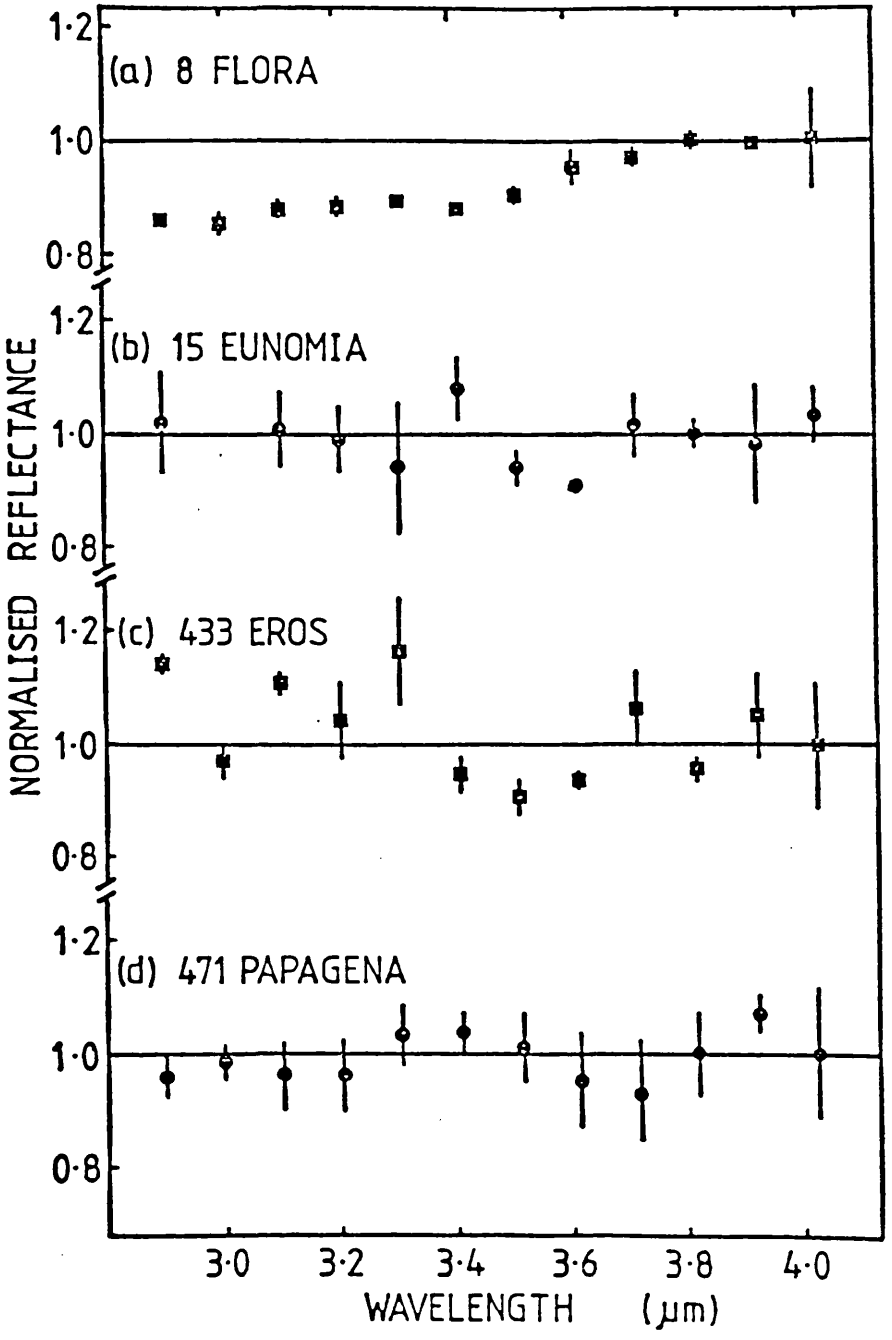


Fig. 3.20 As Fig. 3.18 for the S-type asteroids 8 Flora, 15 Eunomia, 433 Eros and 471 Papagena.

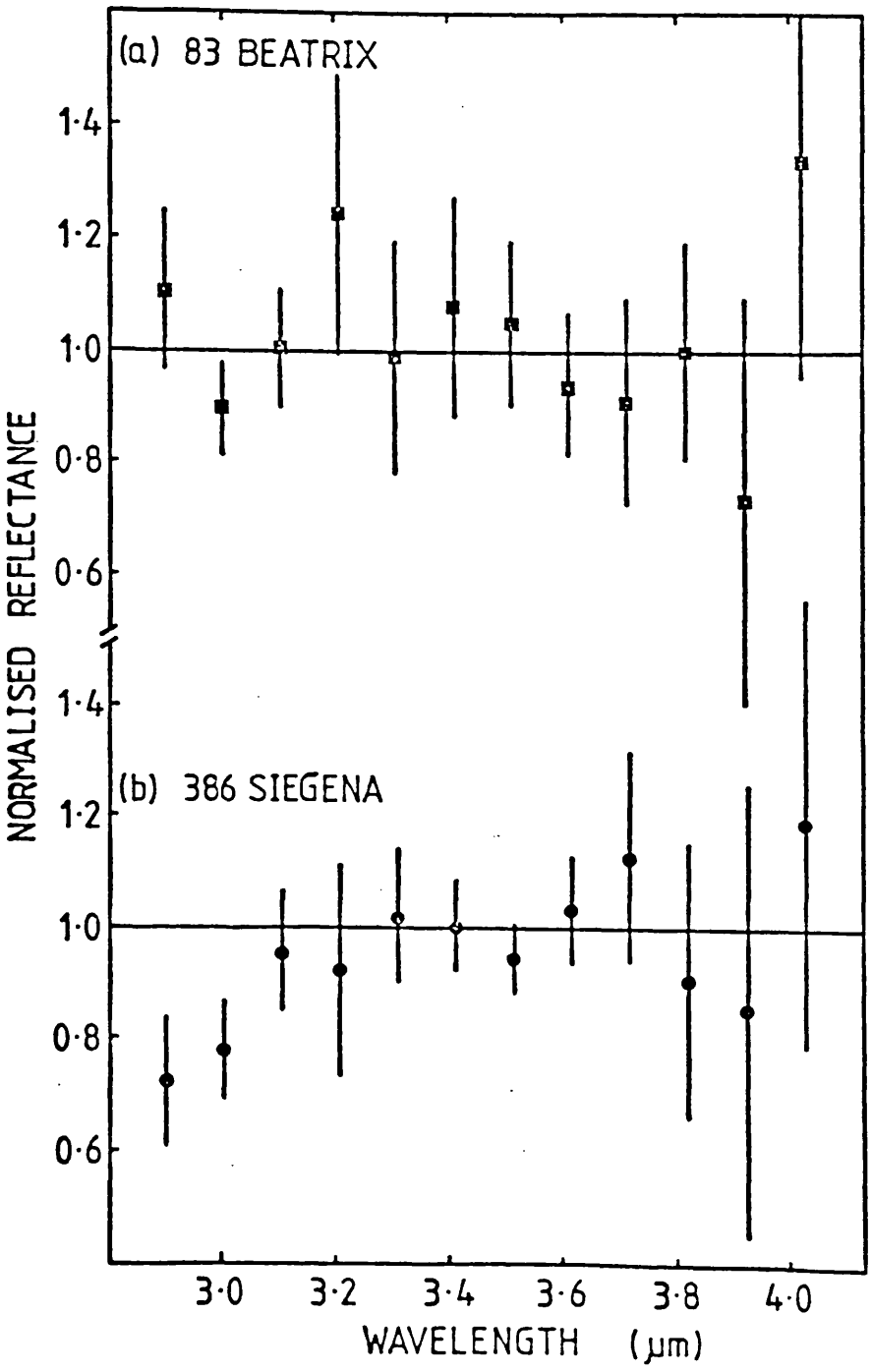


Fig. 3.21 As Fig. 3.18 for the C-type asteroids 83 Beatrix and 386 Siegena.

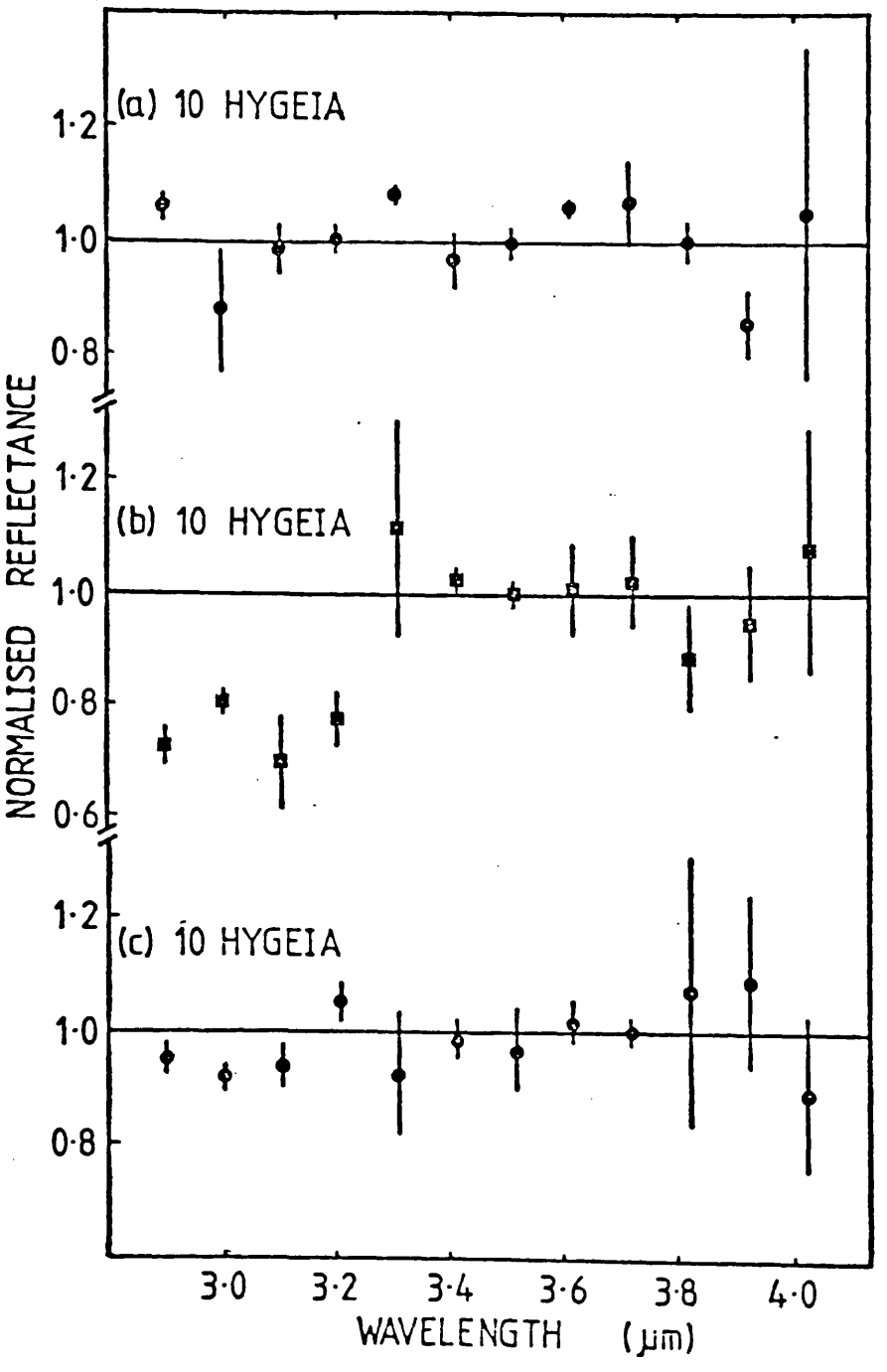


Fig. 3.22 As Fig. 3.18 for the C-type asteroid 10 Hygiea. The observations were obtained on three separate nights.

appears to rise. The 2.9 to 4.0μm spectrum could be a continuation of this reddening, rather than an absorption. Also the classification of Flora firmly in the S-type group suggests that the spectrum is not due to the 3μm water of hydration absorption.

Of the three new C-type asteroid spectra reported here, none shows significant evidence for absorption.

## 3.7 THERMOPHYSICAL MODEL

### 3.7.1 Introduction.

The thermal models described so far have been rather idealised. Their success is due to their simplicity of calculation, reasonable agreement with the properties of large main belt asteroids observed at small phase angles, and the lack of information available for more detailed models. The rotation properties (period, pole position and sense of rotation), shape, surface composition, physical and thermal properties are required to produce a realistic thermal model. At present, the limited accuracy and wavelength coverage of observations do not warrant complicated models except in particular cases.

The Amor asteroid 433 Eros was extensively observed at its 1974-75 apparition (Zellner, 1976). Lebofsky and Rieke (1979) used these and their own high time resolution 1.25-20μm data to compare with predicted fluxes from thermal models which allowed for the non-spherical shape (approximated by a cylinder with hemispherical ends) and shadowing effects. They treated the surface as a homogeneous material with values of

thermal inertia, $I=(k\varrho c)^{1/2}$, of:-

| | | |
|---|---|---|
| 0.001 $Cal.cm^{-2}s^{-1/2}K^{-1}$ | (40 $J.m^{-2}s^{-1/2}K^{-1}$) | "dust"; |
| 0.009 .. | 380 .. | "sand"; |
| 0.052 .. | 2200 .. | "rock". |

The best-fit models (at both lightcurve maximum and minimum) were obtained using a combination of these thermal inertias, implying a surface with 10-50% rocky material. The derived albedo was ~30% lower than previous estimates using simpler models.

Simonelli (1983) used a thermophysical model to fit IRIS data for Amalthea. The model included triaxial ellipsoid shape, eclipses and reflected and thermal emission from Jupiter, and a beaming function of the kind described by Hansen (1977).

These models represent attempts to model unusual objects which have a number of well-observed properties. They use essentially the same method for solving the conduction equation as employed by Wesselink (1948). The basic model is described below, with indications of where modifications for shape and variable properties can be incorporated.

### 3.7.2 Calculation of the model.

Before the surface temperature distribution can be calculated, the orientation of the asteroid must be defined with respect to the sun. Since the duration and angle of insolation, which determines the energy input to the surface, depends on the rotational properties, coordinates are defined in terms of an asterocentric equatorial system $({}_a\theta, {}_a\phi)$. Appendix E explains how the coordinates of the Earth and Sun are calculated from ephemerides and tabulated (or assumed)

pole positions. The coordinates of the surface normal of any point, $(\eta,\zeta)$, on a spherical asteroid are determined simply by the rotational period. Non-spherical shapes can be introduced by redefining the surface coordinate system.

In order to calculate the temperature for any surface element, the one-dimensional heat conduction equation (section 3.1.2) must be solved with the appropriate boundary conditions.

$$\frac{\partial T}{\partial t} = \frac{k}{\varrho c}\frac{\partial^2 T}{\partial x^2}$$

with the boundary condition at the surface

$$(1-A)\ (S_o/r^2)\ \cos\psi_s\ (_a\theta_s, {}_a\phi_s, \eta, \zeta, t) + k\left(\frac{\partial T}{\partial x}\right)_{x=0} - \varepsilon\sigma T_o^4 = 0$$

and $\frac{\partial T}{\partial x} \to 0$ as $x \to \infty$

$\psi_s$ is the angle between the surface normal and the direction of the sun, $T_o$ is the surface temperature.

The equations can be normalised by substituting for the variables $\xi=x/l$, $\tau=t/P$. $l=(4\pi kP/c\varrho)^{1/2}$ is the depth at which the phase lag of the temperature oscillations is $2\pi$, obtained from solution of the heat conduction equation with harmonic variation of surface temperature. The amplitude of the temperature variation at $x=l$ (or $\xi=1$) is $e^{-2\pi}$ or 0.2% of the surface amplitude.

The conduction equation therefore becomes

$$\frac{\partial T}{\partial \tau} = \frac{1}{4\pi}\frac{\partial^2 T}{\partial \xi^2}$$

with the surface boundary condition

$$(1-A)\ (S_o/r^2)\ \cos\psi_s\ (_a\theta_s, {}_a\phi_s, \eta, \zeta, \tau) + \left(\frac{kc\varrho}{4\pi P}\right)^{1/2}\left(\frac{\partial T}{\partial \xi}\right)_{\xi=0} - \varepsilon\sigma T_o^4 = 0$$

The conduction equation can be solved using a step-by-step method with finite difference equations. If $T_{ij}$ is the

temperature at depth $\xi=i\delta\xi$, i=1...n, and time $\tau=j\delta\tau$, j=1...m, then using finite difference approximations (e.g. Smith, 1978) for the derivatives gives

$$T_{i,j+1} = T_{ij} + r\,(T_{i-1,j} - 2\,T_{ij} + T_{i+1,j}) \qquad (2)$$

where $r = \frac{1}{4\pi}\left(\frac{\delta\tau}{\delta\xi}\right)^2$. For convergence, the time and depth intervals should be chosen such that r<0.5. Thus the temperature at one time can be calculated from the temperatures at the previous time step. The new surface temperature $T_{o,j+1}$ is obtained by solution of the boundary condition using Newton's method. If $(T_{o,j+1})_r$ is an approximation to a solution, then a closer approximation $(T_{o,j+1})_{r+1}$, is given by

$$(T_{o,j+1})_{r+1} = (T_{o,j+1})_r + \frac{C_1 - C_2(T_{0,j+1})_r - C_3(T_{o,j+1})_r^4}{C_2 + 4C_3(T_{o,j+1})_r^3} \qquad (3)$$

where $C_1 = (1-A)\,(S_o/r^2)\cos\psi_s({}_a\theta_s, {}_a\phi_s, \eta, \zeta, \tau) + C_2\,T_{i,j}$

$$C_2 = \left(\frac{kc\varrho}{4\pi P}\right)^{1/2}\frac{1}{\delta\xi}$$

$$C_3 = \varepsilon\sigma$$

The inner boundary condition is satisfied by choosing a value of q>1 so that the temperature oscillations are negligible compared to those at the surface.

Modifications such as emissivity and albedo varying with wavelength, and radiative energy transfer (which can be appreciable at high temperatures; Clegg et al., 1966) can be introduced into the surface boundary condition.

The surface temperature distribution is obtained by inputting an initial temperature distribution and succesively solving the conduction equation, (2), and boundary condition, (3), until convergence to a harmonic solution is obtained.

For rapid convergence (~20 revolutions) the initial temperature distribution should be set close to the actual temperature at large depths since the surface variations take longest to affect these regions. Several short iterations of (2) and (3) with relatively large depth and time steps, ($\delta\tau$, $\delta\xi$), will define this temperature to within a few degrees. Seasonal variations can be introduced by allowing a non-zero temperature gradient at the inner boundary.

Once the temperature distribution has been calculated, the flux observed at the Earth is calculated from

$$S(\lambda)=\frac{\varepsilon R^2}{\Delta^2}\int_0^{2\pi}\int_{-\pi/2}^{\pi/2} B(\lambda,T_O)\cos\phi\,\Gamma(\psi_e)\cos\psi_e({}_e\theta_s,{}_e\phi_s,\eta,\zeta,\tau)\,d\phi\,d\theta$$

where $\psi_e$ is the angle between the surface normal and the direction of the Earth. $\Gamma(\psi_e)=0$ if $\psi_e>\pi/2$. Modifications such as for non-isotropic emission can be incorporated here.

### 3.7.3 Application of the model.

As explained above, use of this model is only justified in certain cases where the use of standard models would produce large errors. Often, little is known of the rotation properties of these asteroids, leaving a large number of free parameters in the models. The thermophysical model can, however, be used to indicate the type of surface material present.

Fig. 3.23 shows the equatorial surface temperature for a spherical asteroid, with its rotation pole perpendicular to the ecliptic, a period of 10 hours and at a heliocentric distance of 1A.U. Case 1 is from the fast-rotating model (section 3.5.3); cases 2a and 2b are from the modified projected model (section 3.5.2) with f=0.62 and 0.43

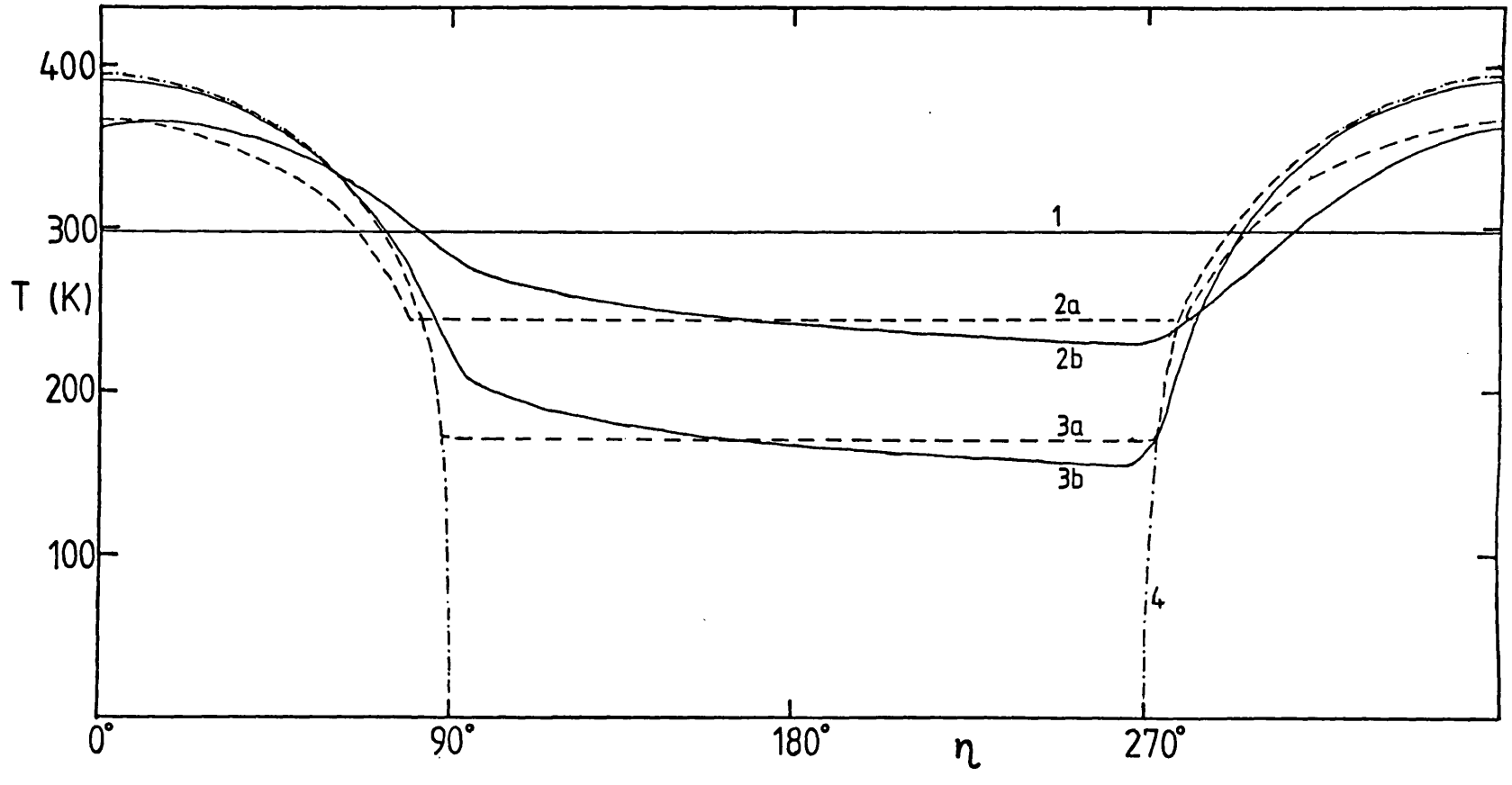


Fig. 3.23 Equatorial surface temperature for a spherical asteroid with r=1A.U., $\beta_s^a = 0°$, $\beta_\rho^a = 0°$ and $P = 10^h$. 1 - fast-rotating model; 2a - modified projected model (f=0.43); 2b - thermophysical model (rocky); 3a - modified projected model (f=0.62); 3b - thermophysical model (dusty); 4 - standard model.

respectively; cases 2b and 3b are from the thermophysical model with "rocky" and "dusty" surfaces respectively; and case 4 from the standard model. In these cases the modified projected model gives a reasonable approximation to the temperature distribution derived from the thermophysical model. If the asteroid was observed "pole-on", the thermophysical model would produce a temperature distribution similar to that from the standard model. Thus, some idea of the minimum value of the thermal inertia can be obtained by comparing thermophysical models with the best fit simple model. This method has been applied to the thermal emission spectrum of (3200) 1983TB in section 5.6.

# CHAPTER 4

# IRAS SEARCH FOR FAST-MOVING SOLAR SYSTEM OBJECTS

## 4.1 INTRODUCTION

The Infrared Astronomical Satellite (IRAS), launched on 26 January 1983, was the first satellite dedicated to infrared astronomical observations. Its primary mission was to produce an all-sky survey in four wavebands centred on 12, 25, 60 and 100μm (bands I, II, III and IV). The satellite carried a liquid-helium-cooled 57cm Ritchey-Chretien reflector, with an array of 64 detectors in the focal plane. Three additional experiments were also carried: 1) the Chopped Photometric Channel (CPC), with wavebands centred at 50 and 100μm with higher spatial resolution than the survey array; 2) the Low Resolution Spectrometer (LRS) (7-23μm), and 3) the Short Wavelength Channel (SWC) (4-8μm), for source counting during the survey. The IRAS is a joint project of the United States NASA, the Netherlands Institue for Space Research and the UK Science and Engineering Research Council. Further information on the satellite, project organisation and data processing can be found in Nature (303, p287, 1983) and the Journal of the British Interplanetary Society (36, No. 1, Special IRAS Issue 1983).

The IRAS survey objectives of high reliability and completeness were achieved by repeated detections in each wavelength band. The detector layout in the focal plane, when combined with overlapping and repeated scans, allowed the positions of sources to be confirmed on timescales of seconds, hours and weeks. As a consequence of this strategy, those objects recognised as moving a distance greater than the expected position reconstruction error over the given timescales are removed. Thus the sources not confirmed

during the survey can be divided into three groups:-

1) Seconds-confirmation failures. These include objects near to the spacecraft, such as Earth satellites, space debris and material evolved from IRAS, but most seconds confirmation failures are attributable to radiation hits on the detectors.

2) Hours-confirmation failures. These include Solar System objects moving across the sky at more than ~1 arcminute per hour (for example, some comets, some main-belt asteroids and most Earth-approaching asteroids).

3) Weeks-confirmation failures. These include slow-moving Solar System objects (such as distant asteroids, comets and planets).

Although the confirmation process is based on positional agreement and not flux comparisons, fixed but variable sources can be rejected if the source variability reduces their brightness below the detection threshold. Source confusion can also affect the confirmation routines.

The survey data processing and catalogue are being produced at the Science Data Analysis System (SDAS) at the Jet Propulsion Laboratory (JPL) in California, but some initial processing was done at the Preliminary Analysis Facility (PAF) at the Rutherford and Appleton Laboratories (RAL) in Oxfordshire where IRAS data were received during the mission. This analysis, confined to seconds and hours-confirmation allowed real-time evaluation of the spacecraft and telescope performance. Detections of slow moving Solar System objects which passed both seconds and hours-confirmation will not be found until analysis is completed at SDAS, so recovery and identification of the many new objects

to be found will hardly be possible. However, detections of inner Solar System objects which failed hours-confirmation, would be among the data rejected during the preliminary analysis. Additional software was developed by Dr Brian Stewart (RAL) and the author to separate these sources (fast-moving objects or FMOs) from the non-hours-confirmed database. The IRAS focal plane and scan strategy and the FMO software will be discussed in sections 4.3-4.5. A network of observatories prepared to cooperate in ground-based confirmation of FMO candidates was established. FMO alerts were sent both to these and to the Central Bureau for Astronomical Telegrams at the Smithsonian Astrophysical Observatory.

The original purpose of the search was an attempt to find new Earth-approaching asteroids (section 4.2), which are of importance in the investigation of how meteoritic material may be transported from the asteroid belt, and the possible connection between comets and asteroids. In fact, only two confirmed Apollo asteroids were found and the software proved more successful at discovering comets. To interpret the results of the FMO search in terms of the total populations of Earth-crossing asteroids and comets it is necessary to assess the selection effects and biases of the search, which differ significantly from those of the main IRAS survey. These are discussed in section 5.2. The observations of numbered asteroids are then used to assess the significance of these selection effects (section 5.3). The results are applied to the observations of new main-belt asteroids (section 5.4), Earth-crossing asteroids (section 5.5), comets (section 5.7), and unobserved FMO alerts (section 5.8).

## 4.2 EARTH-APPROACHING ASTEROIDS

Earth-crossing asteroids have been defined as having an orbit which, as a consequence of secular perturbations, can at some time intersect the orbit of the Earth (Shoemaker et al., 1979). Previous definitions required that the orbit should actually overlap that of the Earth but not necessarily intersect it. Earth-approaching asteroids are divided into three groups; Apollos, Amors and Atens.

Amor asteroids are defined as having perihelion distances 1.017 A.U. $< q \leq$ 1.3 A.U. (Shoemaker and Helin, 1978) where 1.017 A.U. is the present aphelion distance of the Earth. The upper bound of 1.3 A.U. is arbitrary; it was chosen near a minimum in the radial frequency distribution of q for known objects. These are therefore asteroids that make relatively close approaches to the Earth, but do not, at present, overlap the Earth's orbit. About half the known Amors are Earth-crossers.

Apollo asteroids are defined by $a \geq$ 1.0 A.U. and $q \leq$ 1.017 A.U. and most overlap the Earth's orbit in the region of perihelion. Almost all the known Apollos are Earth-crossers, and about half exhibit continuous overlap.

Aten asteroids have orbits with $a <$ 1.0 A.U. and aphelion distance $Q \geq$ 0.983 A.U. (Helin et al., 1978), where 0.983 A.U. is the present perihelion distance of the Earth. These asteroids therefore overlap the Earth's orbit near aphelion. However, there may be Atens with orbits that are at present entirely inside the Earth's orbit.

The first Amor asteroid, 433 Eros, was discovered in 1898, and the first Earth-crosser, the Amor 887 Alinda, in 1918, although Amor itself was not found until 1932. In the same year Apollo was discovered, and, by 1960, 14 Earth-crossers had been found, but over half were lost because their orbits were not sufficiently well determined to predict when they would return. However, a number of them were recovered, either accidentally, or through planned searches. In the 1970's a period of more rapid discoveries began with the Palomar Planet-Crossing Asteroid Survey (PCAS) (Helin and Shoemaker, 1979). Many discoveries have also been made during Schmidt survey work and over 60 Earth-crossers are now known.

The distribution and physical properties of asteroids are of fundamental importance to the study of the formation and evolution of the Solar System. Earth-crossing asteroids are of particular importance because they may represent the link between meteorites, which can be studied in the laboratory, and the source of that material in the asteroid belt. Opik (1951), first noted that they cannot have remained in their present orbits since the formation of the planets, because their average lifetime for collision with the planets, or ejection from the Solar System, is very much less than its age. The impact records on the Earth and Moon, however, show that the population has remained fairly steady for the last $\sim 3 \times 10^9$ years, indicating a fairly constant source of Earth-crossing asteroids. This source cannot be from successive Mars encounters alone, since there are too few observed Mars-crossing asteroids to account for the flux

of Earth-crossers (Opik, 1963; Wetherill and Williams, 1968). Regions of the main belt bordering low order commensurabilities and secular resonances with Jupiter are likely source regions for Earth-approaching asteroids. Large-amplitude oscillations of certain orbital elements occur when asteroids are placed deep in these resonances, most of them becoming Mars or Earth-crossers. Zimmerman and Wetherill (1973), Williams (1973a;1973b), Scholl and Froschlé (1977), Wetherill (1977;1979), and Wetherill and Williams (1979) have shown how meteorites could be delivered to Earth as collisional fragments, injected into resonances from asteroids bordering either the 2:1 or 5:2 Kirkwood gaps, or certain secular resonances, but these can only account for a small proportion of the observed Earth-crossers. Wisdom (1982;1983) has shown how material cleared from the 3:1 Kirkwood gap can be transferred into Mars-crossing and then Earth-crossing orbits.

There is both dynamical and physical evidence for the belief that comets may decay into asteroids. Originally, the main reason for demanding a cometary origin for most of the Apollo objects (Opik, 1963) was the excess of these objects over the number expected from a source in the asteroid main belt. Although most short-period comets are captured by Jupiter's (and the other giant planets') influence, and are unlikely to be captured by encounters with the terrestrial planets into orbits like those of the Earth-approaching asteroids, a few of them have aphelia well inside Jupiter's sphere of influence, presumably due to non-gravitational forces. These forces are due to the lag in heating of the cometary surface as it rotates, so that the jet force on the

surface from sublimation does not act directly towards the Sun but produces a force towards the surface on the afternoon side. This can produce an increase or decrease in the orbital period depending on the sense of the cometary spin. Observed change in the non-gravitational acceleration of P/Encke, which has the smallest known cometary orbit, suggests that it might become extinct due to exhaustion of volatiles at successive perihelion passages in a period as short as 60-70 years (Sekanina, 1972). Comets P/Arend-Rigaux and P/Neujmin 1, although in less stable orbits than Encke, also appear to be nearly extinct. An evolutionary history which would convert comets into asteroids appears best explained by vapourisation of Whipple's dusty-ice conglomerate, or "dirty snowball" model for a comet. As the ices sublime, and larger non-volatile aggregates are left behind, a crust forms which gradually covers the nucleus to a depth such that insufficient heat is transmitted to vaporise the deeper-lying volatiles (Whipple, 1951; Opik, 1963; Levin, 1977). Additional evidence for this model is provided by observations of comet outbursts, survival of Sun-grazing comets and the details of splitting of cometary nuclei (review by Sekanina, 1982). However, a number of comets are known to have faded away without leaving asteroid-like cores, e.g. P/Brorsen and P/Biela.

Apollo asteroids 1978SB=2212 Hephaistos and 1982TA lie in similar orbits to Encke and the Beta Taurid meteor stream (although the longitudes of perihelion and ascending node are not aligned). Other tentative associations with meteor streams have been made. Monte-Carlo simulations using the orbit of comet Encke as a starting point (Wetherill, 1979)

produce an equilibrium distribution of orbits like that observed for the Earth-crossing asteroids. Shoemaker et al. (1979) conclude that the supply of comets which become extinct in orbits safe from Jupiter encounter appears to be adequate to maintain the population of Earth-crossing asteroids; only one comet like Encke is required every few $10^4$ years to maintain it.

Rickmann and Froeschlé (1980) considered a steady state where the Jupiter family of comets are the source for the Apollo-Amors. They concluded from Monte-Carlo simulations that ~50 Apollo-Amor-like inactive comets should have been observed in Jupiter-crossing orbits. At that time none had been discovered, implying that less than 5% of these comets decay to an asteroidal nucleus. Recently, however, the Amors 1982YA and 1983SA, the Mars-crosser 1983XF, and 1984BC have been found in comet-like orbits which cross Jupiter's orbit.

Physical studies, including spectrophotometry, lightcurves, polarimetry and radiometry have only been possible for a few Earth-approaching asteroids due to their faintness and short apparitions, but almost half have UBV observations. The diversity of UBV colours (some have S or C-type colours, but others are unlike those of any other asteroids) indicate that a variety of mineralogical compositions are present. For example, the Aten 2340 Hathor and the Apollo 1566 Icarus have closely similar colours and extremely blue U-B values. Shoemaker and Helin (1978) suggested that the colours and possibly other surface properties have been affected by close approaches to the Sun. Polarimetry and radiometry also suggest a range of albedos from the S to C domains. Computed diameters range from ~20km

for 433 Eros down to a few hundred metres; for 1580 Betulia and 2100 Ra-Shalom the observations can only be reconciled if they have bare rock over part, or all of their surfaces. Optical lightcurves have been observed for a number of Earth-approaching asteroids. A range of periods from less than three hours (1566 Icarus) up to over seventy hours (887 Alinda) have been found. Amplitudes of up to two magnitudes (1620 Geographos), and unusual lightcurves for some objects indicate elongated and irregular shapes; possible evidence for them being collision fragments. McFadden et al. (1984a) have presented spectrophotometry of 17 near-Earth asteroids and divide their spectra into four groups. Comparison with laboratory spectra indicates that their surfaces are composed of common rock-forming minerals such as olivine, pyroxene and phyllosilicates combined with some unidentified opaque components. The one exception was 2201 Oljato which was examined for cometary features because of its high orbital eccentricity and possible meteor stream connection (Drummond, 1982). The possibility that Oljato might be an extinct comet has also been raised by Russell et al. (1984) following observations of disturbances in the interplanetary magnetic field measured by the Pioneer Venus orbiter. The source of the disturbances appeared to be some distance behind the asteroid in its orbit. At present, the spectral features seen in Oljato cannot be attributed to any known type of asteroidal material or cometary activity (McFadden et al., 1984b). The asteroid 1984BC shows no cometary emissions, but has a very low albedo and D-type colours. D-type asteroids are common in the outer Solar System and have colours similar to those found for for distant low-activity comets (Hartmann

et al., 1982). Considered along with its apparent close dynamical relationship with Jupiter, these properties suggest that it could be an extinct cometary nucleus (Helin et al., 1984).

The wide range of properties of the Earth-approaching asteroids is indicative of diverse origins. The density structure of the Apollo system suggests the presence of two distinct populations, one of which, the outer halo, might be of cometary origin (Kresák, 1979). Some meteor streams, (generally associated with comets) and observed fireballs move in orbits of Apollo type, but the structure of most meteorites requires formation in large (several hundred km diameter) bodies, indicating asteroidal origin. Population and dynamical studies indicate that only a fraction of the observed Earth-approaching asteroids can have originated as Mars-crossers, or in the main belt, whereas cometary origins for the remainder can be inferred if even a small fraction of comets decay to inactive nuclei.

## 4.3 THE FOCAL PLANE ARRAY

The IRAS focal plane (Fig. 4.1) contains an array of 62 survey detectors as well as the DAX and 8 visible light detectors for attitude reconstruction. The detectors in the survey array are arranged so that every source crossing the 30arcmin. field of view is seen by at least two detectors in each wavelength band, providing seconds-confirmation. The shaded detectors were inoperative, or essentially so during the mission. The accuracy of measurement for the cross-scan

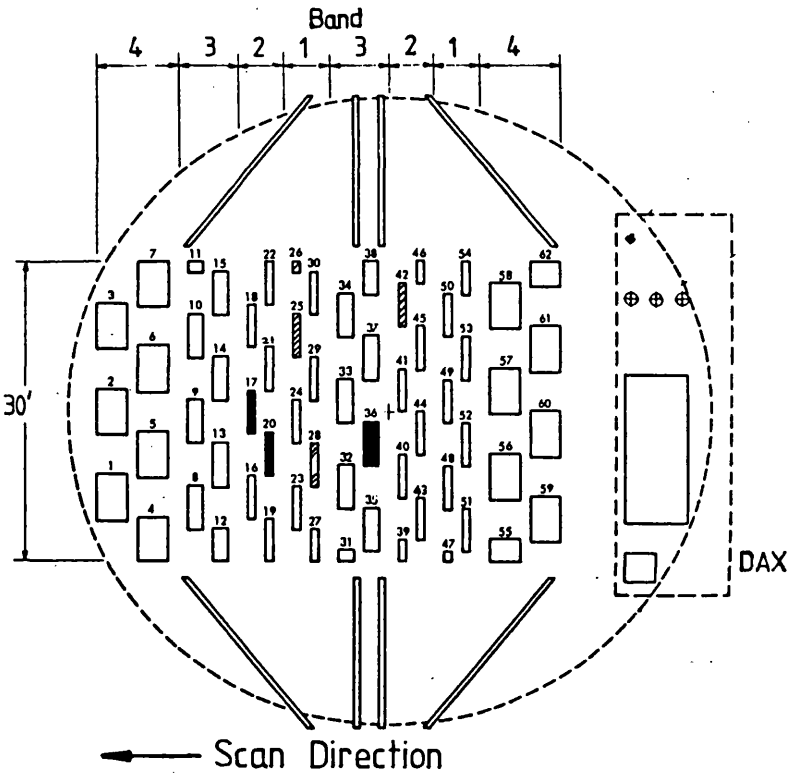


Fig. 4.1 The IRAS focal plane array, showing the layout of the 62 survey detectors, the Dutch Additional Experiment (DAX) and visible star sensors. The shaded detectors were inoperative, or essentially so during the mission. (From Neugebauer et al. 1984.)

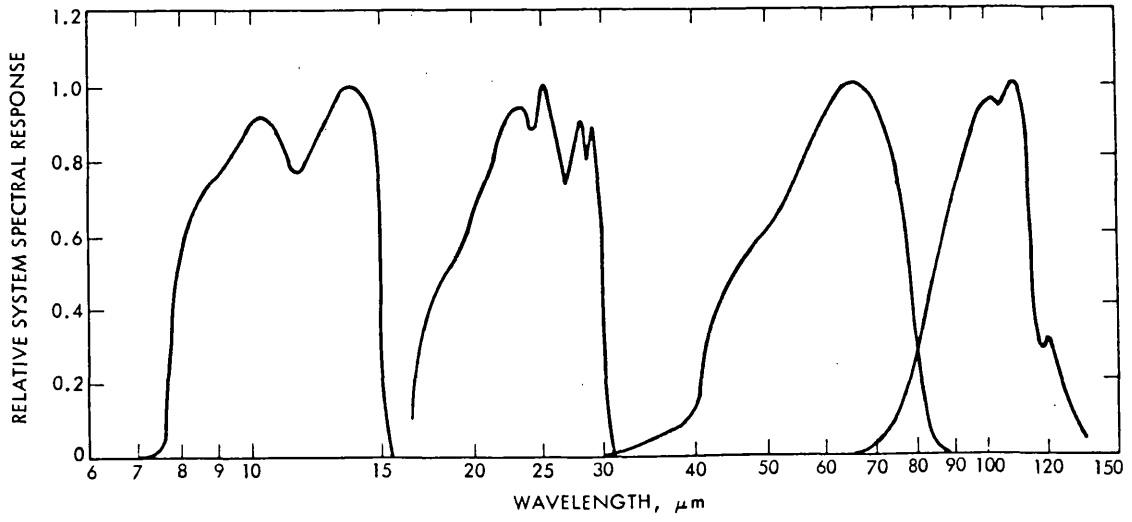


Fig. 4.2 System spectral responses of the four IRAS bands. (From Neugebauer et al. 1984)

TABLE 4.1

IRAS survey detectors

| Band | Centre wave-length | No of detectors | Field of view | Wavelength interval | Detector material | Dwell time | *1982 10σ sensitivity require-ments | 1983 average 10σ sensitivity |
|---|---|---|---|---|---|---|---|---|
| | (μm) | | (arcmin) | (arcmin) | | (sec) | (Jy) | (Jy) |
| I | 12 | 16 | 0.75x4.5 | 8.5-15 | Si:As | 190 | 0.4 | 0.7 |
| II | 25 | 15 | 0.75x4.6 | 19-30 | Si:Sb | 190 | 0.7 | 0.65 |
| III | 60 | 16 | 1.5 x4.7 | 40-80 | Ge:Ga | 390 | 2.0 | 0.85 |
| IV | 100 | 15 | 3.0 x5.0 | 83-120 | Ge:Ga | 780 | 3.0 | 3.0 |

*Infrared Astronomical Satellite Telescope Performance Requirements 623-111; Rev. A. NASA, JPL, 1982.

position of a source is determined by the length of a detector (4.5-5.0 arcmin.) and, for the in-scan position, by the accuracy of measurement of the peak detector signal (∼0.25arcmin.). The focal plane pointing position had errors of ∼0.25arcmin. The two arrays of detectors in each band are arranged so that the errors in cross-scan position of a source measured in two bands can be reduced to ∼1arcmin.

Table 4.1 gives the detector characteristics and Fig. 4.2 the spectral responses of the detector and field lens combination (Neugebauer et al., 1984).

## 4.4 SURVEY SCAN STRATEGY

IRAS was launched into a circular orbit with an altitude of 900km, a period of 100 minutes and an inclination of 99° to the Earth's equator. The plane of the orbit was perpendicular to the Sun direction and precessed at approximately 1° per day to maintain this orientation. The telescope was constrained to point at fixed solar elongation angles between 60° and 120° and scanned at 3.85 arcmin.$sec^{-1}$ in the survey mode. Thus the in-scan direction was nominally along lines of constant ecliptic longitude. Consecutive orbits were displaced by ∼15arcmin. i.e. half the array width, to provide hours confirmation (Fig. 4.3). All pairs of sources which had measured positions agreeing within the uncertainties defined by the detector size and pointing reconstruction were regarded as hours-confirmed. Seven to eleven days later each pair of hours-confirming scans was repeated to provide weeks-confirmation.

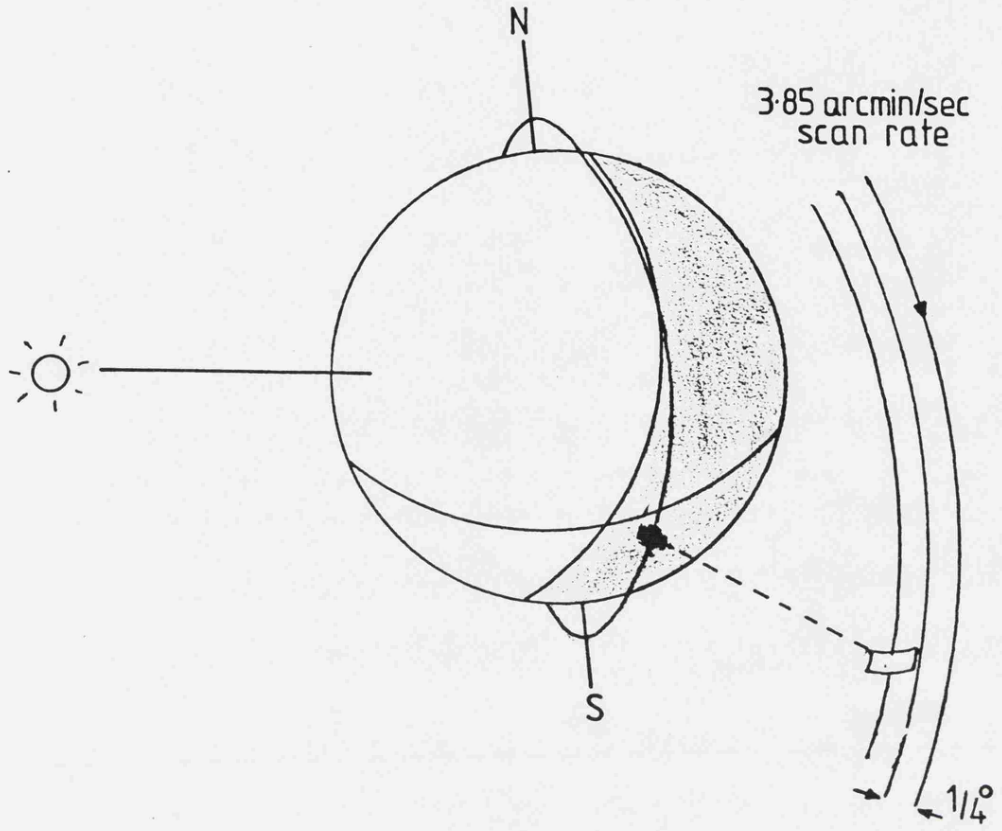


Fig. 4.3 The IRAS scan geometry showing hours-confirming scans

Of the 14 orbits available each day, the 9 orbits least affected by the South Atlantic Anomaly (a region where the Earth´s radiation belts reach down to the orbital altitude of the spacecraft, causing saturation of the detectors by high energy particles) were devoted to the main survey, except when the Moon was within 25° of the pointing direction. For most of the mission, the scans were arranged in lunes, segments bordered by lines of ecliptic longitude 60° apart. Towards the end of the mission simple polar scans were performed. The remaining orbits and part orbits were taken up with calibration observations and additional observations of selected areas. The data for each Spacecraft Operating

Program (SOP) were transmitted twice a day to PAF where initial seconds and hours-confirmation were performed.

## 4.5 THE FMO SOFTWARE

The FMO software was developed from the hours-confirmation software written by Dr. Brian Stewart (RAL). A source was accepted as hours-confirmed if it was seen three out of the possible four times on the two scans making up an hours-confirming pair. The remaining seconds-confirmed sources which were not hours-confirmed were output to the file POTF, from which a search for fast-moving objects was made, using the program FASTEROID in the following way:-

1) Source selection parameters were entered in the file ASTEROIDPARS.
2) Data were read from POTF.
3) Sources which may have been asteroids (according to the selection parameters) were retained. These asteroid-like sources were output to ASTEROIDLOG.
4) Various criteria were used to select pairs of sources which may have been fast-moving asteroids.
5) Listings of these pairs were made from files ASTEROIDCAND and ASTEROIDPOSS and studied manually for any possible candidates.

Fig. 4.4 illustrates the input/output for FASTEROID.

Initial Source Selection.

Data were stored on POTF for each SOP, according to the spacecraft coordinate system $(\theta,\phi)$. Sources were listed in $\phi$

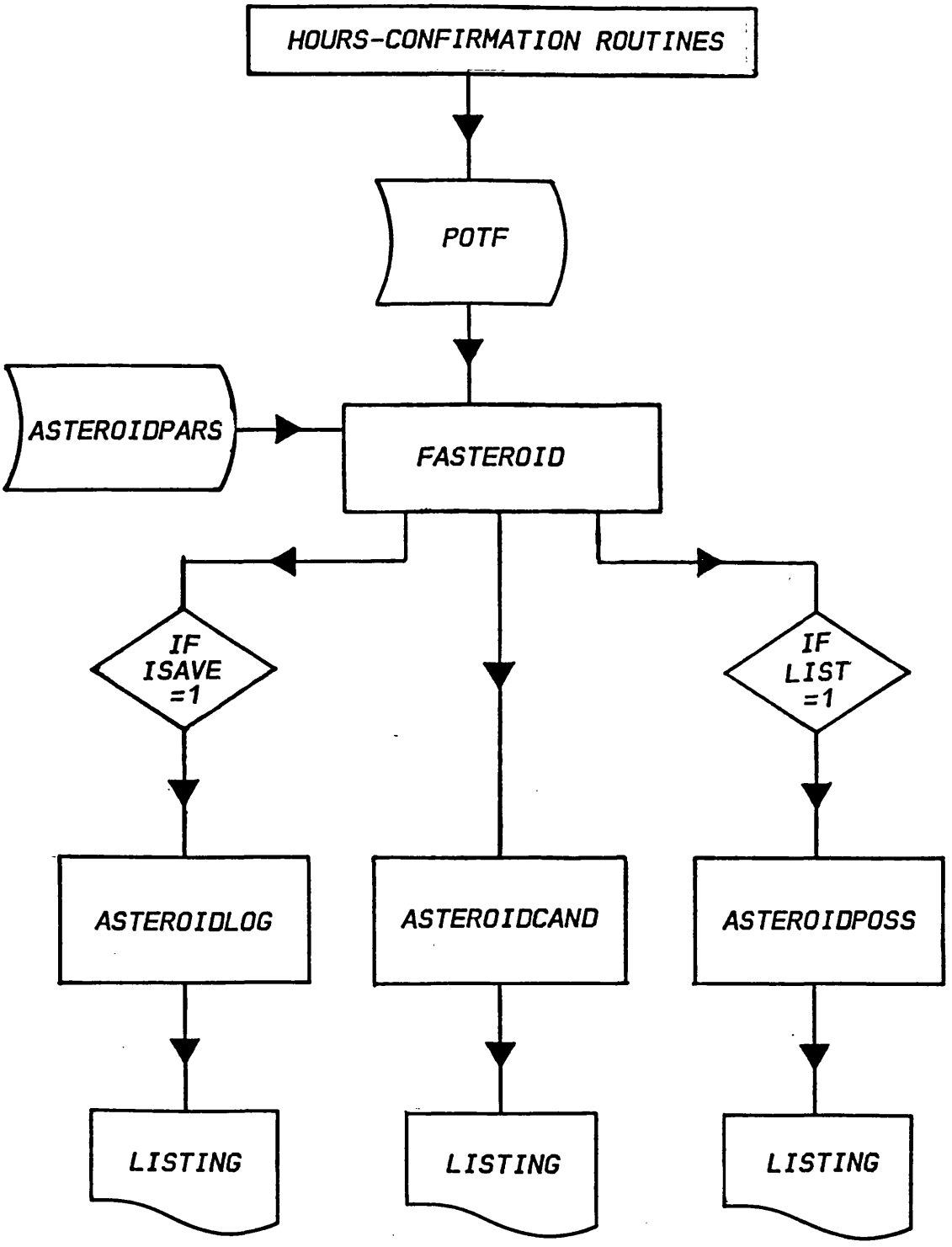


Fig. 4.4 INPUT/OUTPUT for FASTEROID.

order, which approximated to the in-scan direction. Only those sources which may have been asteroids were selected using the following tests:-

1) Rejection of "hot" sources using the parameter RFTST.

   Only those sources with $\frac{\text{Flux(Band I)}}{\text{Flux(Band II)}} < \text{RFTST}$ were accepted.

2) Rejection of "cold" sources using the parameter RFTST4.

   Only those sources with $\frac{\text{Flux(Band II)}}{\text{Flux(Band III)}} > \text{RFTST4}$ were accepted.

3) Galactic latitude test using parameter ALIM2.

   Due to possible source confusion in the region of the galactic plane, only those sources with galactic latitude $|B| >$ ALIM2 were accepted.

This initial selection procedure would have been sufficient if all the band fluxes had been measured. However it was possible that some or all the detectors in one band may not have been working during the mission. When the program was developed (May/June 1982), all of the band IIA and two band IIB detectors had been declared dead. In that situation, some cool sources would not have had their 20μm fluxes measured. To allow these sources (potential asteroid detections) to pass initial selection, the following system was adopted. Each source was assigned a type depending on the presence of band I, II and III flux detections as shown in Table 4.2.

All other possibilities were rejected. The parameter IWORK could be set to:-

1 if all band I detectors working (rejects types 5 and 6)

2 if all band II detectors working (rejects types 3 and 4)

TABLE 4.2

Types assigned to individual sources

| Type | Detections | | | Tests made | | |
|---|---|---|---|---|---|---|
| | Band I | Band II | Band III | RFTST | RFTST4 | ALIM2 |
| 1 | Y | Y | Y | Y | Y | Y |
| 2 | Y | Y | | Y | | Y |
| 3 | Y | | Y | | | Y |
| 4 | Y | | | | | Y |
| 5 | | Y | Y | | Y | Y |
| 6 | | Y | | | | Y |

3 if all band I+II detectors working (rejects types 3,4,5,6)
0 assumes there are dead detectors in bands I and II.

The individual sources selected as asteroid-like were listed in ASTEROIDLOG if the parameter ISAVE was set to 1.

Source comparison.

The parameters PHILIM and THLIM defined the search box size in arcminutes. Each source was compared with every subsequent source within this search box. PHILIM and THLIM were chosen as a compromise between the maximum possible motion of an asteroid and the point at which source confusion would dominate.

For a pair of sources to be observations of the same object they must have been observed on different orbits. Pairs with times of observation more than 1 hour apart were retained. Additionally, to prevent large numbers of unrelated pairings, a maximium time separation of 4 hours was allowed. Earth-crossers would, in general, have been unlikely to remain within the search box area for confirming

scans separated by three or more orbits.

Pairs were selected if their fluxes in each band agreed to within factors defined by the parameters IDIFF (used for bands I and II and IDIFF4 (used for band III). Fluxes could be affected by source confusion, noise, differences both between, and across detectors, and asteroid lightcurves.

Pairs were passed if

$$\frac{F1\ (Band\ I\ (or\ II))}{F2\ (Band\ I\ (or\ II))} > 1 - \frac{RFTST}{100} \text{ and } \frac{F1\ (Band\ III)}{F2\ (Band\ III)} > 1 - \frac{RFTST4}{100}$$

for F1 > F2.

Due to the problems encountered with possible dead detectors, not all these comparisons could be made for each source pair. Two files of candidate FMO's were therefore produced. For a source to be selected as a "strong" candidate and be written to ASTEROIDCAND, it must have contained at least three detections in bands I or II. If the number of selected pairs turned out to be small, a second file ASTEROIPOSS could be produced containing candidate FMO's with two band I, or two band II measurements. This listing was obtained when the parameter LIST was set to 1.

Output

The output files contained for each source:-
source identification number; time of detection; spacecraft, equatorial, ecliptic and galactic coordinates; in-band fluxes; cross-scan position; type.

## 4.6 SELECTION PARAMETERS

In general, the selection parameters were chosen with

generous thresholds to allow any possible inner Solar System object to pass. This did have the effect of increasing the numbers of other sources, but, in practice, the numbers were manageable, so most parameters remained unchanged during the mission.

By the time of launch, the band IIA problem had been resolved, but two band IIB detectors were still inoperative. Band I was found to be less sensitive than expected by a factor $\sim$2, so any Solar System object detected in band I would also be detected in band II at least once. However, the faintest asteroids detectable would only be seen in band II, so IWORK was set to 2.

IRAS in-band fluxes were quoted in units of $W.m^{-2}{}_{x10}{}^{-16}$. The PAF calibration changed twice during the mission so RFTST and RFTST4 were varied. The values were chosen to correspond to effective blackbody temperatures of approximately 400K and 100K, respectively.

ALIM2 was set to $5^{o}$, the galactic latitude at which confusion became dominant. The search box size (PHILIM,THLIM) was set at 25x25arcmin. A faint source detected only twice would not have been recognised if its motion produced a source separation greater than these values.

There were small cross-detector sensitivity variations, but each individual detector was calibrated separately. The greatest contribution to potential flux differences between two detections of the same object would be asteroid lightcurves, which can be large for small irregular Earth-crossers. IDIFF and IDIFF4 were set at 85% corresponding to a difference of $2^{m}.1$.

The parameter ISAVE was set to 1 once the program was working efficiently and the number of sources became manageable.

# CHAPTER 5

# RESULTS OF THE FAST-MOVING OBJECT SEARCH

## 5.1 IMPLEMENTATION OF THE PROGRAM

IRAS was launched on the 26 January 1983 (SOP 1). The cover which kept the telescope free from contamination in the Earth's atmosphere was ejected on the 1 February and after a period of in-orbit checkout and calibration, survey observations were begun on 9 February (SOP 29).

The FMO program was first run on SOP 32 with real data. Modifications and testing lasted about two weeks. The first main-belt asteroid was identified on SOP 61 and the program was run essentially unchanged until the end of the mission (SOP 600). The LOG file was produced from SOP 96, and POSS file for SOPS 32-114 and 265-600. Occasionally, no listings were produced because of software problems. Since non hours-confirmed sources were retained in POTF for 48 hours (4 SOPS) these data were not actually "lost".

On average ∽50 non-hours-confirmed sources per SOP passed the initial selection tests. Of these ∽50% were band II only detections, 10-15% each of i) band I+II (many of which appeared to be stars), ii) band II+III and iii) three or four band sources. The remainder were sources with unusual colours due to noisy detectors or source confusion.

The band II only detections were concentrated towards the ecliptic, although there were significant numbers at high latitude. The majority were of near threshold S/N and examination of the raw data showed them to be noise, mostly in the Zodiacal light background. The density of these sources was such that chance pairings made any faint fast-moving (>5arcmin.hr$^{-1}$) objects indistinguishable unless detected more than twice. Also any single band II source

crossing an inoperable detector would not be seconds-confirmed. Fixed sources entering the survey catalogue would be unaffected, since a source was accepted as hours-confirmed if it was seen three out of the four possible times in the two scans making up the hours-confirming pair, and confirmation was based on positional information only. However, when non seconds-confirmed detections were allowed into POTF, the number of potential pairings increased by several orders of magnitude, effectively reducing the probability of selecting "real" candidates, so this option was not pursued. For the above reasons, candidates were not selected from the POSS file during the early part of the mission.

The first FMO alert was a long time coming, but, fortunately, when it did occur, it was completely unambiguous. The positions were sent to cooperating observatories on 26 April. It was observed by IRAS as a bright four-band source moving at 0.61 arcmin.hr$^{-1}$ in longitude and 0.71 arcmin.hr$^{-1}$ in latitude. Kiso observatory in Japan reported no object, but it was observed on the 28 April by T. Oja at Kvistaborg in Sweden as a comet-like image, and independently discovered by G. Araki in Japan and G.E.D. Alcock in England several days later. Comet IRAS-Araki-Alcock passed closer to the Earth than any recorded comet except Lexell in 1770, and became a prominent naked-eye object.

Since there were many spurious pairings present in the data, particularly for faint sources, optical confirmation was essential. Thus a large proportion of unsuccessful alerts would have caused a waste of valuable telescope time

and a loss of confidence in the project by observers. As discoveries were made, we were better able to differentiate between potentially real objects and spurious pairings, so more alerts were sent for what would have been considered marginal cases earlier in the mission.

In all 38 alerts were sent to cooperating observatories of which 17 were not searched for due to unfavourable position, bright moon, or bad weather. From the remainder, 6 new comets, 2 Apollo asteroids, 2 main-belt asteroids and an infrared tail on comet Tempel-2 were discovered. In addition, about 2000 detections of 500 numbered asteroids and 5 known comets were identified in the data. A list of all alerts sent is given in appendix B. These will be discussed in section 5.8.

On the 22nd November 1983 (SOP 600) the satellite's supply of liquid helium was exhausted and the detector systems became inoperative. 95% of the sky had been observed with at least two hours-confirming scans and 72% with three or more.

## 5.2 SELECTION EFFECTS IN THE FMO SEARCH

The selection criteria which any moving object had to pass to be detected by IRAS and then be identified by the FMO software as a strong candidate were:-

i) it must be scanned by IRAS during the mission;

ii) it must be of adequate signal-to-noise ratio in at least two of the IRAS wavebands;

iii) it must have infrared colours indicative of an inner

solar system object;

iv) it must be detected twice by IRAS within two orbits;

v) its relative motion must be sufficiently large to fail the hours-confirmation processing;

vi) it must be $> 5^{\circ}$ from the Galactic plane.

Since the average sensitivities of the IRAS detectors have been evaluated, and the expected temperatures of Solar System objects are easily calculated, effects ii) and iii) can be quantified with reasonable confidence. Effects i) and iv) depended on the IRAS scan strategy. The hours-confirmation motion limits, v), were dependent both on the position reconstruction for each orbit and the time between confirming scans. Criteria i), iv), and v) are very difficult to quantify for a large population of moving objects, even if a detailed pointing history of the spacecraft is used. In order to make a quantitative estimate of the population, a statistical approach based on detections of numbered asteroids has been used to estimate these effects.

## 5.3 NUMBERED ASTEROIDS

Although the FMO software was set up to search for new Earth-crossing asteroids, a substantial number of main-belt asteroids were detected. This was because their motions (particularly in the inner main belt) were such that a proportion were moving just fast enough to fail hours-confirmation. The output was compared manually with positions from a simple two-body ephemeris program run

previously at Leicester for the numbered asteroids up to 2882. The orbital elements, diameters and albedos were provided by D. Bender (JPL).

Over 2000 detections of 500 asteroids were identified. These included 210 candidate pairs; the remainder were single detections, or pairs separated by more than two orbits. Only 12 "band II only" detections were identified as asteroids.

### 5.3.1 Brightness Detection Limits.

The average sensitivities for each IRAS waveband are given in Table 4.1. The flux densities have been referred to standard wavelengths of 12, 25, 60 and 100μm and are for a source which has a flat spectrum in terms of the flux per logarithmic frequency interval. Because of the large bandwidths of the IRAS detectors, these sensitivities have to be corrected to those of an object with a more realistic asteroidal spectrum. This is done by convolving an asteroid thermal spectrum through the detector spectral responses given in Fig 4.2. The correction factors and method of calculation are given in appendix C. For the purpose of calculating the correction factors the asteroid thermal spectra have been approximated by a blackbody of temperature $T=cT_o r^{-1/2}$ (Jones and Morrison, 1974), where $T_o$=400K, c=0.9 and r is heliocentric distance in A.U. To determine the limiting diameter for detection at a given distance, standard models were calculated using emissivity $\varepsilon$=0.9, modelling constant $\beta$=0.9 and an infrared phase coefficient of 0.01 mag/deg. The emitted infrared flux is only weakly dependent on albedo for the low values of the latter found for most asteroids. A visual geometric albedo of 0.1 was used in the

models. Colour correction factors to account for the difference between the asteroid energy distribution and the assumed energy distribution are given in Appendix C, and are of order unity. The limiting diameters for a 10σ detection in a given band are listed in Table 5.1 for a range of heliocentric distances. This assumes that the nominal IRAS scan orientation is in a plane tangential to the Earth's orbit. The final processing for the survey catalogue at JPL assigns a positive detection to individual sources with a signal-to-noise ratio > 3. However, at PAF, thresholds were set at a somewhat higher level for the initial processing (resulting in S/N~7 for a seconds confirmed source).

TABLE 5.1

Radius limits for IRAS detection of asteroids.

| r | $T_e^*$ | Radius limit for 10σ detection (km) | | | |
|---|---|---|---|---|---|
| (A.U.) | (K) | I | II | III | IV |
| 1.1 | 340 | 1.8 | 1.7 | 3.5 | 11 |
| 1.5 | 290 | 5.3 | 4.5 | 9 | 25 |
| 2 | 250 | 11 | 8 | 15 | 40 |
| 3 | 210 | 30 | 17 | 27 | 75 |
| 4 | 180 | 60 | 30 | 40 | 110 |
| 5 | 160 | 110 | 45 | 60 | 150 |

*Equivalent blackbody temperature

In Fig. 5.1 the catalogued radii for all observed asteroids are plotted against heliocentric distance at the time of detection. Detector-to-detector sensitivity variations and possible light curve effects are not sufficient to explain the number of detections below the

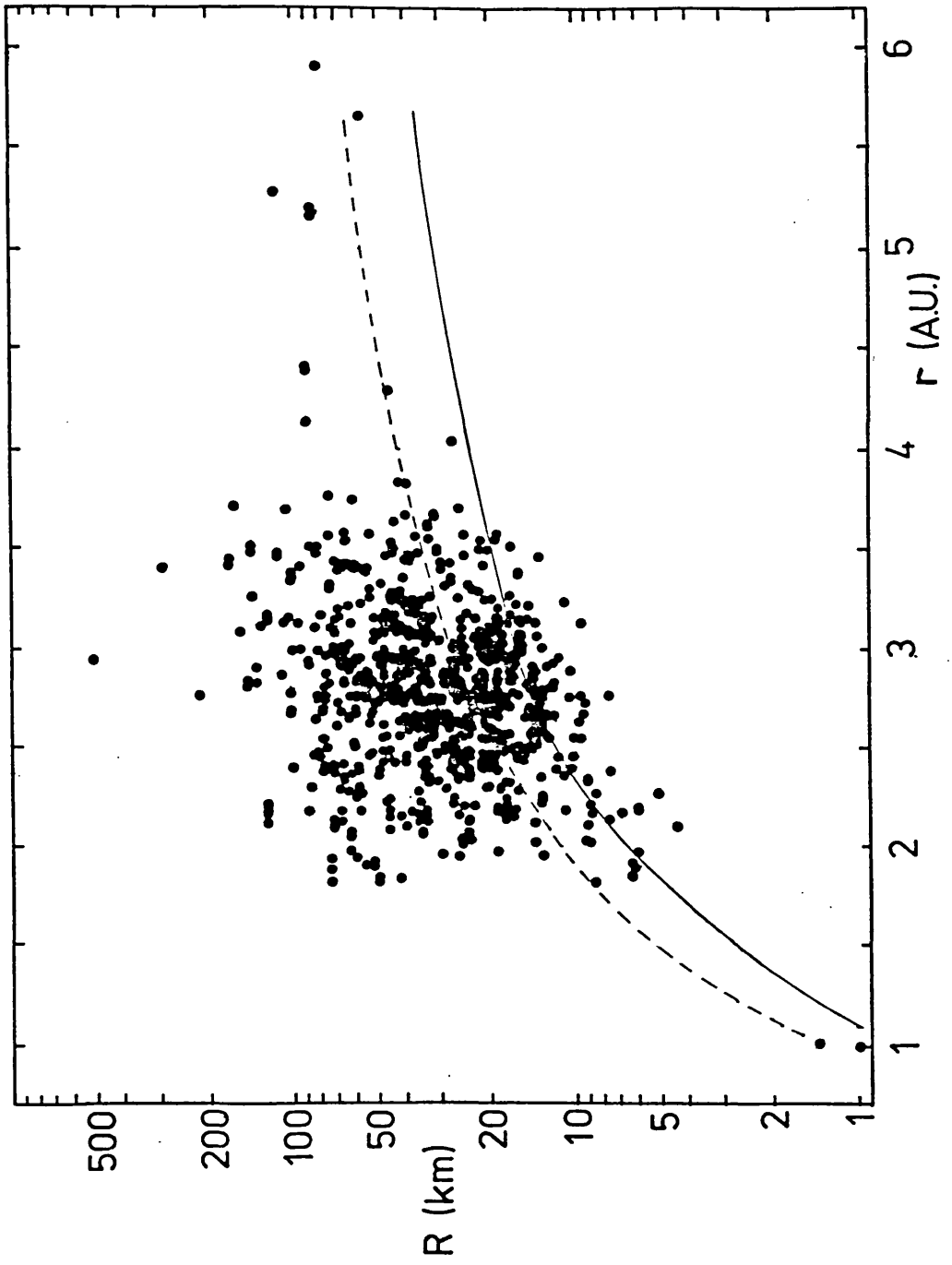


Fig. 5.1 Catalogued radii vs. heliocentric distance at time of IRAS detection for all numbered asteroids (up to 2882) identified from the FMO output. The dashed and solid lines represent predicted 10σ and 3σ limits respectively for a 2 band detection.

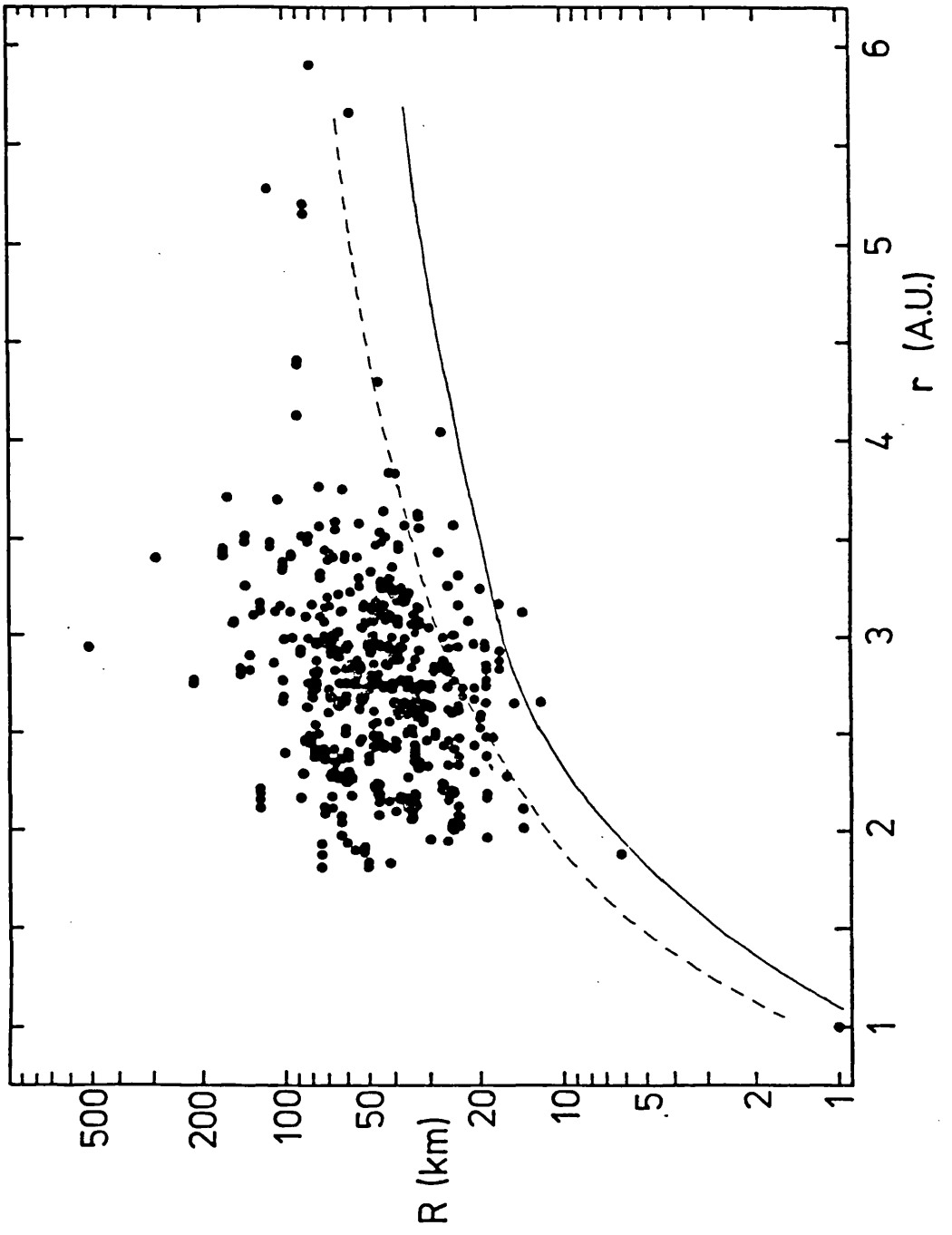


Fig. 5.2 Same as for Fig. 5.1 but with asteroids having catalogued visual albedos ≠0.1. See text.

theoretical limits. The explanation for this discrepancy becomes clear from Fig. 5.2. The radii listed in catalogues are obtained from radiometry (employing the standard model) when available, or from an average albedo for the asteroid type. When no information is available to assign an asteroid type, the albedo is assumed to be 0.1. This means that, if an asteroid has an albedo of 0.04, the diameter will be underestimated by 60%. From Figs. 5.1 and 5.2 it is clear that the majority of these asteroids have low albedos. This is not surprising, since about 75% of main-belt asteroids are C-types. Also, type classification from optical colours is brightness (and therefore albedo) dependent, whereas the IRAS observations are only dependent on diameter.

Since the calibration of the PAF data was changed several times during the mission, and may still be different from that of the final data products, an examination of the flux data was made. In-band fluxes in units of $W.m^{-2}{}_{x10^{-16}}$ were obtained from the FMO program. Correction factors to bring them all to the same calibration are listed in Table 5.2 (PAF internal memo).

TABLE 5.2

PAF Calibration Correction Factors

| SOP | | BAND I | BAND II | BAND III | BAND IV |
|---|---|---|---|---|---|
| 0 - 66 | x | 1.356 | 2.055 | 0.584 | 0.941 |
| 67 - 322 | x | 1.076 | 1.500 | 1.297 | 1.446 |
| 322 - 600 | x | 1.0 | 1.0 | 1.0 | 1.0 |

Figs. 5.3 and 5.4 show colour-colour plots of the in-band fluxes for all detected asteroids. The colours cluster about the calculated blackbody curves. Figs. 5.5 to 5.7 show colour vs heliocentric distance. As would be expected, the colour temperatures are less than the equilibrium blackbody values. The scatter is due partly to the range of albedos present, but mainly to observational error. The broken curves are defined by $T=cT_{o}r^{-1/2}$ which is the effective blackbody temperature used to derive the colour equations. For $T_{o}$=400K the value c=0.9 provides a reasonable fit to the data for wavelengths 12-100μm.

The in-band fluxes were converted to monochromatic fluxes at 12, 25, 60 and 100μm by the method described in appendix C. Standard thermal models were used to produce a predicted flux for each asteroid. Catalogued diameters ($D_{c}$) and albedos ($(p_{v})_{c}$) were used with $\varepsilon$=0.9, $\beta$=0.9 and an infrared phase coefficient of 0.01 mag.deg$^{-1}$. The quantity

$$X(\lambda) = S_{obs}(\lambda) / S_{pred}(\lambda)$$

gives a measure of the fit between the model and observations. $X(\lambda)$ will differ from unity due to one or more of i) observational error, ii) incorrect calibration, iii) errors in the catalogued radii or albedos and iv)a poor fit between the standard model and true spectrum. The value of X(25μm) has been calculated for all the numbered asteroids. Fig. 5.8 shows the numbers of asteroids with given Log[X(25μm)] values. Since the standard model is known to provide a reasonable fit to ground-based observations around 10 and 20μm, effect iv) will be small compared with the others. Fig. 5.8 shows two distinct populations with mean

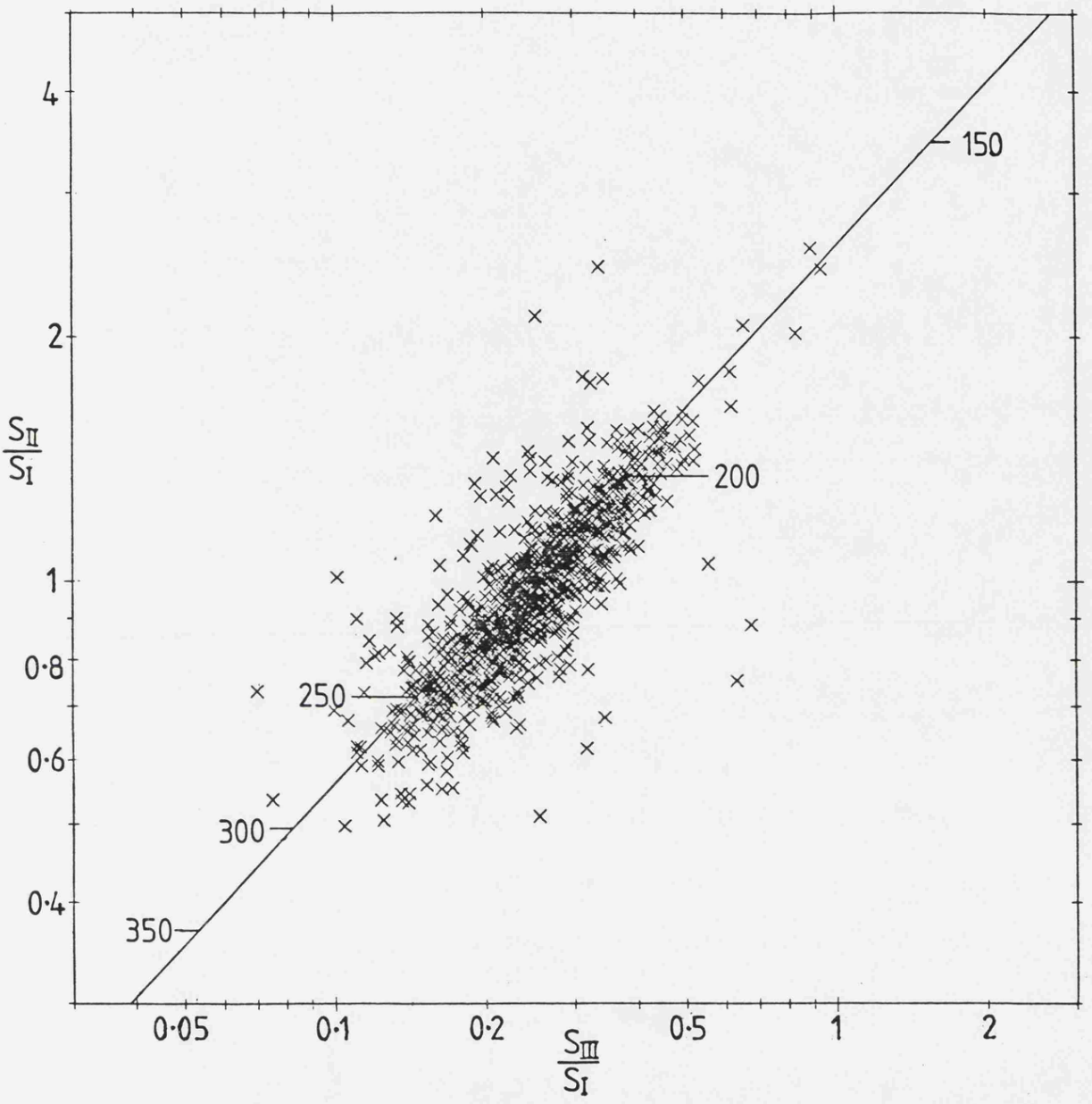


Fig. 5.3 In-band flux colour-colour diagram for numbered asteroids detected by IRAS. Flux ratio S(Band II)/S(Band I) vs. S(Band III)/S(Band I). Colours for blackbodies of various temperatures are shown.

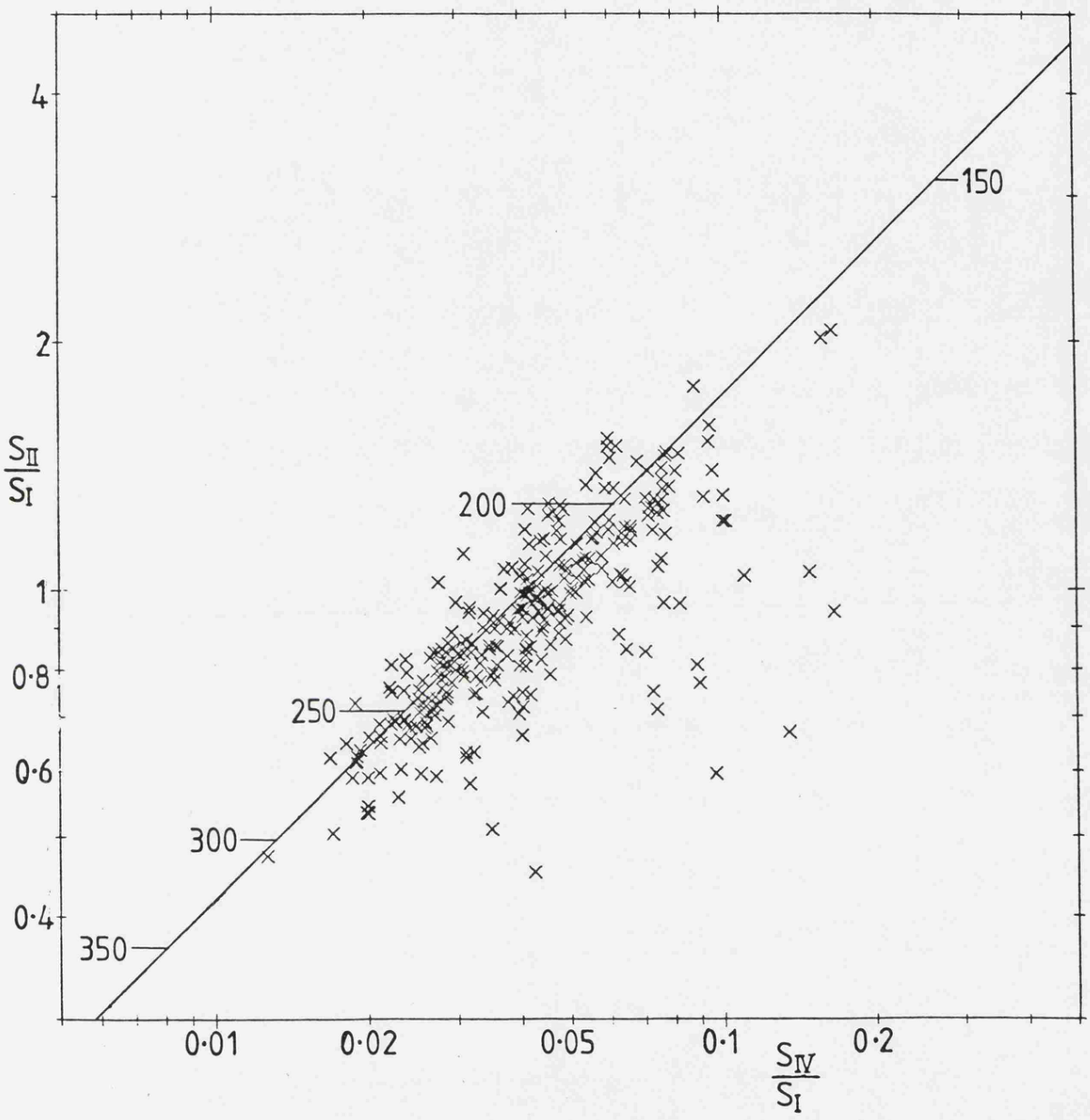


Fig. 5.4 Same as for Fig. 5.3 but for colours S(Band II)/S(Band I) vs. S(Band IV)/S(Band I).

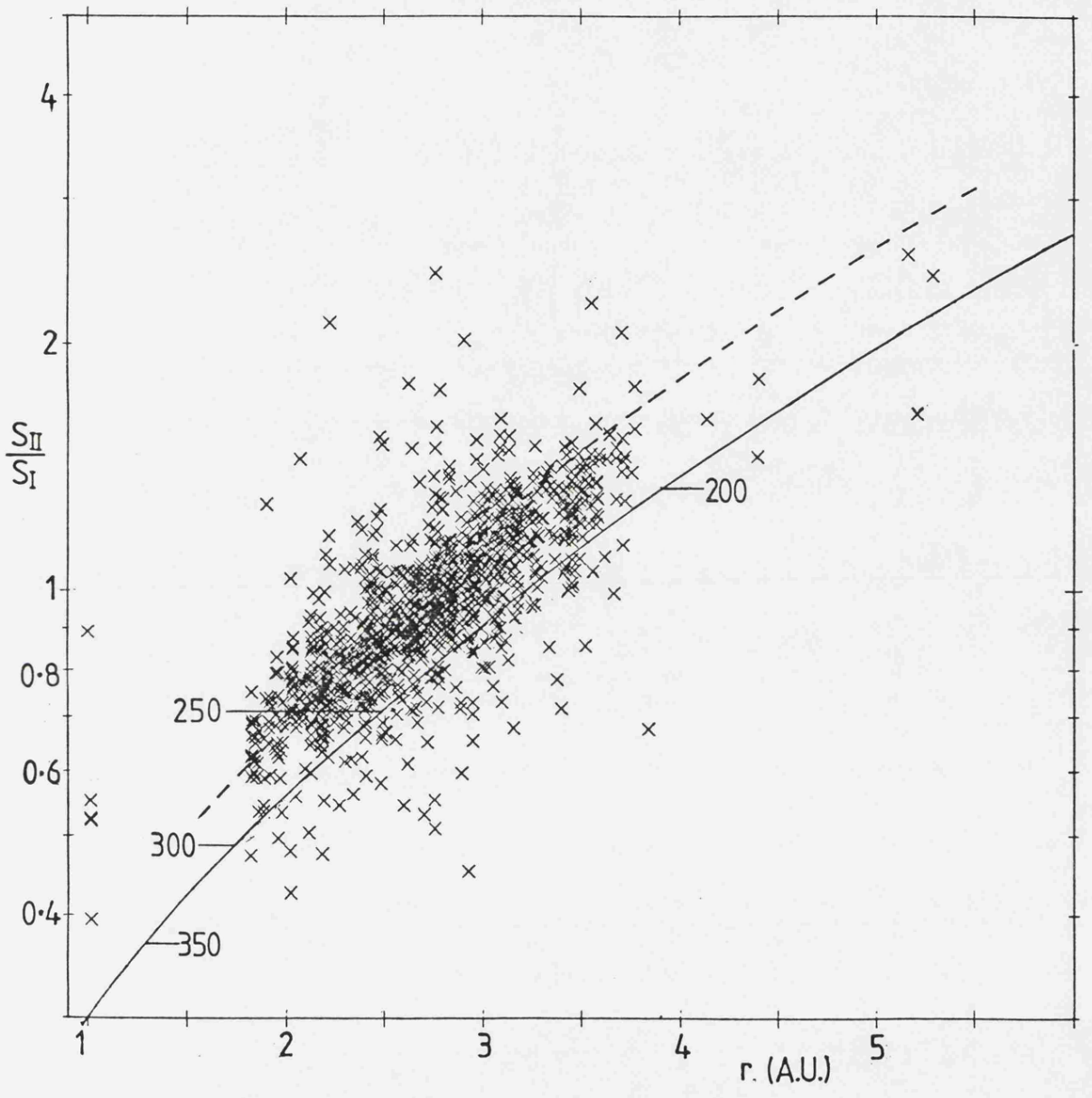


Fig. 5.5 In-band colour S(Band II)/S(Band I) vs. heliocentric distance for numbered asteroids detected by IRAS. The solid curve shows equilibrium subsolar blackbody colours, the broken line, colours for $T_{eff} = cT_o r^{-1/2}$ with $T_o$=400K and c=0.9.

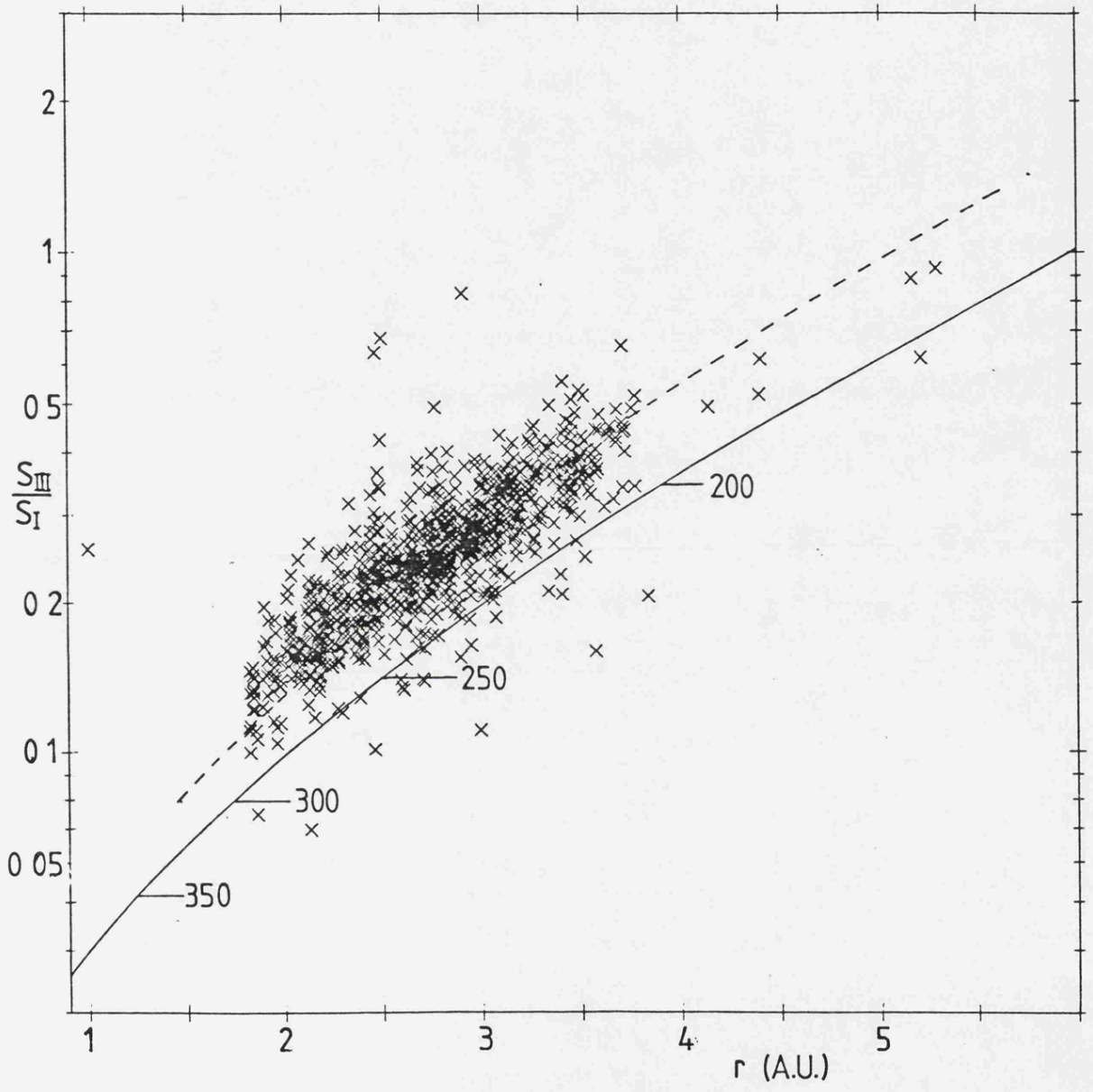


Fig. 5.6 Same as for Fig. 5.5 except for colour S(Band III)/S(Band I).

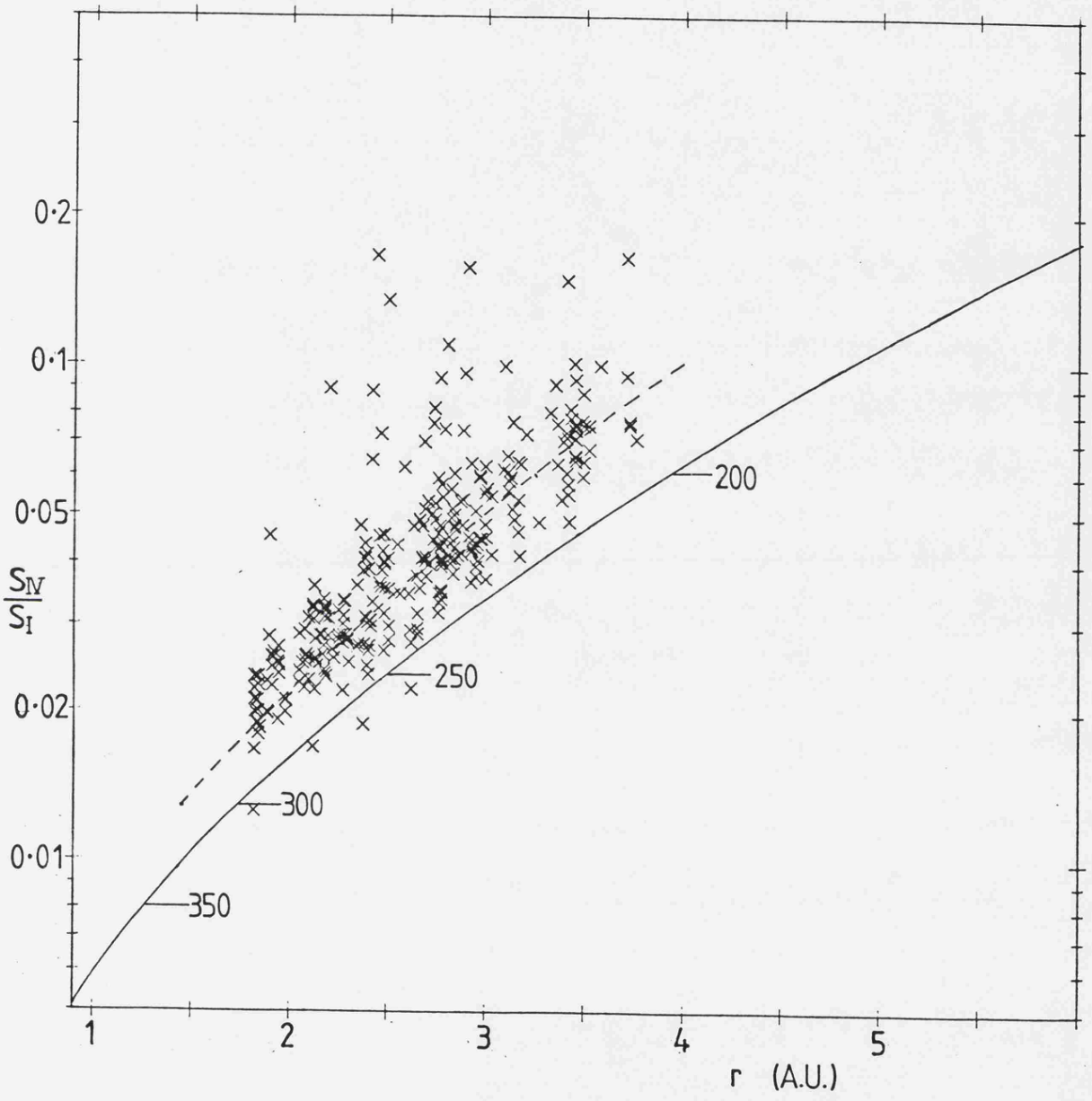


Fig. 5.7 Same as for Fig. 5.5 except for colour S(Band IV)/S(Band I).

Log[X(25μm)] values. This is the effect produced by those asteroids with $(p_V)_c = 0.1$ as discussed earlier. Fig. 5.9 shows the same data split into two groups, a) $(p_V)_c \neq 0.1$ and b) $(p_V)_c = 0.1$. The scatter in Fig 5.9a is due to observational errors and random errors in the catalogued diameters. The gaussian which has been fitted gives a mean value of Log[X(25μm)] of 0.10 ($\sigma$=0.11), which corresponds to the difference between the calibrated flux at 25μm and the flux predicted by a standard model. Fig 5.9b shows two peaks, one with approximately the same mean Log[X(25μm)] value and standard deviation as Fig 5.8a, and the other with a mean Log[X(25μm)] of 0.58 ($\sigma$=0.13). The first group is probably constituted mainly of all those asteroids with measured albedos =0.10 (since the catalogued $(p_V)_c$ values are only recorded to $\pm$0.01) plus a few which have $(p_V)_c$ assigned (correctly) as 0.10. If the second group contains asteroids with $(p_V)_c$ assigned as 0.10, then the difference in Log[X(25μm)] values indicates the error in the calculated diameter, and therefore in the assigned albedo. The same general features were found for histograms of Log[X(12μm)], etc. The results are summarised in Table 5.3.

The following conclusions can be drawn from these data:-

1) The X values are independent of albedo for those asteroids with $(p_V)_c \neq 0.10$. This implies that there are no albedo dependent errors in the method of diameter determination.

2) The half-width of the gaussian ($\sigma$) indicates the combination of observational errors and catalogued diameter errors for individual asteroids. For all bands these correspond to approximately $\pm$30%. Most diameters are known

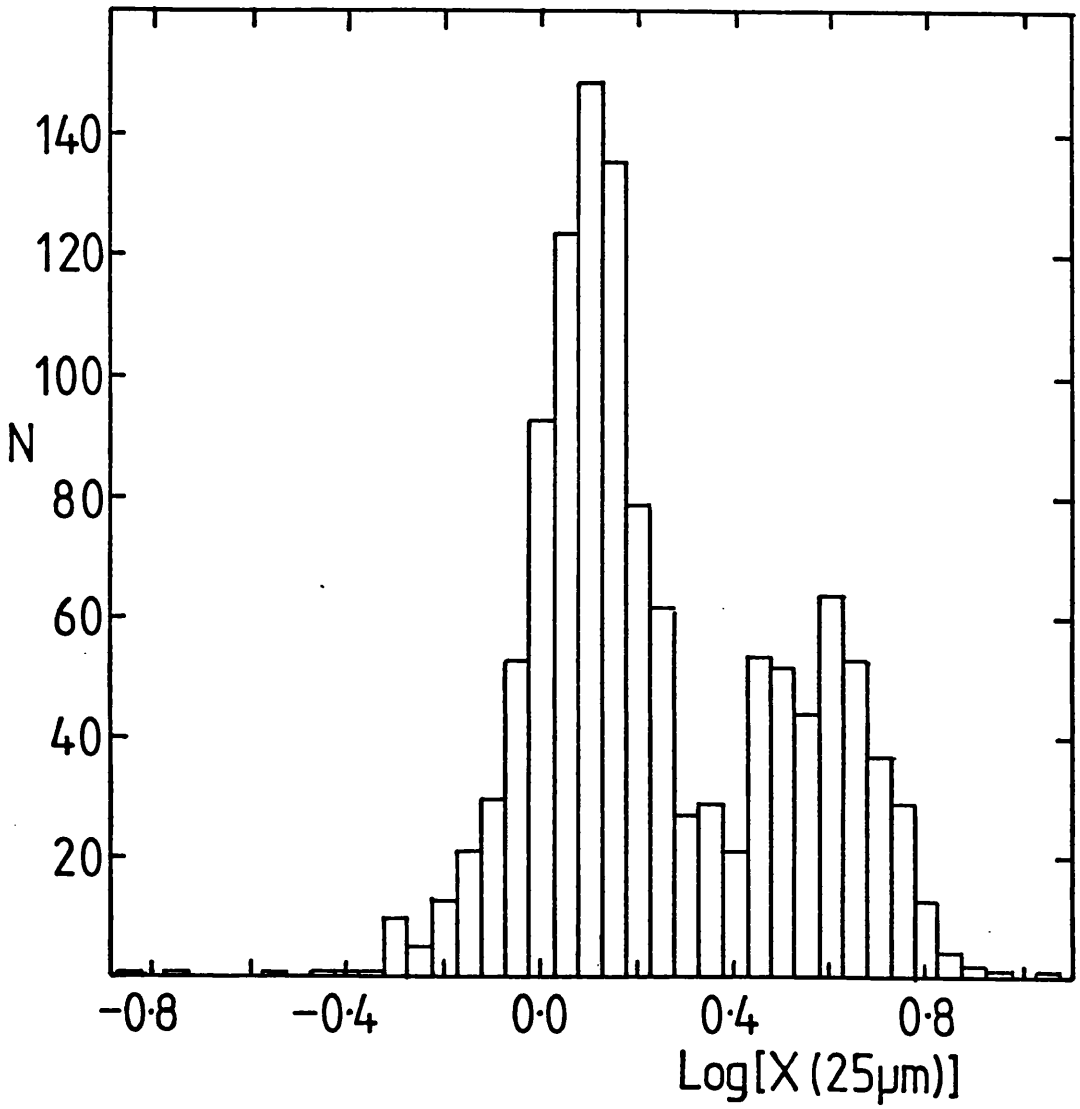


Fig. 5.8 Histogram of numbers of asteroids vs. Log[X(25μm)]. X is the ratio of observed to predicted flux using an asteroid standard model.

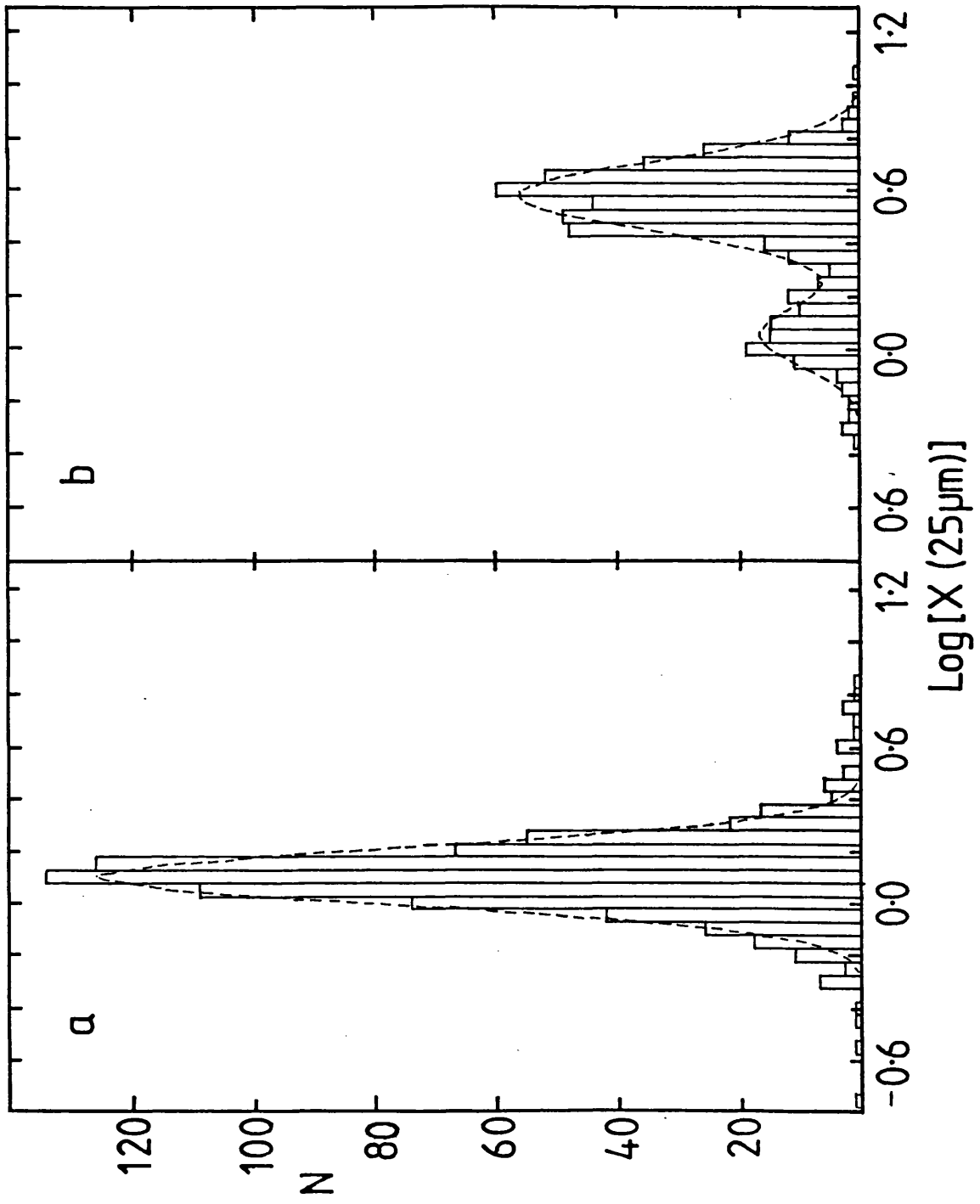


Fig. 5.9 Same as for Fig. 5.8 except for asteroids with catalogued albedos a) $(p_v)_c \neq 0.1$, b) $(p_v)_c = 0.1$. The dashed lines show gaussian fits to the data.

TABLE 5.3

Comparison of observed fluxes with standard model predicted fluxes for numbered asteroids detected by IRAS.

| Band | Mean Log[X(25μm)] values for:- $(p_V)_c > 0.1$ | $(p_V)_c < 0.1$ | $(p_V)_c \neq 0.1$ | $(p_V)_c = 0.1$ | | |
|---|---|---|---|---|---|---|
| | (1) | (2) | (3) | (4) | (5) | (5-3) |
| I | -0.03 (0.13) | -0.02 (0.11) | -0.02 (0.12) | -0.07 (0.10) | 0.46 (0.15) | 0.48 |
| II | 0.12 (0.11) | 0.10 (0.11) | 0.10 (0.11) | 0.05 (0.11) | 0.58 (0.13) | 0.48 |
| III | 0.21 (0.11) | 0.18 (0.11) | 0.19 (0.11) | 0.14 (0.10) | 0.65 (0.13) | 0.47 |
| IV | 0.15 (0.11) | 0.18 (0.08) | 0.18 (0.10) | * | * | |

* Insufficient data.
X(25μm) is the ratio between observed flux and standard model predicted flux.
$(p_V)_c$ is the catalogued geometric visual albedo. A value of 0.1 is assumed for poorly observed asteroids. Columns (4) and (5) represent the two peaks illustrated in Fig 5.19b.

to no better than 10%. Observational errors (which are dependent on S/N) are therefore ~20%.

3) The X values give a measure of the fit between observed and standard model predicted fluxes. The deviation from unity is due to a combination of calibration errors and deviations from a standard model fit.

4) If the asteroids' spectra are assumed to be a perfect fit to the standard model, the X values indicate the calibration errors. Also, the difference between columns 5 and 3 in Table 5.3 indicate the mean difference between the catalogued diameters ($D_c$) and the true diameters for those asteroids with $(p_v)_c$ assigned as 0.10. This is because the infrared flux is almost entirely dependent on diameter for low albedo objects. This value turns out to be remarkably similar for bands I-III, lending credence to the assumption of a consistent standard model fit. The mean $D_c$ values appear to have been under-estimated by a factor of 3.0. Since the optical flux is proportional to $D^2$ and $p_v$, this implies that an assigned value of 0.06 for $p_v$ would fit both the optical and infrared data for the majority of these asteroids. This implies that if no type designation is available, a low albedo should be assumed for statistical studies of size distribution.

5) Conversion factors from PAF calibration to "standard model calibration" are therefore x1.05, x0.79, x0.65 and x0.66 for bands I-IV, respectively.

Results from additional observations processed at ADAS of eight main-belt asteroids (Aumann and Walker, 1984) show that the standard model can predict the observed far-infrared fluxes typically to better than 20% accuracy. They found an

almost 30% deviation of the flux from 1 Ceres and 2 Pallas between 12 and 25μm from the standard model, indicating a steeper temperature distribution on the sunlit side. They also found a 10% excess in the 60-100μm colour of 1 Ceres and 704 Interamnia relative to the other asteroids, which could not be entirely due to the flux from the unilluminated hemisphere (a factor neglected in the standard model). The large decrease in the emissivity of 2 Pallas between 25 and 60μm reported by LeVan and Price (1984) was not observed.

Since the PAF and ADAS data were calibrated differently, it is not possible to compare the results of the FMO program with those of Aumann and Walker. At least part of the deviation of the X values from unity is due to calibration errors, but there may be departures from the standard model predictions ∽20%

5.3.2 Motion Limits.

Main-belt asteroids at quadrature have motions which range from around zero to a few arcminutes per hour and are therefore ideal for examining the minimum motion limits for hours-confirmation. The IRAS detector dimensions (Table 4.1) together with the spacecraft position reconstruction determined the accuracy of the positions of individual sources. Fig. 5.10 shows the observed separations between detections of numbered asteroids. The hours confirmation cutoff operates below about 1.3arcmin. in ecliptic longitude and 0.6arcmin. in latitude (corresponding to motions of 0.8 and 0.36arcmin.$hr^{-1}$ for consecutive orbits). However, since a number of these sources were detected two orbits apart, and all positions are subject to observational error, the true

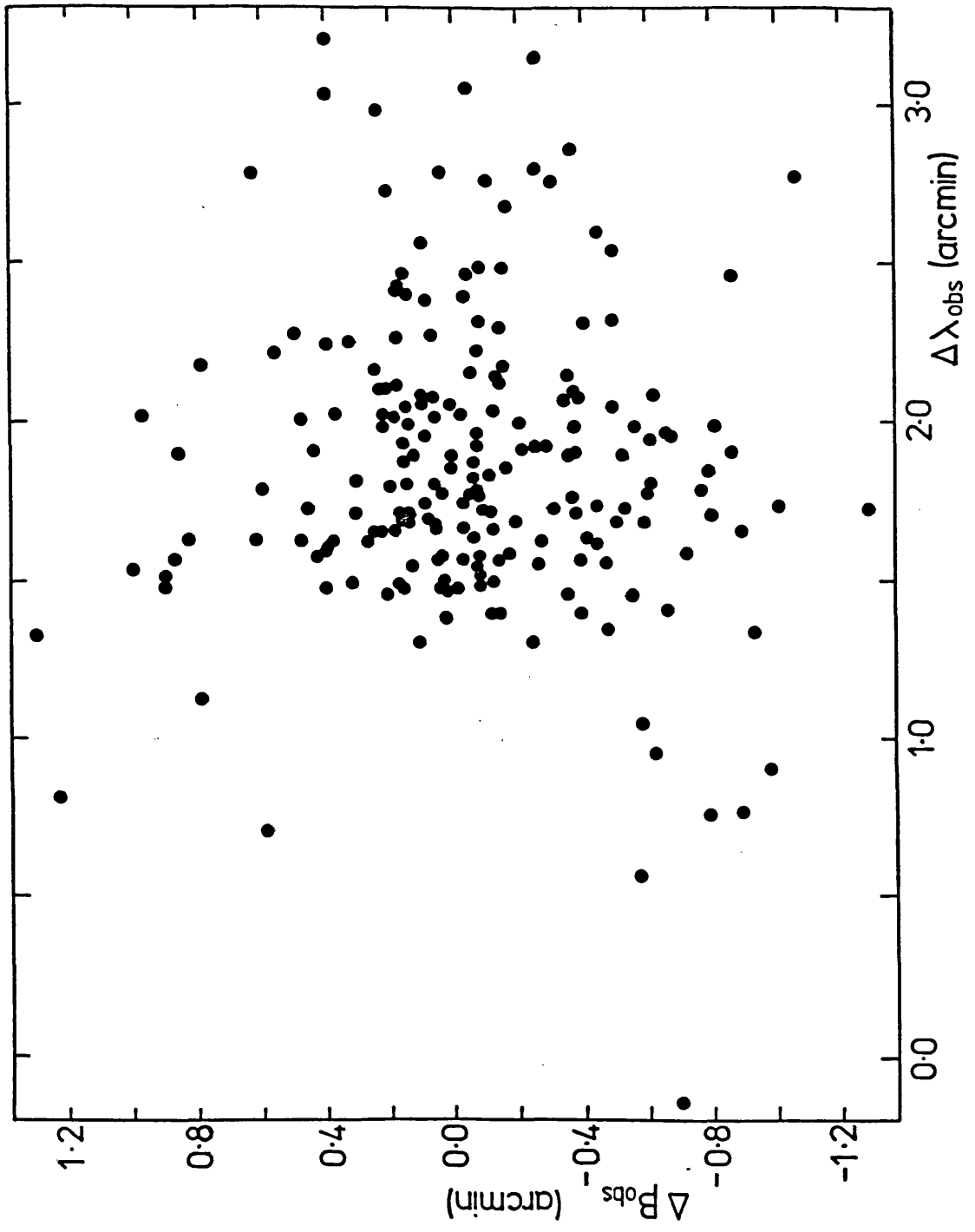


Fig. 5.10 Observed separations between detections of IRAS candidate pairs. $\lambda$ is ecliptic longitude or cross-scan motion, $\beta$ ecliptic latitude or in-scan motion. Any objects lying in the empty region at small separations will have been hours-confirmed.

motions of asteroids seen as FMO's can be smaller.

In theory, the motion limits for non hours-confirmation should be well-defined functions of in-scan and cross-scan motion and the number of detections. In practice, they depend on the scan strategy (i.e. the time interval between confirming scans) and the position reconstruction for a given orbit as well. Since these factors are not readily quantifiable, a subset of numbered asteroids has been used to assess their effects.

The IRAS data appear to be complete for sources which have band I, II, or III fluxes with S/N > 6 (Rowan-Robinson et al., 1984). A subset of numbered asteroids with $|b| > 5^{\circ}$, heliocentric distance (1.7A.U.< r <4.5A.U.) and radius R[km] > 20.(r[A.U.] - 1) was chosen. This corresponds to a predicted S/N > 20 for a two-band detection. (This form of limiting radius was introduced to provide a distance-dependent cutoff). Even if the asteroid radius has been over-estimated, or the object is observed at its lightcurve minimum, it should then still have sufficient S/N for detection if scanned by IRAS. The ecliptic longitude and latitude motions (approximately cross-scan and in-scan, respectively) for this subset were calculated for the time when they were in the nominal IRAS pointing direction (i.e. elongation = $90^{\circ}$), and for the period during which the moving object software was operating (1 March - 22 November 1983). Each time that an asteroid entered the IRAS scan direction was regarded as a moving object detection opportunity. With this subset of 304 asteroids, 325 opportunities for the detection of 273 asteroids were noted. Of these, the FMO software actually identified 42 pairs of 39 asteroids (i.e.

~14% of the total observable as strong FMO candidates). An analysis of these data on observable objects confirms that most of the 86% of known asteroids that were not retrieved were moving too slowly to be detected by the FMO programme.

Table 5.4 shows the distribution of the calculated motions at each observation opportunity and the predicted motions of IRAS-detected asteroids in the subset. Fig. 5.11 shows ratios of the number of observed and calculated motions. From Fig. 5.10, it is clear that failure of hours confirmation, for main-belt asteroids, is in most cases related to the cross-scan motion. However, the majority of the asteroids observed had cross-scan motions less than the apparent threshold of 0.8arcmin.$hr^{-1}$ (1.3arcmin.$orbit^{-1}$). Some of these were detected due to two-orbit scan separation, or high in-scan motion. There are small differences between the predicted motions and the real motion at IRAS detection, since the satellite pointing direction varied between elongations of $60^{\circ}$ and $120^{\circ}$. But the majority of the slow-moving asteroids observed, particularly the excess close to the apparent threshold, were detected due to errors in the positions of the original detections. This can be seen in Fig. 5.12. For true separations less than 1.3arcmin., the errors are usually positive. The few points to the lower left are asteroids which failed hours confirmation through large latitude motion. The errors are due to position reconstruction errors, combined with the effects of finite detector size. For a weeks (or months) -confirmed source, measured at 10 and 25μm, the positional uncertainties (99% confidence limits) are 0.75arcmin. cross-scan and 0.15arcmin. in-scan (Neugebauer et al., 1984). For a non-hours-confirmed

TABLE 5.4

Numbers of predicted and observed asteroids summed into motion bins.

| | Motion bins (arcmin.) | | | | | | | | | | | | |
|---|---|---|---|---|---|---|---|---|---|---|---|---|---|
| | 0.0-0.1 | 0.1-0.2 | 0.2-0.3 | 0.3-0.4 | 0.4-0.5 | 0.5-0.6 | 0.6-0.7 | 0.7-0.8 | 0.8-0.9 | 0.9-1.0 | 1.0-1.1 | 1.1-1.2 | 1.2-1.3 |
| | | | | | | cross-scan (λ) | | | | | | | |
| observed | 0 | 0 | 0 | 2 | 5 | 10 | 5 | 6 | 9 | 2 | 1 | 1 | 1 |
| predicted | 0 | 1 | 22 | 75 | 83 | 72 | 36 | 22 | 5 | 6 | 3 | 1 | 0 |
| obs/pred | - | .0 | .0 | .03 | .06 | .12 | .14 | .27 | >1.0 | .33 | .33 | 1.0 | >1.0 |
| | | | | | | in-scan (β) | | | | | | | |
| observed | 18 | 13 | 6 | 1 | 3 | 1 | 0 | 0 | 0 | | | | |
| predicted | 113 | 108 | 63 | 27 | 9 | 3 | 1 | 2 | 0 | | | | |
| obs/pred | .16 | .12 | .10 | .04 | .33 | .33 | .0 | .0 | - | | | | |
| | | | | | | total | | | | | | | |
| observed | 0 | 0 | 0 | 2 | 4 | 7 | 8 | 6 | 6 | 4 | 3 | 1 | 1 |
| predicted | 0 | 0 | 6 | 63 | 84 | 80 | 47 | 16 | 10 | 7 | 4 | 1 | 1 |
| obs/pred | - | - | .0 | .03 | .05 | .09 | .17 | .38 | .60 | .57 | .75 | 1.0 | 1.0 |

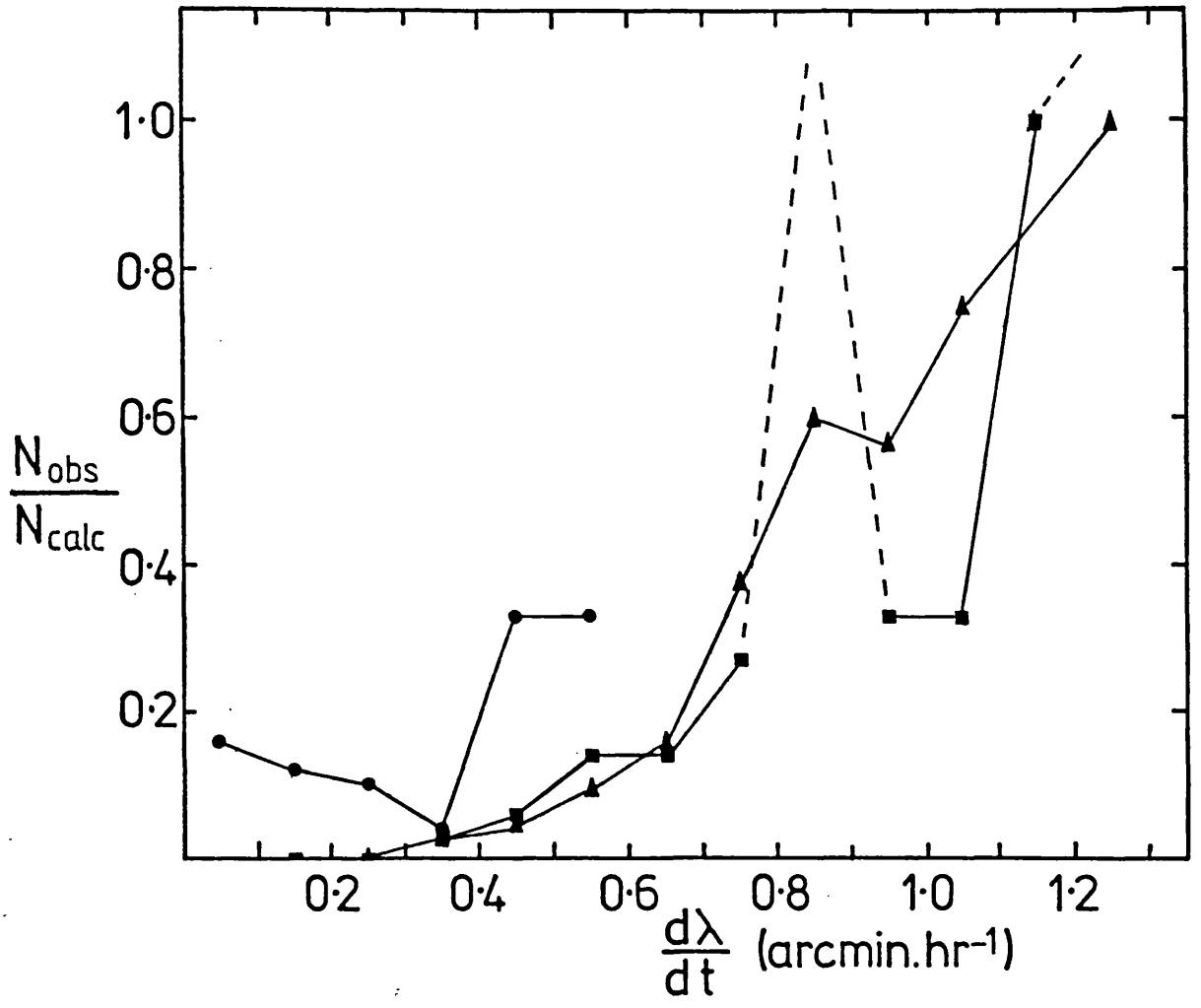


Fig. 5.11 Ratios of numbers of observed to calculated detections of a subset of numbered asteroids, for a range of motions. $N_{calc}$ is the number of these asteroids crossing the IRAS scan direction with galactic latitude $|b| > 5°$ during the operation of the FMO software. $N_{obs}$ is the number actually observed as strong FMO candidates. Squares correspond to cross-scan motion, circles to in-scan motion, and triangles to total motion.

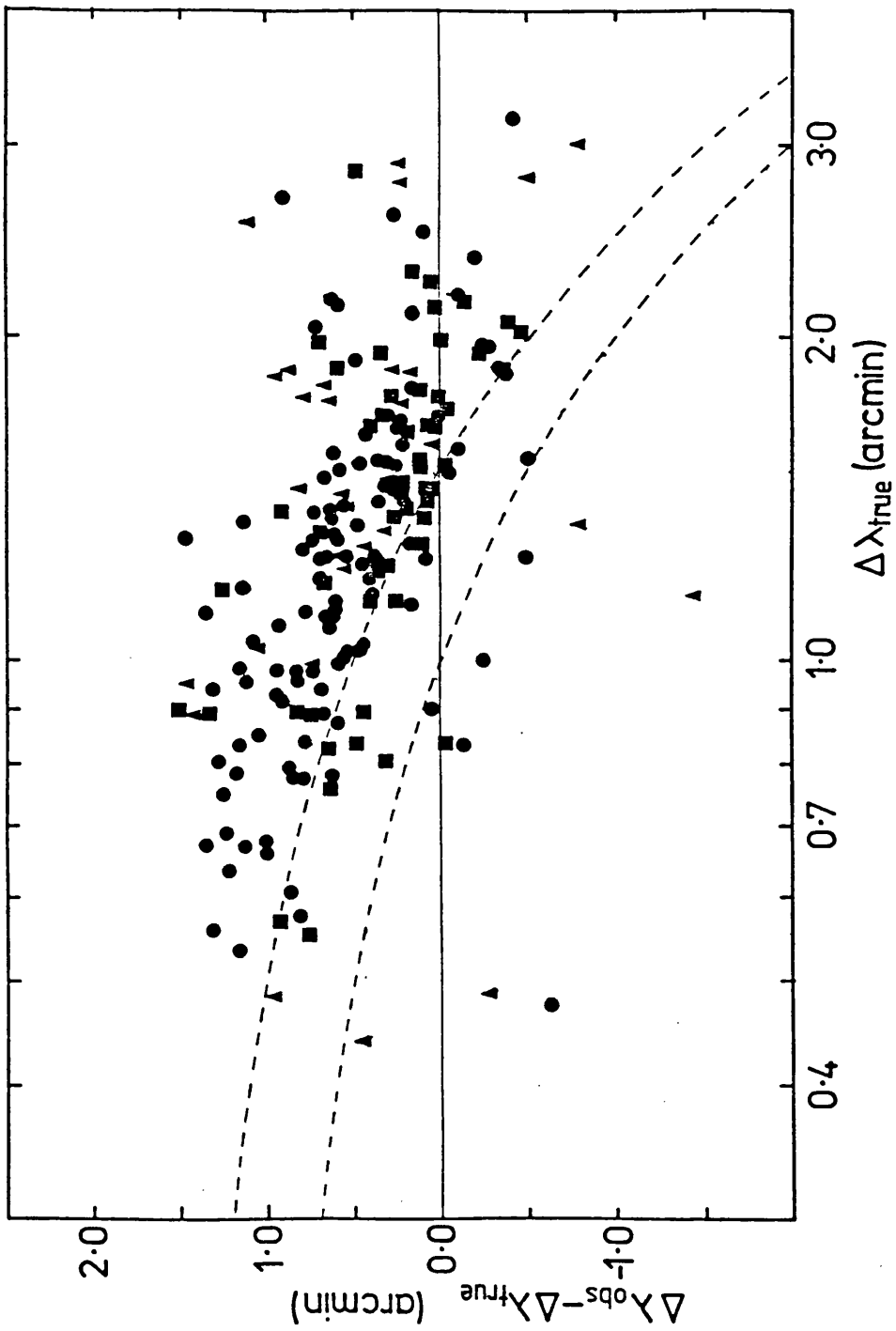


Fig. 5.12 Errors between observed and true cross-scan separations of individual detections of IRAS candidate pairs. The dashed lines correspond to observed separations of 1.0 and 1.5arcmin. Squares correspond to 2 four band detections, circles to 2 detections in at least three bands, and triangles others.

pair of sources, the uncertainties in the distances separating them (99% confidence limits) are 1.9arcmin. and 0.85arcmin., respectively. The cross-scan uncertainty is 1.5arcmin. for four-band detections.

## 5.4 MAIN-BELT ASTEROID DISCOVERIES

### 5.4.1 FMO Detections.

Although many numbered asteroids were identified from the FMO program output, only two new main-belt asteroids were confirmed. The main-belt asteroid population is known down to apparent magnitude ~15 (Zellner, 1979a). Table 5.5 shows the corresponding absolute magnitudes, compared with the IRAS limiting magnitudes calculated for a range of heliocentric distances from:

$2 \log d = 6.244 - 0.4[B(1,0)-(B-V)] - \log p_V$ (Zellner, 1979a)

B-V is assumed to be 0.8; d is the diameter calculated from Table 5.1 for a two band detection at the 6σ level.

The two new asteroids, 1983QF and 1983QG (see Appendix D), have absolute magnitudes B(1,0) of 12.5 and 14.5 respectively and were near threshold detections. Although both have semi-major axes of approximately 2.6A.U., they were discovered near perihelion at 2.3 and 1.7A.U., respectively. From Table 5.5, it is apparent that few new main-belt asteroids would be expected among the FMO data, since the difference between IRAS limiting magnitudes and the visible population completeness limit is only significant at large heliocentric distances, where observed motions will be small. Optical searches for asteroids are usually constrained to

TABLE 5.5

Absolute magnitude limits

| r (A.U.) | B(1,0) for 6σ 2-band IRAS detection. $P_v$=0.04 | $P_v$=0.2 | B(1,0) for B(r,0)=15* |
|---|---|---|---|
| 1.5 | 15.5 | 13.5 | 15.5 |
| 2.0 | 13.5 | 12 | 13.5 |
| 3.0 | 11.5 | 10 | 11 |
| 4.0 | 11 | 9 | 9.5 |
| 5.0 | 10 | 8 | 8.5 |

*Main belt population completeness limit.

regions near the ecliptic plane. The ability of the FMO program to detect high-inclination objects is, on the contrary, enhanced over the detection of objects with in-plane orbits because of the higher in-scan spatial resolution. The IRAS data presented here therefore confirm that there is no sizeable population of inner main-belt asteroids of moderate size at high ecliptic latitudes.

5.4.2 1983QF and 1983QG.

Since the absolute visual magnitudes have been derived from only a few photographic magnitudes it is not possible to derive the albedos of these asteroids using the radiometric method. However, since the infrared magnitudes are almost independent of albedo, diameter estimates can be made. Table 5.6 contains the relevant data. The observed in-band fluxes have been corrected to monochromatic fluxes using the method described in Appendix C. These have been corrected from PAF to "standard model calibration" as described above (section

TABLE 5.6

Diameter determinations for main-belt asteroids discovered by IRAS

| | | | 1983QF | | | | 1983QG | |
|---|---|---|---|---|---|---|---|---|
| | Date | (1983) | 23 Aug | | 31 Aug | | 13 Sep | |
| | r | (A.U.) | 2.303 | | 2.263 | | 1.729 | |
| | Δ | (A.U.) | 2.024 | | 1.772 | | 0.996 | |
| | α | (deg) | 26.0 | | 25.4 | | 30.7 | |
| 1 | T | (K) | 237 | | 239 | | 274 | |
| 2 | S(12μm) | ($W.m^{-2}\mu m^{-1}x10^{15}$) | | | 18.7 | 20.3 | 32.7 | 18.1 |
| | S(25μm) | .. | 5.46 | 5.42 | 7.24 | 7.03 | 10.65 | 7.53 |
| | S(60μm) | .. | | | | 0.81 | | |
| 3 | $S^{*}_{\star}$(12μm) | .. | | | 20.5 | | 34.6 | 19.2 |
| | $S_{\star}$(25μm) | .. | | | 5.64 | | 8.51 | 6.02 |
| | $S_{\star}$(60μm) | .. | | | 0.54 | | | |
| 4 | Diameter | (km) | | | 25 | | 14 | 11.5 |

1 Equivalent blackbody temperature.
2 Monochromatic flux.
3 Monochromatic flux - "standard model calibration".
4 Diameter derived from standard model fits to data with "standard model calibration. See Figs. 5.13 and 5.14

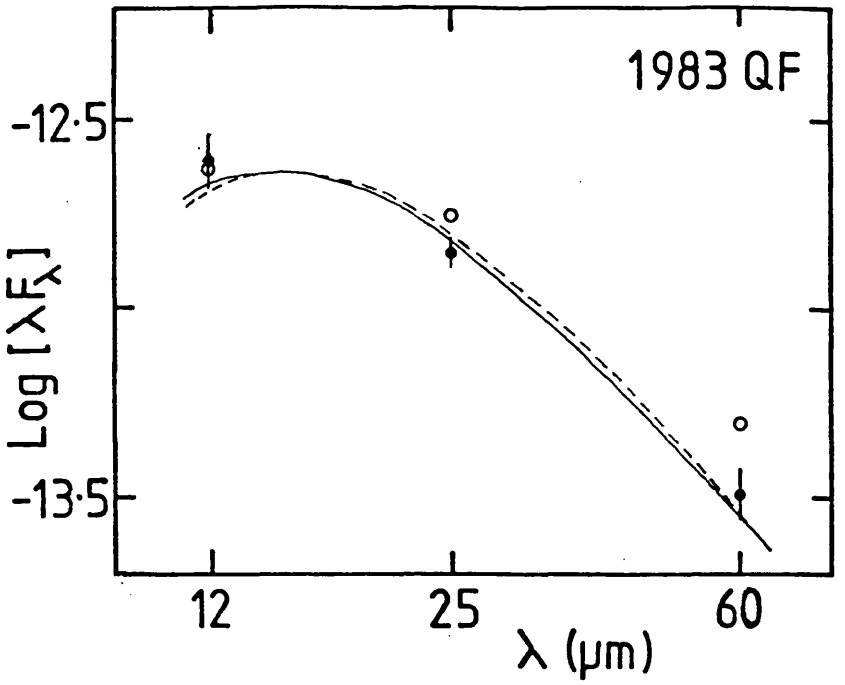


Fig. 5.13 IRAS data for 1983QF (3 Aug) corrected to "standard model calibration". The solid line is a standard model with D=25km, dashed line is a projected model with D=24.5km. The albedo was assumed as 0.1 in both cases, but has negligible effect on the derived diameter.

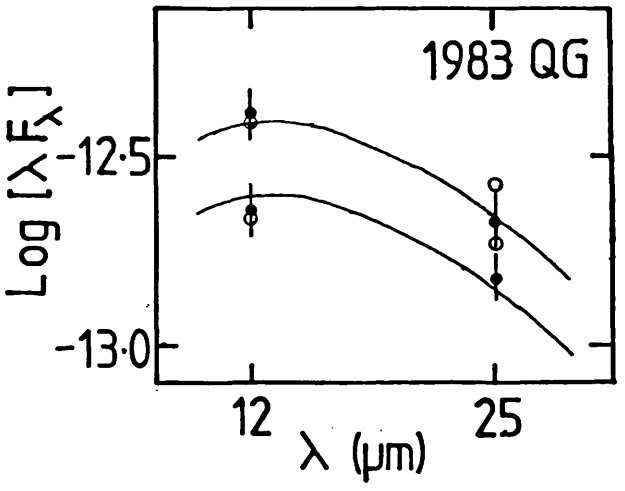


Fig. 5.14 IRAS data for 1983QG corrected to "standard model calibration". The solid lines are standard models with D=14 and 11.5km.

5.3.1). However, it must be remembered that these corrected fluxes are not the true fluxes, since only part of the correction is due to possible calibration errors. The remainder is due to real deviations from the standard model. The derived diameters will, however, be compatible with the radiometric diameters calculated for ground-based observations of asteroids. Figs. 5.13 and 5.14 show standard models fitted to the corrected data. The band II data and colours for 1983QF have been averaged, since there are no apparent lightcurve effects. Absolute errors in the derived diameters are probably of the order of $\pm$15%. The two observations of 1983QG separated by 100 minutes imply a short rotation period and large amplitude lightcurve. The mean diameters derived from these data are 24$\pm$3km for 1983QF and 13$\pm$2km for 1983QG.

5.4.3 Final Asteroid Data Analysis.

The final asteroid data products from ADAS, containing hours-confirmed detections down to a lower brightness threshold, should contain many thousand uncatalogued asteroids, and so allow a more detailed statistical examination. These asteroids will be sought by the U.S. group using an essentially similar technique to that employed for the FMO program. The aim, however will be for completeness rather than reliability. The number of spurious sources found in the non hours-confirmed data has been shown to be large, so single band II only sources (or pairs separated by $\sim$2arcmin.) will have to be regarded as unlikely to be asteroid detections. Because of the extra level of redundancy involved, this problem will not be found for the

weeks-confirmation failures which will constitute the majority (~86%) of the asteroid detections.

For the reduction of the data for unknown asteroids detected in more than one band the following procedure will be used (IRAS Asteroid Workshop Number 3: Report and Recommendations, JPL-1617, 27 July 1984):-

i) A colour temperature will be calculated from the available colours.

ii) This will be used to estimate the heliocentric distance.

iii) The known geometry at the time of detection will give the geocentric distance.

iv) Assuming a typical albedo, the diameter of the unknown asteroid will be determined using the standard model.

Colours vs. distance of known asteroids will be used to test this method. The scatter in Figs. 5.5-5.7 shows the errors in the colour vs. heliocentric distance relation. Although, on average, the data provide a reasonable fit to the theoretical approximation, any individual detection may produce an error in distance of 0.5 or even 1.0A.U. These errors will probably be reduced by the better calibration at SDAS, and by using a subset of well-observed asteroids to define an empirical colour vs. heliocentric distance relation. If the errors can be reduced to ~0.3A.U., the derived diameters will be accurate to better than $\pm$20%.

Biases in the distribution of asteroids detected at SDAS will occur due to departures from uniform sky coverage (e.g. SAA and moon constraints and scan strategy). Close to threshold, asteroids will tend to be detected near perihelion, favouring the discovery of asteroids with high eccentricity. Since the eccentricity vectors of asteroidal

orbits have an appreciable force component due to Jupiter's eccentricity, there will also be a tendency for asteroids close to threshold to be discovered in the direction of Jupiter's perihelion, that is, in the direction of ecliptic longitude 13° (IRAS Asteroid Workshop Number 2: Report and Recommendations, JPL D-8399, 21 Dec 1983).

## 5.5 EARTH-CROSSING ASTEROID DISCOVERIES

### 5.5.1 Selection Effects and Comparison with Previous Population Estimates.

Some time before the IRAS mission, estimates were made of up to 50 Earth-crossing asteroids bright enough for detection by IRAS. In fact, only two new Apollos were confirmed with several other possible detections. There are a number of reasons for this difference.

The initial estimates of brightness limits for Earth-crossing asteroids were based on the expected detector sensitivities before launch. In the event, band I proved to be less sensitive than expected. Earth-crossing asteroids which were expected to be near threshold detections in both bands I and II pre-mission, would have actually been observed as band II only sources. The large density of faint band II sources prevented recognition of most possible FMO's of this type, effectively raising the brightness limits.

The second reason is that the estimates were made on the assumption that all asteroids crossing the IRAS scan direction would be detected by the FMO software. In the case of main-belt asteroids (or at least those moving faster than

the minimum motion limits) this was true, since the maximum expected motion was only one or two arcminutes per hour. Because of their proximity to the Earth, Apollo asteroids can have large relative motions. Fig. 5.15 demonstrates several cases where the path of an Earth-crossing asteroid crosses successive IRAS scans. For successive hours-confirming scans the maximum cross-scan separation was 30-45arcmin. for prograde motion and 0-15arcmin. for retrograde motion. Of course, if the scan separation is more than one orbit, the maximum motion limits are reduced even further. It is also possible that an Earth-crosser might pass through the region being scanned during non-survey time. Since near-Earth asteroids have a broader distribution in ecliptic latitude than the main-belt asteroids discussed above, their discovery rate is more dependent on the scan strategy. Thus the asteroid 1983TB was discovered at high ecliptic latitude during a sequence of polar scans. Of the known Earth-crossing asteroids only 2201 Oljato and 1620 Geographos crossed the IRAS scan direction and were bright enough for detection. Geographos, with a cross-scan motion of $-8\text{arcmin.hr}^{-1}$ ($-13\text{arcmin.orbit}^{-1}$) was detected only once. The detection was found in the LOG file by comparison with an ephemeris. The newly discovered Amor asteroid 1983LC passed right through the scan direction without being detected on 4 July 1983. In fact its cross-scan motion was $-20\text{arcmin.hr}^{-1}$ ($-33\text{arcmin.orbit}^{-1}$) and it passed between successive scans in the manner of case e in Fig. 5.15. However, Oljato with a cross-scan motion of 12 $\text{arcmin.hr}^{-1}$ ($19\text{arcmin.orbit}^{-1}$) was identified as an FMO candidate with six detections on consecutive orbits.

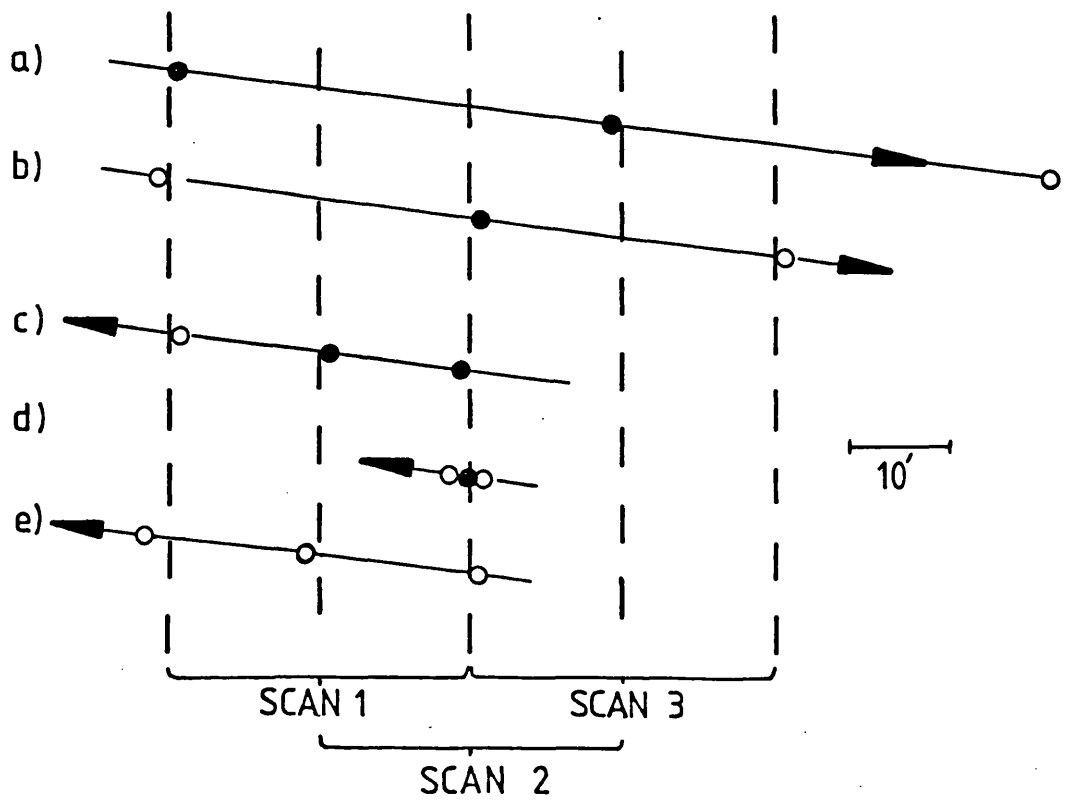


Fig. 5.15 Examples of detections (solid circles) or failures (open circles) illustrating how an object may be observed as an FMO (two detections) or completely missed , depending on its direction and rate of cross-scan motion and its position relative to the IRAS scans. Cross-scan motions are a)44 arcmin.orbit$^{-1}$ (26.4 arcmin.hour$^{-1}$); b)29 arcmin.orbit$^{-1}$ (17.4 arcmin.hour$^{-1}$); c)-14 arcmin.orbit$^{-1}$ (-8.4 arcmin.hour$^{-1}$); d)-1 arcmin.orbit$^{-1}$ (-0.6 arcmin.hour$^{-1}$); e)-16 arcmin.orbit$^{-1}$ (9.6 arcmin.hour$^{-1}$).

Since so few Apollo-type asteroids were detected, it is impossible to produce a population estimate. Helin and Shoemaker (1979) estimate $700\pm300$ Apollos, 1000-2000 Amors and $\sim$100 Atens with V(1,0) < $18^m$ (corresponding to diameters of 1.7km for low albedo and 0.7km for moderate albedo asteroids). Assuming typical orbits, effective IRAS sensitivities for the FMO search, and a magnitude-frequency distribution given by $N_V = k^{e^{bV(1,0)}}$, with b = 1 (Helin and Shoemaker, 1979), $10\pm5$ asteroids should have passed through the IRAS scan direction with sufficient S/N for detection. Three FMO's were confirmed as Apollos - 2201 Oljato, 1983TB and 1983VA. When allowance is made for several non-confirmed alerts (in particular 487-1, designated 1983SN (Marsden, 1984b)), those moving fast and retrograde ($\sim$30%), non-survey time ($\sim$35%) and galactic plane confusion ($\sim$10%), the observed and predicted numbers appear to be compatible. The ground-based observation imply a concentration of Earth-crossing asteroids towards the ecliptic plane. The agreement with IRAS data can therefore be taken as confirmation of this degree of concentration.

5.5.2 Diameter Determinations.

The FMO program detected the numbered Apollo asteroids 1620 Geographos and 2201 Oljato as well as discovering 1983TB and 1983VA. Because of their close proximity to the Earth, and the IRAS scan geometry, they were all observed at large phase angles. In these circumstances, the standard model does not describe the asteroids' spectra well (see sections 3.3 and 3.5) because of the large fraction of the unilluminated hemisphere which is visible.

TABLE 5.7

1620 Geographos - Diameter determination.

| | | |
|---|---|---|
| Date | | 22 March 1983 |
| r | (A.U.) | 1.003 |
| Δ | (A.U.) | 0.101 |
| α | (deg) | 83.8 |
| T | (K) | 230 |
| S(12μm) | ($W.m^{-2}\mu m^{-1}x10^{15}$) | 37.8 |
| S(25μm) | .. | 16.1 |
| S(60μm) | .. | 1.58 |
| $S_*^*$(12μm) | .. | 39.7 |
| $S_*$(25μm) | .. | 12.7 |
| $S_*$(60μm) | .. | 1.03 |
| Diameter | (km) | |
| (Standard) | | 1.7 |
| (Fast-rotating) | | 1.5 |

Tables 5.7-5.10 contain the aspect data and observed fluxes converted to monochromatic magnitudes in the manner described in appendix C. When multiple observations were made, the data have been co-added by taking the mean of the band II fluxes and the mean band II:band I and band II:band III colours. Neither 1983TB nor 2201 Oljato showed systematic lightcurve effects in the separate bands. The data have then been corrected to "standard model calibration" (section 5.3.1). Since this "calibration" was based on observed main belt asteroids at moderate phase angles, it is not strictly applicable to these data because part of the corrections are due to real differences between the standard model and the IRAS observed spectra. However, these corrections have been used, since they appear to produce a

TABLE 5.8

2201 Oljato - Diameter determination.

| | | | | | | | | |
|---|---|---|---|---|---|---|---|---|
| Date | | | | 20 June | | | | |
| r | (A.U.) | | | 1.016 | | | | |
| $\Delta$ | (A.U.) | | | 0.184 | | | | |
| $\alpha$ | (deg) | | | 85. | | | | |
| T | (K) | | | 300 | | | | |
| S(12μm) | ($W.m^{-2}\mu m^{-1}x10^{15}$) | 24.9 | 28.7 | 27.8 | 24.3 | | 26.5 | |
| S(25μm) | .. | 6.34 | 7.71 | 7.06 | 6.16 | 5.84 | 5.09 | |
| $S_*^*$(12μm) | .. | | | 27.7 | | | | |
| $S^*$(25μm) | .. | | | 5.03 | | | | |
| Diameter | (km) | | | | | | | |
| (Standard) | | | | 1.9 | | | | |
| (Fast-rotating) | | | | 1.9 | | | | |

TABLE 5.9

1983TB - Diameter determination.

| Date | | 11 November | | | | | | |
|---|---|---|---|---|---|---|---|---|
| r | (A.U.) | 1.02 | | | | | | |
| Δ | (A.U.) | 0.37 | | | | | | |
| α | (deg) | 76. | | | | | | |
| T | (K) | 270 | | | | | | |
| S(12μm) | ($W.m^{-2}\mu m^{-1}x10^{15}$) | 66.1 | 51.7 | 55.7 | 54.4 | 53.7 | 52.6 | 47.6 |
| S(25μm) | .. | 15.9 | 18.1 | 16.7 | 17.0 | 14.5 | 16.6 | 16.0 |
| S(60μm) | .. | 1.02 | 0.88 | 1.06 | 0.98 | 1.25 | | 1.36 |
| $S^*_*$(12μm) | .. | 57.5 | | | | | | |
| $S_*$(25μm) | .. | 13.0 | | | | | | |
| $S^*$(60μm) | .. | 0.69 | | | | | | |
| Diameter | (km) | | | | | | | |
| (Standard) | | 6.0 | | | | | | |
| (Fast-rotating) | | 5.6 | | | | | | |

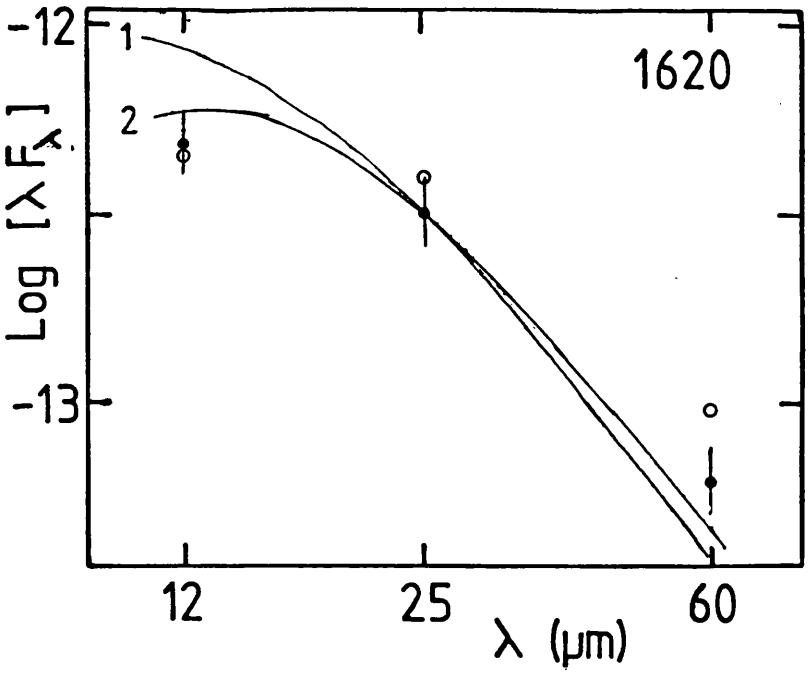


Fig. 5.16 IRAS data for 1620 Geographos, fitted by: 1 - standard model, 2 - Fast-rotating model. Error bars correspond to 20% uncertainties for an individual measurement.

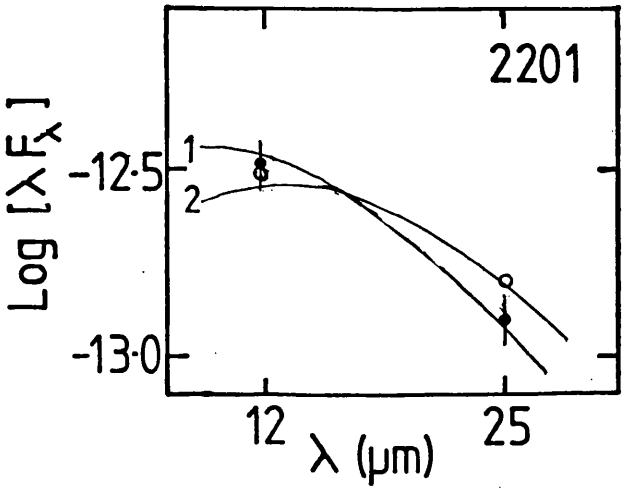


Fig. 5.17 As Fig. 5.16 for 2201 Oljato.

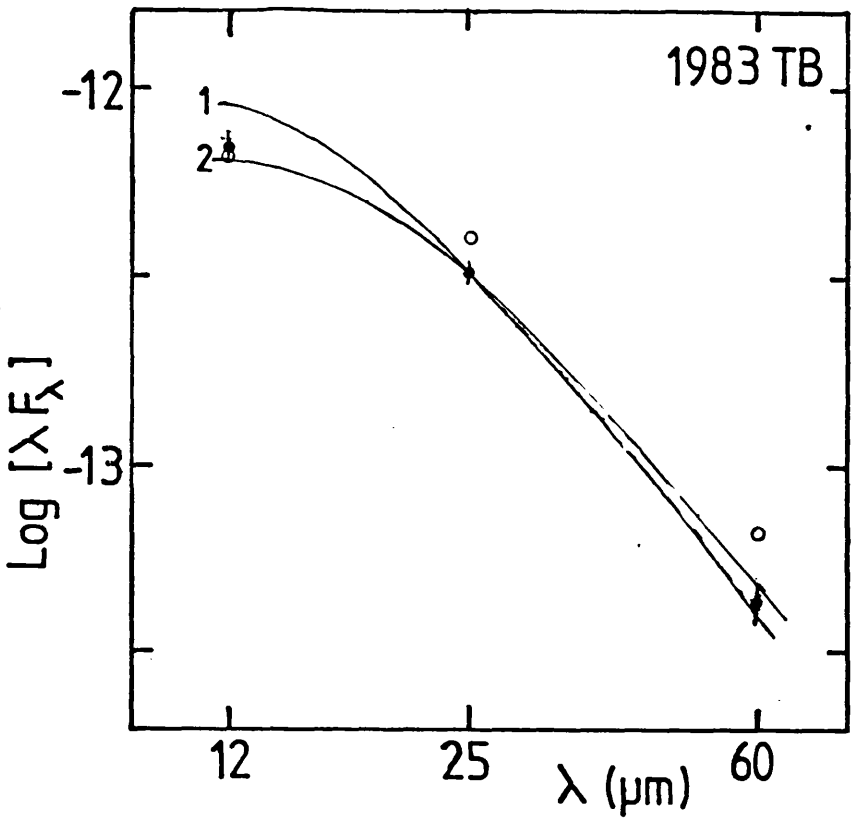


Fig. 5.18 As Fig. 5.16 for 1983TB.

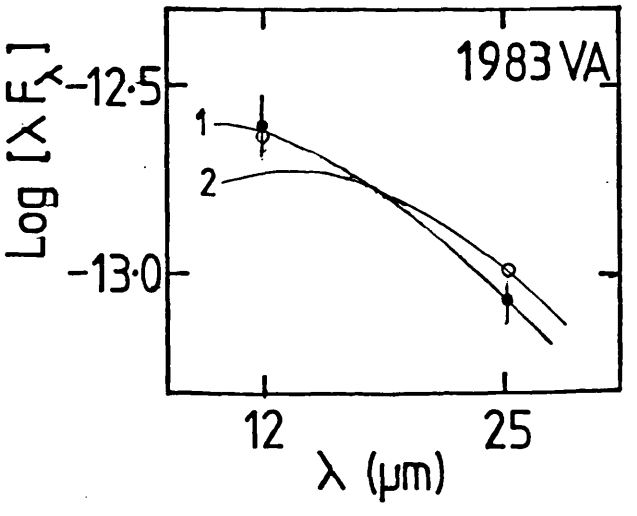


Fig. 5.19 As Fig. 5.16 for 1983VA.

better fit to the models, presumably because they do, in part, correct for calibration errors in the PAF data. Figs. 5.16-5.19 show the extreme cases of the standard model (1) and the fast-rotating model (2) fitted to the data. With the exception of Geographos, the IRAS data lie between these two models. The error bars are obtained from combining the ~20% uncertainties in each measurement. Both of uncetainties both in the data themselves, and in the calibration, it is not possible to deduce the thermal properties of the surfaces with any confidence.

TABLE 5.10

1983VA - Diameter determination.

| | | | |
|---|---|---|---|
| Date | | 1 November 1983 | |
| r | (A.U.) | 1.065 | |
| Δ | (A.U.) | 0.359 | |
| α | (deg) | 68.7 | |
| T | (K) | 320 | |
| S(12μm) | ($W.m^{-2}.\mu m^{-1} \times 10^{15}$) | | 19.6 |
| S(25μm) | .. | 4.54 | 4.15 |
| $S_*^*$(12μm) | .. | 16.2 | |
| $S^*$(25μm) | .. | 4.56 | |
| Diameter | (km) | | |
| (Standard) | | 3.0 | |
| (Fast-rotating) | | 3.1 | |

1620 Geographos was observed only once as a three-band source from which a mean diameter of (1.6±0.3)km can be derived. Since Geographos has a lightcurve amplitude of $1\text{-}2^m$ (Dunlap, 1974), implying an elongated shape, the poor fit of

the models to the data is not surprising. 2201 Oljato has a rotation period of ~24 or 48 hours, with a lightcurve amplitude $>0^m.1$ (Harris and Young, 1982). The derived diameter is (1.9±0.2)km.

1983TB was discovered on 11 October as a series of seven three-band detections moving at 7arcmin.hr$^{-1}$ (12arcmin. orbit$^{-1}$) near the North ecliptic pole, and was optically confirmed by C. Kowal at Mt. Palomar a few hours later. The mean diameter derived from these data is (5.6±0.6)km. The second FMO to be confirmed visually as an Apollo was 1983VA. It was rather fainter than 1983TB and was found on 1 November moving retrograde at moderate ecliptic latitude. Although it was approaching the Earth, it was not extensively observed because of its high Southerly declination and its position relative to the Sun. The derived diameter is (3.0±0.6)km.

## 5.6 1983TB - AN EXTINCT COMETARY NUCLEUS?

### 5.6.1 Introduction.

Although a number of possible detections of new Earth-crossing asteroids were made (see section 5.8), the first confirmed discovery was of 1983TB. Further observations showed that 1983TB was indeed an unusual object. Not only did it have the smallest perihelion distance of any known asteroid, but it was soon noted (Whipple, 1983) that the orbital elements were remarkably similar to the Geminid meteor stream. Fox et al. (1982; 1983) in their investigation of the structure of the observed meteor shower stated, "Meteoroid streams are produced from the dust emitted

by decaying cometary nuclei. ...the orbit of the causative comet for the Geminids (a comet which has not been identified and which probably completely decayed a long time ago) is assumed to be the same as that of the mean orbit of the stream as seen today." A few months later 1983TB was discovered in just such an orbit (Appendix D).

Optical observations during the discovery apparition showed no evidence for cometary activity (Marsden, personal communication) and examination of the raw data from IRAS (a technique which proved successful in differentiating between asteroids and comets (section 5.7), showed no evidence for extension. Cochran and Barker (1984) found no emission features using an IDS spectrograph; this had been shown to be a powerful technique for detecting weak cometary emissions. Apart from its association with the Geminid meteors, all the observations indicated that 1983TB is a normal Apollo asteroid. Nevertheless, the discovery of an object dynamically similar to a comet, but apparently physically asteroidal, has again raised the possibility of an evolutionary link between Apollo asteroids and short-period comets. This link has been challenged by Hughes (1982a), who argued that the failure to discover any objects in transition between the two states implied that there is no evolutionary relationship between the two types of object. Whipple (1981) has pointed out the difficulties of producing meteorites, some of which are believed to be fragments of Apollo objects, inside a cometary nucleus. Although meteor streams are usually associated with cometary orbits, it is theoretically possible for a stream to be associated with an asteroid which has undergone a recent collision. Such a stream would have a

lifetime of $\sim 10^4$ years (Wetherill and ReVelle, 1982). The recent apparition of 1983TB was particularly favourable, with a close approach to within 0.3 A.U. of the Earth, allowing observations with a wide spectral coverage.

5.6.2 Ground-based Observations.

Observations were carried out on 20 and 21 December 1984 (UT) using the 3.8m United Kingdom Infrared Telescope on Mauna Kea, Hawaii. Photometry from 2 to 5μm was obtained using the infrared photometer UKT9 on the nights of the 20 and 21 December with a 7".8 aperture and 20" E-W chop. A number of standards from the UKIRT list (A. Longmore, personal communication) (Table 5.11) were observed on both nights for airmass corrections. Photometry from 5 to 20μm was obtained on the 20 December only, using the bolometer UKT8 with an aperture of 6" and a 20" E-W chop. The standard stars α Tau, β And and β Peg were used for airmass correction and calibration. The adopted magnitudes are from Hanner et al. (1984) with slight corrections for the difference in reference wavelengths of the UKIRT wide-band filters and those on the IRTF (Table 5.11). Wide bandpass photometric measurements are normally reduced to monochromatic magnitudes at a reference wavelength for each filter. These reference wavelengths have been defined as in Hanner et al. (1984) and appendix C, using a 6000K blackbody for the source spectrum. (Blackbodies from 3000-10000K produce the same reference wavelengths, so no corrections were required for the standard stars.) The Mauna Kea sky transmission was obtained from Traub and Stier (1976) and the filter responses from The Royal Observatory Edinburgh. The reference wavelengths are

TABLE 5.11

Infrared Standards used for 1983TB observations.

| Star | [1]N(20) | [2]N(21) | J | H | K | L | L′ | M |
|---|---|---|---|---|---|---|---|---|
| HD 77281 | 3 | 1 | 7.11 | 7.05 | 7.03 | 6.99 | (6.98) | (6.98) |
| GL 347A | 1 | | 8.465 | 7.86 | 7.63 | 7.40 | | |
| BS 718 | | 3 | 4.385 | 4.39 | 4.39 | 4.395 | 4.40 | 4.37 |
| HD 225023 | | 1 | 7.08 | 6.99 | 6.96 | 6.935 | 6.955 | (6.95) |
| HD 1160 | | 1 | 7.06 | 7.05 | 7.04 | 7.045 | 7.03 | (7.03) |
| BS 3314 | | 1 | 3.92 | 3.92 | 3.94 | 3.93 | 3.925 | (3.93) |

| | | M | N | Q | 8.7 | 9.8 | 10.3 | 11.6 | 12.5 |
|---|---|---|---|---|---|---|---|---|---|
| β And | 3 | -1.80 | -2.09 | -2.10 | -1.97 | -2.05 | -2.07 | -2.14 | -2.18 |
| β Peg | 1 | -2.20 | -2.57 | -2.62 | -2.45 | -2.53 | -2.55 | -2.64 | -2.70 |
| α Tau | 1 | -2.76 | -3.01 | -3.09 | -2.98 | -2.99 | -2.99 | -3.08 | -3.14 |

[1]Number of observations on 20 December.

[2] .. .. .. .. 21 ..

( ) Indicates estimated values from other magnitudes.

Uncertainties $+0^{m}.02$

given in Table 5.12. Adopted zero magnitude fluxes were also obtained from Hanner et al. (1984) (Table 5.12).

The derived magnitudes and fluxes for 1983TB are given in Table 5.13. The corrections ($\Delta$m) to the magnitudes obtained with the wide-band filters are to allow for the difference between the stellar spectra (approximated by a blackbody for the 2-20$\mu$m region) used to calculate the reference wavelengths, and the asteroid spectrum, over the bandpass. The asteroid spectrum was represented by the best-fit model (see section 5.6.3) to the data between 5 and 20$\mu$m where the required corrections are small. The corrections for the L and L' filters were made by assuming this thermal model to be correct and adding the contribution from the reflected solar spectrum (Labs and Neckel, 1970) fitted to the J and H data. The J, H and K filters, which measure the reflected component of the asteroid spectrum, and the narrow-band filters did not require any corrections. The 10.3$\mu$m magnitude has been corrected to allow for a short wavelength leak corresponding to 10% of the measured flux for the standard stars (Hanner, personal communication).

The errors in the magnitudes account for statistical variations in the asteroid and standard star measurements, and uncertainties in the airmass corrections and standard star magnitudes. However, errors in derived colours may be larger if the measurements are separated in time by more than a few minutes. Tholen (1985) reported a lightcurve amplitude in excess of $0^m.4$ and a rotational period probably slightly under $4^h$, from observations in November and December 1984. Since the period is uncertain, and there is no published lightcurve, it is not possible to correct the magnitudes for

this effect. From the three measurements using the N filter, it appears that differential corrections will be $<0^m.1$ for the UKT8 data. Since the UKT8 and UKT9 measurements were made about $2^h$ apart, lightcurve effects could change the relative brightness by up to 50% between the reflected and emitted components. However, as $2^h$ is about half the estimated period, one might expect the effect to be much smaller if the lightcurve has the characteristic double-peaked shape found for many asteroids. Since the two measurements in the M filter agree within the quoted errors, the likely effect is probably ~15%. Changes in aspect between the two nights will produce a change of $-0^m.10$ in the JHK data.

TABLE 5.12

Reference wavelengths and adopted zero magnitude fluxes

| Filter | $\lambda_{ref}$ ($\mu$m) | $^1\Delta\lambda$ ($\mu$m) | $F_\lambda$ for $0^m.0$ ($W.m^{-2}\,\mu m^{-1}$) |
|---|---|---|---|
| J | 1.25 | 0.3 | $3.31 \times 10^{-9}$ |
| H | 1.65 | 0.3 | $1.36 \times 10^{-9}$ |
| K | 2.2 | 0.4 | $3.98 \times 10^{-10}$ |
| L | 3.53 | 0.6 | $6.61 \times 10^{-11}$ |
| L′ | 3.73 | 0.6 | $5.25 \times 10^{-11}$ |
| M | 4.73 | 0.5 | $2.11 \times 10^{-12}$ |
| | 8.7 | 1.2 | $1.92 \times 10^{-12}$ |
| | 9.7 | 1.0 | $1.25 \times 10^{-12}$ |
| | 10.3 | 1.0 | $9.91 \times 10^{-13}$ |
| N | 10.6 | 2.6 | $8.95 \times 10^{-13}$ |
| | 11.6 | 1.25 | $6.21 \times 10^{-13}$ |
| | 12.5 | 1.2 | $4.63 \times 10^{-13}$ |
| Q | 19.2 | 4.5 | $8.64 \times 10^{-14}$ |

[1] F.W.H.M. of convolution of sky and filter transmissions.

TABLE 5.13

Infrared photometry of 1983TB - Dec. 1984

| Time (UT) | Integration time (secs) | Aperture (arcsec) | Filter | $\lambda_{ref}$ ($\mu_m$) | [1]Magnitude | [2]$\Delta m$ | Log $F_\lambda$ ($Wm^{-2}\,\mu m^{-1}$) |
|---|---|---|---|---|---|---|---|
| Dec 20 | | | | | | | |
| 0955 | 20 | 7.8 | J | 1.25 | 12.52±0.03 | | -13.488 |
| 0957 | 20 | " | H | 1.65 | 12.26±0.04 | | -13.770 |
| 0940 | 20 | " | K | 2.2 | 12.28±0.03 | | -14.312 |
| 0943 | 50 | " | L | 3.53 | 10.19±0.05 | +0.08 | -14.288 |
| 0948 | 40 | " | L' | 3.73 | 9.59±0.07 | +0.08 | -14.148 |
| 0958 | 55 | " | M | 4.73 | 7.26±0.08 | +0.01 | -13.584 |
| 0724 | 100 | 6 | M | 4.73 | 7.38±0.17 | +0.01 | -13.632 |
| 0729 | 60 | " | | 8.7 | 3.19±0.04 | | -12.993 |
| 0732 | 60 | " | | 9.7 | 2.73±0.06 | | -12.995 |
| 0736 | 50 | " | | 10.3 | 2.56±0.06 | | -13.027 |
| 0711 | 110 | " | N | 10.6 | 2.37±0.06 | -0.02 | -12.988 |
| 0747 | 40 | " | N | 10.6 | 2.49±0.06 | -0.02 | -13.036 |
| 0832 | 60 | " | N | 10.6 | 2.43±0.06 | -0.02 | -13.012 |
| 0739 | 60 | " | | 11.6 | 2.03±0.05 | | -13.019 |
| 0744 | 80 | " | | 12.5 | 1.84±0.06 | | -13.070 |
| 0717 | 100 | " | Q | 19.2 | 0.76±0.06 | -0.02 | -13.359 |
| Dec 21 | | | | | | | |
| 0804 | 40 | 7.8 | J | 1.25 | 12.55±0.03 | | -13.500 |
| 0806 | 50 | " | H | 1.65 | 12.28±0.02 | | -13.778 |
| 0748 | 50 | " | K | 2.2 | 12.24±0.02 | | -14.296 |
| 0752 | 60 | " | L | 3.53 | 10.15±0.04 | +0.08 | -14.271 |
| 0756 | 50 | " | L' | 3.73 | 9.33±0.05 | +0.08 | -14.044 |
| 0759 | 60 | " | M | 4.73 | 7.12±0.08 | +0.01 | -13.528 |

On 20 December $08^h$ UT, r = 1.131 AU; $\Delta$ = 0.246 AU; $\alpha = 48^o.3$

On 21 December $08^h$ UT, r = 1.115 AU; $\Delta$ = 0.245 AU; $\alpha = 52^o.2$

1 In-band magnitude.

2 Correction to monochromatic magnitude at reference wavelength $\lambda_{ref}$.

5.6.3 Discussion.

Colour-colour diagrams have been used in asteroid classification for many years (section 2.3). The most commonly used classification scheme (Bowell et al., 1978) has been extended by Veeder et al., (1982;1983a) to include near-infrared (JHK) colours. Hartmann et al. (1982) have also used broadband (VJHK) photometry to describe compositional groups of solar system objects such as asteroids, comets and outer planetary satellites.

Tholen (1985) found broad-band colours (between 0.3 and 0.9μm) for 1983TB slightly bluer than the Sun, implying an F classification at variance with the S-type colours observed by Cochran and Barker (1984) and Belton et al. (1985), which were based on single spectroscopic observations. F-type asteroids have flat reflectance spectra sloping gradually downwards towards longer wavelengths and low albedos (<0.065), corresponding to an unknown, but possibly carbonaceous composition. The mean JHK colours of 1983TB derived from the present observations are $J-H=0.27\pm0.03$, $H-K=0.01\pm0.06$. The larger uncertainty in the H-K colour is due to the 18-minute delay between the measurements on both nights. These colours are bluer than found for most asteroids, but are not inconsistent with the proposed F classification. However, a number of other types have similar optical spectra to F-types but are distinguished by their albedos (Zellner et al., 1985). J-H colours of distant comets (Hartmann et al., 1982) lie in the range 0.4-0.55.

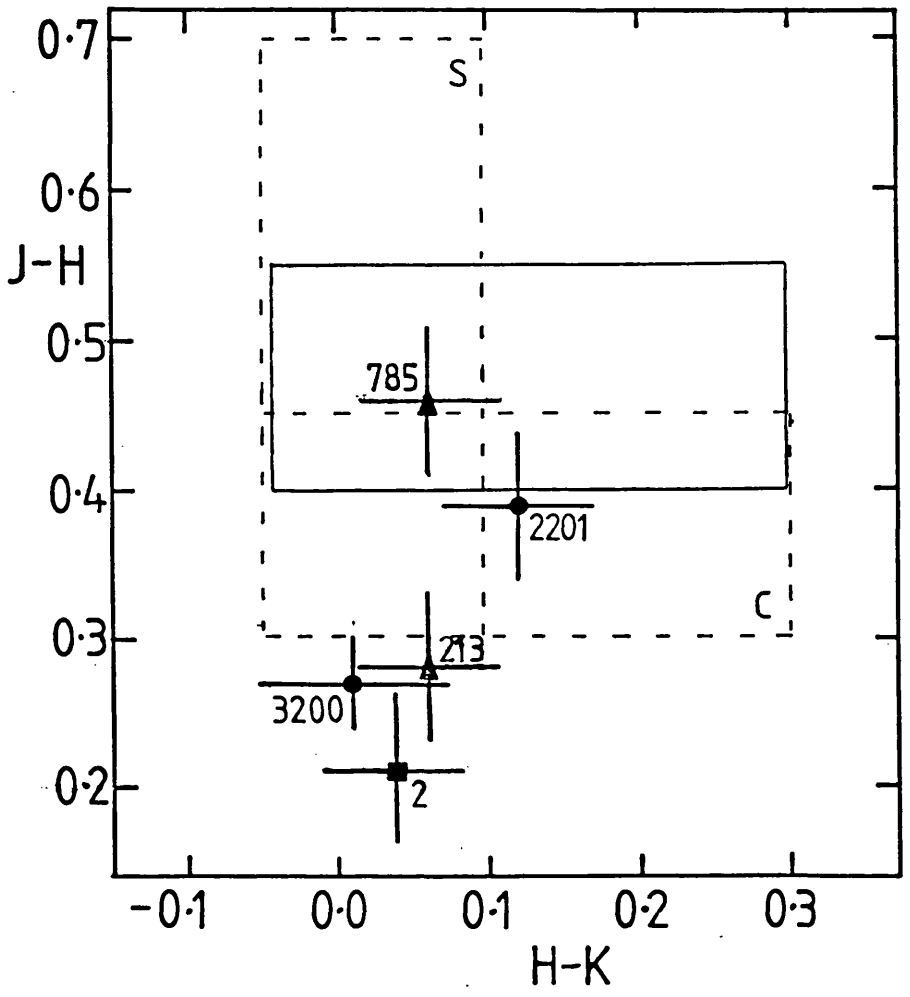


Fig. 5.20 J-H vs. H-K for 1983TB compared with the C and S asteroid domains (broken lines) and those for distant comets (solid lines) (Hartmann et al. 1982). Also shown are the Earth-crosser 2201 Oljato (McFadden et al. 1984b), the F-types 213 Lilaea and 785 Zwetana, and the B-type Pallas. Asteroid data is from Veeder et al. (1982;1983a).

P/Neujmin 1, a very low activity comet, was also observed during this run. Its JHK colours lie in the comet domain, despite the fact that it showed no trace of a coma. Fig. 5.20 shows a JHK colour-colour plot comparing 1983TB with comets and with C- and S-type asteroids. Two F-type asteroids, 213 Lilaea and 785 Zwetana, with measured JHK colours are shown for comparison. 2 Pallas is a member of the newly defined B-type which are spectrally similar to F-types, but have moderate albedos.

Fig. 5.21 shows the spectrum measured for 1983TB from 1.2 to 20μm The reflected solar spectrum was fitted to the J and H points and the thermal model spectrum to the 5-20μm data for a range of values of $p_V$ and R. (For F-type asteroids $p_V \approx p_J$.) The value of the visible phase coefficient $\gamma_V$ was derived from the mean properties of a large number of asteroids (Bowell & Lumme, 1979). The "best-fit" standard model (section 3.3), and projected model (section 3.5.1), (Table 5.14), clearly do not provide a good fit to the thermal data. This appears to be related to the large phase angle of the observations. Model 3 shows the best fit (which occurs for $f=0.65\pm0.02$) for the modified projected model (section 3.5.2). Model 4 shows the extreme case of a fast-rotating model (section 3.5.3), where the temperature is constant for any given latitude. This model would correspond to a value of f=0.73 for 1983TB at the time of observation. The high value of f for the best-fit model to the 1983TB data is difficult to explain simply in terms of a fast rotation period. Solving the one-dimensional conduction equation for an equatorial surface element with lunar properties and a 4-

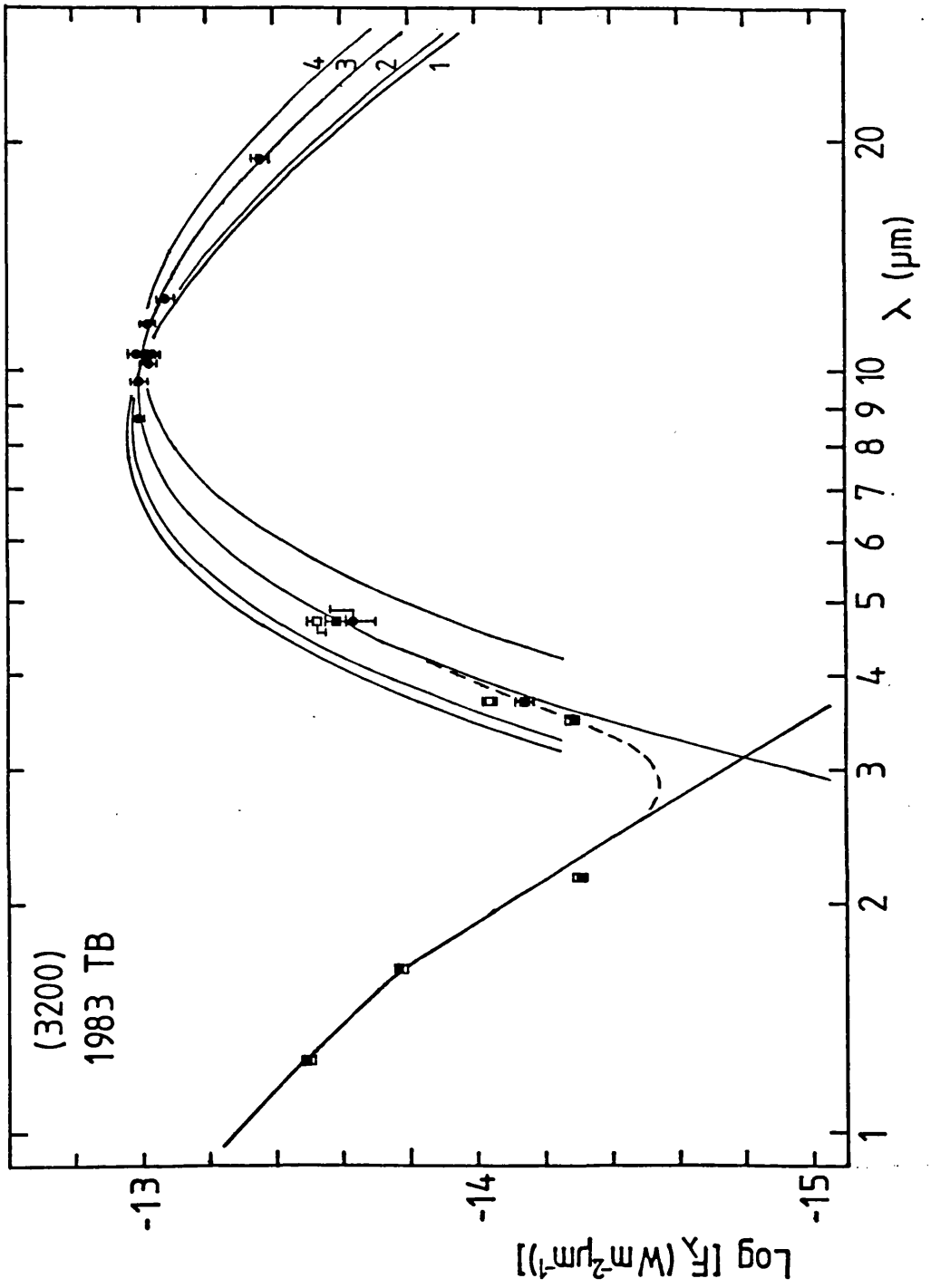


Fig. 5.21 The observed spectrum of (3200) 1983TB is shown by:- squares for UKT9 data, circles for UKT8 data; solid symbols correspond to observations on 20 December, open symbols to 21 December. No corrections have been made for possible lightcurve effects or changes in aspect. The reflected solar spectrum has been fitted to the J and H points and the thermal models to the 5-20μm data (see Table 5.14). 1 - Standard thermal model, 2 - Projected model, 3 - Modified projected model, 4 - Fast-rotating model.

TABLE 5.14

Best-fit models to the 20 December data for (3200) 1983TB

| | | Visual phase coefficient $\gamma_V$ (mag/deg) | Maximum surface temperature $T_{max}$ (K) | Darkside temperature factor f | Visual geometric albedo $P_V$ | Diameter D (km) |
|---|---|---|---|---|---|---|
| 1 | Standard model | 0.033 | 382 | - | 0.135 | 4.0 |
| 2 | Projected model | 0.033 | 372 | - | 0.14 | 4.0 |
| 3 | Modified projected model | 0.035 | 344 | 0.65 ± 0.02 | 0.11 | 4.7 |
| 4. | Fast-rotating model | 0.037 | 282 | 0.73 | 0.08 | 5.6 |

For all models:

Phase integral q = 0.6; bolometric emissivity $\varepsilon$ = 0.9.

For the standard model: Infrared phase coefficient $\gamma_{IR}$ = 0.01 mag/deg; modelling constant $\beta$ = 0.9.

hour rotation period gives a night-time minimum temperature which implies f$\sim$0.4. A value of f$\sim$0.6 is obtained for a rocky surface with no regolith. Even allowing for errors in the data due to lightcurve effects, this implies that much of the surface of 1983TB must have thermal properties similar to those of solid rock. This would not be expected on the basis of the normally postulated model for an extinct cometary nucleus, since this should lead to the presence of an insulating layer of dust.

The derived diameter of (4.7$\pm$0.5)km is somewhat lower than that derived from the IRAS observations, but is in agreement within the quoted errors. At least part of the discrepancy could be due to lightcurve effects which were not recognisable in the IRAS data.

5.6.4 Conclusions.

The infrared spectrum of (3200) 1983TB implies a surface with the thermal properties of solid rock. The derived albedo and effective diameter, taking into account possible errors in the assumed model parameters, and lightcurve effects, are 0.11$\pm$0.02 and (4.7$\pm$0.5)km. The near-infrared colours, albedo and visual photometry imply a B-type classification. These results are at variance with the usually accepted model for an inert cometary nucleus. The reason for the association with the Geminid meteor stream remains unclear, and 1983TB may be a unique object. However, these results may provide support for the supposition that the meteors have, in this case, been derived from some collisional process.

## 5.7 COMETS

### 5.7.1 Comet Discoveries and Population Estimates.

The FMO program proved more effective at detecting comets than originally expected with the discovery of six new comets, as well as an extensive infrared tail on Comet Tempel-2 (section 5.7.3). This success suggests that there may be a number of comets, which must be distinguished from asteroids, among the hours-confirmed data being processed by ADAS.

Comet IRAS-Araki-Alcock which was the first FMO alert to be made, was observed well away from the ecliptic plane and appeared very bright in the infrared. After its identification as a comet, the raw data from each detector in the focal plane were examined. Fig. 5.22 shows the raw data from the band I detectors for one observation of the comet, compared with those of a point source. The comet exhibited both in-scan and cross-scan extension. Although the other comets discovered were much fainter, they all showed slight extension in the in-scan direction, thereby providing a method of distinguishing comets from asteroids in the IRAS database.

IRAS-Araki-Alcock is classed as a long-period (P>200y) comet. The other periodic comets discovered, P/IRAS 1983j and P/Hartley-IRAS 1983v, both had orbital inclinations of over $45^{\circ}$ (Appendix D). In fact, 1983v is the only known short-period comet with an orbit nearly perpendicular to the ecliptic, and has the shortest period for a comet with a retrograde orbit. High inclination short-period comets are

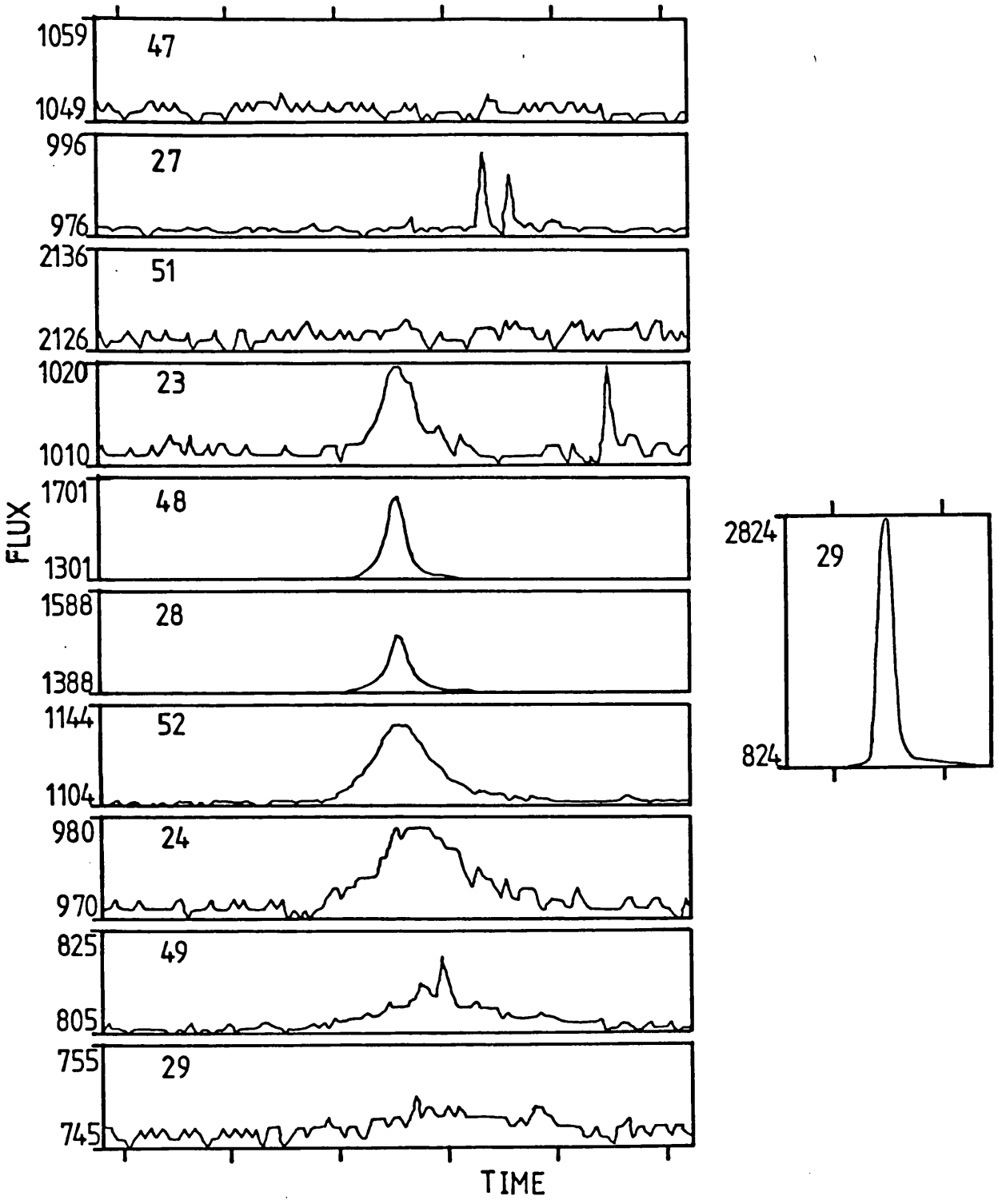


Fig. 5.22 Raw data from band I detectors during an observation of comet IRAS-Araki-Alcock 1983d. Each time interval is one second. Data from a point source (1 ceres) is shown for comparison. The slight assymmetry in the profile for Ceres is an instrumental effect.

rare, since capture into the inner Solar System can only occur by a close encounter with a third body, usually one of the major planets. The orbit of 1983j intersects the plane of the Solar System close to its aphelion, which lies on Saturn's orbit, while 1983v passes close to the orbits of Jupiter and Mars (Fig. 5.23).

Comet IRAS 1983o was detected by IRAS on the 27 July, but was not then recovered by ground-based telescopes. A subsequent IRAS detection on 1 September was recognised, from its infrared fluxes, as being a second observation of the same object. An ephemeris based on the two sets of positional measurements was then used to recover the comet from the ground. This seems to have been the first occasion on which a comet has been discovered, and an ephemeris allowing recovery calculated, purely on the basis of satellite observations.

Several known comets passed perihelion in 1983, but were not detected by the FMO program. They either did not pass through the region being scanned, or were moving too slowly, or were too faint. The exception was comet Sugano-Saigusa-Fujikawa 1983e which was both fast-moving and very extended and diffuse. In this instance, the comet may not have been scanned by IRAS as it passed through the scan plane, or was not recognised as a point source.

Although cometary brightness is notoriously difficult to quantify, some conclusions can be drawn from the IRAS comet observations. With the exception of Comet IRAS-Araki-Alcock 1983d, all the discoveries were of optically faint comets at heliocentric distances of 1.5-2.5 A.U. The reported

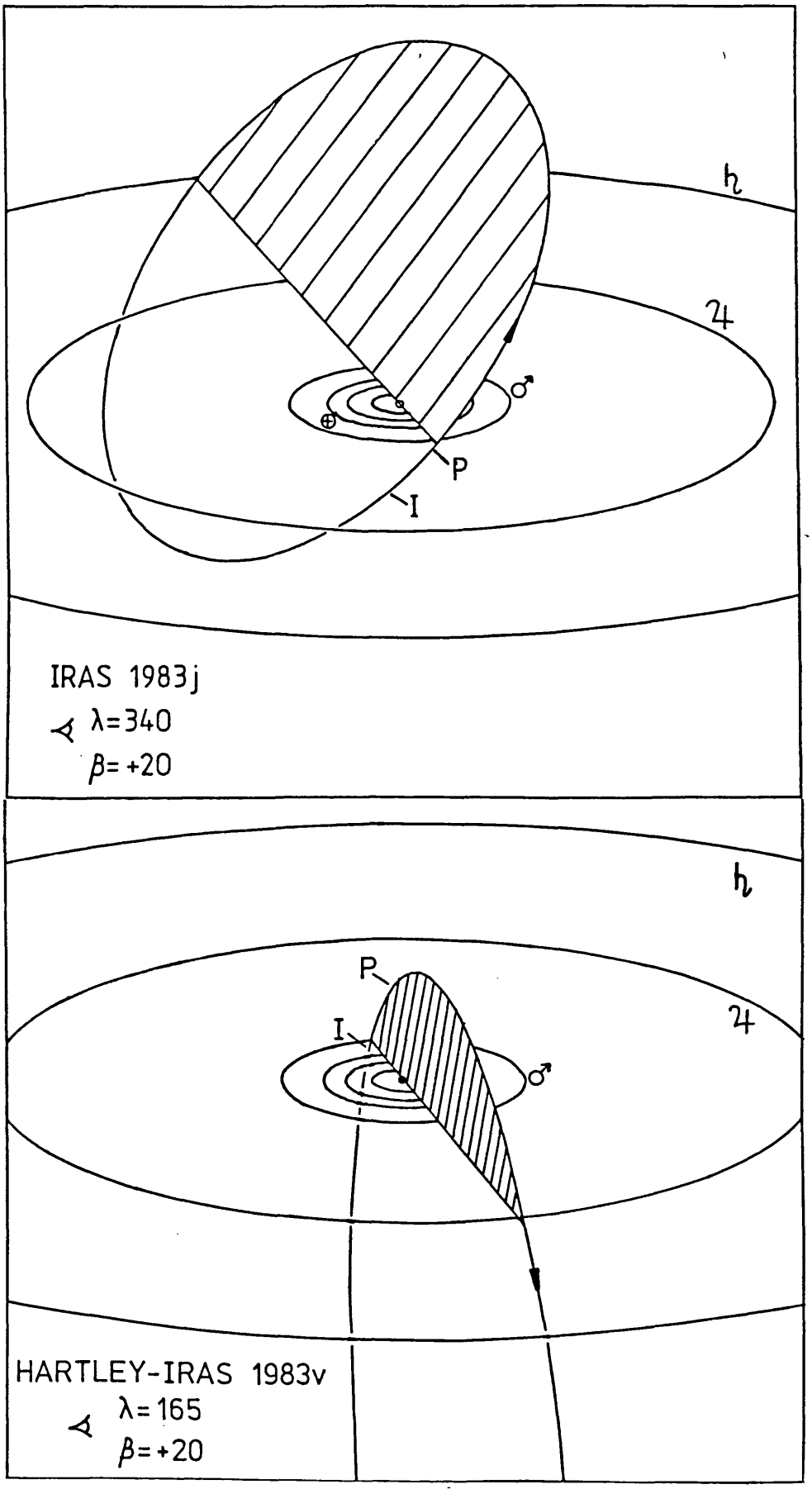


Fig. 5.23 Orbits of the two short-period comets discovered by IRAS. "I" indicates the position at discovery, "P", the point of perihelion passage.

photographic magnitudes at discovery covered a range of three magnitudes, while the fluxes recorded by IRAS differed by only one magnitude approximately. Comet 1983d was ~500 times brighter than the other comets in the optical, but only ~100 times brighter in the infrared. This difference is presumably due to (1) the angular size of the comet overflowing the beam size of the detectors, and (2) an underestimate of the infrared brightness as a result of using a point-source algorithm. In the same way, the band III fluxes were higher than expected from the temperature inferred from bands I and II, due to the larger band III detector area. Unfortunately, the colour temperatures are not a suitable method for distinguishing comets from asteroids in the IRAS data. The effect described above for band III is a mean property for all the observed comets and the scatter in colours due to observational error can make a comet detection indistinguishable from that of an asteroid (Fig 5.24).

Since the total number of comets entering the inner Solar System is highly uncertain, it would be useful to compare estimates of the population from the IRAS detection rate with those from other sources. Unfortunately, whereas the larger asteroids can be modelled in a fairly consistent way, cometary magnitudes are extremely difficult to predict. This difficulty is compounded by the uncertainty regarding the ratio of optical-to-infrared brightness of a comet (which depends on the gas-to-dust ratio of each object and the variation of brightness with heliocentric distance).

The absolute magnitude of a comet can be calculated from the equation

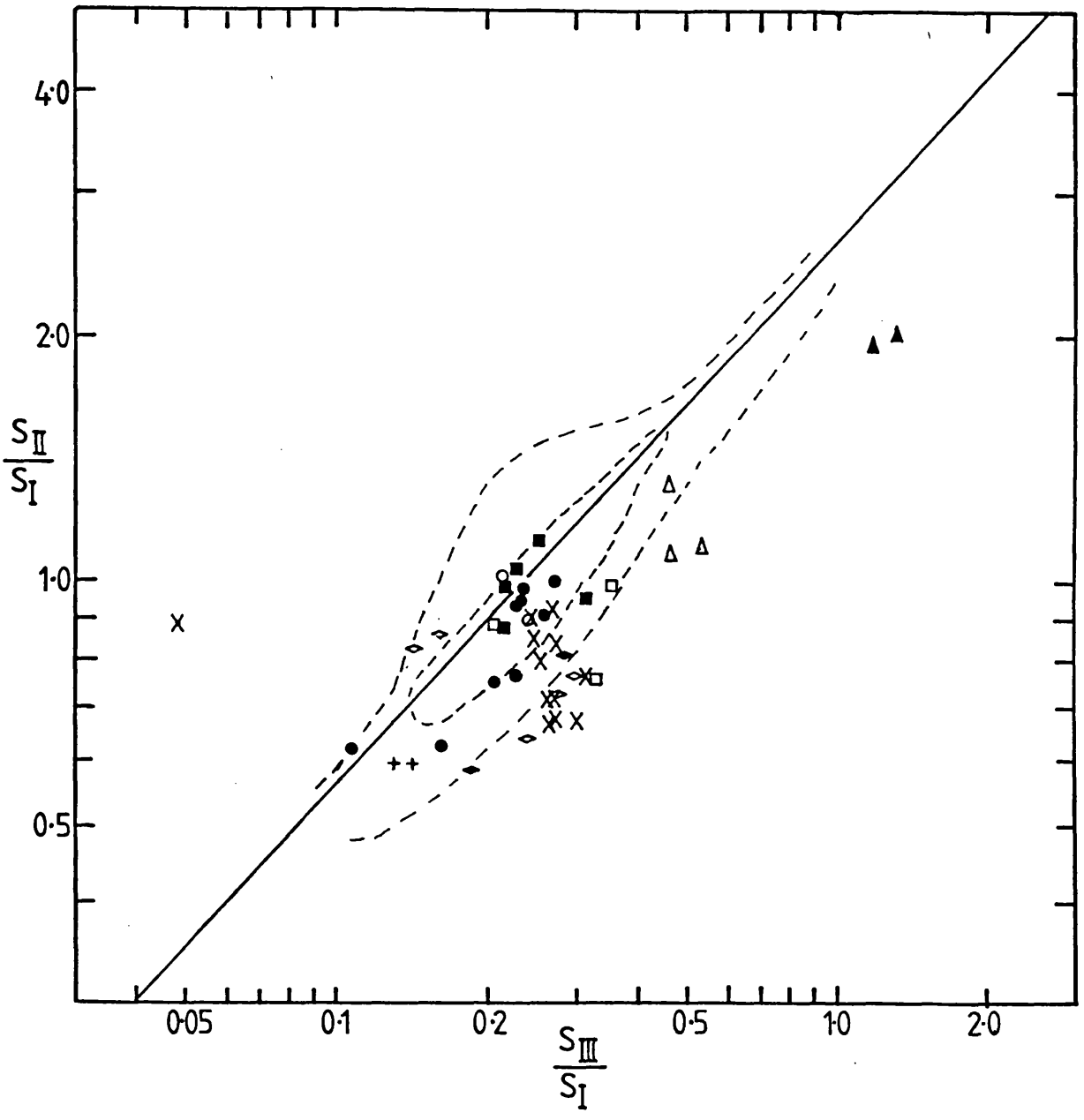


Fig. 5.24 In-band colours for comets observed by IRAS. (+) P/IRAS-Araki-Alcock 1983d; (Δ) IRAS 1983f; (●) P/IRAS 1983j; (o) P/Hartley-IRAS 1983v; (X) P/Tempel-1; (◇) P/Tempel-2; (◆) Tempel-2 infrared tail; (□) P/Kopff; (▲) Cernis 1983l; (■) P/Pons-Winnecke. The solid line shows blackbody colours. The dashed lines are regions of increasing density of asteroid colours.

$$H_0 = m - 5\log\Delta - 2.5n \log r$$

The change of brightness with heliocentric distance indicated by n, varies considerably from comet to comet, and even for an individual comet. It can only be determined for a specific object by combining a consistent set of observations over a long period of time. For population studies, it is usual to choose n=4 as a reasonable approximation for all comets, and the magnitude thus derived is referred to as $H_{10}$.

Hughes (1982b) derives an equation for the number of discoverable comets entering the inner Solar System (roughly defined as a sphere of radius 1.2AU from the Sun) per decade as

$$N = 3.43 \times 10^{-2} \times 1.57^{H_{10}} + 0.1543 \times 1.98^{H_{10}}$$

where the first term refers to comets with P<200 years. He suggests this is certainly valid for $H_{10}<6$, and probably valid for $H_{10}<11$. $H_{10}$ values are usually derived from observations of total visual magnitude when the comet is around heliocentric distance 1 A.U. Magnitudes derived from photographic plates are often $2^m$ or more fainter and generally refer only to the central condensation. Visual observations were used to derive the following $H_{10}$ values: 1983d $H_{10}=9.7$ (Bortle, 1983); 1983v $H_{10}=7.7$ (Bortle, 1984); 1983j $H_{10}=9.2\pm0.5$ (12 observations). The known comets detected by the FMO program also had $H_{10}<10$. Hughes' equation predicts for $H_{10}=10$, that 10 non-periodic comets should be discoverable during the IRAS mission, but that there was only a one in five chance of discovering a periodic comet. IRAS discovered 2 periodic ($P<200^y$) and 4 non-periodic comets, all but one with q>1.2A.U. The Hughes' equation is derived from previous comet discoveries and is

biased towards in-plane, low q orbits. Because of the IRAS orbit and focal plane geometry, the IRAS observations are biased towards larger q and high inclination orbits.

A fairer comparison is with the FMO search by Helin and Shoemaker (1979) who looked for Apollo-Amor asteroids to a magnitude limit of $\sim 15^m.5$. Only one comet was found between 1973-78, during which 80,570 sq. degrees were searched. This compares with the IRAS success rate of 6 comets in $\sim$100,000 $deg^2$ (allowing for the galactic exclusion zone, and the repeated sky coverage of the IRAS mission). Hughes and Daniels (1980) give the absolute magnitude distribution index for comets as $N \alpha 2^M$. Thus, given the IRAS comet detection limit of $18^m$ (photographic magnitude of the faintest IRAS comet at detection), we might expect six times more comets per unit area searched than Helin and Shoemaker. This agrees with the observational results despite the limited statistics.

Gehrels (1981) estimates a discovery rate for comets at 1 per 600$deg^2$ down to $20^m$ for his photographic search for faint comets near the ecliptic plane. He also quotes Kowal's rate of 1 per 1300$deg^2$ to a limit of $19^m$. These searches cannot be compared directly with the IRAS FMO programme since they are optimised for distant, and hence, slow-moving objects, and were concentrated towards the ecliptic plane. They can, however, be used to predict the total number of comets in the ecliptic plane in the IRAS data. IRAS scanned $\sim$30,000 $deg^2$ of the ecliptic plane ($\pm 15^o$) with hours confirmation implying a total of 11 slow-moving comets in the data. Assuming the distant non-periodic comets are evenly distributed Gehrels found 1 per 3600 $deg^2$ implying 7 in the

IRAS data.

Although the figures quoted above are of low accuracy due to the small number statistics, they imply that 20-30 new comets should be present in the hours-confirmed IRAS data allowing for the improved detection threshold at ADAS.

5.7.2 Temperatures and dust production.

The thermal emission from comets originates predominantly from dust grains in the coma. Most observed comets have shown colour temperatures hotter than a theoretical blackbody at the same heliocentric distance. This implies small (micron-sized) absorbing grains which cannot radiate efficiently at wavelengths significantly larger than their radius. Some comets show a broad emission feature near 10μm, attributed to silicate grains. The strength or presence of this feature is dependent on particle size and composition, and varies both with heliocentric distance and location relative to the coma. The observations imply two components to the cometary dust: hot absorbing grains and silicate grains. Theoretical emission spectra have been produced using Mie theory for the scattering and emission properties of the grains, and dynamical analysis of cometary dust tails (section 5.7.3) to deduce a grain size distribution (Hanner, 1980;1983; Campins and Hanner, 1982; Eaton, 1984). Observations of dust comae through different sized apertures show surface brightness proportional to $R^{-1}$ (where R is the radial distance from the nucleus), implying number densities proportional to $R^{-2}$.

Ney (1982) has used a simple model to derive approximate dust masses and production rates from observed colour

temperatures. This method relies on the fact that, for grains smaller than a few microns, the infrared luminosity measures the mass of the grains independently of particle size. The observed grain mass is given by

$$M = 1.7 \times 10^{28} \Delta^2 (\lambda F_\lambda)_{max} / T^4$$

where $\Delta$ is the geocentric distance in A.U.; $(\lambda F_\lambda)_{max}$ is in $W.m^{-2}$; M is in kg. The mass loss rate is calculated by dividing this mass by the residence time for the grains within the coma observed in the aperture from which T and $(\lambda F\lambda)_{max}$ were calculated. The grain ejection velocity is of the order of sonic velocity in the gas (Finson and Probstein, 1968a) and is taken to be $0.5(T_{bb}/300)^{1/2}$ $km.sec^{-1}$ where $T_{bb}$ is the equilibrium blackbody temperature. Uncertainties in the assumptions involved in this analysis could produce errors of at least a factor of two, but if the grain material does not vary much from comet to comet, relative errors will be smaller.

For the comets observed by IRAS, the values of $(\lambda F_\lambda)_{max}$ and T must be derived from the band II:band I ratio only, since the band III and IV detectors are a different size. Fig. 5.25 shows a) The band II:band I and b) the band III:band I colours vs. heliocentric distance. Also shown are the equilibrium blackbody temperature curve ($T_{bb}=277r^{-1/2}$) and a curve representing the temperatures of a number of observed comets ($T_{pred}=329r^{-0.53}$) (Eaton, 1984). Although individual comets varied by up to 50K from $T_{pred}$, the curve represented the best fit to the data as a whole. However, the band II:band I ratios do not scatter about the $T_{pred}$ curve. Table 5.15 shows these predicted values, compared with the observed colour temperatures $T_{obs}$. Errors in the

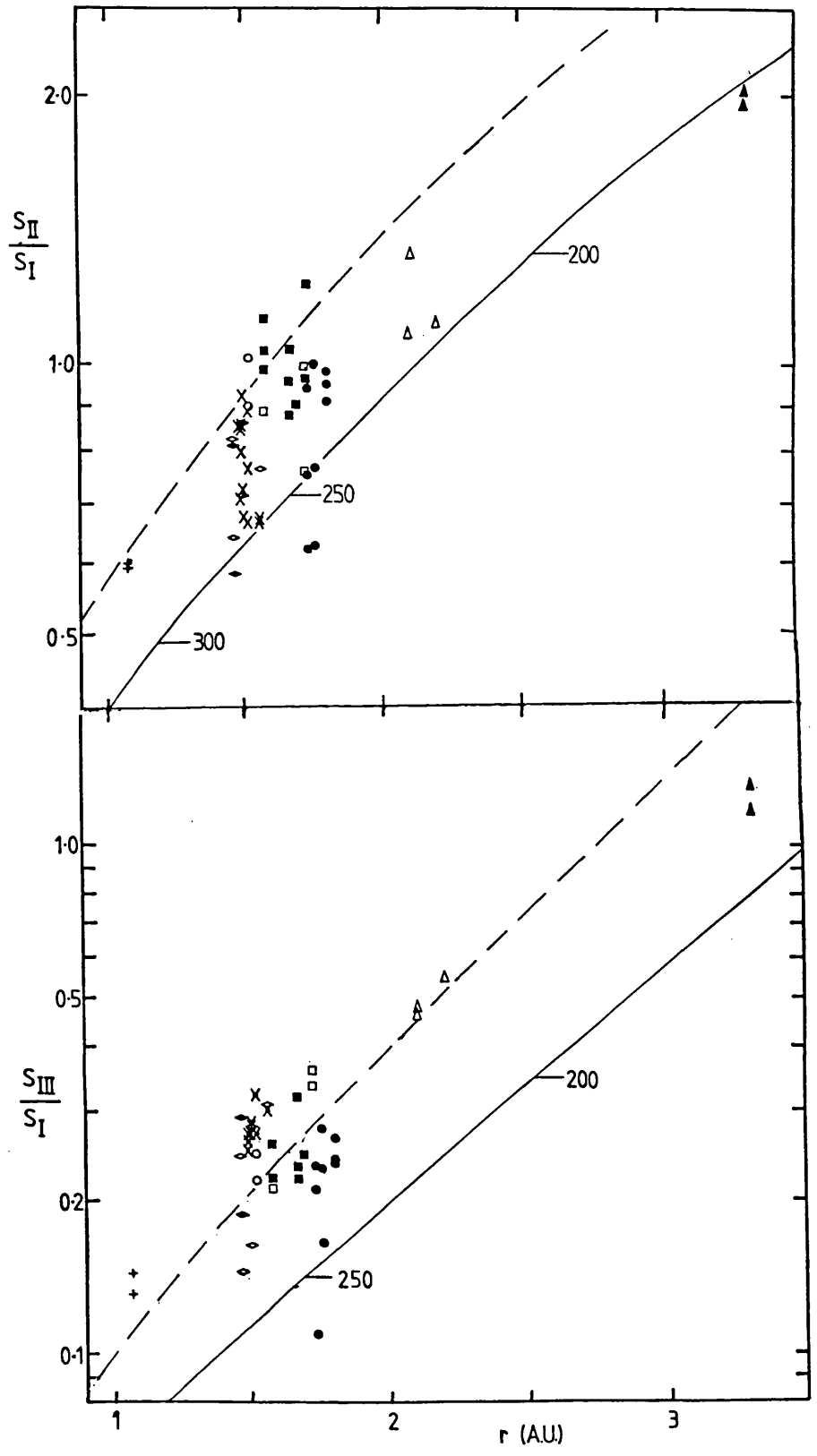


Fig 5.25 In-band colours vs. heliocentric distance for comets observed by IRAS. Symbols as in Fig. 5.24. The dashed curves show equilibrium blackbody temperatures, solid curves show mean temperatures for previously observed comets (Eaton 1984).

TABLE 5.15

Temperatures of comets observed by IRAS.

| Comet | N | r (A.U.) | Δ (A.U.) | $T_{bb}$ (k) | $T_{pred}$ (k) | $T_{obs}$ (K) | $T_{corr}$ (K) | Aperture ($10^3$ km) | M ($10^6$ kg) |
|---|---|---|---|---|---|---|---|---|---|
| P/IRAS 1983d | 2 | 1.083 | 0.394 | 266 | 315 | 270+10 | 315+10 | 77x13 | 2.3 |
| IRAS 1983f | 2 | 2.114 | 1.767 | 191 | 221 | 203-20 | 225-20 | 346x58 | 6.8 |
| (1) | 4 | 2.212 | 2.059 | 186 | 216 | 207 30 | 232 30 | 403x67 | 5.4 |
| P/IRAS 1983j | 3 | 1.808 | 1.552 | 206 | 240 | 222 15 | 250 15 | 304x51 | 6.1 |
| | 3 | 1.761 | 1.372 | 209 | 244 | 240 15 | 274 15 | 269x45 | 8.5 |
| | 3 | 1.738 | 1.259 | 210 | 245 | 243 15 | 277 15 | 247x41 | 4.6 |
| IRAS 1983k (0) | 2 | 2.538 | 2.251 | 174 | 201 | | | 441x74 | 8.4 |
| (0) | 2 | 2.577 | 2.478 | 173 | 199 | | | 485x81 | 8.6 |
| IRAS 1983o (0) | 2 | 2.652 | 2.429 | 170 | 196 | | | 476x79 | 8.8 |
| (0) | 2 | 2.465 | 2.728 | 176 | 204 | | | 534x89 | 10 |
| P/Hartley-IRAS 1983v | 2 | 1.523 | 1.135 | 224 | 263 | 222 15 | 250 15 | 222x37 | 27 |
| Cernis 1983l | 2 | 3.323 | 3.037 | 152 | 174 | 171 10 | 186 10 | 595x99 | 26 |
| P/Kopff | 1 | 1.577 | 0.946 | 221 | 258 | 227 10 | 258 10 | 185x31 | 18 |
| | 2 | 1.724 | 1.520 | 211 | 247 | 230 10 | 261 10 | 297x50 | 12 |
| P/Pons-Winnecke | 3 | 1.577 | 1.248 | 221 | 258 | 213 15 | 239 15 | 244x41 | 3.1 |
| | 3 | 1.670 | 1.242 | 214 | 251 | 221 15 | 249 15 | 243x41 | 2.8 |
| | 1 | 1.693 | 1.240 | 213 | 249 | 226 20 | 256 20 | 243x41 | 2.2 |
| | 2 | 1.732 | 1.237 | 210 | 246 | 211 20 | 237 20 | 242x40 | 2.6 |
| P/Tempel-1 | 3 | 1.492 | 0.796 | 227 | 266 | 240 10 | 274 10 | 191x32 | 9.5 |
| | 5 | 1.503 | 1.061 | 226 | 265 | 238 10 | 271 10 | 208x35 | 9.6 |
| | 3 | 1.522 | 1.147 | 225 | 263 | 241 10 | 275 10 | 225x37 | 9.0 |
| | 2 | 1.561 | 1.265 | 222 | 260 | 257 10 | 288 10 | 248x41 | 7.4 |
| P/Tempel-2 | 2 | 1.466 | 1.115 | 229 | 269 | 247 10 | 281 10 | 218x36 | 11 |
| | 2 | 1.503 | 1.093 | 226 | 265 | 239 10 | 273 10 | 214x36 | 10 |
| | 1 | 1.562 | 1.065 | 222 | 260 | 222*20 | | | |

N is the number of observations. ( ) is the number of band I detections if different.

$T_{bb}=277r^{-1/2}$ is the equilibrium blackbody temperature. $T_{pred}=329r^{-0.53}$ is the best fit temperature to previous observations. (Eaton 1984). $T_{obs}$ is the colour temperature from IRAS observetions (see Appendix C). $T_{corr}$ is the colour temperature after correction to "standard model calibration (see section 5.3.1). * confusion with a confirmed source.

observed colour temperatures depend on the number of detections, brightness and temperature of the comet. On average, the colour temperatures are lower than $T_{pred}$. If the fluxes are corrected to "standard model calibration" (section 5.3.1), and the in-band colours recomputed, a colour temperature $T_{corr}$ is obtained. These values (with the exception of P/IRAS 1983j) give a much better fit to the predicted temperatures, providing further evidence for the belief that the corrections to "standard model calibration" are mainly due to calibration errors.

Table 5.15 also shows the aperture size at the comet and computed grain masses calculated using $T_{corr}$. It is not possible to calculate the mass loss rates for these comets, since they do not in general fill the aperture (typical coma diameters are $10^4$-$10^6$km). From Fig. 5.22, it is clear that the angular size of comet IRAS-Araki-Alcock was larger than the detector size. Assuming an effective aperture corresponding to 20000km, a mass loss rate of $\sim$50kg.sec$^{-1}$ is derived for the FMO detections.

The derived temperature of P/IRAS-Araki-Alcock of 315K agrees with the predicted value, unlike the results obtained from additional observations by Walker et al. (1984), who found T=254K for r=1.01A.U. ($T_{pred}$=327K). Ground-based infrared observations (Brown et al., 1983) showed a temperature of 325-335K, and optical observations (A'Hearn and Millis, 1984) implied a much lower dust production rate than the 130kg.sec$^{-1}$ quoted by Walker et al. There is no obvious explanation to account for this discrepancy.

The observed masses are a function of the intrinsic infrared brightness of the comets. For example, comet Cernis

(with an $H_{10}$ of $\sim 3^m.5$) and P/Kopff (H=2.9, n=10.4) were both intrinsically bright, while P/Pons-Winnecke ($H_{10}$=10) was relatively faint. It is not possible to infer anything about the gas to dust ratios for these comets because of the large uncertainties in the dust masses, in most cases the visual magnitudes were not well defined and several of the comets exhibited outbursts of 1 magnitude or more.

5.7.3 The Infrared Tail of P/Tempel-2.

During the period 12-18 July, the FMO software detected about 50 faint, seconds-confirmed sources, having S/N$\sim$5 in band II, which appeared to be related to comet Tempel-2. Fig. 5.26 shows the detections together with the position of the Tempel-2 nucleus at the times corresponding to their detection. With the $\sim 1^\circ day^{-1}$ progression of the IRAS scan, several days were required to build up a full picture of these features. That they represented sections through a continuous tail was verified during the weeks-confirming survey scans (22-27 July). These showed detections in a similar sequence relative to the comet. An examination of the raw data subsequently indicated that the tail was recorded by all band II detectors across the focal plane (Fig. 5.27). Only the most sensitive of these registered S/N greater than the PAF processing threshold. The width of the tail was $\sim$4arcmin., although its angular length was $\sim 10^\circ$. The position of the tail was passed to ground observers (as FMO alerts 337-1 and 345-1, Appendix B), but no optical detection was reported. No similar features were observed for the other comets detected by the FMO program.

At the time of observation, the Earth was close to the

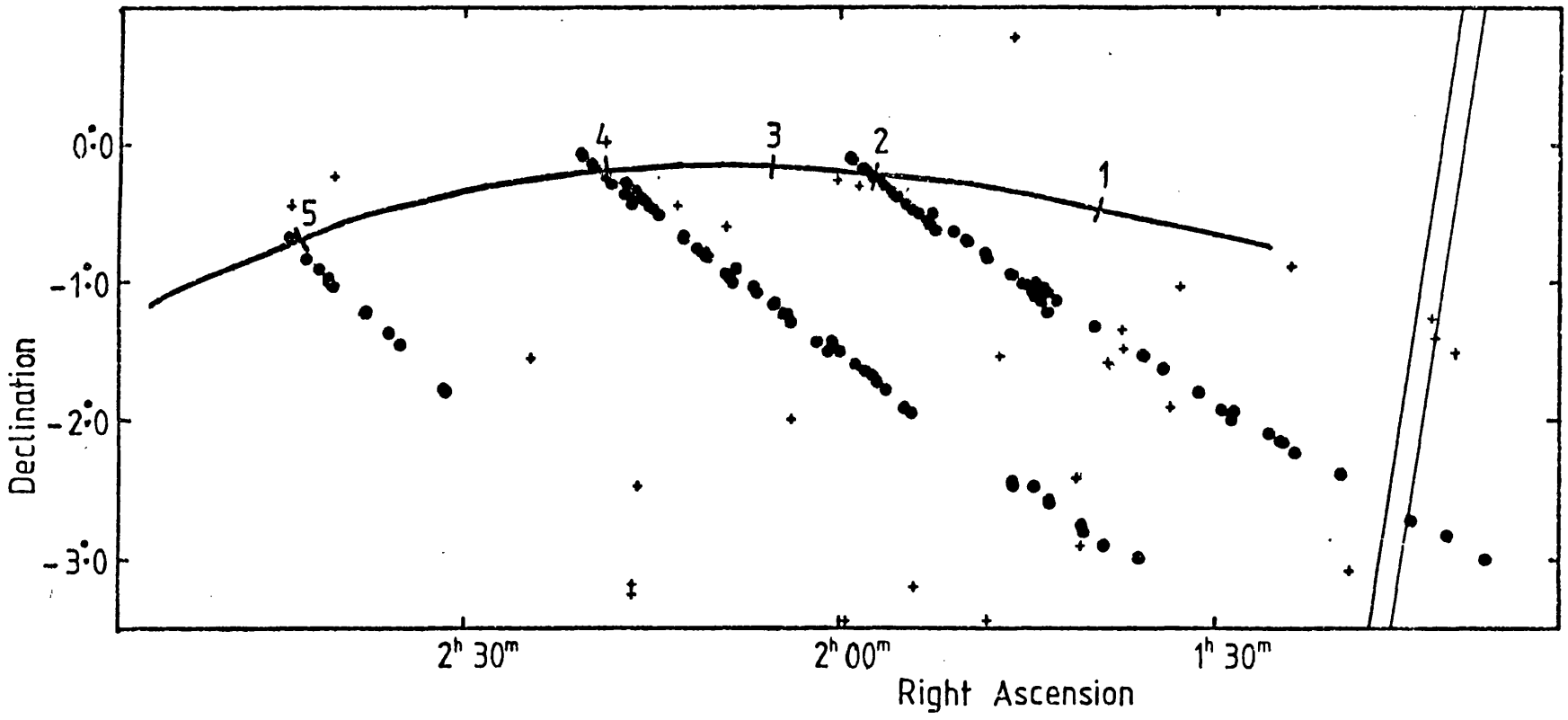


Fig. 5.26 Positions of non-hours-confirmed sources detected 10-17 July, 21-27 July and 8-9 August 1983. (o) Detections of the tail of comet Tempel-2; (+) other sources. Positions of the comet on (1) 10 July, (2) 17 July, (3) 21 July, (4) 27 July, (5) 9 August, are marked along its track. A single IRAS scan track is shown at the right hand side of the diagram.

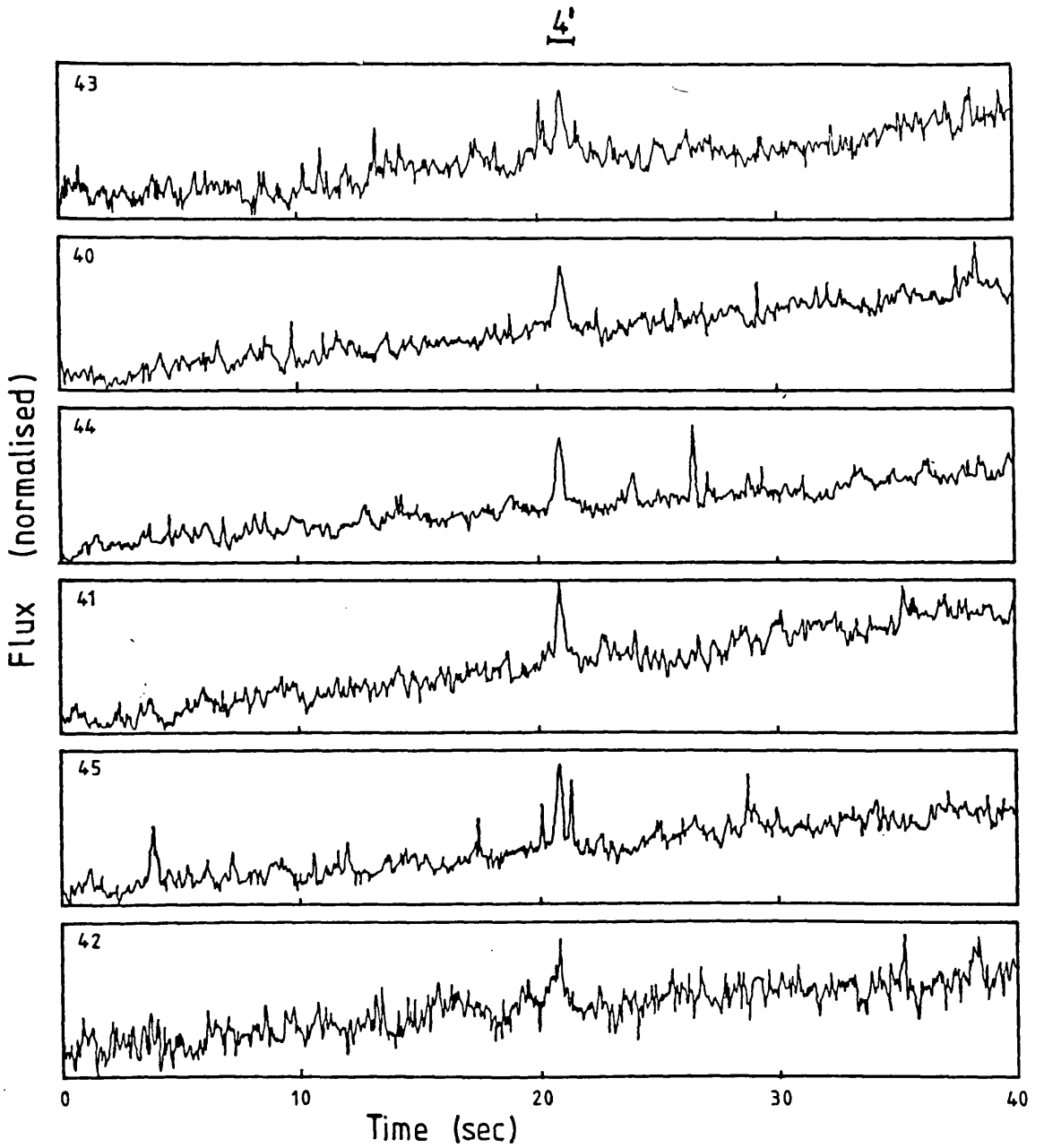


Fig. 5.27 Raw data from a row of band II detectors. The infrared tail of P/Tempel-2 is the peak at the centre of the diagram.

orbital plane of the comet, and passed through the plane on the 22 July. The position of the tail, assuming it to be in the plane of the comet orbit, can be found by transforming the sky coordinates (right ascension and declination) into cometocentric coordinates using the equations defined by Finson and Probstein (1968a, appendix B). The cometocentric coordinate system is defined as having the comet nucleus at the origin and an axis $\xi$ pointing radially away from the Sun. An orthogonal axis $\eta$ points in the direction opposite to the comet's motion. A third axis $\zeta$ measures distance from the orbit plane, forming a right-hand set.

In Fig. 5.28 are plotted the positions of the tail elements for the first set of IRAS detections, assuming the tail lies in the orbit plane ($\zeta$=0). The position of the Sun and Earth in these coordinates for the date JD 2445530.0 (14 July 1983) are (-1.458,0,0) and (-0.805,0.780,-0.031), respectively. Although the Earth was close to the orbit plane, the scatter of the points after transformation is quite small, and the tail still appears as a very narrow feature. This implies that the narrowness of the tail as seen on the sky is not due to viewing dust spread out in the orbit plane almost edge on. This conclusion was confirmed by repeating the transformation for the second and third set of tail positions. During the second set, the Earth passed through the comet orbit plane, and the third set was seen from the side opposite to the first set, and yet the derived cometocentric coordinates still show a very narrow tail at the same position angle with respect to the nucleus.

Dynamical analysis of cometary dust tails, as defined by Finson and Probstein (1968a), uses integration of syndynes or

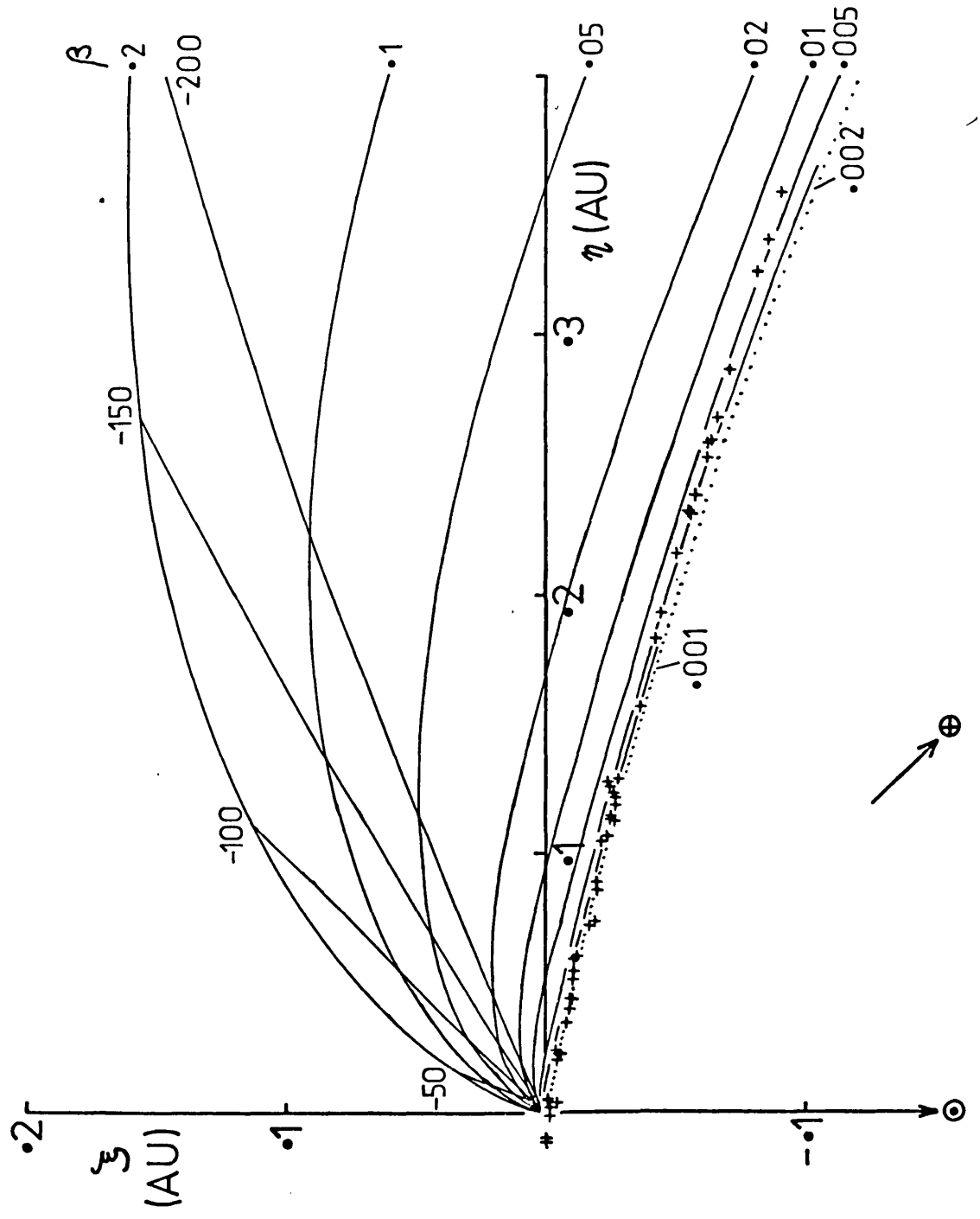


Fig. 5.28 The crosses indicate the observed tail elements of comet Tempel-2 in the plane of the orbit. The curved lines show the syndynes for a range of values of β from 0.2 to 0.001. The synchrones are shown for release dates 50, 100, 150 and 200 days prior to the observation; further synchrones have been omitted for the sake of clarity. The orbital path of the comet is indicated by the dotted line. The direction of the Earth at the time of the observation is also indicated.

synchrones to match the observed dust distribution with a model. For a given time of observation, a syndyne is defined as the locus in cometocentric coordinates of similar sized particles (rigorously, particles experiencing the same accelerative force due to radiation pressure) released from the nucleus with zero initial relative velocity at different times in the past. A synchrone is defined as the locus in cometocentric coordinates of different sized particles having the same release date. Syndynes appear as curves, emanating from the origin in a direction radially away from the Sun. Synchrones appear as almost straight lines having initial tail angles significantly non-radial, and whose position angle increases with increasing time since release. Fig. 5.28 shows the syndynes and synchrones for Tempel-2 on JD2445530.0 (Eaton et al., 1984). The theoretical dust orbits were calculated using Keplerian orbit theory for dust particles experiencing a reduced gravitational force, where $\beta$ defines the ratio of the radiation pressure to gravitational forces. The dimensional parameter $\beta$ is given by Sekanina (1980) as

$$\beta = 0.585 \times 10^{-3} \, Q_{pr} / \varrho a \ \mathrm{kg.m^{-2}}$$

where $Q_{pr}$ is the integrated efficiency factor for radiation pressure, $\varrho$ is the particle density ($\mathrm{kg.m^{-2}}$) and a is the particle radius (m). The value of $\beta$ is inversely proportional to the particle size and density, thus the smaller and less dense particles are blown furthest and most quickly away from the nucleus. In Fig. 5.28 the syndynes are plotted for a range of values of $\beta$ from 0.2 to 0.001. The synchrones have been terminated for release dates 2000 days prior to observation for $\beta$=0.001 and 0.002. For very small

values of $\beta$, the syndynes crowd closely together and become parallel to the orbit path of the comet. This is because a small increase in the radial distance, due to radiation pressure, will result in a significant orbital lag over long periods. For very large particles and infinite time, the syndynes (for zero initial relative velocity) will lie along the orbital path. In this limiting direction, since the syndynes for these slow-moving particles are parallel to each other, the synchrones must also lie in the same direction. This means that it is impossible to distinguish between particle size/density and time of release for grains lying along this line. Fig. 5.28 shows that the positions of the tail elements observed by IRAS lie close to this large particle asymptote. Hence the particles must have small accelerations and result from "old" emissions. The extreme tail element has $\beta<0.01$ and would take >1500 days to reach its present position. For reasonable values of $Q_{pr}$ ($\sim$1), and $\varrho$ ($\sim$2000), the particles must be in the sub-millimetre range or larger.

The narrowness of the tail implies a velocity dispersion of less than 2 $m.sec^{-1}$, which is of the order of the escape velocity for a kilometre-sized object and is much less than has been used to model comet dust tails (Finson and Probstein, 1968b), or meteor streams (Fox et al., 1983).

Neither the Poynting-Robertson effect, nor perturbations by Jupiter affect the stability of the tail over a few revolutions (Eaton et al., 1984).

A rough estimate of the dust mass in the tail can be gained from the IRAS detections. The peak flux over most of the length of the tail was $\sim$PAF threshold, i.e. $\sim 2 \times 10^{-15}$

$W.m^{-2}\mu m^{-1}$ at 25μm. The flux distribution across the tail can be approximated by a square profile 2arcmin. wide at $10^{-15}$ $W.m^{-2}\mu m^{-1}$. Since the tail was $\sim 10^{\circ}$ long and the band II detectors (which were aligned parallel to the tail) are 4.5x0.75arcmin., the total flux from the tail was $\sim 4x10^{-13}$ $W.m^{-2}\mu m^{-1}$. For $\beta \leq 0.005$, the grain radii are $>5x10^{-5}$ m (assuming $\rho=2000$ and $Q^{pr}=1$). The grains are considerably larger than the wavelength of peak emission, so they can be assumed to be at equilibrium blackbody temperature for r=1.5A.U. With $\Delta=1.0$A.U., the effective emitting area in the tail is $\sim 3x10^{10} m^2$. The grain mass is therefore $\sim a.2x10^{14}$ kg. A lower limit to the grain mass is therefore $\sim 10^{10}$kg. This is $\sim$1000 times larger than the dust mass of the coma (Table 5.15) but cannot be seen in the optical because the mass is contained in larger grains with a lower number density. Taking a typical mass loss rate for a periodic comet at 1.5A.U. of $50kg.sec^{-1}$, the observed tail would take a minimum of $\sim$2000 days to form; a figure which is in good agreement with the "dynamical age" of the tail.

## 5.8 UNIDENTIFIED FMO'S

Of the 38 alerts sent to cooperating observatories for ground-based confirmation, 17 were not searched for. Of the remainder, four FMO's were not positively identified with any object. In addition, four other candidate objects were found during post-mission analysis. Details of all the alerts sent are given in appendix B.

In order to determine how many of these sources were

possible detections of comets or asteroids, the raw data were examined. Nine candidates were found to contain at least one detection which was a "spike" in the band II background, just above the PAF processing threshold. The remainder were classed as possible asteroids or comets depending on whether there was a slight extension in the raw data flux profiles.

At least some of the possible asteroids may have been separate detections of different main belt asteroids which were closely aligned. This was probably the case with 315-2 which was observed by the UK Schmidt as a main belt asteroid (1983NH). However, the motions were not consistent with the IRAS positions, and it was not subsequently recovered. Alert 415-1 consisted of three detections, any two of which may have been related. One of the sources appeared close to a faint numbered asteroid and the other sources appeared to be just noise.

363-1 was observed as a possible Apollo asteroid at Palomar, but poor conditions prevented recovery. Examination of the raw data indicated that only one detection of the pair was "real".

478-1 was found to be close to the position of the newly discovered comet Kowal-Vavrova 1983t, but the motions were not consistent. Also the comet was moving at just below the motion threshold for hours confirmation and was at visual magnitude 18.

487-1 was found as a series of five detections moving extremely rapidly. Unfortunately, the alerts arrived too late for confirmation, but the orbital elements fitted to the IRAS observations by Marsden (personal communication) showed it to be an Apollo object, which was subsequently designated

1983SN.

Two unidentified single detections which had asteroidal colours were also sent as alerts (458-1 and 576-2). The former appeared as an unidentified fixed source in the IRAS point source catalogue, so its presence in the non-hours-confirmed data was probably due to confusion. The nature of 576-2 remains undetermined.

Analysis of the unobserved FMO alerts indicates that only ~50-70% of the real objects observed by IRAS were optically confirmed.

# CHAPTER 6

# IRAS ADDITIONAL OBSERVATIONS

## 6.1 THE AO PROGRAM

The primary aim of the IRAS mission was to produce an all-sky survey in the four wavelength bands 12-100μm. In addition, extra observations were made of regions and objects of special interest. The survey occupied about 60% of the available observation time (usually the best 9 orbits out of the 14 available each day). The remaining time which was not affected by the SAA was used for calibration, in-flight testing and the additional observation (AO) program. About 10% of the AO time was made available to UK astronomers. The AO's, which used either the chopped photometric channel (CPC) or the survey detectors, allowed observations to be made with higher sensitivity (by repeating scans) and better resolution (by displaced rastering).

A consortium of UK astronomers interested in the study of asteroids was awarded 10 AO units in the first round of applications, and a further 7 units after the first two hours confirmation of the sky were complete.

Accepted AO observations were scheduled by entering each individual observation into a file which was then searched by programs which selected the most efficient combination of objects to utilise the available observation time. In practice, this meant that observations of asteroids were difficult to schedule for two reasons. Firstly, since the asteroids moved, each observation had to be entered individually for a given observation opportunity. Secondly, because of the polar orbit and scan strategy, the survey occupied the majority of the time when the satellite was pointing towards the ecliptic, so observations of objects

near the ecliptic plane were very difficult to schedule. This meant that even though there were personnel present at PAF throughout the mission who could search for observation opportunities, it was not possible to schedule time for the prime targets originally selected. Table 6.1 summarises the observations actually obtained.

TABLE 6.1

Asteroid additional observations.

| Asteroid | Date | SOP | MACRO | Comments |
|---|---|---|---|---|
| 40 Harmonia | Apr 4 | 199 | DPS52B | Observations at |
| | Sep 11 | 518 | DPS60D | opposite phase. |
| 44 Nysa | Aug 13 | 401 | DPS60D | Lightcurve coverage |
| | 14 | 402 | DPS60D | of well observed |
| | 14 | 403 | DPS60D | asteroid. |
| | 14 | 403 | DPS60D | Preliminary data |
| | 15 | 405 | DPS60D | received. |
| | 15 | 405 | DPS60D | |
| 1620 Geographos | Mar 21 | 111 | DPS02B | Small asteroid at |
| | 21 | 111 | DPS02B | large phase angle. (+ obs. by US science team.) |
| 2131 Mayall | Sep 22 | 539 | DPS61D | Small, high inclination asteroid. Repeat observation not scheduled. |

The available AO macros, which specified the number of rasters, possible offsets and scan tracks, changed during the mission as more was learnt about the performance of the detector system. Table 6.2 gives the details for macros chosen for the asteroid observations.

The AO processing was undertaken at JPL. The first run through the data (up to SOP 600) was completed by April 1984, under what is now referred to as "old" operations. Due to various problems, the data up to SOP 446, and possibly up to

TABLE 6.2

Macros used for additional observations.

| MACRO | Length of scan (arcmin) | Cross-scan step (arcmin) | Number of raster legs | Central detector |
|---|---|---|---|---|
| DPS02B | 92.4 | 0.3 | 6 | 0+ or 37 |
| DPS52B | 92.4 | 0.0 | 6 | 0 or 37 |
| DPS60D | 52.0 | 0.4 | 5 | 37 |
| DPS61D | 52.0 | 0.4 | 10 + 5* | 37 |

+ Central track.
* 2 interleaved raster scans.

SOP 600 are being processed under "new" operations. At the date of writing, only "old" data have been received for 44 Nysa. The data are obtained on tape with a hard-copy summary. The data are in the form of 2-D grids which have been de-striped, flat-fielded and calibrated in one of two modes: INTN, unfiltered data with intensities in $W.m^{-2}.Sr^{-1}$; FLUX, point source filtered with fluxes in $W.m^{-2}$. Noise maps are also produced for each mode. The hard copy summary contains information on detector performances and individual sources identified in the data.

## 6.2 44 NYSA

### 6.2.1 Introduction

Seven observations of 44 Nysa were made between 13 and 15 August 1983. Nysa is an E-type asteroid with high albedo and a large amplitude lightcurve. The lightcurve has been extensively observed, allowing determination of the pole

position (McCheyne, 1985). A V lightcurve was obtained in October 1983 using the People's Photometer on the 20" telescope at SAAO, and BVJK lightcurves were observed in November 1983 using the Leicester optical/infrared photometer on the 1.5m telescope of the Observatorio del Teide, Tenerife. No colour variations larger than $0^m.01$ were observed, indicating a relatively homogeneous surface. A third lightcurve (Di Martino, personal communication) was obtained in October 1983. These data, when combined with those from previous apparitions, produced ecliptic coordinates of the rotation axis ($290^\circ \pm 10^\circ, 65^\circ \pm 10^\circ$) with axial ratios $\sim$3:2:1 (McCheyne, 1985).

When the IRAS maps were examined, another moving source was found, which was identified as the asteroid 384 Burdigala. This has been classified as an S-type on the basis of UBV colours alone. This fortuitous coincidence has allowed a comparison of the IRAS data from the two asteroids. The aspect data for all the observations are summarised in Table 6.3.

## 6.2.2 Observations.

The asteroid detections were identified in each map from the point sources summarised in the hard copy output. The data from the FLUX and noise maps for the region surrounding each detection were extracted, and the peak fluxes identified. Monochromatic fluxes were calculated as described in appendix C, and are given in Table 6.4. A correction of +10% has been applied to the band I data obtained before SOP 404 (points 1-5) to bring it into line with the calibration applied to subsequent data (IRAS

TABLE 6.3

Aspect data.

| | Date 1983 | r (A.U.) | Δ (A.U.) | α (deg) | δdays | δλ (deg) | motion (deg/day) | $P_{syn}$ (days) | δΔ (A.U.) | Travel time (phase) |
|---|---|---|---|---|---|---|---|---|---|---|
| 44 Nysa | | | | | | | | | | |
| IRAS | Aug 14 | 2.427 | 1.990 | 23.8 | | | | | | |
| SAAO | Oct 4 | 2.343 | 1.405 | 11.0 | 51 | 1.1 | 0.0220 | 0.267584 | 0.5855 | 0.0126 |
| Di Martino | Oct 11 | 2.332 | 1.368 | 8.3 | 58 | 0.0 | 0.0000 | 0.267581 | 0.6214 | 0.0134 |
| Tenerife | Nov 28 | 2.247 | 1.407 | 16.8 | 106 | -10.5 | -0.0986 | 0.267569 | 0.5826 | 0.0126 |
| 384 Burdigala. | | | | | | | | | | |
| IRAS | Aug 14 | 2.458 | 2.003 | 23.2 | | | | | | |

Newsheet - Additional observations, R.E. Jennings, 6/11/85).

Calculating the rotational phase of observations separated by many weeks is not a simple matter of counting sidereal periods. The observed synodic rotation period of the asteroid is dependent on its motion across the sky. For 44 Nysa the relation is linear, with a slope of $0.00012 day.deg^{-1}$ (Taylor and Tedesco, 1983). The synodic period is equal to the sidereal period when the observed motion is zero. When counting periods over intervals exceeding several weeks, it is necessary to calculate the mean synodic period from the mean motion. The dates in Table 6.3 are convenient zero points ($0^h$ on the date given) from which to calculate the motions and, hence, the synodic periods. It is also necessary to correct for the change in light-travel time (Earth-asteroid distance), since this changes by $\sim 0.01$ of a period between the IRAS observations and the visible lightcurves. After applying these corrections, the lightcurve data have been individually folded with the sidereal period of 0.267581 days (Taylor and Tedesco, 1983) and the phases of the IRAS observations calculated.

6.2.3 Discussion.

Figs. 6.1 and 6.2 show the folded IRAS and lightcurve data for 44 Nysa. The 25 and 60μm data follow the lightcurve most accurately, with good agreement between data obtained at the same rotational phase. The 12 and 100μm data show considerable scatter about the lightcurve and poor consistency. This is probably due, in the former case, to noisy detectors in band I, and in the latter case, to the low

TABLE 6.4

IRAS fluxes for 44 Nysa and 384 Burdigala.

| | | | Fluxes ($W.m^{-2}\mu m^{-1} x10^{15}$) + errors (%) | | | | | | | |
|---|---|---|---|---|---|---|---|---|---|---|
| | Date | Phase | 12μm | | 25μm | | 60μm | | 100μm | |
| 44 Nysa | $T_{eff}$=231 | | | | | | | | | |
| 1 | 2445560.9361 | 1.623 | (49.9) | 48.8 7 | 30.3 | 5 | 2.96 | 6 | 0.791 | 5 |
| 2 | 2445561.6490 | 4.294 | (63.8) | 58.0 6 | 31.9 | 5 | 2.93 | 4 | 0.701 | 5 |
| 3 | 2445561.7963 | 4.845 | (58.1) | 52.8 13 | 33.2 | 4 | 3.02 | 9 | 0.659 | 12 |
| 4 | 2445561.8675 | 5.111 | (75.5) | 68.6 4 | 36.5 | 4 | 3.38 | 8 | 0.716 | 7 |
| 5 | 2445561.9379 | 5.374 | (72.7) | 66.1 7 | 38.3 | 4 | 3.39 | 8 | 0.708 | 8 |
| 6 | 2445562.8695 | 8.856 | 77.4 | 3 | 35.5 | 5 | 3.01 | 9 | 0.744 | 9 |
| 7 | 2445562.9398 | 9.119 | 81.1 | 4 | 36.8 | 5 | 3.34 | 6 | 0.967 | 7 |
| Mean | | | 68.4 | 3 | 34.6 | 2 | 3.15 | 3 | 0.755 | 3 |
| 384 Burdigala | $T_{eff}$=230 | | | | | | | | | |
| 1 | 2445560.9361 | | (20.5) | 18.6 6 | 8.06 | 6 | 0.70 | 5 | 0.09 | 60 |
| 2 | 2445561.6490 | | (20.5) | 18.6 8 | 8.61 | 5 | 0.60 | 11 | 0.18 | 30 |
| 3 | 2445561.7963 | | (21.8) | 19.8 4 | 7.95 | 16 | 0.78 | 16 | 0.12 | 47 |
| 4 | 2445561.8675 | | (20.6) | 18.7 7 | 8.03 | 6 | 0.71 | 6 | 0.12 | 48 |
| 5 | 2445561.9379 | | (20.9) | 19.0 4 | 8.95 | 5 | 0.82 | 9 | | |
| 6 | 2445562.8695 | | 27.7 | 4 | 12.00 | 5 | 1.03 | 6 | 0.16 | 36 |
| 7 | 2445562.9398 | | 27.3 | 5 | 9.90 | 13 | 0.97 | 7 | 0.20 | 27 |
| Mean | | | 22.8 | 2 | 9.07 | 3 | 0.80 | 3 | 0.14 | 17 |

Values in brackets do not have 10% correction for data processed before SOP 404
Quoted errors are statistical uncertainties in observed data only.

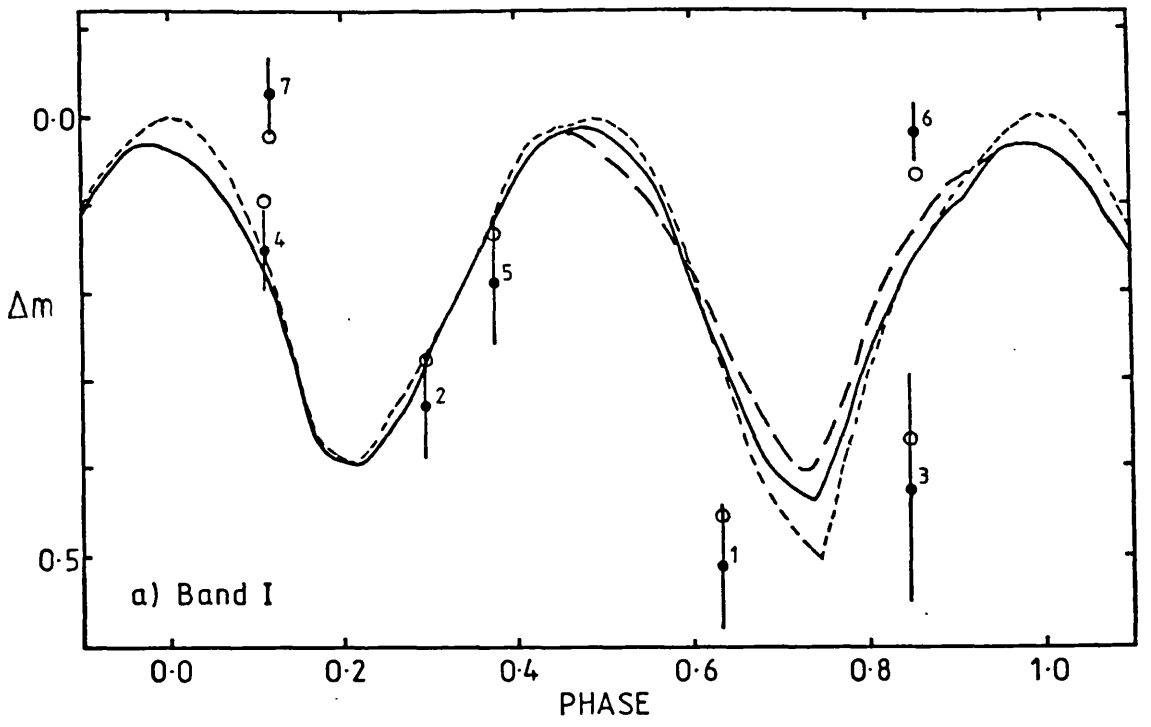


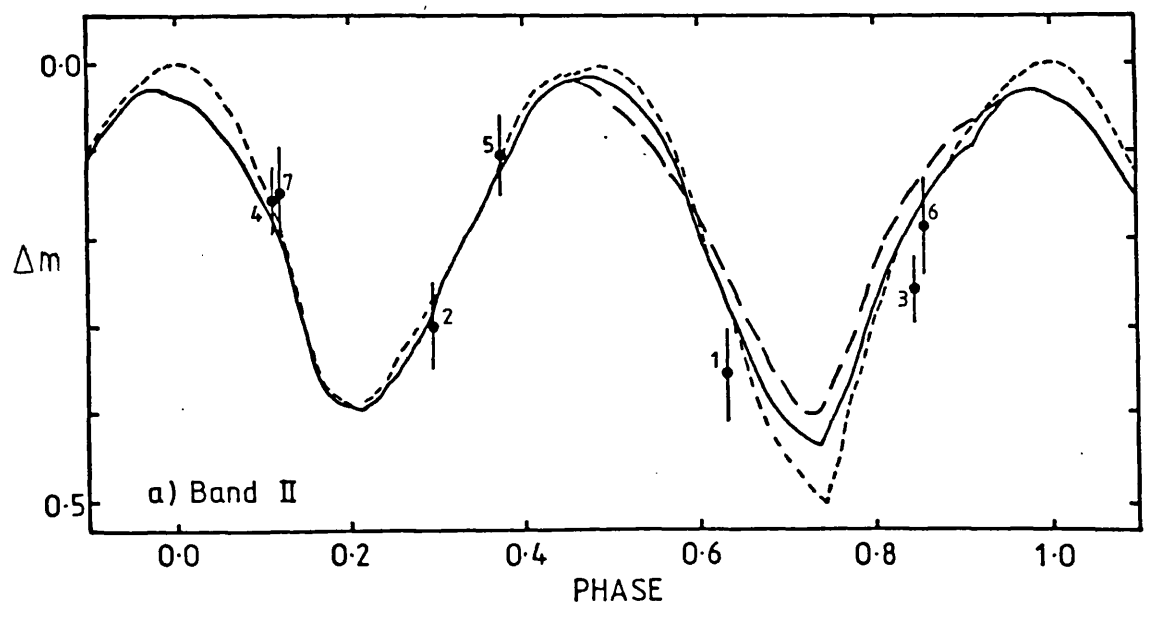


Fig. 6.1 IRAS data for 44 Nysa a) 12μm, b) 25μm, fitted to the visible lightcurve data: solid line, SAAO; long broken line, Di Martino; short broken line, Tenerife. Open circles for 12μm data have +10% correction applied to pre-SOP 404 data (see Table 6.3).

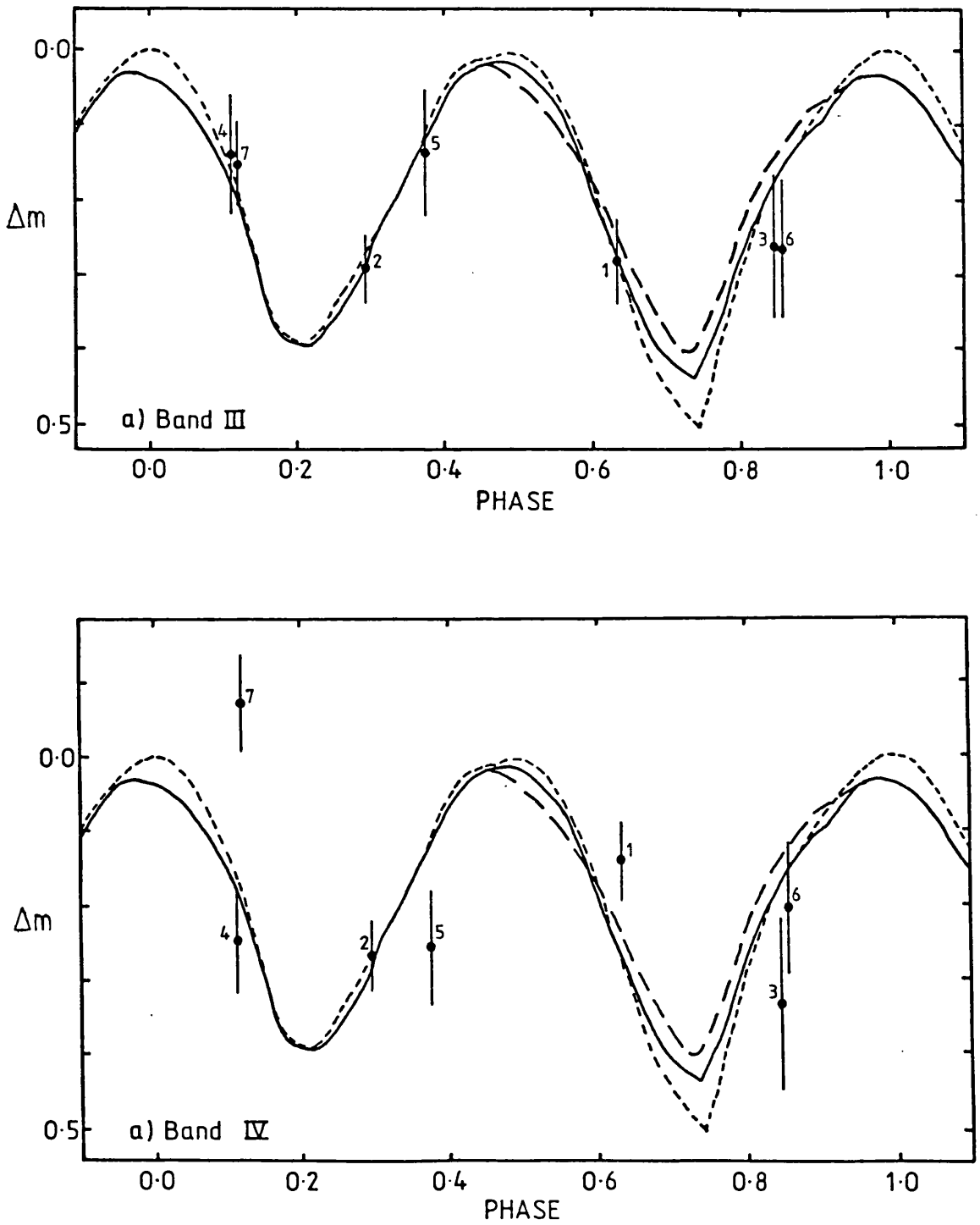


Fig. 6.2 As Fig. 6.1 but for a) 60μm and b) 100μm.

signal at 100μm. The corrected values for band I provide a better fit to the lightcurve and have been used in all subsequent model fitting. Phase shifts between the thermal and visual lightcurves might be expected since the phase dependences are different. The optical lightcurve depends only on the illuminated area which is visible, while the infrared curve depends on the whole cross-sectional area of the asteroid. For the Nysa observations at phase $<30^{o}$, any expected phase differences would be small and undetectable due to the limited phase coverage and accuracy of the photometry.

Nysa has a diameter of 69km and visual geometric albedo of 0.48 derived from radiometric data (Morrison and Zellner, 1979). The uncertainties in these values are probably $\pm$10% and $\pm$20% respectively. Because of the high albedo, the IRAS measurements alone are not sufficient to determine an accurate independent diameter (sections 3.2 and 3.3). No optical ground-based observations were made at the same time, so a range of models have been fitted to the IRAS data. These are given in Table 6.5. Initially, the catalogued albedo and usual model parameters (section 3.3) of $q=0.6$, $\beta=0.9$, $\varepsilon=0.9$ and $\gamma_N=0.01 mag.deg^{-1}$ were employed. The standard model was fitted to the mean 25μm data to derive a diameter. Data from the other bands were then ratioed with the predicted model fluxes.

The standard model fits the data reasonably well, except at 100μm. This is surprising, since the calibration transfer between 60 and 100μm was made using observations of a number of main-belt asteroids. One possibility is that there are errors in the bandwidths and colour corrections used to

TABLE 6.5

Thermal model fits to 44 Nysa data.

| | $T_{max}$ (K) | f | Diameter from 25μm fit (km) | Observed:Model flux ratios 12μm | 25μm | 60μm | 100μm |
|---|---|---|---|---|---|---|---|
| Standard model | 245 | 0 | 75 | 0.87 | 1.0 | 1.13 | 1.63 |
| Best fit standard model | 233 | 0 | 81 | 1.00 | 1.0 | 1.06 | 1.51 |
| Modified projected model $p_v$=0.48 | 233 | 0.49 | 75 | 1.00 | 1.0 | 1.05 | 1.47 |
| modified projected model $p_v$=0.48 | 225 | 0.60 | 79 | 1.11 | 1.0 | 1.00 | 1.39 |

produce the monochromatic fluxes. However, unless the filter responses given by Neugebauer et al., (1984) are considerably in error, this effect should be, at most, 10%, and probably much smaller. It is interesting to note how the corrections to fit the standard model to the AO data compare with those required for the survey data processed at PAF (section 5.3.1). The values are x0.98, x0.85, x0.75 and x0.52 for bands I-IV respectively, compared with the PAF data corrections to "standard model calibration" of x1.05, x0.79, x0.65 and x0.66. Despite the calibration methods being different for the two data sets, the trend is similar except for band IV. Aumann and Walker (1984) also found a consistent pattern for the differences between the standard model and IRAS data.

Table 6.5 also gives the "best fit" standard model to the 12 and 25μm data by treating the maximum surface temperature $T_{max}=[S_o(1-qp_v)/r^2\varepsilon\sigma\beta]^{1/4}$ as a free parameter.

This results in a reasonable fit to the 60μm, but not the 100μm data. However, the derived diameter is larger than that obtained from ground-based observations, and a correction of over 20% is required to the quantity $(1-qp_v)/\varepsilon\sigma\beta$. The excess 100μm flux cannot be explained by emission from the dark side, since a modified projected model fitted to the 25 and 60μm data considerably underestimates the 100μm flux.

TABLE 6.6

Thermal model fits to 384 Burdigala data.

| | $T_{max}$ (K) | f | Diameter from 25μm fit (km) | Observed:Model flux ratios 12μm | 25μm | 60μm | 100μm |
|---|---|---|---|---|---|---|---|
| Standard model | 258 | 0 | 36 | 0.97 | 1.0 | 1.17 | 1.24 |
| Best fit standard model | 255 | 0 | 36 | 1.00 | 1.0 | 1.15 | 1.22 |
| Modified projected model | 230 | 0.65 | 39 | 1.33 | 1.0 | 1.00 | 1.03 |

The data obtained for 384 Burdigala allows a comparison between two different asteroids observed and calibrated simultaneously. No lightcurve data are available for Burdigala. The IRAS fluxes show an increase of about $0^m.3$ between the first five points and the last two. A typical albedo for S-type asteroids of 0.16 has been used in the models (Table 6.6). When the standard model is fitted to the 25μm data, the 12μm point provides a good fit, but there is a 60 and 100μm excess of ~20%. If a modified thermal model is fitted to the 60μm data, the f value obtained is rather

higher than would be expected for a regolith-covered body, and the 12μm is over-estimated, as was found for Nysa. The S/N at 100μm is hardly sufficient to determine whether Burdigala behaves in a significantly different way to Nysa.

### 6.2.4 Conclusions.

The IRAS data for 44 Nysa and 384 Burdigala agree with the standard model to within ~20% between 12 and 60μm. Derived diameters are $75\pm7$km and $36\pm4$km respectively. The differences from the model appear to be systematic and cannot be completely explained by calibration and colour correction errors or dark side emission. There is no sign of a reduction in flux from 25 to 60μm as observed by LeVan and Price (1983), but Nysa shows a 100μm excess of at least 50%. The elongated shape of Nysa could affect the temperature distribution at different phases, but it is difficult to see how it could produce a consistently high flux at 100μm. Emissivity variations with wavelength could produce the observed spectra, but a large sample of asteroids is required to examine any differences between compositional types.

# CHAPTER 7

# CONCLUSION

The classification of asteroids has been extended as new observations have provided improved data. In the last couple of years two new data sets have been obtained for a large number of asteroids. The IRAS asteroid catalogue will provide diameter and albedo data produced in a systematic manner for most of the numbered asteroids. Ground-based results for 589 minor planets have been obtained using the 8-colour photometric system specially designed to isolate diagnostic spectral features (Zellner et al., 1985a). This work has already indicated subdivisions in the accepted asteroid groups, with, for example, the new B and G-types closely related to C-types, and a new group T spectrally similar to D-types. These new types emphasise the findings from numerical taxonomy (section 2.4) that there do not appear to be rigid boundaries between types and that a range of surface properties exist. In addition, Zellner, Thurinagari and Bender (paper in preparation) have defined 18 orbital zones which they believe will adequately isolate the selection biases in survey programs of the physical properties of asteroids. Only ten asteroids had exceptional orbits which did not fall in any zone. These new data will provide useful input for numerical classification techniques which can give a good indication of the significance of defined group boundaries both in physical and orbital parameter space.

The necessity for the development of sophisticated asteroid thermal models is determined by the quality of data obtainable, and the degree of success of certain assumptions which are made in the simpler models. Ground-based

observations of large main belt asteroids can be adequately described using the standard thermal model (section 3.3). The radiometric method (section 3.2), using wide-band observations and the standard model, produces albedos and diameters in reasonable agreement with those from other methods. Variations in emissivity from the assumed value of 0.9 over the 10μm window are small, and emission features appear to be rare (section 3.4). The use of simple thermal models appears to be adequate for the removal of the emission component to allow reflectance spectra to be examined for specific mineral absorption features (section 3.6). In certain circumstances the standard model does not provide an adequate description of the thermal emission spectrum. Thermophysical models (section 3.7) provide a more realistic representation of the asteroid, but require a knowledge of the rotational properties and shape to be applied satisfactorily. In cases where these data are unknown, modifications to the standard model (section 3.5) can be used to obtain some idea of the thermal properties, diameter and albedo (section 5.6).

The wealth of IRAS data will provide an opportunity to examine the thermal properties of asteroids in relation to taxonomic type and heliocentric distance. The IRAS data obtained from the FMO survey (chapter 4) show systematic deviations from the standard model (section 5.3.1). Since these results were produced, the IRAS catalogue has been published. The explanatory supplement (Infrared Astronomical Satellite (IRAS), Catalogues and Atlases, Explanatory Supplement, (eds. C.A. Beichmann, G. Neugebauer, H.J. Habimg, P.E. Clegg, T.J. Chester) JPL D-1855) contains spectral

response curves for the IRAS detector system which differ slightly from those derived in appendix C. The corrections required to convert the monochromatic fluxes derived in this thesis to be consistent with those quoted in the IRAS catalogue are given in Table 7.1. The only significant differences are found for the band III data. The analysis of the FMO data will essentially be unchanged since all the data have been corrected to "standard model calibration" (section 5.3.1) and therefore implicitly corrected for the above errors which are not highly temperature dependent.

TABLE 7.1

Monochromatic flux corrections for errors in IRAS spectral response curves.

| Spectrum | Corrections to calculated monochromatic fluxes 12μm | 25μm | 60μm | 100μm |
|---|---|---|---|---|
| $\lambda F_\lambda$ = const | 1.02 | 1.01 | 0.97 | 0.97 |
| $T_{bb}$ = 100K | 1.04 | 1.02 | 0.93 | 0.96 |
| 200K | 1.02 | 1.01 | 0.93 | 0.99 |
| 300K | 1.02 | 1.01 | 0.93 | 0.99 |
| 400K | 1.01 | 1.00 | 0.92 | 1.00 |

Asteroids with unusual properties will be recognised by deviations from the "average" asteroid spectrum. These could then be observed at greater resolution using ground-based telescopes (as was the case for 1983TB; section 5.6). The asteroid 44 Nysa may represent one of these unusual objects, due to its apparent 100μm excess. The corrections from Table 7.1 only increase this effect, since the 60μm flux will be closer to that expected from the standard model while the 100μm flux will be unchanged. Thermal observations at a range of phase angles and wavelengths for a number of

asteroids are required for the study of shape effects and determination of the sense of rotation.

The FMO search not only resulted in the discovery of several asteroids and comets, but also provided information on the problems of extracting asteroid and comet detections from the IRAS database. The asteroid and comet discoveries were in reasonable agreement with estimates of the populations from ground-based searches (sections 5.4.1, 5.5.1, 5.7.1). However, the comets proved much brighter and more extended than expected in the infrared. The presence of an extensive dust tail for comet Tempel-2 (section 5.7.3) was completely unexpected. The sub-mm sized dust grains were ejected at a very low velocity from the comet over a considerable time. Subsequently, comet Bowell (identified in the hours-confirmed data) was found to have an infrared tail when at a heliocentric distance of over 5A.U. (Walker and Rowan-Robinson, 1984). However, this tail was closely aligned to the projection of the radius vector and was significantly extended normal to the orbit plane. This indicates a high-velocity outburst of smaller particles; a completely different origin to that of the Tempel-2 tail. Both these comets were observed when the Earth was approximately in the orbit plane of the comet. Observations of a number of comets under similar geometric conditions should be made to search for evidence for these features in the optical. P/Tempel-2 will reach perihelion again in 1988 when it will be well place for observation in the early summer, as the Earth crosses the comet's orbit plane.

From the FMO data it is clear that comets can only be

distinguished from asteroids by their extension, and about 20-30 new comets may be present in the hours-confirmed database (section 5.5.1).

The Apollo asteroid 1983TB, found in a highly eccentric orbit almost identical to that of the Geminid meteor stream, was thought to be a candidate for an extinct cometary nucleus (section 4.2). In fact it showed no cometary attributes, and ground-based observations (section 5.6) indicate a rocky surface, incompatible with the postulated structure for a cometary nucleus. The Geminid meteor stream, which consists of particles of relatively high density in comparison with other observed streams (Hughes, 1983) may have an asteroidal origin.

The asteroid and comet data catalogue which will be produced in 1986 or 1987 will contain a wealth of information on most of the numbered asteroids and some comets. In addition, there will be many thousand detections of unknown Solar System objects. A major task will be to try and link the IRAS detections with the many catalogued but unnumbered asteroids, and new discoveries. The launch of the Infrared Space Observatory (ISO) in the late 1980's or early 90's will provide a further opportunity to observe a number of interesting objects at higher sensitivity and spectral resolution.

# *REFERENCES*

A'HEARN M.F., R.L. Millis, (1984) Comet 1983d: A contrast between data from IRAS and data from the ground. Astrophys. J. 282 L43.

ALLEN D.A., (1970) The infrared diameter of Vesta. Nature 227 158.

ALLEN D.A., (1971) The method of determining infrared diameters. In "Physical Studies of Minor Planets" (ed. T. Gehrels), NASA SP-267 Washington D.C. p4.

ARNOLD J., (1969) Asteroid families and "jet streams". Astron J. 74 1235.

AUMANN H.H., R.G. Walker, (1984) IRAS observations of asteroids. Bull. Amer. Astron. Soc. 16 689. (Abstract).

BARNARD E.E., (1895) Micrometrical determinations of the diameters of the minor planets Ceres (1), Pallas (2), Juno (3) and Vesta (4),made with the filar micrometer of the 36 inch equatorial of the Lick observatory, and on the albedos of those planets. M.N.R.A.S. 56 55.

BASTIN J.A., D.O. Gough, (1969) Intermediate scale lunar roughness. Icarus 11 289.

BELTON M.J.S., H. Spinrad, P.A. Wehinger, S. Wyckoff, (1985) IAUC 4029.

BENDER D.F., (1979) Osculating orbital elements of the asteroids. In "Asteroids" (ed. T Gehrels), Univ of Arizona Press, p1014.

BOBROVNIKOFF N.T., (1929) The spectrum of minor planets. Lick Obs. Bull. XIV 18.

BORTLE J.E., (1983) Sky and Tel. 66 271.

BORTLE J.E., (1984) Sky and Tel. 67 188.

BOWELL E., K. Lumme, (1979) Colorimetry and magnitudes of

asteroids. In "Asteroids" (ed. T. Gehrels), Univ. of Arizona Press, Tucson. p132.

BOWELL E., B. Zellner, (1974) Polarisations of asteroids and satellites. In "Planets Stars and Nebulae Studied with Polarimetry" (ed. T. Gehrels), Univ. of Arizona press, Tucson, p381.

BOWELL E., C.R. Chapman, J.C. Gradie, D. Morrison, B. Zellner, (1978) Taxonomy of asteroids. Icarus 35 313.

BOWELL E., T. Gehrels, B. Zellner, (1979) Magnitudes, colors, types, and adopted diameters of the asteroids. In "Asteroids", (ed. T. Gehrels), Univ. of Arizona press, Tucson, p1108.

BROUWER D., (1951) Secular variations of the orbital elements of minor planets. Astron J. 56 9.

BROWN R.H., (1984) Ellipsoidal geometry in the standard radiometric model. Bull. Amer. Astron. Soc. 16 689. (Abstract).

BROWN R.H., D.P. Cruikshank, D. Griep, (1983) Temperature of comet IRAS-Araki-Alcock (1983d). Bull. Amer. Astron. Soc. 15 802. (Abstract).

BROWN R.H., D. Morrison, (1984) Diameters and albedos of thirty-six asteroids. Icarus 59 20.

BROWN R.H., D. Morrison, C.M. Telesco, W.E. Brunk, (1982) Calibration of the radiometric asteroid scale using occultation diameters. Icarus 52 188.

BUHL D., W.J. Welch, D.G. Rea, (1968a) Reradiation and thermal emission from illuminated craters on the lunar surface. J. Geophys. Res. 73 5281.

BUHL D., W.J. Welch, D.G. Rea, (1968b) Anomalous cooling of a cratered lunar surface. J. Geophys. Res. 73 7593.

CAMERON A.G.W., (1979) On the origin of asteroids. In "Asteroids" (ed. T. Gehrels), Univ. of Arizona Press, p992.

CAMPINS H., M.S. Hanner, (1982) Interpreting the thermal properties of cometary dust. In "Comets" (ed. L.L. Wilkening), Univ. of Arizona press, Tucson, p341.

CARUSI A., E. MASSARO, (1978) Statistics and mapping of asteroid concentrations in the proper elements' space. Astron. Astrophys. Suppl. 34 81.

CHAPMAN C.R., (1971) Surface properties of asteroids. Ph.D. Thesis, Mass. Inst. Tech.

CHAPMAN C.R., (1973) Mineralogy of the asteroid belt and relationships to meteorites. Bull. Amer. Astron. Soc. 5 388. (Abstract).

CHAPMAN C.R., (1974) Asteroid size distribution: Implications for the origin of stony-iron and iron meteorites. Geophys. Research Letters 1 341.

CHAPMAN C.R., M.J. Gaffey, (1979) Spectral reflectances of the asteroids. In "Asteroids" (ed. T. Gehrels), Univ. of Arizona press, Tucson, p1064.

CHAPMAN C.R., T.B. McCord, T.V. Johnson, (1973) Asteroid spectral reflectivities. Astron. J. 78 126.

CHAPMAN C.R., D. Morrison, B. Zellner, (1975) Surface properties of asteroids: A synthesis of polarimetry, radiometry and spectrophotometry. Icarus 25 104.

CHAPMAN C.R., J.G. Willliams, W.K. Hartmann, (1978) The asteroids. Ann. Rev. Astron. Astropys. 16 33.

CLEGG P.E., J.A. Bastin, A.E. Gear, (1966) Heat transfer in lunar rocks. M.N.R.A.S. 133 63.

COCHRAN A.L., E.S. Barker, (1984) Minor planet 1983TB: A dead comet? Icarus 59 296.

CREMERS C.J., R.C. Birkebak, J.E. White, (1971) Lunar surface temperatures from Apollo 12. Moon 3 346.

CRUIKSHANK D.P., (1977) Radii and albedos of four Trojan asteroids and Jovian satellites 6 and 7. Icarus 30 224.

CRUIKSHANK D.P., D. Morrison, (1973) Radii and albedos of asteroids 1,2,3,4,6,15,51,433, and 511. Icarus 20 477.

DEGEWIJ J., C.J. van Houten, (1979) Distant asteroids and outer Jovian satellites. In "Asteroids" (ed. T. Gehrels), Univ. of Arizona Press, Tucson, p417.

DOLLFUS A., (1971) Diameter measurements of asteroids. In "Physical Studies of Minor Planets" (ed. T. Gehrels), NASA SP-267, Washington D.C., p25.

DOLLFUS A., B. Zellner, (1979) Optical polarimetry of asteroids and laboratory samples. In "Asteroids" (ed. T. Gehrels), Univ. of Arizona Press, Tucson, p170.

DRUMMOND J.D., (1982) Theoretical meteor radiants of Apollo, Amor and Aten asteroids. Icarus 49 143.

DUNLAP J.L., (1974) Minor planets and related objects XV. Asteroid (1620) Geographos. Astron. J. 79 324.

DUNLAP J.L., (1976) Lightcurves and the axis of rotation of 433 Eros. Icarus 28 69.

EATON N., (1984) Comet dust - Applications of Mie scattering. Vistas in Astronomy, 27 111.

EATON N., J.K. Davies, S.F. Green, (1984) The anomalous dust tail of comet P/Tempel-2. M.N.R.A.S. 211 15p.

FEIERBERG M.A., H.P. Larson, C.R. Chapman, (1982) Spectroscopic evidence for undifferentiated S-type asteroids. Astrophys. J. 257 361.

FEIERBERG M.A., L.A. Lebofsky, H.P. Larson, (1981) Spectroscopic evidence for aqueous alteration products on the surfaces of low albedo asteroids. Geochim. Cosmochim. Acta. 45 971.

FEIERBERG M.A., F.C. Witteborn, L.A. Lebofsky, (1983) Detection of silicate emission features in the 8-13 μm spectra of main belt asteroids. Icarus 56 393.

FINSON M.L., R.F. Probstein, (1968a) A theory of dust comets I. Model and equations. Astrophys. J. 154 327.

FINSON M.L., R.F. Probstein, (1968b) A theory of dust comets II. Results for comet Arend-Roland. Astrophys. J. 154 353.

FOX K., I.P. Williams, D.W. Hughes, (1982) The evolution of the orbit of the Geminid meteor stream. M.N.R.A.S. 200 313.

FOX K., I.P. Williams, D.W. Hughes, (1983) The rate profile of the Geminid meteor shower. M.N.R.A.S. 205 1155.

GAFFEY M.J., T.B. McCord, (1977) Asteroid surface materials - Mineralogical characterizations from reflectance spectra. Space Science Review 21 555.

GEHRELS T., (1981) Faint comet searching. Icarus 47 518.

GILLETT F.C., F.J. Low, W.A. Stein, (1968) Stellar spectra from 2.8 to 14 microns. Astrophys. J. 154 677.

GILLETT F.C., K.M. Merrill, (1975) 7.5 - 13.5 micron spectra of Ceres and Vesta. Icarus 26 358.

GRADIE J.C., (1978) An astrophysical study of the minor

planets in the Eos and Koronis asteroid families. Ph.D. Thesis, Univ. of Arizona.

GRADIE J., E. Tedesco, (1982) Compositional structure of the asteroid belt. Science 216 1405.

GRADIE J., B. Zellner, (1977) Asteroid families: Observational evidence for common origins. Science 197 254.

GRADIE J.C., C.R. Chapman, J.G. Williams, (1979) Families of minor planets. In "Asteroids" (ed T. Gehrels), Univ of Arizona Press, Tucson, p359.

GREEN S.F., N. Eaton, D.K. Aitken, P.F. Roche, A.J. Meadows, (1985) 8-13μm spectra of asteroids. Icarus, in press.

HAMY M., (1899) Mesure interferentuelle des diametres des satellites de Jupiter et de Vesta, effectuee au grand equatorial coude de l'observatoire de Paris. Comptes Rendus, 128 583.

HANNER M.S., (1980) Physical characteristics of cometary dust from optical studies. In "Solid particles in the Solar System" (eds. I. Halliday, B. McIntosh), Reidel, Dordrecht, p223.

HANNER M.S., (1983) The nature of cometary dust from remote sensing. In "Cometary exploration" (ed. T.I. Gambosi), Hungarian Acad. Sciences 3 1.

HANNER M.S., A.T. Tokunaga, G.J. Veeder, M.F. A'Hearn, (1984) Astron. J. 89 162.

HANSEN O.L., (1972) Thermal radiation from the Galilean satellites measured at 10 and 20 microns. Ph.D. thesis, Cal. Inst. Tech.

HANSEN O.L., (1976a) Radii and albedos of 84 asteroids from

visual and IR photometry. Astron. J. 81 74.

HANSEN O.L., (1976b) Thermal emission spectra of 24 asteroids and the Galilean satellites. Icarus 27 463.

HANSEN O.L., (1977) An explication of the radiometric method for size and albedo determination. Icarus 31 456.

HAPKE B.W., (1971) Inferences from optical properties concerning the surface texture and compositions of asteroids. In "Physical Studies of Minor Planets" (ed. T. Gehrels), NASA SP-267, Washington D.C., p359.

HARRIS A.W., J.W. Young, (1983) Asteroid rotation. Icarus 54 59.

HARTMANN W.K., D.P. Cruikshank, J. Degewij, (1982) Remote comets and related bodies: VJHK colorimetry and surface materials. Icarus 52 337.

HELIN E.F., R.S. Dunbar, J. Gradie, L.A. Lebofsky, D.J. Tholen, (1984) Asteroid 1984BC - An extinct comet? Bull. Amer. Astron. Soc. 16 691 (Abstract).

HELIN E.F., E.M. Shoemaker, R.F. Wolfe, (1978) Ra-Shalom: Third member of the Aten class of Earth-crossing asteroids. Bull. Amer. Astron. Soc. 10 732. (Abstract).

HELIN E.F., E.M. Shoemaker, (1979) The Palomar planet-crossing asteroid survey 1973-1978. Icarus 40 321.

HIRAYAMA K., (1918) Groups of asteroids probably of common origin. Proc. Phys-Math. Soc. Japan II 354.

HIRAYAMA K., (1919) Further notes on the families of asteroids. Proc. Phys-Math. Soc. Japan Ser. 3, 1.

HIRAYAMA K., (1923) Families of asteroids. Jap. J. Astron. Geophys. Trans. 1 55.

HIRAYAMA K., (1928) Families of asteroids second paper. Jap. J. Astron. Geophys. Trans. 5 137.

HIRAYAMA K., (1933) Present state of the families of asteroids. Proc. Imp. Acad. Japan 9 482.

HOUSEN K.R., L.L. Wilkening, C.R. Chapman, R.J. Greenberg, (1979) Regolith development and evolution on asteroids and the moon. In "Asteroids" (ed. T. Gehrels), Univ. of Arizona press, Tucson, p601.

HUGHES D.W., (1982a) In "Proceedings of the workshop on interstellar comets" Occas. Rep. Roy. Obs. Edinburgh. p9.

HUGHES D.W., (1982b) Finding comets. J. Brit. Astron. Assoc. 92 61.

HUGHES D.W., (1983) Cometary dust, its source and characteristics. In "Asteroids, comets, meteors" (eds. C-I Lagerkvist, H. Rickmann) Uppsala University press, p239.

HUGHES D.W., P.A. Daniels, (1980) The magnitude distribution of comets. M.N.R.A.S. 191 511.

HUNT G.R., L.M. Logan, (1972) Variation of single particle mid-infrared emission spectrum with particle size. Appl. Opt. 11 142.

INGRAO H.C., A.T. Young, J.L. Linsky, (1966) A critical analysis of lunar temperature measurements in the infrared. In "The Nature of the Lunar Surface" (ed. W.N. Hess, D.H. Menzel, J.A. O'Keefe), John Hopkins Press, Baltimore, p185.

JAEGER J.C., (1953a) The surface temperature of the Moon. Aus. J. Phys. 6 10.

JAEGER J.C., (1953b) Conduction of heat in a solid with

periodic boundary conditions with an application to the surface temperature of the moon. Proc. Cambridge Phil. Soc. 49 355.

JAEGER J.C., A.F.A. Harper, (1950) Nature of the surface of the Moon. Nature 166 1026.

JOHNSON K.J., P.K. Seidelmann, C.M. Wade, (1982) Observations of 1 Ceres and 2 Pallas at centimeter wavelengths. Astron. J. 87 1593.

JONES T.J., D. Morrison, (1974) A re-calibration of the radiometric/photometric method of determining asteroid sizes. Astron. J. 79 892.

KENKNIGHT C.E., D.L. Rosenberg, G.K. Wehner, (1967) Parameters of the optical properties of the lunar surface powder in relation to solar wind bombardment. J. Geophys. Res. 72 3105.

KIRKWOOD D., (1867) Meteoric astronomy: A treatise on shootingstars, fireballs and aerolites. J.B. Lippincott & Co., Philadelphia, p129.

KITAMURA M., (1959) Photoelectric study of colours of asteroids and meteorites. Publ. Astron. Soc. Japan 11 79.

KRESÁK L., (1979) Three-Dimensional distributions of minor planets and comets. In "Dynamics of the Solar System" IAU Symp. 81, (ed. R.L. Duncombe), Reidel, Dordrecht, p239.

LABS D., H. Neckel, (1970) Transformation of the absolute solar radiation data into the "International practical temperature scale of 1968". Solar Phys. 15 79.

LARSON H.P., M.A. Feierberg, L.A. Lebofsky, (1983) The composition of asteroid 2 Pallas and its relation to primitive meteorites. Icarus 56 398.

LARSON H.P., G.J. Veeder, (1979) Infrared spectral reflectances of asteroid surfaces. In "Asteroids", (ed. T. Gehrels), Univ. of Arizona press, Tucson, p724.

LEBOFSKY L.A., (1978) Asteroid 1 Ceres: Evidence for water of hydration. M.N.R.A.S. 182 17p.

LEBOFSKY L.A., (1980) Infrared reflectance spectra of asteroids: a search for water of hydration. Astron. J. 85 573.

LEBOFSKY L.A., M.A. Feierberg, A.T. Tokunaga, H.P. Larson, J.R. Johnson, (1981) The 1.7 to 4.2μm spectrum of asteroid 1 Ceres: Evidence for structural water in clay minerals. Icarus 48 453.

LEBOFSKY L.A., G.J. Veeder, M.J. Lebofsky, D.C. Matson (1978) Visual and radiometric photometry of 1580 Betulia. Icarus 35 336.

LEBOFSKY L.A., M.J. Lebofsky, G.H. Rieke, (1979) Radiometry and surface properties of Apollo, Amor and Aten asteroids. Astron. J. 84 885.

LEBOFSKY L.A., G.H. Rieke, (1979) Thermal properties of 433 Eros. Icarus 40 297.

LeVAN P.D., S.D. Price, (1983) 85μm fluxes from asteroids: 2 Pallas, 7 Iris, 15 Eunomia and 45 Eugenia. Icarus 57 35.

LEVIN B.J., (1977) Relationships between meteorites, asteroids and comets. In "Comets, asteroids and meteorites" IAU Coll. 39, (ed. A.H. Delsemme), Univ. of Toledo press, p307.

LINDBLAD B.A., R.B. Southworth, (1971) A study of the

asteroid families and streams by computer techniques. In "Physical Studies of Minor Planets" (ed. T. Gehrels), NASA SP-267, Washington D.C., p337.

LINSKY J.L., (1966) Models of the lunar surface including temperature dependent thermal properties. Icarus 5 606.

LUMME K., E. Bowell, (1981a) Radiative transfer in the surfaces of atmosphereless bodies. I. Theory. Astron. J. 86 1694.

LUMME K., E. Bowell, (1981b) Radiative transfer in the surfaces of atmosphereless bodies. II. Interpretation of phase curves. Astron. J. 86 1705.

McCHEYNE R.S., (1985) Optical and infrared studies of asteroids. Ph.D. Thesis, University of Leicester.

McCORD T.B., C.R. Chapman, (1975) Asteroids: Spectral reflectance and colour characteristics. Astrophys. J. 195 553.

McFADDEN L.A., M.J. Gaffey, T.B. McCord, (1984a) Mineralogical-petrological characterisation of Near-Earth asteroids. Icarus 59 25.

McFADDEN L.A., S.J. Ostro, E.S. Barker, A.L. Cochran, D.P. Cruikshank, W.K. Hartmann, B.T. Soifer, G.J. Veeder, (1984b) 2201 Oljato: An asteroid, a comet, or both? Bull. Amer. Astron. Soc. 16 691 (Abstract).

MATSON D.L., (1971a) Infrared observations of asteroids. In "Physical Studies of Minor Planets" (ed. T. Gehrels), NASA SP-267, Washington D.C. p45.

MATSON D.L., (1971b) Infrared emission from asteroids at wavelengths of 8.5, 10.5 and 11.6 μm. Ph.D. thesis, Cal. Inst. Tech.

MATSON D.L., (1983) Mystery of the Galilean satellites' brightness temperatures. Bull. Amer. Astron. Soc. 15 852. (Abstract).

MATSON D.L., G.J. Veeder, L.A. Lebofsky, (1978) Infrared observations of asteroids from Earth and space. In "Asteroids: An exploration assessment" NASA Conf. Publ. 2053, (ed. D. Morrison, W.C. Wells), p127.

MATSON D.L., G.J. Veeder, L.A. Lebofsky, (1984) Asteroid thermal models and the IRAS calibration. JPL Publication 1604. (In preparation).

MILLIS R.L., J.L. Elliot, (1979) Direct determinations of asteroid diameters from occultation observations. In "Asteroids" (ed. T. Gehrels), Univ. of Arizona Press, Tucson, p98.

MILLIS R.L., E. Bowell, D.T. Thompson, (1976) UBV Photometry of asteroid 433 Eros. Icarus 28 53.

MORRISON D., (1973) Determination of radii of satellites and asteroids from radiometry and photometry. Icarus 19 1.

MORRISON D., (1974) Radiometric diameters and albedos of 40 asteroids. Astrophys. J. 194 203.

MORRISON D., (1976) The diameter and thermal inertia of 433 Eros. Icarus 28 125.

MORRISON D., (1977a) Asteroid sizes and albedos. Icarus 31 185.

MORRISON D., (1977b) Radiometric diameters of 84 asteroids from observations in 1974-76. Astrophys. J. 214 667.

MORRISON D., C.R. Chapman, (1976) Radiometric diameters for an additional 22 asteroids. Astrophys. J. 204 934.

MORRISON D., L.A. Lebofsky, (1979) Radiometry of asteroids, in "Asteroids" (ed. T. Gehrels), Univ. of Arizona Press,

Tucson, p184.

MORRISON D., J. Gradie, G.H. Rieke, (1976) Radiometric diameter and albedo of the remarkable asteroid 1976AA. Nature 260 691.

MORRISON D., B. Zellner, (1979) Polarimetry and radiometry of asteroids. In "Asteroids" (ed. T. Gehrels), Univ. of Arizona press, Tucson, p1108.

MUNCEY R.W., (1958) Calculations of lunar temperature. Nature 181 1458.

MUNCEY R.W., (1963) Properties of the lunar surface as revealed by thermal radiation. Aus. J. Phys. 16 24.

MURRAY B.C., R.L. Wildey, (1964) Surface temperature variations during the lunar nighttime. Astrophys. J. 139 734.

NEUGEBAUER G., H.J. Habing, R. van Duinen, H.H. Aumann, B. Baud, C.A. Beichmann, D.A. Beintema, N. Boggess, P.E. Clegg, T. de Jong, J.P. Emerson, T.N. Gautier, F.C. Gillett, S. Harris, M.G. Hauser, J.R. Houck, R.E. Jennings, F.J. Low, P.L. Marsden, G. Miley, F.M. Olnon, S.R. Pottasch, E. Raimond, M. Rowan-Robinson, B.T. Soifer, R.G. Walker, P.R. Wesselius, E. Young, (1984) The Infrared Astronomical satellite (IRAS) mission. Astrophys. J. 278 L1.

NEY E.P., (1982) Optical and infrared observations of bright comets in the range 0.5 to 20μm. In "Comets" (ed. L.L. Wilkening), Univ. of Arizona press, Tucson, p323.

OLBERS W., (1805) Entdeckung eines bewiglichen Sterne, den man gleichfalls fur einen Zwischen Mass und Jupiter nich

aufhaltenden planetarischen Korper halten kann. Berlin. Astr. Jarbuch. p108.

O'LEARY B., (1972) Frequencies of occultations of stars by planets, satellites and asteroids. Science 175 1108.

O'LEARY B., B.G. Marsden, R. Dragon, E. Hauser, M. McGrath, P. Backus, H. Robkoff., (1976) The Occultation of κ Geminorum by Eros. Icarus 28 133.

OPIK E.J., (1951) Collision probabilities with the planets and distribution of interplanetary matter. Proc. Roy. Irish Acad. 54A 165.

OPIK E.J., (1963) The stray bodies in the Solar System, part 1: Survival of cometary nuclei and the asteroids. Advan. Astron. Astropys. 2 219.

PETTIT E., (1935) Lunar radiation as related to phase. Astrophys. J. 81 17.

PETTIT E., (1940) Radiation measurements on the eclipsed Moon. Astrophys. J. 91 408.

PETTIT E., S.P. Nicholson, (1930) Lunar radiation and temperatures. Astrophys. J. 71 102.

PIDDINGTON J.H., H.C. Minnett, (1949) Microwave thermal radiation from the Moon. Aus. J. Sci. Res. 2 63.

ROSSE L., (1869) On the radiation of heat from the Moon. Proc. Roy. Soc. London 27 436.

RICKMANN H., C. FROESCHLE (1980) A Monte Carlo estimate of the fraction of comets developing into sizeable asteroidal bodies. Moon and Planets 22 125.

ROWAN-ROBINSON M., P.E. Clegg, C.A. Beichman, G. Neugebauer, B.T. Soifer, H.H. Aumann, D.A. Beintema, N. Boggess,

J.P. Emerson, T.N. Gautier, F.C. Gillett, M.G. Hauser, J.R. Houck, F.J. Low, R.G. Walker, (1984) The IRAS minisurvey. Astrophys. J. 278 L7.

RUSSELL H.N., (1916) On the albedo of the planets and their satellites. Astrophys. J. 43 173.

RUSSELL C.T., R. Aroian, M. Arghavani, K. Nock, (1984) Interplanetary magnetic field enhancements associated with the asteroid Oljato. Science 226 43.

SAFRONOV V.S., (1979) On the origins of asteroids. In "Asteroids" (ed. T. Gehrels), Univ. of Arizona Press, Tucson, p975.

SCALTRITI F., V. Zappala, (1976) Photometric lightcurves and pole determination of 433 Eros. Icarus 28 29.

SCHOLL H., C. Froechlé, (1977) The Kirkwood gaps as an asteroidal source of meteorites. In "Comets, Asteroids, Meteorites" (ed. A.H. Delsemme), Univ. of Toledo press, p293.

SEKANINA Z., (1972) A model for the nucleus of Encke's comet. In "The motion, evolution of orbits and origin of comets" (eds. G.S. Chebotarev, E.I. Kazimirchak-Polovskaya), Reidel, Dordrecht, p301.

SEKANINA Z., (1980) On the particle size distribution function of cometary dust. In "Solid particles in the Solar System", IAU Symp. 90, (eds. I Halliday, B.A. McIntosh), Reidel, Dordrecht, p251.

SEKANINA Z., (1982) The problem of split comets in review. In "Comets", (ed. L.L. Wilkening), Univ. of Arizona press, Tucson, p251.

SEXL R.U., H. Sexl, H. Stremnitzer, D.G. Burkhard, (1971)

The directional characteristics of lunar infrared radiation. Moon 3 189.

SHOEMAKER E.M., E.F. Helin, (1978) Earth-approaching asteroids: Populations, origin and compositional types. NASA Conf. Publ. 2053, p161.

SHOEMAKER E.M., J.G. Williams, E.F. Helin, R.F. Wolfe, (1979) Earth-crossing asteroids: Orbital classes, collision rates with Earth, and origin. In "Asteroids" (ed. T. Gehrels), Univ. of Arizona press, Tucson, p253.

SHORTHILL R.W., (1972) The infrared Moon. In "Thermal Characteristics of the Moon" (ed. J.W. Lucas), M.I.T. Press, Cambridge, Mass. p3.

SIMONELLI D.P., (1983) Amalthea: Implications of the temperature observed by Voyager. Icarus 54 524.

SIMPSON J.P., J.N. Cuzzi, E.F. Erickson, D.W. Strecker, A.T. Tokunaga, (1981) Mars: Far-infrared spectra and thermal emission models. Icarus 48 230.

SMITH G.D., (1978) Numerical solutions of partial differential equations - Finite difference methods. Oxford University press.

SOKAL R.R., P.H.A. Sneath, (1963) Principles of Numerical Taxonomy. Freeman, London.

SPENCER J.R., (1983) Surface properties of Ganymede as inferred from Voyager IRIS observations. Bull. Amer. Astron. Soc. 15 860. (Abstract).

TAYLOR R.C., E.F. Tedesco, (1983) Pole orienatation of the asteroid 44 Nysa via photometric astrometry, including a discussion of the methods, application and its limitations. Icarus 54 13.

TEDESCO E.F., D.J. Tholen, B. Zellner, (1982) The eight-colour asteroid survey: Standard stars. Astron. J. 87 1585.

THOLEN D.J., (1985) IAUC 4034.

TRAUB W.A., M.T. Stier, (1976) Theoretyical atmospheric transmission in the mid- and far-infrared at four altitudes. Applied Optics 15 373.

VAN HOUTEN C.J., I. van Houten-Grouneveld, P. Herget, T. Gehrels, (1970) The Palomar-Leiden survey of faint minor planets. Astron. Astrophys. Suppl. 2 339.

VEEDER G.J., D.L. Matson, G. Hoover, C. Kowal, (1983a) Infrared (JHK) photometry of asteroids - II. Astron. J. 88 1060.

VEEDER G.J., D.L. Matson, C. Kowal, (1982) Infrared (JHK) Photometry of asteroids. Astron J 87 834.

VEEDER G.J., D.L. Matson, J.C. Smith, (1978) Visual and infrared photometry of asteroids. Astron. J. 83 651.

VEEDER G.J., D.L. Matson, E.F. Tedesco, (1983b) The R asteroids reconsidered. Icarus 55 177.

WALKER R.G., H.H. Aumann, J. Davies, S. Green, T. de Jong, J.R. Houck, B.T. Soifer, (1984) Observations of comet IRAS-Araki-Alcock 1983d. Astrophys. J. 278 L11.

WALKER R.G., M. Rowan-Robinson, (1984) The peculiar infrared tail of Comet Bowell. Bull. Amer. Astron. Soc. 16 443. (Abstract).

WESSELINK A.J., (1948) Heat conductivity and nature of lunar surface material. Bull. Ast. Inst. Netherlands 10 351.

WETHERILL G.W., (1977) Fragmentation of asteroids and

delivery of fragments to Earth. In "Comets" (ed. L.L. Wilkening), Univ. of Arizona press, Tucson, p283.

WETHERILL G.W., (1979) Steady state populations of Apollo-Amor objects. Icarus 37 96.

WETHERILL G.W., D.O. ReVelle, (1982) Relationships between comets, large meteors and meteorites. In "Comets" (ed. L.L. Wilkening), Univ. of Arizona press, Tucson, p297.

WETHERILL G.W., J.G. Williams, (1968) Evaluation of the Apollo asteroids as sources of stone meteorites. J. Geophys. Res. 73 635.

WETHERILL G.W., J.G. Williams, (1979) Origin of differentiated meteorites. In "Proc. 2nd Internat. Conf. on Origin and Abundance of the Elements" (ed. H. de la Roche), Pergamon press, New York.

WHIPPLE F.L., (1951) A comet model II. Physical relations for comets and meteors. Astrophys. J. 113 464.

WHIPPLE F.L., (1981) The nature of comets. In "Comets and the origin of life" (ed. C Ponnamperuna), Univ. of Maryland press, p1.

WHIPPLE F.L., (1983) IAUC 3881.

WIDORN T., (1967) Zur photometrishen bestimmung der durchmesser der kleinen planeten. Annal. Universitats. Sternwarte Wien 27 111.

WILLIAMS J.G., (1971) Proper elements, families and belt boundaries. In "Physical studies of minor planets" (ed. T. Gehrels), NASA SP-267, Washington D.C., p177.

WILLIAMS J.G., (1973a) Meteorites from the asteroid belt? Eos: Trans. Amer. Geophys. Union. 54 233. (Abstract).

WILLIAMS J.G., (1973b) Secular resonances. Bull. Amer. Astron. Soc. 5 363. (Abstract).

WILLIAMS J.G., (1975) Asteroid families. Bull. Amer. Astron. Soc. (Abstract) 5 363.

WILLIAMS J.G., (1979) Proper elements and Family memberships of the asteroids. In "Asteroids" (ed. T. Gehrels), Univ. of Arizona Press, Tucson, p1040.

WINTER D.F., J.A. Krupp, (1971) Directional characteristics of infrared emission from the Moon. Moon 2 279.

WINTER D.F., J.M. Saari, (1969) A particulate thermophysical model of the lunar soil. Astrophys. J. 156 1135.

WISDOM J., (1982) The origin of the Kirkwood gaps: A mapping for asteroidal motion near the 3/1 commensurability. Astron. J. 87 577.

WISDOM J., (1983) Chaotic behaviour and the origin of the 3/1 Kirkwood gap. Icarus 56 51.

WOOD H.J., G.P. Kuiper, (1963) Photometric studies of asteroids - X. Astrophys. J. 137 1279.

WORDEN S.P., (1979) Interferometric determinations of asteroid diameters. In "Asteroids" (ed. T. Gehrels), Univ. of Arizona Press, Tucson, p119.

ZELLNER B., (1973) Photometric albedos of asteroids. Bull. Amer. Astron. Soc. 5 338. (Abstract).

ZELLNER B., (1976) Physical properties of asteroid 433 Eros. Icarus 28 149.

ZELLNER B., (1979a) Asteroid Taxonomy and the distribution of compositional types. In "Asteroids" (ed. T. Gehrels), Univ. of Arizona Press, Tucson, p783.

ZELLNER B., (1979b) The Tucson Revised Index of Asteroid Data. In "Asteroids" (ed. T. Gehrels), Univ. of Arizona press, Tucson, p1090.

ZELLNER B., E. Bowell, (1977) Asteroid compositional types and their distributions. In "Comets, Asteroids and Meteorites" (ed. A.H. Delsemme), Univ. of Toledo, p185.

ZELLNER B., T. Gehrels, J. Gradie, (1974) Minor planets and related objects - XVII polarimetric diameters. Astron. J. 79 1100.

ZELLNER B., J. Gradie, (1976) Minor planets and related objects - XX polarimetric evidence for the albedos and compositions of 94 asteroids. Astron. J. 81 986.

ZELLNER B., M. Leake, T. Lebertre, M. Duseaux, A. Dollfus, (1977a) The asteroid albedo scale I: Laboratory polarimetry of meteorites. Proc. Lunar Sci. Conf. VIII, Pergamon Press, Oxford p1091.

ZELLNER B., M. Leake, D. Morrison, J.G. Williams, (1977c) The E asteroids and the origin of the enstatite achondrites. Geochim. Cosmochim Acta, 41 1759.

ZELLNER B., T. Lebertre, K. Day, (1977b) The asteroid albedo scale II: Laboratory polarimetry of dark carbon bearing silicates. Proc. Lunar Sci. Conf. VIII, Pergamon press, Oxford, p1111.

ZELLNER B., D.J. Tholen, E.F. Tedesco, (1985) The eight colour asteroid survey: Results for 589 minor planets. submitted to Icarus.

ZELLNER B., W.Z. Wizniewski, L. Andersson, (1975) Minor planets and related objects - XVIII UBV photometry and surface composition. Astron J. 80 986.

ZIMMERMAN P.D., G.W. Wetherill, (1973) Asteroidal source of meteorites. Science 182 51.

# *APPENDICES*

## APPENDIX A

### Published Occultation Diameters

| Asteroid | Date | Occulted star | Obs. $p^1$ | Obs. $v^2$ | Mean Diam (km) | Comments | Ref. |
|---|---|---|---|---|---|---|---|
| 2 | 2/Oct/61 | BD-5°5863 | 1 | | >430 | | 1 |
| 2 | 29/May/78 | SAO 85009 | 7 | | 538±12 | 558x526x532 | 2 |
| 2 | 29/May/83 | 1 Vul | 15 | * | 523±5 | Preliminary Near min. Flattened. | 3 |
| 3 | 19/Feb/58 | BD+6°808 | 1 | | >110 | | 1 |
| 3 | 19/Jul/78 | SAO 144070 | 1 | | >256 | | 4 |
| 3 | 11/Dec/79 | AGK3+0°1022 | 15 | 3 | 267±5 | 290x246 | 5 |
| | | | 2 | | | 290x236 | 6 |
| 6 | 5/Mar/77 | γ Ceti A | 2 | | 186±9 | 195x170 | 7 |
| 9 | 11/Dec/79 | SAO 184440 | (1) | | >127 | | 8 |
| 15 | 30/Mar/82 | SAO 77636 | | | | | 9 |
| 18 | 11/Dec/78 | SAO 114159 | 6 | 2 | 135 | Satellite? | 10,11 |
| 18 | 7/Aug/81 | | 1 | | >126 | | 8 |
| 19 | 3/Feb/83 | AGK3+11°201 | 1 | 1 | | | 12 |
| 47 | 16/Sep/84 | SAO 146599 | (12) | | | | 28 |
| 51 | 17/Aug/79 | SAO 144417 | 2 | | 153±15 | | 13 |
| 51 | 11/Sep/83 | 14 Psc | + | + | | longest chord 160 | 14 |
| 65 | 17/Oct/79 | AGK3+19°599 | 1 | 2 | 230±16 | | 15 |
| 78 | 14/Sep/80 | SAO 75392 | 10 | | 140 | | 16 |
| 88 | 7/Oct/81 | SAO 187124 | 3 | 9 | 232±12 | | 17 |
| 93 | 22/Nov/82 | AGK3+29°398 | 5 | + | 170 | | 18 |
| 105 | 5/Oct/81 | HD 197999 | 2 | | >110 | | 19 |
| 106 | 27/Jan/83 | | | + | 120±10 | | 20 |
| 134 | 24/Nov/80 | SAO 74963 | | | 110 | | 8 |

| | | | | | | | |
|---|---|---|---|---|---|---|---|
| 146 | 18/Apr/82 | AGK3+17° 1309 | 1 | | | | 21 |
| 216 | 10/Oct/80 | SAO 128066 | 4 | 5 | | 130x95 near min | 16 |
| 344 | 11/Jan/82 | SAO 042418 | 1 | | | possible | 22 |
| 375 | 15/Nov/82 | AGK3+39° 303 | 2 | 4 | 216±10 | nearly spherical | 23 |
| 433 | 24/Jan/75 | κ Gem A | | 8 | | 12-23 Irregular | 24 |
| 444 | | SAO 138868 | | | | | 27 |
| 532 | 7/Jun/78 | SAO 120774 | 1 | 2 | 217 | Satellite? | 25 |
| 690 | 14/Nov/82 | BD+24° 522 | | 2 | | | 26 |

[1] Photoelectric

[2] visual

* Over 100 observations

+ Unknown

References


1. G.E. Taylor, J. Brit. Astron. Assoc. 72 212, 1962.
2. L.H. Wasserman et al., Astron. J. 84 259, 1979.
3. D.W. Dunham et al., Bull. Amer. Astron. Soc. 15 822, 1983.
4. D.W. Dunham, Y. Sheffer, Occultation newsletter 2 12, 1979.
5. R.L. Millis et al., Astron. J. 86 306, 1981.
6. H.J. Reitsema et al., Astron. J. 86 121, 1981.
7. G.E. Taylor, D.W. Dunham, Icarus 34 89, 1978.
8. G.E. Taylor, Sun & Planetary System, ed. W. Fricke, G. Teleki, Reidel Astrophysics and Space Science Lib. 96 287, 1982.
9. M.D. Overbeek, Mon. Not. Astron. Soc. South Africa 41 25, 1982.
10. R.L. Millis, J.L. Elliot, Asteroids, ed. T. Gehrels, Univ.

of Arizona Press, 98, 1979.

11. R.M. Williamon, Astron. J. 85 174, 1980.

12. I.A.U.C. 3776, 1983.

13. L.K. Kristensen, Astron. Astrophys. Suppl. Ser. 44 375, 1981.

14. D.W. Dunham, I.A.U.C. 3869, 1983.

15. G.E. Taylor, J. Brit. Ast. Assoc. 92 13, 1981.

16 D. Dunham, P. Maley, Bull. Amer. Astron. Soc. 12 814, 1980.

17. R.L. Millis et al., Astron. J. 88 229, 1983.

18. L.H. Wasserman et al., Bull. Amer. Astron. Soc. 15 822, 1983.

19. P.B. Byrne et al., M.N.R.A.S. 200 65p, 1982.

20. G.E. Taylor, Asteroids, Comets, Meteors, ed. C-I. Lagerkvist, H. Rickman, Proc. of meeting held at Uppsala Univ., p104, 1983.

21. D.W. Dunham, I.A.U.C. 3699, 1983.

22. J.O. Piironen, H. Jantumen, I.A.U.C. 3659, 1982.

23. R.L. Millis et al., Astron. J. 89 592, 1984.

24. B. O'Leary, Icarus 28 133, 1976.

25. E. Bowell, Bull. Amer. Astron. Soc. 10 594, 1978.

26. A. Lowe, I.A.U.C. 3747, 1982.

27. X.-h. Zhou, Chin. Astron. Astrophys. 7 169, 1983.

28. R.L. Millis et al., Bull. Amer. Astron. Soc. 16 1027, 1985.

## APPENDIX B

### IRAS FMO Alerts

The table lists the following data for each IRAS FMO alert:-

Alert number - identification number.

Source ID - individual detection identification number. Contains SOP, block and source number.

JD - Julian date of detection. Obtained from SATCAL (time in seconds from $0^h$ 26 Jan 1983 as measured by the spacecraft clock) by the formula

JD = 2445360.5 + (SATCAL)/(0.9999470966x86400)

the constant ~1 corrects the IRAS clock rate to UT seconds.

R.A. Dec - Observed coordinates of source.

ORB - Number of IRAS orbits between detections.

$\Delta\lambda$ $\Delta\beta$ - Separations in ecliptic longitude and latitude (arcmin).

Comments - Identification of object. See sections 5.4, 5.5, 5.8.

$(r,\Delta,\alpha)$ - heliocentric and geocentric distances and phase angle at time of detection.

* - These FMO's were identified during post -mission analysis.

| Alert | Source | ID | JD | R.A. | DEC | ORB | Δλ | Δβ | Comments |
|---|---|---|---|---|---|---|---|---|---|
| 180-1 | 180 | 3 63 | 2445450.35479 | 19 6.29 | 48 38.6 | | | | COMET IRAS-ARAKI-ALCOCK 1983D |
| | 180 | 3 64 | 2445450.42648 | 19 6.15 | 48 39.4 | 1 | -1.04 | 1.22 | (1.083 0.394 68.3) |
| 201-1 | 201 | 1 46 | 2445460.11367 | 8 40.12 | 5 28.3 | | | | * NO ALERT SENT |
| | 201 | 1 45 | 2445461.18813 | 8 40.96 | 5 26.1 | 15 | 12.68 | 1.17 | PROBABLE ASTEROID |
| 214-1 | 215 | 1 53 | 2445467.63340 | 9 16.89 | -15 19.7 | | | | COMET IRAS 1983F |
| | 215 | 1 52 | 2445467.70495 | 9 16.89 | -15 17.5 | 1 | -.76 | 2.06 | (2.114 1.767 26.4) |
| 242-1 | 241 | 1 61 | 2445481.09295 | 9 46.75 | -12 54.9 | | | | * NO ALERT SENT |
| | 242 | 1 48 | 2445481.52750 | 9 46.88 | -12 54.2 | 6 | 1.51 | 1.35 | PROBABLE COMET |
| 272-1 | 271 | 1 20 | 2445496.11718 | 12 3.01 | 15 .1 | | | | * NO ALERT SENT |
| | 272 | 1 16 | 2445496.54681 | 12 3.34 | 14 55.0 | 6 | 6.45 | -2.69 | PROBABLE ASTEROID |
| 305-1 | 305 | 1 6 | 2445512.79525 | 13 .91 | 15 51.2 | | | | NOT SEARCHED FOR |
| | 305 | 1 7 | 2445512.85681 | 13 .90 | 15 50.5 | 1 | .16 | -.70 | PROBABLE ASTEROID |
| 308-1 | 308 | 1 61 | 2445514.26006 | 1 22.40 | -21 59.3 | | | | |
| | 308 | 1 62 | 2445514.33154 | 1 22.48 | -21 57.8 | 1 | 1.64 | .89 | COMET P/IRAS 1983J |
| | 308 | 1 63 | 2445514.40325 | 1 22.64 | -21 55.8 | 1 | 2.86 | .87 | (1.808 1.552 34.2) |
| 313-1 | 313 | 1 12 | 2445516.94788 | 12 21.97 | 10 48.8 | | | | * NO ALERT SENT |
| | 313 | 1 13 | 2445517.01961 | 12 22.11 | 10 47.6 | 1 | 2.37 | -.26 | PROBABLE ASTEROID |
| 314-1 | 314 | 1 52 | 2445517.52395 | 11 53.53 | - 7 46.3 | | | | NOT SEARCHED FOR |
| | 314 | 1 51 | 2445517.66742 | 11 55.89 | - 7 37.7 | 2 | 28.58 | 21.95 | PROBABLY FALSE |
| 315-1 | 315 | 1 65 | 2445517.95714 | 11 26.57 | -23 45.4 | | | | NOT SEARCHED FOR |
| | 315 | 1 64 | 2445518.02842 | 11 29.09 | -23 15.5 | 1 | 18.28 | 41.97 | PROBABLY FALSE |
| 315-2 | 315 | 1 67 | 2445517.95897 | 11 3.22 | -32 30.7 | | | | POSSIBLE M-B ASTEROID 1983NH |
| | 315 | 1 66 | 2445518.03038 | 11 3.30 | -32 30.3 | 1 | .70 | .83 | OBSERVED BY UK SCHMIDT - LOST |
| 333-1 | 333 | 1 66 | 2445526.97986 | 11 57.75 | -48 59.3 | | | | COMET IRAS 1983K |
| | 333 | 1 65 | 2445527.05141 | 11 57.78 | -48 56.8 | 1 | -1.14 | 2.25 | (2.538 2.251 23.5) |
| 334-1 | 333 | 2 16 | 2445527.20861 | 4 12.01 | -65 16.6 | | | | |
| | 334 | 1 67 | 2445527.35193 | 4 13.47 | -65 10.1 | 2 | 9.15 | -6.55 | NO OBJECT <18MAG OBSERVED |
| 337-1 | 338 | 2 3 | 2445529.37010 | 1 24.93 | - 2 8.6 | | | | NO OBJECT <18MAG OBSERVED |
| | 338 | 2 2 | 2445529.44176 | 1 25.10 | - 2 25.1 | 1 | -3.86 | -16.24 | PART OF TEMPEL-2 INFRARED TAIL |
| 345-1 | 345 | 1 40 | 2445533.08380 | 1 54.16 | - 0 27.5 | | | | NO OBJECT <18MAG OBSERVED |
| | 345 | 1 36 | 2445533.23190 | 1 55.98 | - 0 19.8 | 2 | 28.25 | -2.52 | PART OF TEMPEL-2 INFRARED TAIL |

| Alert | Source ID | JD | R.A. | DEC | ORB | Δλ | Δβ | Comments |
|---|---|---|---|---|---|---|---|---|
| 354-1 | 354 1 58 | 2445537.31042 | 1 42.46 | -10 13.5 | | | | NOT SEARCHED FOR |
| | 354 1 57 | 2445537.38198 | 1 42.69 | -10 12.9 | 1 | 3.37 | -.74 | POSSIBLE APOLLO ASTEROID |
| 363-1 | 363 1 32 | 2445541.93418 | 14 2.64 | -10 22.0 | | | | POSSIBLE APOLLO ASTEROID |
| | 363 1 34 | 2445542.00587 | 14 2.30 | -10 30.7 | 1 | -1.73 | -9.89 | OBSERVED AT PALOMAR - LOST |
| 365-1 | 365 2 8 | 2445543.09027 | 10 55.04 | -67 20.4 | | | | COMET IRAS 19830 1ST DETN - NOT |
| | 365 2 7 | 2445543.16774 | 10 55.44 | -67 18.5 | 1 | -.32 | 2.96 | SEARCHED FOR (2.652 2.429 22.5) |
| 415-1 | 415 31 21 | 2445567.91344 | 15 5.70 | -19 40.6 | | | | |
| | 415 31 9 | 2445567.98498 | 15 5.98 | -19 32.0 | 1 | 1.45 | 9.36 | NOT SEARCHED FOR |
| | 415 31 21 | 2445567.91344 | 15 5.70 | -19 40.6 | | | | PROBABLY SINGLE DETN OF NUMBERED |
| | 415 31 34 | 2445567.98502 | 15 6.56 | -19 50.0 | 1 | 14.25 | -5.72 | ASTEROID + CONFUSION |
| 418-1 | 418 43 7 | 2445569.51972 | 3 31.72 | 1 45.6 | | | | M-B ASTEROID 1983QF 1ST DETN - NOT |
| | 419 54 7 | 2445570.02637 | 3 32.37 | 1 41.4 | 7 | 8.39 | -6.50 | SEARCHED FOR (2.303 2.024 26.0) |
| 424-1 | 424 66 9 | 2445572.38880 | 3 27.54 | 30 20.3 | | | | NOT SEARCHED FOR |
| | 424 66 13 | 2445572.46051 | 3 28.15 | 30 39.6 | 1 | 12.46 | 16.72 | PROBABLY FALSE |
| 424-2 | 424 47 21 | 2445571.37894 | 3 54.01 | - 7 58.6 | | | | |
| | 424 47 20 | 2445571.45062 | 3 54.08 | - 8 5.6 | 1 | -.63 | -7.05 | NO OBJECT <18MAG OBSERVED |
| 429-1 | 428 20 28 | 2445573.99834 | 14 12.92 | - 9 38.0 | | | | |
| | 428 20 31 | 2445574.06994 | 14 13.20 | - 9 40.5 | 1 | 4.74 | -.98 | NOT SEARCHED FOR |
| | 429 29 15 | 2445574.85721 | 14 17.48 | -10 1.9 | 11 | 66.77 | .75 | POSSIBLE APOLLO ASTEROID |
| | 429 29 20 | 2445574.92882 | 14 17.76 | -10 3.9 | 1 | 4.56 | -.53 | |
| 436-1 | 436 59 2 | 2445578.32311 | 2 43.61 | -10 .2 | | | | MAIN-BELT ASTEROID 1983QG |
| | 436 59 1 | 2445578.39481 | 2 43.75 | -10 .2 | 1 | 1.95 | -.68 | (1.729 0.996 30.7) |
| 438-1 | 438 54 32 | 2445579.94471 | 12 34.33 | -50 42.6 | | | | COMET IRAS 19830 2ND DETN |
| | 438 54 31 | 2445579.01630 | 12 34.41 | -50 40.5 | 1 | -.47 | 2.18 | (2.465 2.728 21.7) |
| 458-1 | 458 14 31 | 2445589.53085 | 16 57.49 | -27 33.7 | | | | NOT SEARCHED FOR - SINGLE DETN |
| 458-3 | 458 26 83 | 2445589.34243 | 3 45.58 | -20 10.4 | | | | NOT SEARCHED FOR |
| | 458 26 82 | 2445589.41399 | 3 45.82 | -20 11.9 | 1 | 2.82 | -2.39 | PROBABLY FALSE |
| 460-1 | 460 8 22 | 2445590.49081 | 3 53.75 | - 1 51.9 | | | | MAIN-BELT ASTEROID 1983QF 2ND |
| | 460 8 21 | 2445590.56239 | 3 53.81 | - 1 52.9 | 1 | .65 | -1.18 | DETECTION (2.263 1.772 25.4) |
| 463-1 | 462 1 55 | 2445591.60330 | 15 39.94 | -14 51.2 | | | | NOT SEARCHED FOR |
| | 463 5 55 | 2445591.67493 | 15 39.77 | -14 55.2 | 1 | -1.48 | -4.46 | PROBABLY FALSE |

| Alert | Source ID | JD | R.A. | DEC | ORB | Δλ | Δβ | Comments |
|---|---|---|---|---|---|---|---|---|
| 465-1 | 465 14 43 | 2445592.96313 | 15 49.52 | -16 57.6 | | | | NOT SEARCHED FOR |
| | 465 14 40 | 2445593.03471 | 15 50.53 | -16 57.4 | 1 | 14.11 | 3.30 | PROBABLY FALSE |
| 471-1 | 471 29 28 | 2445595.68312 | 16 3.82 | -20 3.2 | | | | NOT SEARCHED FOR |
| | 471 30 28 | 2445595.75474 | 16 5.04 | -20 32.1 | 1 | 22.40 | -25.06 | PROBABLY FALSE |
| 471-2 | 471 71 52 | 2445596.07949 | 4 11.30 | 28 3.8 | | | | NOT SEARCHED FOR |
| | 471 71 53 | 2445596.14994 | 4 11.14 | 28 4.8 | 1 | -1.90 | 1.37 | PROBABLY FALSE |
| 478-1 | 475 22 9 | 2445597.90123 | 16 22.73 | -17 39.4 | | | | CLOSE TO NEWLY DISCOVERED COMET |
| | 478 15 52 | 2445599.61888 | 16 32.35 | -18 24.4 | 24 | 142.56 | -22.97 | KOWAL-VAVROVA - NO OBJ OBSERVED |
| 481-1 | 481 39 43 | 2445600.90816 | 16 40.35 | -24 31.1 | | | | NOT SEARCHED FOR |
| | 481 39 30 | 2445600.97971 | 16 41.65 | -24 23.2 | 1 | 16.53 | 10.22 | PROBABLY FALSE |
| 487-1 | 487 1 56 | 2445603.76627 | 17 4.34 | 0 15.4 | | | | |
| | 487 1 65 | 2445603.83781 | 17 5.42 | 0 25.6 | 1 | 15.06 | 11.81 | NOT SEARCHED FOR |
| | 487 1 60 | 2445603.90935 | 17 6.66 | 0 35.8 | 1 | 17.47 | 12.03 | PROBABLY APOLLO ASTEROID |
| | 487 1 58 | 2445603.98090 | 17 7.64 | 0 45.9 | 1 | 13.63 | 11.51 | DESIGNATED 1983SN |
| | 487 1 56 | 2445604.05245 | 17 8.80 | 0 55.9 | 1 | 16.34 | 11.65 | |
| 516-1 | 516 1 1 | 2445618.56872 | 17 26.36 | 59 30.5 | | | | |
| | 516 1 2 | 2445618.64030 | 17 28.60 | 59 29.9 | 1 | 12.36 | 4.81 | APOLLO ASTEROID 1983TB |
| | 517 1 3 | 2445618.78343 | 17 31.82 | 59 27.8 | 1 | 23.50 | 7.34 | (1.02 0.37 76.) |
| | 517 1 4 | 2445618.85501 | 17 33.47 | 59 26.7 | 1 | 12.16 | 3.39 | |
| | 517 1 5 | 2445618.92659 | 17 35.15 | 59 25.7 | 1 | 12.42 | 3.32 | |
| | 517 1 6 | 2445618.99817 | 17 36.79 | 59 24.6 | 1 | 12.23 | 2.88 | |
| | 517 1 7 | 2445619.06975 | 17 38.31 | 59 22.8 | 1 | 11.62 | 1.70 | |
| 559-1 | 559 1 56 | 2445639.91525 | 22 10.36 | -57 33.7 | | | | APOLLO ASTEROID 1983VA |
| | 559 1 55 | 2445639.98682 | 22 10.13 | -57 33.4 | 1 | -1.48 | 1.15 | (1.065 0.359 68.7) |
| 576-1 | 576 1 39 | 2445648.45680 | 9 29.15 | 8 12.2 | | | | NOT SEARCHED FOR |
| | 576 1 38 | 2445648.52834 | 9 29.12 | 8 11.2 | 1 | -.11 | -1.09 | PROBABLE ASTEROID |
| 576-2 | 576 1 21 | 2445648.63867 | 21 32.94 | -16 34.6 | | | | NOT SEARCHED FOR - SINGLE DETN |
| 577-1 | 577 1 23 | 2445648.85188 | 21 33.22 | -16 47.6 | | | | COMET P/HARTLEY-IRAS 1983V |
| | 577 1 21 | 2445648.99497 | 21 32.94 | -16 34.6 | 2 | .33 | 13.60 | (1.523 1.135 40.6) |
| 588-1 | 588 2 54 | 2445654.46722 | 10 7.74 | 7 9.0 | | | | NOT SEARCHED FOR |
| | 588 2 55 | 2445654.53881 | 10 9.23 | 7 18.2 | 1 | 17.51 | 16.43 | POSSIBLE APOLLO ASTEROID |

## APPENDIX C

IRAS Spectral Responses and Correction Factors.

Wide bandpass photometric data are usually reduced to a reference wavelength defined for each filter. The IRAS spectral responses $T(\lambda)$ are shown in Fig. 4.2.

The mean wavelength is defined as

$$\lambda_o = \frac{\int \lambda\ E(\lambda)\ T(\lambda)\ d\lambda}{\int\ E(\lambda)\ T(\lambda)\ d\lambda}$$

where $E(\lambda)$ is the sky transmission. $E(\lambda)$ can be regarded as unity, since IRAS is orbiting above the atmosphere. The effective bandwidth $\Delta\lambda_o = \int E(\lambda)\ T(\lambda)\ d\lambda$.

For a wide bandpass, however, one needs to take into account the spectrum of the observed source, $S(\lambda)$. The effective wavelength is defined as

$$\lambda_{eff} = \frac{\int \lambda\ E(\lambda)\ T(\lambda)\ S(\lambda)\ d\lambda}{\int\ E(\lambda)\ T(\lambda)\ S(\lambda)\ d\lambda}$$

and the effective bandwidth

$$\Delta\lambda_{eff} = \frac{\int E(\lambda)\ T(\lambda)\ S(\lambda)\ d\lambda}{S(\lambda_{eff})}.$$

The observed quantity is the in-band flux S where

$$S = \int E(\lambda)\ T(\lambda)\ S(\lambda)\ d\lambda$$

so $S(\lambda_{eff}) = S/\Delta\lambda_{eff}$.

IRAS fluxes quoted in the literature have been calculated from the observed in-band fluxes assuming a source spectrum which is flat in flux per logarithmic frequency interval, ie $\nu S_\nu$ = constant ($\lambda S_\lambda$ = constant), at reference wavelengths $\lambda_{ref}$ of 12, 25, 60 and 100μm. To produce a consistent data set, these reference wavelengths have been adopted for all the data discussed here.

Using $S(\lambda) = \text{const}/\lambda$, $\lambda_{eff} = \lambda_{ref}$, $E(\lambda) = 1$, and $T(\lambda)$ from Fig. 4.2, the resultant bandwidths $\Delta\lambda_{ref}$ are 6.61, 10.85, 29.8 and 32.0μm for bands I-IV respectively.

Different source spectra will produce different values for the effective bandwidth. The table below gives correction factors for various blackbody spectra such that

$$S(\lambda_{ref}) = S.(\text{correction factor})/\Delta\lambda_{ref}$$

| S(λ)=Blackbody K | Correction factors Band I | Band II | Band III | Band IV |
|---|---|---|---|---|
| 100 | 0.90 | 1.18 | 0.99 | 0.95 |
| 110 | 1.00 | 1.15 | 0.97 | 0.94 |
| 120 | 1.07 | 1.12 | 0.96 | 0.94 |
| 130 | 1.12 | 1.10 | 0.94 | 0.93 |
| 140 | 1.16 | 1.07 | 0.93 | 0.93 |
| 150 | 1.19 | 1.05 | 0.92 | 0.93 |
| 160 | 1.20 | 1.03 | 0.91 | 0.93 |
| 170 | 1.21 | 1.01 | 0.91 | 0.92 |
| 180 | 1.22 | 0.99 | 0.90 | 0.92 |
| 190 | 1.21 | 0.98 | 0.89 | 0.92 |
| 200 | 1.21 | 0.96 | 0.89 | 0.92 |
| 210 | 1.20 | 0.95 | 0.88 | 0.92 |
| 220 | 1.19 | 0.94 | 0.88 | 0.92 |
| 230 | 1.18 | 0.93 | 0.87 | 0.92 |
| 240 | 1.17 | 0.92 | 0.87 | 0.91 |
| 250 | 1.15 | 0.91 | 0.87 | 0.91 |
| 260 | 1.14 | 0.90 | 0.86 | 0.91 |
| 270 | 1.13 | 0.89 | 0.86 | 0.91 |
| 280 | 1.12 | 0.88 | 0.86 | 0.91 |
| 290 | 1.10 | 0.88 | 0.86 | 0.91 |
| 300 | 1.09 | 0.87 | 0.85 | 0.91 |
| 310 | 1.08 | 0.86 | 0.85 | 0.91 |
| 320 | 1.07 | 0.86 | 0.85 | 0.90 |
| 330 | 1.05 | 0.85 | 0.85 | 0.90 |
| 340 | 1.04 | 0.85 | 0.85 | 0.90 |
| 350 | 1.03 | 0.84 | 0.85 | 0.90 |
| 360 | 1.02 | 0.84 | 0.84 | 0.90 |
| 370 | 1.01 | 0.84 | 0.84 | 0.90 |
| 380 | 1.00 | 0.83 | 0.84 | 0.90 |
| 390 | 0.99 | 0.83 | 0.84 | 0.90 |
| 400 | 0.99 | 0.83 | 0.84 | 0.90 |
| 1000 | 0.78 | 0.75 | 0.81 | 0.90 |

The correction factors agree with those quoted by Neugebauer et al. (1984) for 1000K and 300K blackbodies to within 4% for bands II and III and 2% for bands I and IV. (See Ch.7)

In order to calculate the monochromatic fluxes for an observed source, the source spectrum itself is required. In practice, this can be approximated by the observed colour temperature for a multiple-band source. The table below gives blackbody temperatures for observed in-band flux ratios.

| Blackbody temperature K | In-band colours S(Band II)/S(Band I) | S(Band III)/S(Band I) | S(BandIV)/S(Band I) |
|---|---|---|---|
| 100 | 16.3 | 21.1 | 5.70 |
| 110 | 10.5 | 10.2 | 2.56 |
| 120 | 7.3 | 5.5 | 1.29 |
| 130 | 5.2 | 3.3 | 0.73 |
| 140 | 4.0 | 2.1 | 0.44 |
| 150 | 3.1 | 1.40 | 0.28 |
| 160 | 2.5 | 0.98 | 0.19 |
| 170 | 2.0 | 0.71 | 0.14 |
| 180 | 1.7 | 0.55 | 0.10 |
| 190 | 1.44 | 0.43 | 0.077 |
| 200 | 1.26 | 0.39 | 0.060 |
| 210 | 1.10 | 0.28 | 0.048 |
| 220 | 0.97 | 0.23 | 0.039 |
| 230 | 0.86 | 0.19 | 0.032 |
| 240 | 0.78 | 0.17 | 0.028 |
| 250 | 0.71 | 0.14 | 0.023 |
| 260 | 0.65 | 0.126 | 0.020 |
| 270 | 0.60 | 0.111 | 0.018 |
| 280 | 0.56 | 0.098 | 0.016 |
| 290 | 0.50 | 0.086 | 0.014 |
| 300 | 0.48 | 0.081 | 0.0125 |
| 310 | 0.46 | 0.073 | 0.0113 |
| 320 | 0.43 | 0.067 | 0.0104 |
| 330 | 0.40 | 0.061 | 0.0095 |
| 340 | 0.38 | 0.057 | 0.0087 |
| 350 | 0.36 | 0.053 | 0.0081 |
| 360 | 0.34 | 0.050 | 0.0075 |
| 370 | 0.33 | 0.047 | 0.0070 |
| 380 | 0.32 | 0.044 | 0.0065 |
| 390 | 0.30 | 0.041 | 0.0061 |
| 400 | 0.30 | 0.039 | 0.0058 |
| 1000 | 0.13 | 0.012 | 0.0016 |

## APPENDIX D

Orbital Elements of IRAS Discoveries.

### Asteroids

| | Mean distance a (A.U.) | Eccentricity e | Inclination i (deg) | Argument of perihelion ω (deg) | Longitude of ascending node Ω (deg) | Mean anomaly M (deg) | Epoch E (JD) | Reference |
|---|---|---|---|---|---|---|---|---|
| 1983QF | 2.6909 | 0.2164 | 22.66 | 277.46 | 167.34 | 323.52 | 2445580.5 | MPC 8207 |
| 1983QG | 2.6430 | 0.3463 | 14.30 | 279.55 | 80.24 | 98.80 | 2446000.5 | MPC 8467 |
| 1983VA | 2.5821 | 0.6888 | 16.20 | 11.74 | 76.94 | 349.26 | 2445640.5 | MPC 8395 |
| 1983TB | 1.2715 | 0.8903 | 22.04 | 321.69 | 265.03 | 290.30 | 2446000.5 | MPC 8394 |
| | | | | | | | | I.P. Williams |
| Geminids | 1.35 | 0.896 | 23.6 | 324.8 | 260.6 | | | |

### Comets

| | Perihelion distance q (A.U.) | e | i (deg) | ω (deg) | Ω (deg) | Perihelion Time T (JD) | E (JD) | |
|---|---|---|---|---|---|---|---|---|
| P/IRAS-Araki-Alcock 1983d | 0.9913 | 0.9901 | 73.25 | 192.84 | 48.40 | 2445477.73 | 2445480.5 | MPC 8272 |
| IRAS 1983f | 1.4165 | 1.0 | 152.19 | 227.07 | 118.93 | 2445353.53 | | MPC 8052 |
| P/IRAS 1983j | 1.6968 | 0.6956 | 46.18 | 356.89 | 357.16 | 2445570.30 | 2445560.5 | MPC 8386 |
| IRAS 1983k | 2.4182 | 1.0 | 138.84 | 265.60 | 171.10 | 2445457.22 | | IAUC 3925 |
| IRAS 1983o | 2.2546 | 1.0 | 120.74 | 333.99 | 200.56 | 2445666.53 | | MPC 8272 |
| P/Hartley-IRAS 1983v | 1.2843 | 0.8370 | 95.77 | 46.93 | 0.77 | 2445708.02 | | MPC 8387 |

## APPENDIX E

Coordinate systems for calculation of thermal models

The known (or assumed) quantities are:-

$(\alpha_a, \delta_a)$, Right ascension and declination of asteroid; $\Delta$, geocentric distance of asteroid; ${}_e\lambda_s$, geocentric ecliptic longitude of the Sun; $r_e$, heliocentric distance of the Earth; $({}_a\lambda_p, {}_a\beta_p)$, asterocentric ecliptic coordinates of the rotation pole.

The geocentric ecliptic coordinates of the asteroid $({}_e\lambda_a, {}_e\beta_a)$ are given by:-

$${}_e\beta_a = \text{ASIN}\ [\ \cos\varepsilon \sin {}_e\delta_a + \sin\varepsilon \cos {}_e\delta_a \cos(\pi/2 + {}_e\alpha_a)\ ]$$

$${}_e\lambda_a = \text{ASIN}\ [\ (\sin {}_e\delta_a - \cos\varepsilon \sin {}_e\beta_a)/(\sin\varepsilon \cos {}_e\beta_a)\ ]$$

if $\alpha \leqslant \pi/2$ or $\alpha \geqslant 3\pi/2$

$${}_e\beta_a = \text{ASIN}\ [\ \cos\varepsilon \sin {}_e\delta_a + \sin\varepsilon \cos {}_e\delta_a \cos(3\pi/2 - {}_e\alpha_a)\ ]$$

$${}_e\lambda_a = \pi/2 + \text{ACOS}\ [\ (\sin {}_e\delta_a - \cos\varepsilon \sin {}_e\beta_a)/(\sin\varepsilon \cos {}_e\beta_a)\ ]$$

if $\pi/2 \leqslant \alpha \leqslant 3\pi/2$.

Fig. A.1 shows the Earth-Sun-Asteroid geometry.

$$\underline{SA}' = [\ \Delta^2 \cos^2 {}_e\beta_a + r_e^2 - 2\,\Delta\, r_e \cos {}_e\beta_a \cos({}_e\lambda_s - {}_e\lambda_a)\ ]^{1/2}$$

The Sun-asteroid distance, $r = [\ (\underline{SA}')^2 + \Delta^2 \cos^2 {}_e\beta_a\ ]^{1/2}$

The asterocentric ecliptic coordinates of the Earth, $({}_e\lambda_a, {}_e\beta_a)$, are ${}_a\lambda_e = {}_e\lambda_a - \pi$, ${}_a\beta_e = -{}_e\beta_a$.

The asterocentric ecliptic coordinates of the Sun, $({}_a\lambda_s, {}_a\beta_s)$, are $\lambda_{e\,s} = {}_e\lambda_s \pm \text{ACOS}\ [\ (r_e - \Delta \cos {}_e\beta_a \cos({}_e\lambda_s - {}_e\lambda_a))/\underline{SA}'\ ]$

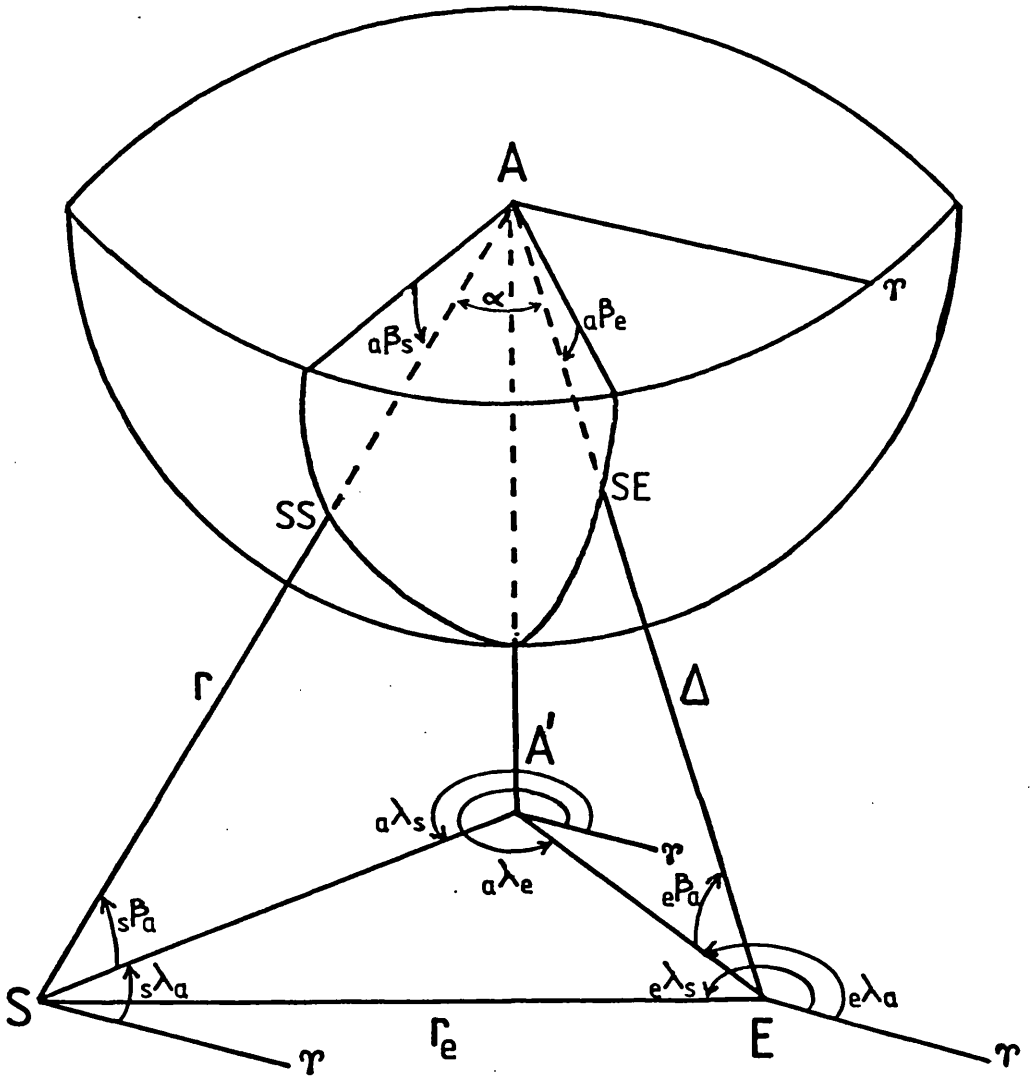


Fig. A.1 Orientation of asteroid, A, with respect to the Sun, S, and the Earth, E. A´ is the position of the asteroid projected onto the ecliptic plane. SS and SE are the subsolar and sub-Earth directions respectively.

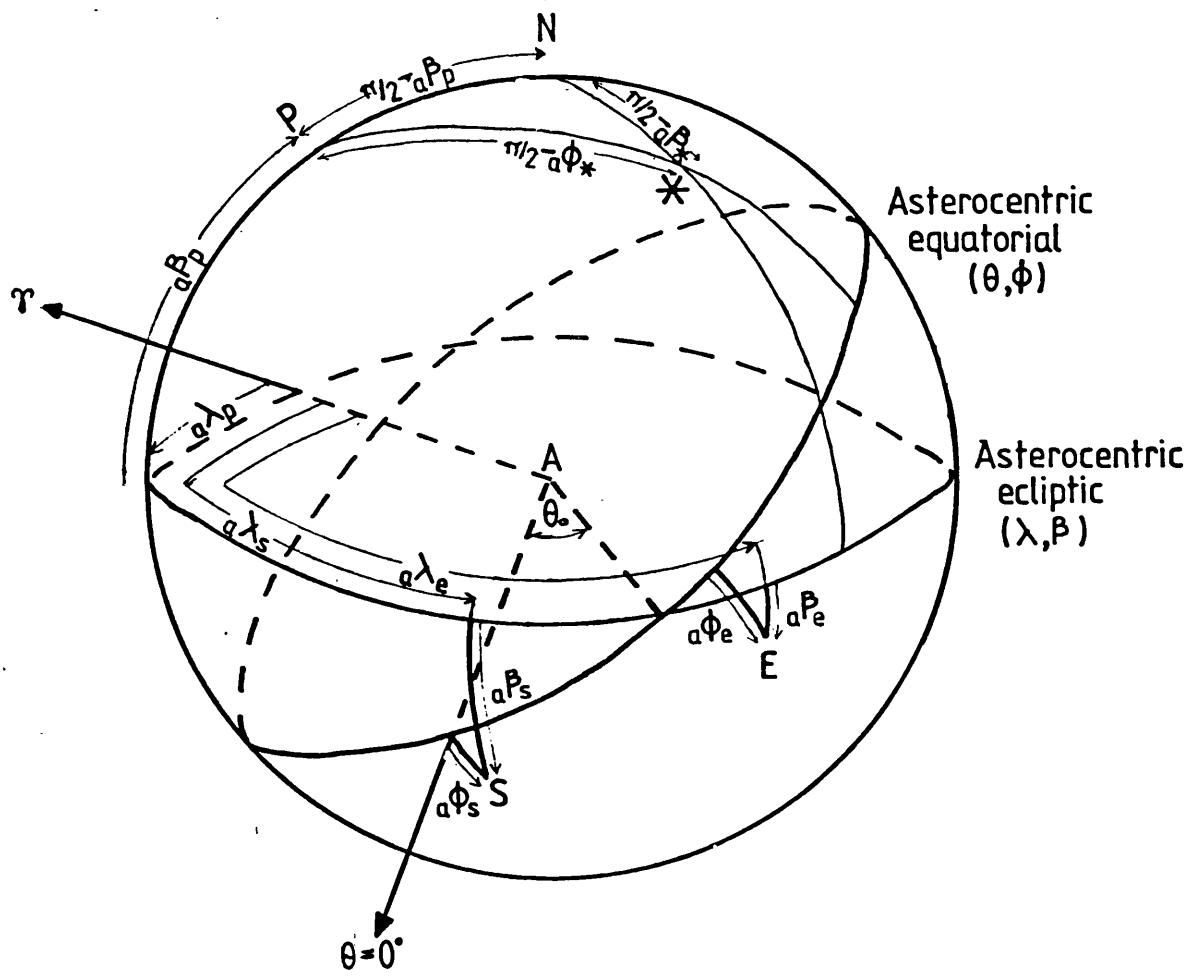


Fig. A.2 Orientation of the asterocentric equatorial and ecliptic planes. S and E are directions of the Sun and Earth respectively.

"+" when $0 \leq {}_e\lambda_s - {}_e\lambda_a < \pi$, or ${}_e\lambda_s - {}_e\lambda_a < -\pi$,

"-" when $-\pi \leq {}_e\lambda_s - {}_e\lambda_a < 0$, or ${}_e\lambda_s - {}_e\lambda_a > \pi$.

$${}_a\beta_s = -\text{ATAN}\ [\ \Delta \sin {}_e\beta_a / \underline{SA}'\ ]$$

The phase angle $\alpha = \text{ACOS}\ [\ (\ r^2 + \Delta^2 - r_\varepsilon^2\ )/(\ 2\ r\ \Delta\ )\ ]$

Fig. A.2 shows the orientation of the asterocentric ecliptic, $({}_a\lambda, {}_a\beta)$, and equatorial, $({}_a\theta, {}_a\phi)$, coordinates. The prime meridian of the asterocentric equatorial coordinate system ($\theta$=0) passes through the solar direction.

To convert from ecliptic to equatorial coordinates (solving the N-P-* spherical triangle):-

$${}_a\phi_\star = \text{ASIN}\ [\ \sin {}_a\beta_\star \sin {}_a\beta_p + \cos {}_a\beta_\star \cos {}_a\beta_p \cos({}_a\lambda_\star - {}_a\lambda_p)\ ]$$

$$\theta_\star = \theta_0 + \pi/2 \pm \text{ACOS}\ [\ (\sin {}_a\beta_\star - \sin {}_a\phi_\star \sin {}_a\beta_p)/(\cos {}_a\phi_\star \cos {}_a\beta_p)\ ]$$

"+" for ${}_a\lambda_\star < {}_a\lambda_p$, or ${}_a\lambda_\star > \pi + {}_a\lambda_p$

"-" for ${}_a\lambda_p \leq {}_a\lambda_\star \leq \pi + {}_a\lambda_p$

where $\theta_0$ is given by:-

$$\theta_0 = 3\pi/2 \pm \text{ACOS}\ [\ (\sin {}_a\beta_s - \sin {}_a\phi_s \sin {}_a\beta_p)/(\cos {}_a\phi_s \cos {}_a\beta_p)\ ]$$

"+" for ${}_a\lambda_p \leq {}_a\lambda_s \leq \pi + {}_a\lambda_p$

"-" for ${}_a\lambda_s < {}_a\lambda_p$ or ${}_a\lambda_s > \pi + {}_a\lambda_p$

When solving the conduction equation for a surface element, the angle between the surface normal and the direction of the Sun is required for each time step. The surface coordinate system, which rotates with the asteroid, $(\eta, \zeta)$, is defined as equal to $({}_a\theta, {}_a\phi)$ for $\tau$=0. For a spherical asteroid, the coordinates of the surface normal are

$$({}_a\theta_n, {}_a\phi_n) = (\ \eta + 2\pi\tau,\ \zeta\ )$$

## APPENDIX F

List of Publications.


Eaton N., S.F. Green, R.S. McCheyne, A.J. Meadows, G.J. Veeder. Observations of Asteroids in the 3- to 4-μm Region. Icarus 55 245-249, 1983.

Davies J.K., N. Eaton, S.F. Green, R.S. McCheyne, A.J. Meadows. The Classification of Asteroids. Vistas in Astronomy 26 243-251, 1982.

Walker R.G., H.H. Aumann, J. Davies, S. Green, T. de Jong, J.R. Houck, B.T. Soifer. Observations of Comet IRAS-Araki-Alcock 1983d. Astrophys. J. 278 L14-18, 1984.

Davies J.K., S.F. Green, B.C. Stewart, A.J. Meadows, H.H. Aumann. The IRAS Fast-moving Object Search. Nature 309 315-319, 1984.

Stewart B.C., J.K. Davies, S.F. Green. IRAS Fastmover Program. J. Brit. Interplan. Soc. 37 348-352, 1984.

McCheyne R.S., N. Eaton, S.F. Green, A.J. Meadows. B and V Lightcurves and Pole Positions of Three S-Class Asteroids. Icarus 59 286-295, 1984.

Eaton N., J.K. Davies, S.F. Green. The Anomalous Dust Tail of Comet P/Tempel 2. M.N.R.A.S. 211 15P-19P, 1984.

Green S.F., N. Eaton, D.K. Aitken, P.F. Roche, A.J. Meadows. 8-13μm Spectra of Asteroids. Icarus, in press.

Green S.F., A.J. Meadows, J.K. Davies. Infrared observations of the extinct cometary candidate (3200) 1983TB. M.N.R.A.S., in press.

Conferences etc.

+Meteoritical Society 46th Annual Meeting, Mainz, Sep 3-9 1983. Symposium "From Asteroids to Meteorites."

*Green, S.F., N. Eaton, R.S. McCheyne, A.J. Meadows. Spectrophotometry of Asteroids in the Infrared. (Abstract) Meteoritics 18 306, 1983.

*McCheyne, R.S., N. Eaton, S.F. Green, A.J. Meadows. Asteroid Light Curves and surface Properties. (Abstract) Meteoritics 18 350, 1983.

18th European Space Symposium, London, June 6-9 1983.

*Davies, J.K., S.F. Green. IRAS, The First Four Months in Orbit. In "Space: A Developing Role For Europe" (ed L.J. Carter, P.M. Bainum. American Astronautical Soc., San Diego, California.) Science and Technology Series, 56 117-122, 1984.

15th Annual Meeting of the Division for Planetary Sciences, Ithaca N.Y. 16-20 Oct 1983.

Davies, J.K., S.F. Green, N. *Eaton. The Discovery of Comets with IRAS. (Abstract) Bull. Amer. Astron. Soc. 15 804, 1983.

+The Eighth U.K. Geophysical Assembly, Univ. of Newcastle, April 9-11 1984.

*Green, S.F., Asteroid Thermal Emission. (Abstract) Geophysical Journal 77 324, 1984.

+Royal Astronomical Society Discussion Meeting, "The First Results from IRAS." London, May 11, 1984.

*Thermal Modelling of Asteroids and its Application to IRAS Data.

+Attended

*Presented paper

# Infrared Observations and Thermal Emission Models of Asteroids.

Simon F. Green 1985

A review of the classification of asteroids according to their orbital and physical properties is presented and the technique of numerical taxonomy is applied to catalogued optical data.

The size distribution of minor bodies is of fundamental importance for theories of the origin and formation of the Solar System. Methods of diameter determination are reviewed with particular reference to the radiometric method. Thermal emission models of asteroids are essential for the reduction of infrared observations to obtain radiometric diameters and albedos. Various thermal models are described, with an emphasis on the assumptions made, and their limitations. The models are applied to observations in the 8-13μm region to examine possible variations of emissivity with wavelength, to remove the thermal component from reflection spectra in the 3-4μm region, and to determine the nature of the surface of the unusual asteroid (3200) 1983TB.

The Infrared Astronomical Satellite (IRAS) was launched in 1983 to provide an all-sky survey in four infrared wavebands. In order to prevent detections of the thermal emission from moving objects from being lost, software was written to search the rejected survey data in near real-time. As well as detecting several hundred numbered asteroids and five known comets, two main belt asteroids, two Apollo asteroids, six comets and an infrared tail on comet Tempel-2 were discovered. A description of the moving object software and its implementation is presented, together with estimates of the selection effects and completeness of the search, and analysis of the data. The ground-based observations of the Apollo asteroid (3200) 1983TB do not support the cometary nucleus hypothesis inferred from its orbital characteristics. A preliminary analysis of some IRAS additional observations of asteroids is also presented.